FRM II
Forschungs-Neutronenquelle
Heinz Maier-Leibnitz

Annual Report 2010

FRM II
Forschungs-Neutronenquelle
Heinz Maier-Leibnitz

Technische Universität München
Forschungs-Neutronenquelle
Heinz Maier-Leibnitz (FRM II)
www.frm2.tum.de

Content

1 Directors' Report

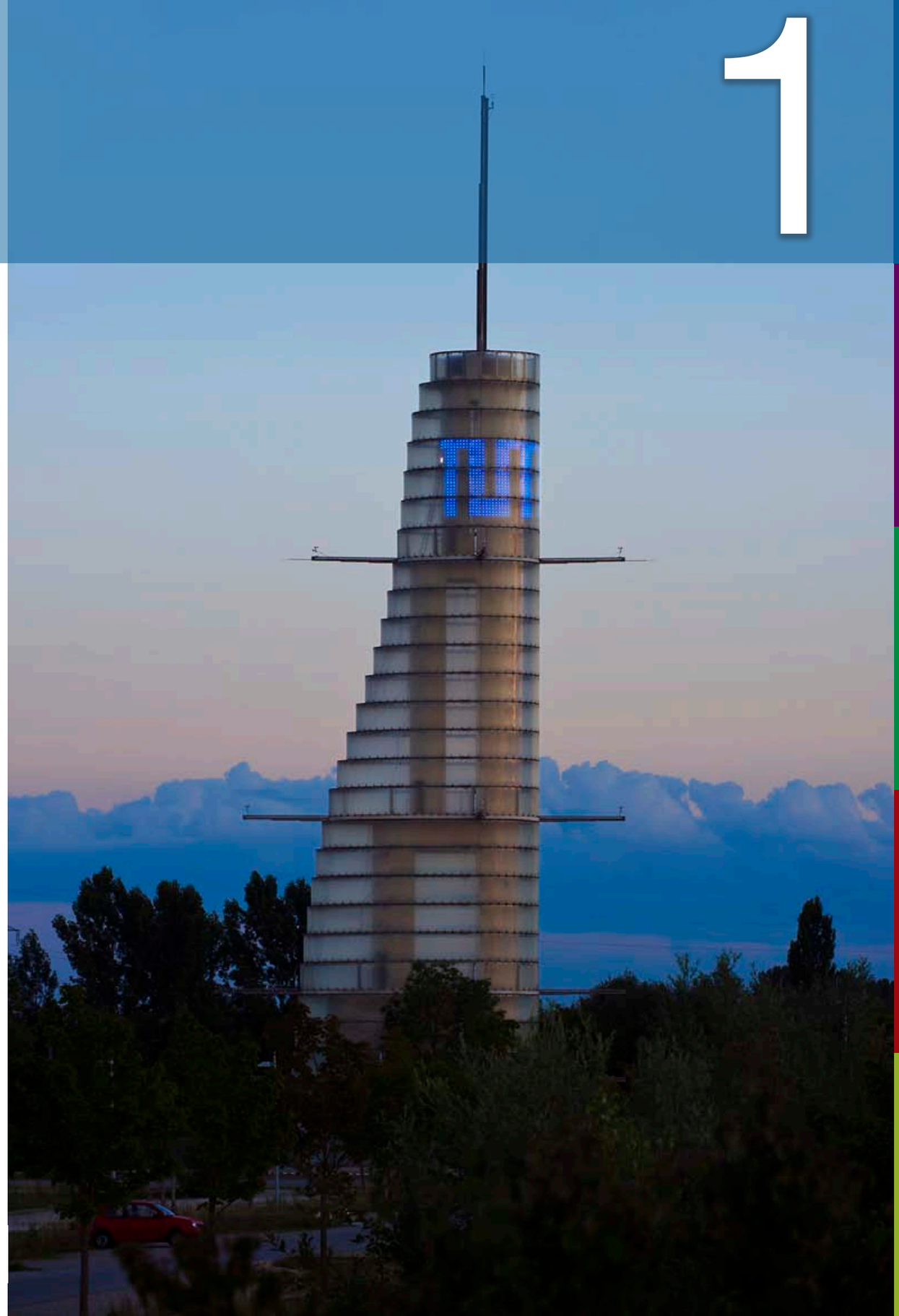

The new meteo tower of the Technische Universität München,
measuring weather data for the FRM II.

Directors' Report: Progress through change

In hindsight, the year 2010 will surely rank as a major milestone in the fledgling history of the FRM II. On December 17th, the Technische Universität München and the Helmholtz Centres in Jülich, Geesthacht and Berlin signed a contract confirming their collaboration and the promotion of the scientific use of the FRM II. At this time, an agreement was also reached between the Bavarian State Ministry of Science, Research and Arts and the Federal Ministry of Education and Research (BMBF) on the financial contribution of the Federal Republic to the scientific exploration of the FRM II to the tune of 198 Mio€ over the following ten years. Together with the annual budget of 25 Mio€ from Bavaria and 10.5 Mio€ from the HGF centres, this will allow us to further improve the service and optimise use of the German neutron source.

Late 2010 saw the beginning of our first long maintenance period in order to exchange the beam tube (SR) 11 and, thus, rebuild the positron source. The cadmium inside the beam nose had burned up and had to be replaced. On this occasion, an elongated thimble was installed in the heavy water moderator tank in order to accommodate the future irradiation facility for ^{99}Mo production: A small but important step to prepare the FRM II for the production of this medical isotope which is in such high demand. In addition, a comprehensive number of maintenance procedures were undertaken by the reactor department under the guidance of our new technical director, Dr. Anton Kastenmüller.

In parallel, the science division dismantled entirely the radiography and tomography station ANTARES which will move from beam port SR4b to SR4a in order to free the SR4b port for the particle physics instrument MEPHISTO, which will become the first instrument operational in the new neutron guide hall east. The beam dump in SR9a was removed to allow for a new beam port for PoliHeidi, the single crystal neutron diffractometer using hot polarized neutrons. In this way, it will become an independent instrument in the future. A major upgrade involved the addition of 400 detector tubes for the time-of-flight instrument TOFTOF. Under commission and ready for the first friendly users are our single diffractometer for large structures BIODIFF (joint project of TUM and JCNS) and the high intensity reflectometer MARIA of the JCNS. From the perspective of the expectant first users, great strides were made in the commissioning of the huge SANS-1 machine (HZG and TUM).

Looking towards the future, new large projects will appear as the DFG funded PERC instrument for particle physics at the instrument MEPHISTO, and a large number of instrumentation projects funded by the BMBF within the context of Collaborative Research (Verbundforschung), having a three year budget for instruments at the FRM II, totalling 10.2 Mio€. The ultra cold neutron source with projected instruments to investigate the neutron life time and the electric dipole-moment, respectively, progresses well. Besides these fascinating topics on site, the FRM II is looking even further, across the borders to the new European Spallation Source in Scandinavia, ESS. In May 2010, the FRM II signed a Memorandum of Understanding with the ESS to collaborate in the area of scientific, educational and industrial applications. Together with our colleagues from the Helmholtz Centres we will, over the next three years, contribute to the design update phase of the ESS funded mainly by the BMBF.

Klaus Seebach

Winfried Petry

Anton Kastenmüller

The year in pictures

April 30th

The new laboratory in the industrial applications centre of the FRM II is inaugurated. It is dedicated to the preparation of samples and offers the analysis of organic colloidal samples.

November 22nd

Works to exchange the beam tube SR11 of the positron source NEPOMUC have started. The experimental tube is being removed.

September 3rd

The Consul General of the United States in Munich, Conrad R. Tribble (4th from the right), visits the neutron source. He is accompanied by members of the company General Electric. The directorate of the FRM II guides the group.

September 11th

The mayor of Garching, Hannelore Gabor (m.), meets the Technical Director of the FRM II, Anton Kastenmüller (r.). She introduces her new office manager Hans-Martin Weichbrodt.

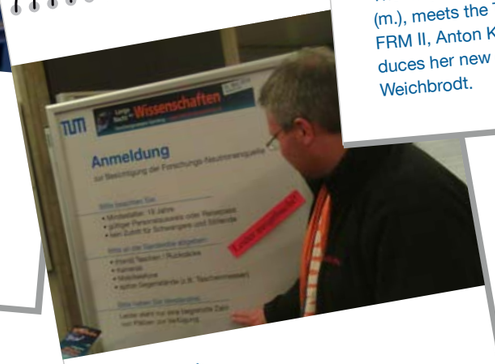

May 15th

Visitor of the German Church Congress in front of a poster for the FRM II Long Night of Science announcing that the tours are fully booked. More than 400 visitors got the chance to take a look a the interior of the neutron source.

July 25th

A dozen students decided to tour the neutron source on the „Schülertag" at the Technische Universität München. They were interested in studying physics.

March 16th

Chun Loong of the Tsinghua University in Peking presents the compact pulsed hadron source to members of the FRM II.

April 13th

At the VDI expert meeting, 60 participants from business and academia discussed methods for non-destructive testing of industrial components.

April 8th

FRM II Scientific Director, Winfried Petry is interviewed by the German broadcasting company 3sat. The focus is on nuclear energy.

May 15th

Children of FRM II staff members were allowed to meet the reactor drivers on the occasion of the Long Night of Science. They could enter the switch room, gaze into the reactor pool and look at the instruments in the neutron guide hall west.

The year in pictures

July 22nd

The FRM II sends its own running team to the be2run, a corporate challenge in Munich. The twelve members ran 6.4 km. Stefan Söllradl (back row, left), the fastest of the team, became 20th of a total of 20,000 participants in 21 min. 55 sec.

June 29th

A Canadian delegation of physicians and businessmen interested in the production of radioisotopes at the FRM II, visits the neutron source guided by Administrative Director, Klaus Seebach (l.) and deputy Scientific Director, Jürgen Neuhaus (4th from right).

August 12th

Students of the Erasmus Mundus MaMaSELF programm, having performed their master thesis at the FRM II, with their tutor, Scientific Director Winfried Petry.

July 26th

The President of the Technische Universität München, Wolfgang Herrmann, welcomes Prime Minister Horst Seehofer at the neutron source Heinz Maier-Leibnitz.

July 26th

The Bavarian Prime Minister, Horst Seehofer, gazes at the positron source NEPOMUC. During his first visit of the FRM II, Seehofer praised the neutron source as a symbol for the strong research in Bavaria.

November 4th

Women of the German Physicists Association DPG meet at a congress in Munich. One of the highlights of the program was the visit at the FRM II, with two accompanying men.

November 11th

The old storage building of the company Kraftanlagen München at the FRM II area is taken down to make way for a new storage depot to be built in 2011.

March 5th

The FRM II will play a major role in the project on alternative techniques for ^{3}Helium-based detectors for neutron scattering applications. This is decided at a meeting at the Institut-Laue-Langevin in Grenoble including FRM II Scientific Director Winfried Petry.

September 27th

The member of the German parliament, Stefan Kaufmann (CDU, m.), takes a tour of the neutron source. He is accompanied by the FRM II Adminstrative Director Klaus Seebach (l.) and the Scientific Deputy Director Jürgen Neuhaus.

October 5th

The Director General of the IAEA, Yukiya Amano (r.), visits the FRM II guided by the Scientific Director Winfried Petry (2nd from right). He is accompanied by the Bavarian Minister for Science, Wolfgang Heubisch, and Sebastian Schmidt (l.) of FZ Jülich.

The year in pictures

March 5th

Members of the German Ministry for Education and Research look at the reactor pool and listen to the explanations of the FRM II Technical Director Ingo Neuhaus (r.) and the Adminstrative Director Klaus Seebach (l.).

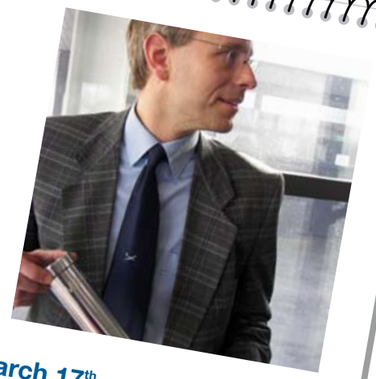

March 17th

After four years presiding over the operation of the FRM II, Ingo Neuhaus leaves the neutron source in Garching for the nuclear power plant Krümmel equipped with a mini-replica of the FRM II fuel element.

June 22nd

Thanks to the great effort of the reactor operation staff, the defect motor of the compressor operating the cold source is quickly exchanged. The 24th cycle is continued, the missing days are added to the cycle.

June 18th

Harald Breitkreutz recieves the European Young Scientists' Award of the International Association for Radiation Protection represented by Alfred Hefner for his diploma thesis at the medical instrument MEDAPP.

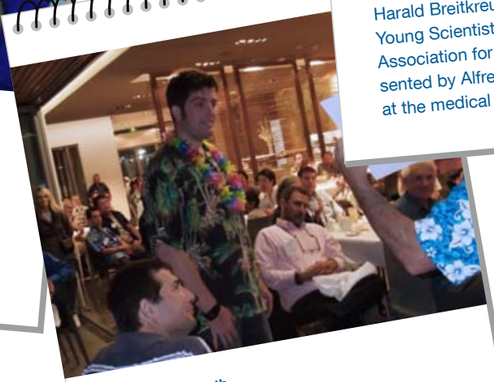

August 6th

Hubert Ceeh (FRM II) receives a student prize for his talk about his diploma thesis at the international workshops on Slow Positron Beam Techniques in Australia. The next international conference on positrons will be held in 2013 at the FRM II.

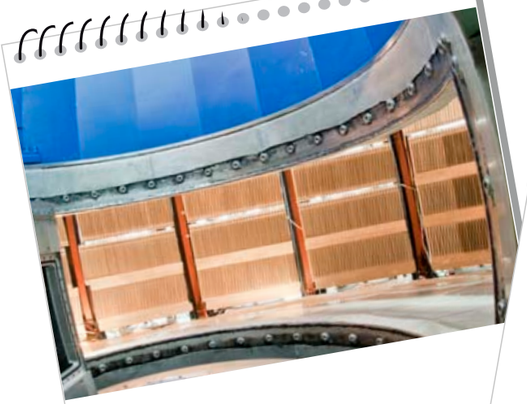

December 2nd

The time-of-flight spectrometer TOFTOF's capacity is increased from 600 to 1000 detectors improving its resolution by a factor of 1.8.

November 15th

The shielding of the radiography and tomography instrument ANTARES is deconstructed and shifted from beam tube 4b to 4a to enable the construction of a neutron guide towards the new neutron guide hall east.

April 28th

Memorandum of understanding between the FRM II and the ESS (from left): Director of the ESS, Colin Carlile, Danish Minister of Science Charlotte Sahl-Madsen, Bavarian Minister of Science Wolfgang Heubisch and FRM II Scientific Director Winfried Petry.

July 13th

Staff members of the FRM II queue patiently for grilled sausages at the annual FRM II summer festival.

November 25th

Decorating the Christmas tree in front of the main entrance with the help of a lifting platform.

Instruments & Methods

2

Changing the beam tube at the positron source
in the experimental hall.

Instrumental improvements

A. Ostermann[1], A. Heinemann[2], S. Mattauch[3], R. Georgii[1], V. Hutanu[4], M. Hofmann[1], B. Pedersen[1],

[1]Technische Universität München, Forschungs-Neutronenquelle Heinz Maier-Leibnitz (FRM II), Garching, Germany
[2]Helmholtz-Zentrum Geesthacht, Outstation @ FRM II, Garching, Germany
[3]Forschungszentrum Jülich GmbH, Jülich Centre for Neutron Science at FRM II, Garching, Germany
[4]RWTH Aachen, Institut für Kristallographie, Aachen, Germany

During 2010 we continued in our efforts to provide the user community with state-of-the-art instrumentation. Some instruments were upgraded (including KWS-2, MIRA and STRESS-SPEC), others, such as BIODIFF, MARIA and POLI became operational, and new projects such as the proton electron radiation channel PERC were started.

BIODIFF: First neutron availability

The new monochromatic single crystal diffractometer BIODIFF is designed to collect data from crystals with large unit cells. The main field of application is the structure analysis of proteins, especially the determination of hydrogen atom positions. The first neutron beam struck a protein crystal at BIODIFF in October. At this time, the CCD camera was already mounted and had been successfully tested with neutrons (see fig. 1).

In December 2010, the image plate detector was installed. The commissioning phase of the instrument will start in 2011 with the first reactor cycle. After which BIODIFF will be available to friendly users.

Full detector distance at KWS-2

The small angle scattering facility KWS-2, in a short version with a maximum detector distance of 8 m, has been in user-operation since September 2007. In order to correct this disadvantage, a huge effort is currently being undertaken, and it will be possible to offer users the full 20 m detector distance (fig. 2) in April 2011.
Furthermore, a double-disk chopper will provide high resolution SANS measurements with a Q-resolution of typically 1 %. The new neutron lens chamber will be installed in parallel. The cooling of the lenses to 70 K will suppress parasitic phonon scattering.

Figure 1: The instrument BIODIFF.

Figure 2: At KWS-2 an upgrade to a 20 m detector tank and improved neutron optics has been undertaken.

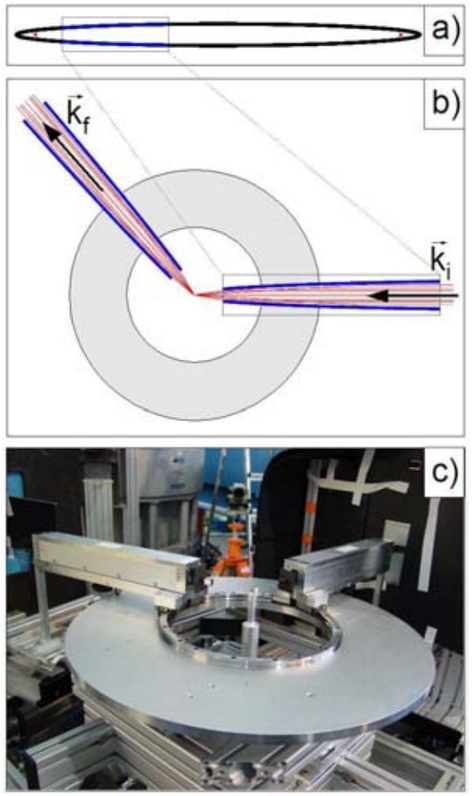

Figure 3: The focussing guide setup at MIRA.

Serving the field of spintronics: MARIA

The new high flux polarized neutron reflectometer MARIA (**MA**gnetism **R**eflectometer with high **I**ncident **A**ngle) of the JCNS is optimised for the study of magnetic nanostructures, serving the rapidly growing field of spintronics or magnetoelectronics, i.e. information storage, transport and processing using the spin of the electrons. Therefore MARIA is optimised for layer thicknesses between 3 and 300 Å, lateral structures of nm to µm sizes and sample sizes of 10 x 10 mm².
Beside the reflectometer mode with good resolution in the horizontal scattering plane, MARIA is able to measure in the GISANS mode with additional resolution in the vertical direction. The latter mode allows to measure lateral structures down to the nm-scale.

Focussing elliptic neutron guide at MIRA

MIRA performed first proof of principle measurements with a focussing elliptic neutron guide set-up. After successful alignment, magnetic Bragg reflections of the antiferromagnet chromium and incoherent scattering of vanadium were measured. As a result, for small samples, an intensity gain of 5.5 for the coherent elastic scattering of chromium and 19 for the incoherent scattering of vanadium was achieved.
The highly improved signal to noise ratio makes the new set-up usable for neutron scattering experiments with high-pressure cells (fig. 3). First measurements with the magnetic Bragg reflections of MnSi in a pressure clamp cell (2.5 kbar) were successfully performed.

Polarized neutrons at PANDA and POLI

The first user experiment using the polarized neutrons option at PANDA was successfully performed in 2010. The full routine availability is expected for 2011. The sample setup can be seen in figure 4.
Polarized **n**eutron **d**iffraction (PND) and 3D polarization analysis or **s**pherical **n**eutron **p**olarimetry (SNP) will be implemented on the new polarized single crystal diffractometer at the FRM II, named POLI (**pol**arization **i**nvestigator diffractometer). SNP was successfully tested in 2010

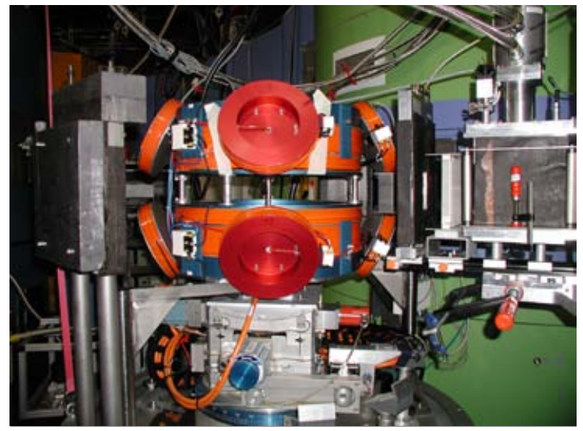

Figure 4: Sample setup for polarized neutron experiments at PANDA.

Figure 5: The new STRESS-SPEC robot system in operating position, the beam coming from the left. The detector is in the back.

and became available to the users of the FRM II. Taking into account the large demand on beam time for both polarized and non-polarized experiments (the actual overbooking factor at SR9 is more than 3), it was decided to build a separate beam port for POLI on the available SR9a channel. During the maintenance break 2010/2011, the second beam port at SR9 will be opened to allow POLI to move to its own dedicated beam and monochromator. The full operation of POLI is planned for 2013.

New detector installed at SANS-1

Significant progress towards the commissioning of the new SANS-1 facility at FRM II has been made. To allow magnetic measurements, the polarised neutron option has been optimised by installing a new spin-flipper now reaching a measured polarisation of 96 %. The whole guide field has been painstakingly measured and improved where necessary. In order to further improve the accuracy and reproducibility of the collimation system, a laser alignment system was installed. This will not only allow a redundant neutron guide alignment but also an exceptional sample and sample environment positioning for the SANS-1 instrument. The new 1 x 1 m² detector has been physically and electrically installed and tests and calibration routines are in progress. As for new options, a high resolution velocity selector and detector will soon become available. The very flexible Huber table installed in 2010 is working as a basis for all alignment and positioning tasks within the sample environment.

STRESS-SPEC goes robotic

In order to overcome spatial limitations in gradient investigations of residual stresses and crystallographic textures in semi-finished or finished products at STRESS-SPEC, a robot system supported by the BMBF was developed. This robot project began at the end of 2007 through cooperation between TU Clausthal, IWB at TUM, HZG (former GKSS) and FRM II. The robot is now available for bulk, local texture and stress investigations in cooperation with the instrument group.

The robot system consists of a standard Stäubli RX160 industrial robot (fig. 5), a laser tracker and a heavy vibration free basement. It has 6 degrees of freedom for sample movement with a load capacity to 25 kg. A maximum workspace of 500 mm in all directions is possible with this setup. Before the actual measurement, the movement of the robot can be simulated offline to ensure its correct path and avoid collisions with the optical systems of the diffractometer. In March 2010, the first successful combined stress and texture analysis on a rotary friction welded (RFW) Al7020/Austentic steel 316L sample was conducted, demonstrating the advantages of the robot system.

Figure 6: X-ray tomography station at the IMETUM.

New instrument for X-ray tomography

To improve the use of complementary methods, the Chair of Biomedical Physics at the Technische Universität München (IMETUM) and FRM II have started to operate a high resolution computer tomography facility (see fig. 6). The “micro CT VtomeX” is also available to users of the FRM II. Samples that can be examined include geo and composite materials, semiconductors and biomedical specimens.

Ongoing upgrades

The cold neutron tomography station ANTARES has started its move from beam port 4b to port 4a in preparation for the guide system to the new guide hall east. This task includes a redesigned shielding, new shutter inserts and improved neutron optics.

The high intensity positron source NEPOMUC effected a major upgrade of its in-pile component. The cadmium which is used in the beam tube for positron generation is exhausted and now replaced by isotopically enriched Cd. This ensures that the beam tube is usable for a much longer time. During this replacement the beam optics in the tube were also replaced with improved versions.

Future instrument: PERC

PERC (**p**roton **e**lectron **r**adiation **c**hannel), proposed by D. Dubbers, is a versatile instrument providing a clean and bright beam of charged neutron decay products. The users can concentrate on the construction of secondary spectrometers and no longer need to worry about the neutron beam.

PERC is funded by the priority programme “Precision experiments in particle- and astrophysics with cold and ultracold neutrons” (SPP 1491) of the Deutsche Forschungsgemeinschaft. It will be built in collaboration between Universität Heidelberg, Technische Universität Wien, Institut Laue Langevin and Universität Mainz at the FRM II.

Figure 7: View into the neutron guide hall west.

Decay rate measurement of the negative positronium ion

H. Ceeh[1], S. Gärtner[2], C. Hugenschmidt[1,3], K. Schreckenbach[1], D. Schwalm[4], P. Thirolf[2]

[1]Technische Universität München, Physik Department E21, Garching, Germany
[2]Ludwig Maximillians-Universität, Fakultät für Physik, Garching, Germany
[3]Technische Universität München, Forschungs-Neutronenquelle Heinz Maier-Leibnitz (FRM II), Garching, Germany
[4]Max-Planck-Institut für Kernphysik, Heidelberg, Germany

The negative positronium ion Ps^- is a bound system consisting of two electrons and a positron. Its three constituents are point-like and stable leptonic particles with equivalent mass, which are only subjected to the electroweak and the gravitational force. Several high precision measurements of the decay rate Γ have been performed at the NEPOMUC facility. The combined results of systematic test measurements are discussed and the prospect for future measurements as well as the results of the most recent beam time will be given.

Since its prediction by Wheeler in 1946 [1], the Ps^- has been the subject of numerous theoretical investigations as it resembles a unique model system for three-body quantum mechanics. Since all its constituents are point-line particles with the same mass, the Born-Oppenheimer approximation, which drastically simplifies the theoretical treatment, cannot be applied, other than in comparable systems like the He^+ or the H^- ion. Therefore, special techniques for the solution of the full quantum mechanical three-body problem had to be developed. However, few experimental studies dealt with Ps^-. It took until 1981 for the experimental proof of its existence to be presented by Mills, followed by the first determination of the Ps^- decay rate in 1983 [5,6]. In 2006, Frank Fleischer successfully applied a combination of the beam-foil technique and a stripping based detection setup to produce Ps^- and to measure its decay rate [2,3].

Due to the low intensity positron sources used by Mills as well as by Fleischer, the measurements were largely limited by statistics. Therefore, the Heidelberg setup was slightly modified and transferred to the NEPOMUC facility in Munich, in order to increase statistics to allow a first critical test of the calculated QED-corrections to the decay rate [2]. Once the remoderation stage became available [4], the beam energy could be decreased from ≈ 1000 eV to 20 eV. This made a systematic study of the Ps^- decay rate as a function of the incident positron beam energy possible. This investigation revealed a dependence of the measured Ps^- decay rate on the energy of the incident positrons, which was eliminated by a modified setup (for details see [10]). The technical details of the advanced Ps^- setup and first results of the decay rate measurement are presented.

The positronium ion is stripped

The beam-foil technique was applied to produce Ps^- and a tandem-like setup was used for the detection of Ps^-.

The principle of this decay rate measurement is based on the measurement of the amount of surviving Ps^- ions as a function of their eigen time. Therefore, Ps^- are produced and then drifted with defined energy over a decay gap with variable length. The intensity of the surviving Ps^- ions is measured as a function of the width of the decay gap d: $I \propto e^{-\mu \cdot d}$. Hence, the decay rate Γ in the eigen system can be derived from the decay constant μ in the lab system provided that the velocity of the Ps^- is known to sufficient accuracy.

A schematics of the used setup is shown in figure 3. The high intense positron beam provided by NEPOMUC is guided onto a DLC foil. On passing through the foil the positron loses its energy and picks up two electrons to form Ps^-. The Ps^- ions, which emerge from the foil, are accelerated in an electric field to their final energy of $(U_{accel} - U_{prod})\ e = 2500$ eV. After the acceleration the Ps^- enters the field-free decay gap. The surviving Ps^-, which hurdle the decay gap, are further accelerated in a tandem-accelerator-like setup, where the two electrons are stripped off the Ps^- ion and only the positron remains. This highly energetic (40 keV) positron, which serves as a fingerprint for Ps^-, is magnetically guided onto a silicon particle detector.

The Ps^- vacuum decay rate Γ can hence be calculated from the measured decay constant μ:

$$\Gamma = \mu\beta\gamma c \qquad (1)$$

with

$$\beta = \sqrt{1 - \frac{1}{\left(1 + \frac{(U_{accel} - U_{prod})e + E_0}{3m_e c^2}\right)^2}} \qquad (2)$$

the Lorentz factor $\gamma = (1 - \beta^2)^{-1/2}$, e the electron charge and m_e the electron mass.

Decay rate measured more accurately

The evaluation of a recently completed beam time of about 10 days shows that with the increased statistics and the refined setup we are able to increase the accuracy for the decay rate measurement by a factor of 2-3 compared to previous measurements:

$$\Gamma = 2.0869(67)\ ns^{-1}$$

This value is in perfect agreement with recent theoretical calculations for the decay rate of $\Gamma_{Th} = 2.087963(12)\ ns^{-1}$ [8] as well as with the value obtained in Heidelberg $\Gamma_{Exp} = 2.089(15)\ ns^{-1}$ [3]. The measurement was performed using the setup with the field-free decay gap, which we presented here. A complete discussion of the measurement and the data and error treatment is about to be published.

Outlook

Complementary to the decay rate measurement, an experiment for the Ps^- photo detachment and the production of a mono energetic ortho-positronium beam is already in preparation and will soon be operational.

[1] J.A. Wheeler, Annals of The New York Academy of Science, 48, 219 (1946).
[2] F. Fleischer, PhD Thesis, Max-Planck-Institut für Kernphysik Heidelberg (2005).
[3] F. Fleischer et al., Phys. Rev. Lett., 96 (6), 063401 (2006).
[4] C. Piochacz et al., Appl. Surf. Sci., 255 (1), 98 (2008).
[5] A.P. Mills, Phys. Rev. Lett., 46 (11), 717 (1981).
[6] A.P. Mills, Phys. Rev. Lett., 50 (9), 671 (1983).
[7] A.P. Mills et al., NASA Conference Publication, 3058, 213 (1990).
[8] M. Puchalski et al., Phys. Rev. Lett., 99 (20), 203401 (2007).
[9] H. Ceeh, Diploma Thesis, Technische Universität München (2009).
[10] H. Ceeh et al, JPCS, 262, in press.

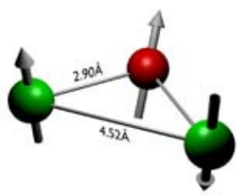

Figure 1: Artist concept of the Ps^- ion. The spins of the two electrons (green) are aligned in anti-parallel directions. The spin orientation of the positron (red) is not fixed.

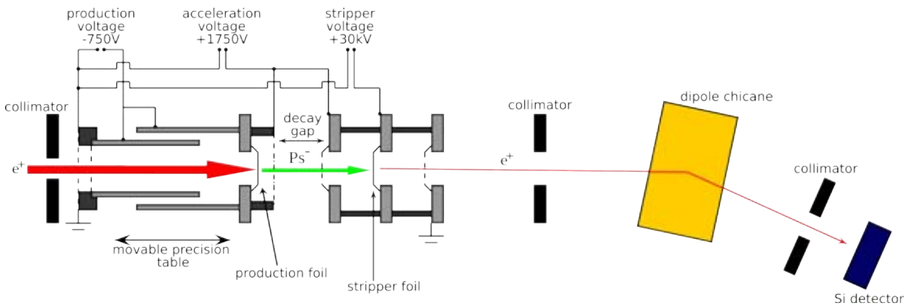

Figure 2: Above: Schematics of the Ps^- setup. From left to right: Production and acceleration device, field-free decay gap and tandem-like stripping and detection unit. Below: The landscape of the electric potential.

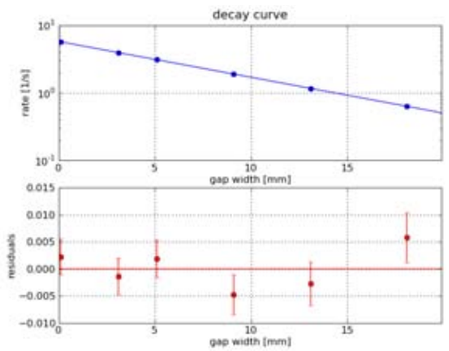

Figure 3: Decay curve of Ps^- for an acceleration voltage of 2500 V (error bars are smaller than the point symbols) and residuals of the χ^2-fitting procedure.

SEOP polarized ^{3}He for polarization analysis at the JCNS

E. Babcock, S. Mattauch, V. Pipich, A. Radulescu, S. Staringer, A. Ioffe

Forschungszentrum Jülich GmbH, Jülich Centre for Neutron Science at FRM II, Garching, Germany

Neutron polarization analysis is a key feature of instruments at the JCNS. We are working to develop polarized ^{3}He neutron spin analyzers based on the **s**pin-**e**xchange **o**ptical **p**umping (SEOP) method to create unique and optimal solutions for each application. Two early applications are in-situ, ^{3}He polarizers for reflectometry and SANS. The system optimized for reflectometry is complete and achieved a ^{3}He polarization of > 80 % in testing. It has already been used as an analyzer for polarized GISANS on the MARIA reflectometer. Feasibility testing of polarization analysis using ^{3}He was also performed on KWS-2 (SANS) using off-line polarized gas. Based on that experience we are currently constructing another in-situ SEOP polarizer that has been optimized for the KWS instruments.

The polarizer

The ^{3}He polarizer for the MARIA reflectometer is shown in figure 1. It uses a mu-metal shielded magnetostatic cavity which has been measured to provide magnetic relaxation times for the ^{3}He cell of the order of 1000 hours at 1 bar ^{3}He pressure, even in the presence of stray magnetic fields from the sample magnet. The system features two grating spectrum-narrowed and stabilized diode laser arrays for optical pumping of up to a 15 cm diameter ^{3}He cell and has a high performance adiabatic fast passage system to reverse the direction of the ^{3}He polarization. This allows a reversible analysis direction and therefore a neutron flipper when the sample is no longer required.

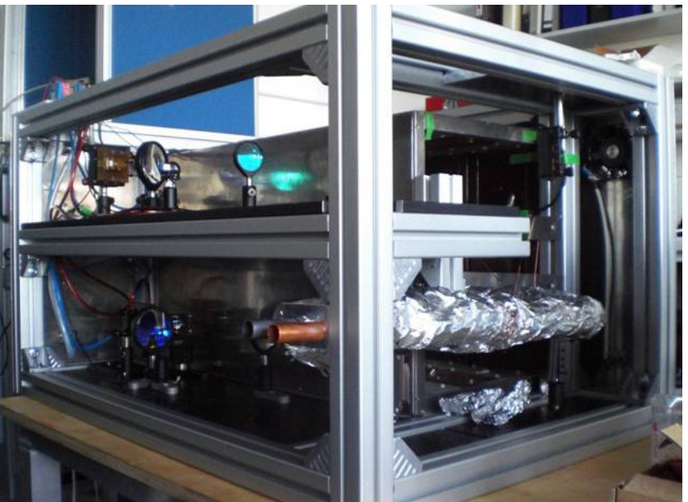

Figure 1: The in-situ SEOP polarizer.

When tested on the TREFF reflectometer, a high performance 6 cm diameter cell was used. After optimization of parameters, the system achieved a high level of stability and obtained a saturated ^{3}He polarization of over 80 % [1]. The ^{3}He polarization, monitored via the unpolarized neutron transmission of the cell, is shown in figure 2.

Polarization analysis at MARIA

During the last reactor cycle of 2010, the system was installed for **p**olarization **a**nalysis (PA) on MARIA for the first polarized GISANS measurement. To obtain an angular coverage over a circle of 4.6°, we used a 9 cm I.D. cell. The system was fully operational and stable over the week-long experiment. The neutron analyzing efficiency at 4.5 Å was 95 % and the neutron transmission was high at > 40 % for the polarized beam due to the constantly maintained 73 % ^{3}He polarization. The use of the sample electromagnet at fields up to 1 T and routine AFP reversal of the ^{3}He polarization did not perturb the analyzer performance. Another application of polarized ^{3}He at the JCNS is PA for SANS. Measuring weak coherent scattering of protonated biological samples, or biological samples in protonated solvents, is a fundamental limitation of standard SANS techniques for soft matter research. The incoherent scattering from the protons can make measurement of the coherent scattering, which gives the structure factors of the sample, very difficult or impossible to observe [2].

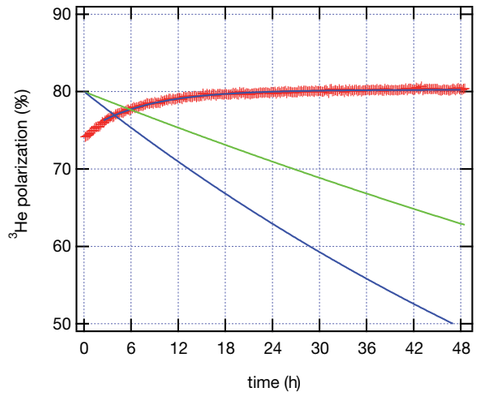

Figure 2: ^{3}He polarization vs. time (red markers). For comparison the solid blue and solid green lines are the calculated polarizations vs. time with lifetime of 100 hours and 200 hours respectively.

Polarization analysis at KWS-2

We polarized the beam on KWS-2 with a single super mirror in transmission geometry and obtained an incident beam polarization of 97 % at 4.5 Å. Two shielded end-compensated solenoids provided an appropriate magnetic environment. To allow polarization analysis over a wide angle, the sample was placed close to the cell, resulting in a solid angle coverage of 15° corresponding to Q < 0.35 Å^{-1}. A ^{3}He cell was polarized in the JCNS SEOP laboratory up to the starting polarization of 72 %, which gave a good polarization efficiency at 4.5 Å of 95 % at the beginning of the experiments and remained over 93 % after over 36 hours (the lifetime was 430 hours). This level of polarization lifetime would allow operation for 4 to 5 days on a single cell polarization with good neutron performance.

A sample of the data is shown in figure 3. Here grey/green circles are results of measurements with an unpolarized neutron beam of the sample in the solvent and the solvent alone, respectively. After data treatment one obtains the black circles for the standard SANS; the blue dotted line is the presumed background level from the fit of this data. The red circles are results using a polarized incident beam with ^{3}He PA and clearly demonstrate the removal of the incoherent background. The red and black solid lines are Beaucage fits to unpolarized and polarized data respectively, where for the latter the background parameter is held to zero. One can see an increase in the signal-to-noise ratio on the order of 100. Further, the data using PA can be unambiguously fitted to a Q^{-4} structure factor in contrast to the unpolarized neutron data.

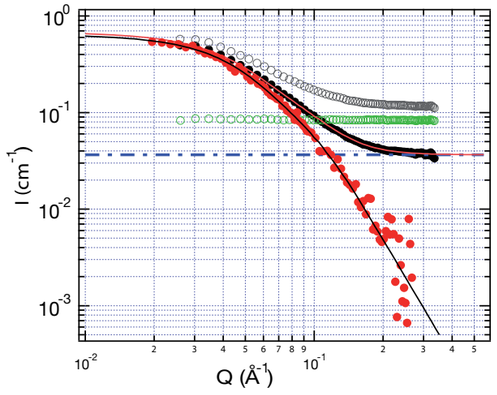

Figure 3: A sample of the data obtained on a non-deuterated protein in a D_20 buffer solvent. Descriptions of the curves are in the text.

Tasks for the future

Work is underway to construct an optimal system for the SANS application to allow in-situ polarization, increase the available Q range to over 0.6 Å^{-1} and use standard sample environment. Adding in-situ polarization is important for several reasons: it will minimize technical support, simplify data treatment and maximize neutron performance. Improvements to the MARIA system will include increasing angular coverage by further minimizing the sample to cell distance and using a larger diameter cell which we are currently developing. The MARIA PA system will be available for user operation in 2011.

[1] E. Babcock et al., Nucl. Instrum. Meth. A, 625 (1), 43 (2011).

[2] A. Ioffe et al., submitted to IOP J. Phys. special issue for "Modern Trends in Production and Applications of Polarized ^{3}He" workshop, Ismaning/ Germany 2010.

Visualization of water uptake in a trunk

T. Bücherl, C. Lierse von Gostomski

Technische Universität München, ZTWB Radiochemie München RCM, Garching, Germany

The visualization of slow dynamic processes using fission neutron radiography at the NECTAR facility of FRM II enables the investigation of even bulky samples of hydrogen containing materials like water or oil. This is demonstrated qualitatively and quantitatively for the water uptake of a trunk of about 12 cm diameter.

The visualization of dynamic processes in sealed objects is of vital interest for many investigations and applications. For example, it results in knowledge of the mechanisms of root growth in soil allowing the optimization of watering and manuring for plant growth. The visualization of oil distributions in running or starting engines can give information on further aspects for its optimization reducing the fuel consumption. Both examples, like many more, might have large economic and ecological impacts.

The main aspect of non-destructive inspection techniques should be that the investigated samples are in their natural surroundings. Plants should be placed in large sized soil containers, i.e. wall effects should not influence their growth, engines should not require special windows to be inserted to gain access to the required information, i.e. the processes visualized should not be influenced by using different materials etc.

Figure 1: Photograph of the experimental set up for the measurement of water uptake in a trunk. The trunk is loaded by an iron cylinder. In the background the converter plate of the detector system is visible.

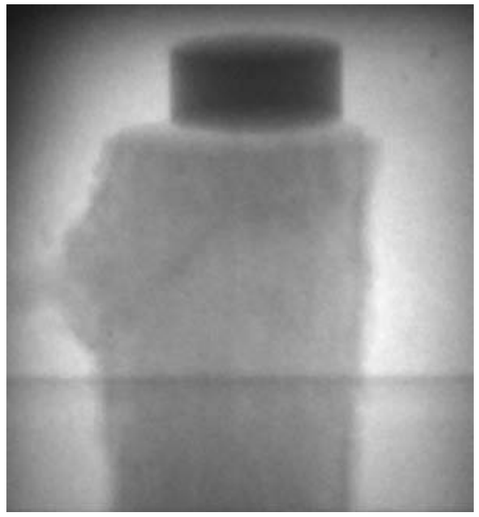

Figure 2: Radiograph of the initial set-up. The image of the trunk shows both, the structures of the bark and of the inner area. The horizontal line in the lower part of the image corresponds to the upper rim of the bowl. On top of the trunk, the iron cylinder is visible.

Therefore, large and/or dense samples often have to be investigated. Here, radiography using fission neutrons can give valuable information. These neutrons have a high penetration power for dense materials while being sensitive to hydrogen containing materials like water, oil etc.

A highly interesting material for this type of investigations is wood, as it is of manifold use even in sensitive areas like building construction, and especially its reactions with water. As an example, the water uptake in a trunk was investigated.

Measurements at NECTAR

NECTAR at FRM II is a versatile facility for radiography, tomography and activation measurements using fission neutrons [1]. The neutron spectrum can be adapted to the specific requirements of the individual experiments by means of different filters and collimators. For the real time measurements of a trunk of about 12 cm diameter a neutron flux of $5.4 \cdot 10^5$ $cm^{-2}s^{-1}$ and a L/D of about 230 were selected. The trunk was placed in an empty bowl and loaded by an iron cylinder on the top to stop it floating when the bowl was filled with water (fig. 1). Using a CCD based detection system, operated at a temperature of -50°C, first a radiograph of the initial set-up (i.e. trunk in bowl without water) was measured (fig. 2). This was referred to as the reference image. Then, the bowl was filled with about 250 ml of water and a series of 1000 back-to-back radiographs was started immediately, each lasting 60 seconds, thus covering a time period of about 52 hours.

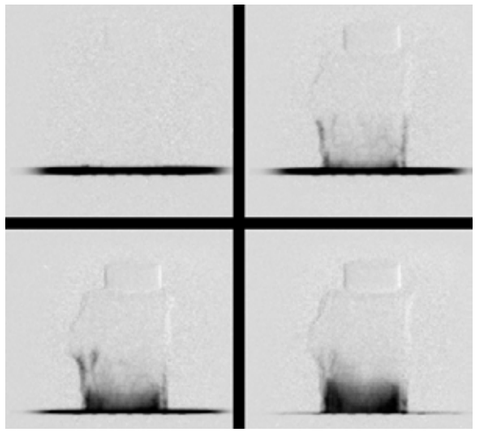

Figure 3: Radiographs of the water uptake in a trunk at different time intervals after adding water in the bowl. Upper left: After 2 minutes only the water in the bowl is visible. Upper right: After 200 minutes soaring within the bark has started. Lower left: After 1000 minutes the uptake within the trunk started. Lower right: After 2000 minutes the water content in the bark is reduced.

What happened

All images were filtered [2], and the dark image corrected, normalized and then subtracted by the adequately treated reference image. Figure 3 shows some of these difference images at 2 minutes, 200 minutes, 1000 minutes and 2000 minutes respectively, after the filling of water in the bowl. The dark areas indicate the location of water. After 2 minutes nearly all water is still in the bowl while after 2000 minutes it is mainly in the lower part of the trunk. A qualitative investigation showed that within the first 200 minutes the water is mainly climbed within the bark until it reached a maximum height of about 5 cm. Here gravity seems to prevent a further ascent, i.e. levels out the effect of the transport mechanism in the bark. For the remaining time the water uptake in the inner parts of the trunk is the dominant effect while the amount of water in the bark decreases. These results are confirmed by a quantitative data evaluation [3]. The climbing within the bark, well described by an exponential rise, is the dominant mechanism for the first 750 minutes, while for the remaining 1250 minutes, the water uptake in the inner areas of the trunk be-comes dominant and is described by a linear function (fig. 4). By the end of the experiment about 80 ml of water are absorbed by the trunk.

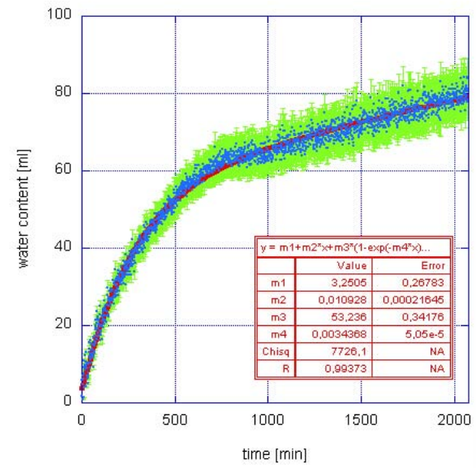

Figure 4: Results of the quantitative evaluation of the experiment (blue: water content derived from radiograph; green: corresponding uncertainty; red: fit on data).

It is shown that real time measurements of slow processes on bulky objects like a trunk are possible at the NECTAR facility using fission neutrons. The visualization of the dynamics of such processes can act as a starting point for new or improved physical models trying to describe reality more accurately. Although in this experiment the time frame was quite large (60 seconds), it can be reduced to a few seconds or even less but only at the expense of spatial resolution.

[1] T. Bücherl et al., Nucl. Instrum. Meth. A, in press.

[2] K. Osterloh et al., Nucl. Instrum. Meth. A, in press.

[3] T. Bücherl et al., Nucl. Instrum. Meth. A, in press.

Optimising the neutron diffractometer STRESS-SPEC for surface strain scanning

J. Rebelo Kornmeier[1], J. Gibmeier[2], M. Hofmann[1], R. Wimpory[3]

[1]Technische Universität München, Forschungs-Neutronenquelle Heinz Maier-Leibnitz (FRM II), Garching, Germany
[2]Karlsruher Institut für Technologie (KIT), Institut für Werkstoffkunde I, Karlsruhe, Germany
[3]Helmholtz-Zentrum Berlin für Materialien und Energie, Berlin, Germany

Neutron strain measurements are critical at the surface. In this study it will be demonstrated that by optimising the bending radius of a Si (400) monochromator, spurious surface strains can be greatly reduced. For optimised monochromator settings it was possible to measure the residual stress depth gradient of a shot peened SAE 4140 steel sample through the surface dispensing of the laborious and tremendously time consuming reference measurements. These results open very promising possibilities for bridging the gap between high energy X-ray diffraction and neutron diffraction for non destructive residual stress analysis close to surfaces.

Spurious strains from surface effects

When performing neutron strain measurements, the gauge volume is defined by the primary and secondary optics systems. A well known (mainly) geometrical problem arises when the gauge volume plunges into the sample surface [1-5]. Pseudo peak shifts arise because the gauge volume is not completely filled by material and, hence, the centre of the gauge volume does not coincide with the centre of the irradiated material.

For a material showing homogeneous absorption of neutrons within the material, three main effects can give rise to surface related peak shifts, the first arising because of a wavelength spread (gradient) across the incident beam, the second being the so called geometrical effect and the third the peak clipping effect [4]. The wavelength spread and the geometrical effect are strongly dependent on the divergence of the beam. Vrana and Mikula [5] showed that there is a strong interrelation between the wavelength and the direction of the incident as well as the diffracted beam, which can be altered by the monochromator bending radius. This can be utilized to suppress surface effects in through surface strain scanning once the peak clipping effect is eliminated.

Minimization of spuriuos strains

In the present study first the magnitudes of the spurious strains are analyzed as a function of the bending radius of a Si (400) monochromator. A secondary radial collimator in front of the detector was used, thus any potential peak clipping should not occur [6,7]. Through surface strain scans were performed on a stress free steel sample using the Fe (211) interference line in reflection and transmission mode. The selected wavelength was 1.68 Å to provide an optimal 90° scattering geometry. In figure 1 the resulting spurious strains for the optimal monochromator radius in reflection and transmission geometry are plotted versus the depth of centroid of sampled gauge volume [2]. The resulting optimised configuration of the Si (400) monochromator was then applied to surface residual stress analysis of a shot peened plate of steel SAE 4140 with dimensions of 50 × 50 × 10 mm³. This sample was selected as a typical representative example of high practical relevance for non-destructive residual stress analysis. The residual stress gradient of this sample had already carefully characterized through previous investigations within a round robin exercise [8].

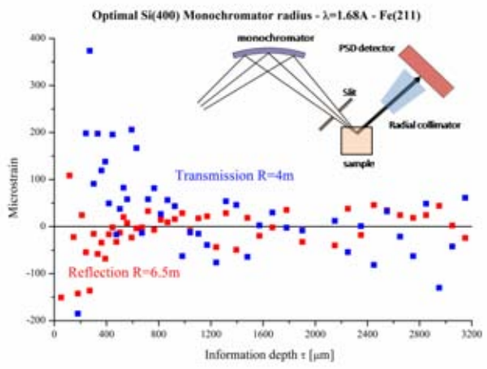

Figure 1: Optimal Si (400) monochromator radius for Fe (211) interference line in reflection and transmission mode (analysis carried out for 'stress free' steel plate). It can be clearly seen that the spurious strains can be reduced to values of ±100 µε up to a centroid position of 50 µm when the monochromator radius of 6.5 m for reflection mode is used. In transmission mode the spurious strains are between ±200 µε for a bending radius of 4 m even when the centroid is at approximately 200 µm. The insert shows a schematic representation of the STRESS SPEC setup.

Direct surface measurements

The measurements were carried out using the Fe (211) interference line of the ferrite phase of the shot peened steel plate. For the strain measurements the Si (400) monochromator bending radius was set to 4 m in transmission and 6.5 m in reflection mode, respectively. A nominal gauge volume of 2 x 10 x 2 mm³ was selected, commonly used as a gauge volume for in depth neutron measurements. This allowed a good compromise between intensity and measuring time for each depth at the near surface. In figure 2 the resulting residual stress depth profile for the in plane direction is presented for the shot peened plate of steel SAE 4140. For data analysis the universal plot method was applied [9,10]. Figure 2 presents the residual stress profiles in Laplace space σ(τ) as well as the back calculated real space stress distribution σ(z). Only the first two points were corrected to the stress free sample spurious strains. The surface stress scan, measured with neutrons, is in good agreement with those obtained by the round robin. The results clearly indicate that it is possible to measure surface strain scans dispensing with the laborious and tremendously time consuming reference measurements in order to compensate for the surface effects for information depths larger than 0.2 mm.

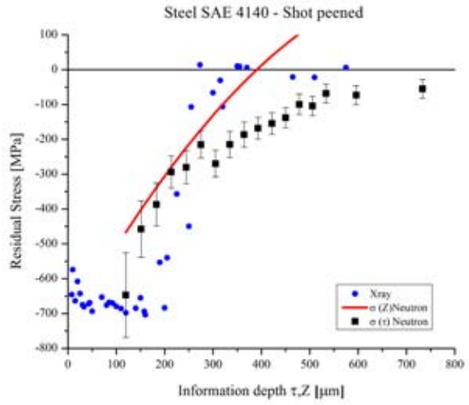

Figure 2: Comparison of the residual stress profiles, for each penetration depth, obtained with X-ray and neutron diffraction. Residual depths distribution for the in plane direction in Laplace space σ(τ) as well as the respective distribution in real space σ(z).

These results open up very promising possibilities for bridging the gap between high energy X-ray and neutron radiation for non destructive residual stress analysis for scanning information depth below the sample surfaces up to 0.2 mm.

[1] M.T. Hutchings et al., Introduction to the characterization of residual stress by neutron diffraction, Taylor & Francis Group, LLC (2005).
[2] S. Spooner and X.L. Wang, J. Appl. Cryst., 30 (4), 449 (1997).
[3] X.L. Wang et al., J. Appl. Cryst., 31 (1), 52 (1998).
[4] P.J. Webster et al., J. Neutron Res., 3, 223 (1995).
[5] M. Vrána and P. Mikula, Mat. Sci. Forum, 490-491, 234 (2005).
[6] P.J. Withers et al., Physica B, 292 (3-4), 273 (2000).
[7] T. Pirling, Mater. Sci. Forum, 347-349, 107 (2000).
[8] J. Gibmeier et al., Mater. Sci. Forum, 404-407, 659 (2002).
[9] H. Ruppersberg et al., Phys. Status Solidi A, 116 (2), 681 (1989).
[10] H. Ruppersberg et al., Z. Kristallogr., 195 (3-4), 189 (1991).

Direct observation of the surface segregation of Cu in Pd

C. Hugenschmidt[1,2], J. Mayer[1,2], K. Schreckenbach[1,2]

[1]Technische Universität München, Forschungs-Neutronenquelle Heinz Maier-Leibnitz (FRM II), Garching, Germany
[2]Technische Universität München, Physik Department E21, Garching, Germany

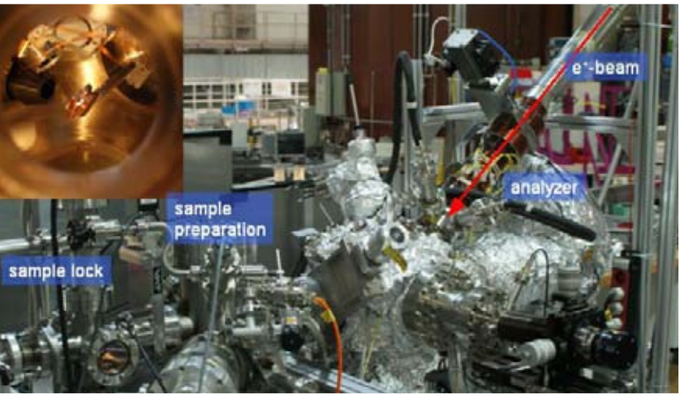

Figure 1: The Auger-spectrometer at the positron beamline NEPOMUC was used for surface studies with high elemental selectivity.

Density functional theory calculations predict the surface segregation of Cu in the second atomic layer of Pd which has not been unambiguously confirmed by experiment so far. We report measurements on Pd surfaces covered with three and six monolayers of Cu using element selective **p**ositron-annihilation induced **A**uger **e**lectron **s**pectroscopy (PAES) which is sensitive to the topmost atomic layer. Moreover, time-resolved PAES, which was applied for the first time, enables the investigation of the dynamics of surface atoms and hence the observation of the segregation process. The time constant for segregation was experimentally determined to τ = 1.38(0.21) h, and the final segregated configuration was found to be consistent with calculations. Time-dependent PAES is demonstrated to be a novel element selective technique applicable for the investigation of, e.g. heterogeneous catalysis, corrosion, or surface alloying.

Topmost layer stability of CuPd revealed by low-energy positrons

Pure Pd and Pd-based alloys are important materials, e.g., for hydrogen storage, hydrogen purification, and heterogeneous catalysis. In Cu-Pd alloys in particular, the amount of Cu atoms and their exact position strongly affect the mechanical stability and the catalytic properties of Pd membranes. Density functional theory calculations for Cu-Pd alloys predict the segregation of Cu in the second atomic layer of Pd [1], but the available experimental data for this system are still poor and the experiments done so far do not unambiguously confirm the theory.

In the experiment described here we investigate the stability and dynamics of thin Cu layers on the Pd surface. Our approach uses the extremely surface sensitive and elemental selective analysis method of **p**ositron-annihilation-induced **A**uger **e**lectron **s**pectroscopy (PAES) for the direct measurement of the surface segregation. In contrast to **e**lectron-induced **A**uger **e**lectron **s**pectroscopy (EAES), which was applied as well, PAES intrinsically analyzes the topmost atomic layer of a sample almost exclusively. In addition to the high surface sensitivity that arises from the efficient positron trapping in a delocalized surface state, one benefits from the positron affinity which makes PAES a highly elemental selective technique.

First time dependent Auger-spectroscopy induced by positron-electron annihilation

Up to now, the time for a single PAES measurement amounted to several days, and hence it was not possible to investigate dynamic surface processes. We cope with this challenge by using the PAES spectrometer [2] at the high intensity **ne**utron-induced **po**sitron source **Mu**nic**h** (NEPOMUC) which delivers 9·10[8] monoenergetic positrons per second. Additionally, the experimental setup was improved in order to enable time dependent PAES and hence to monitor the dynamic behaviour of Cu atoms on a Pd surface for the first time.

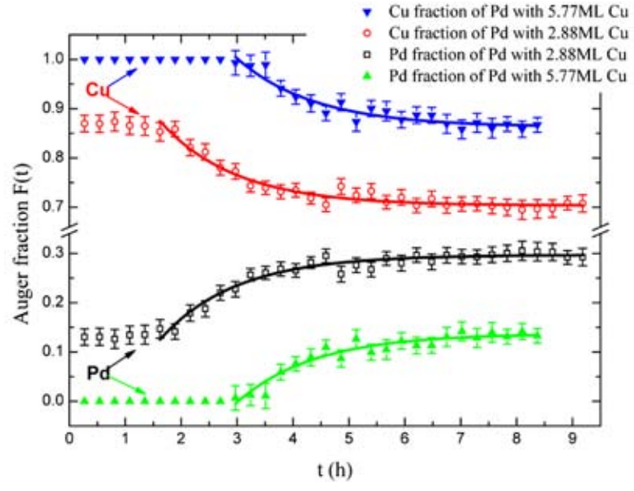

Figure 2: Fraction of the Auger intensities from Cu and Pd, respectively, as a function of time for two different Cu initial covers on Pd: 2.88 ML Cu on Pd and 5.77 ML Cu on Pd. In both cases a similar time dependency is observed due to the segregation of Cu in the second atomic layer of Pd. The exponential fit (solid lines) reveals the time constant of segregation of τ = 1.38 h.

Two samples were prepared with different Cu covers on Pd: 2.88 ML Cu on Pd and 5.77 ML Cu on Pd. The measured fractions of the Auger intensities from Cu and Pd, respectively, as a function of time are shown in figure 2.

The exponential intensity profile for both Cu-covered Pd samples is attributed to the migration of Cu atoms from the surface into the second atomic layer of Pd. Alternative interpretations such as surface contamination are dismissed since an increase in the Auger fraction of Pd at the expense of the Cu intensity is observed. Bulk diffusion is also excluded since it would lead to a vanishing Cu intensity, which is in contrast to the measured saturation values for both samples. Also, surface diffusion is ruled out because it would require time scales of several minutes, which is well below the observed value of 1.38 h. A more detailed presentation can be found in [3]. Hence, the observed increase in the Pd Auger intensities at the expense of the Cu intensities until a saturation value is reached, is attributed to the segregation of Cu in Pd. The reason for this segregation is that the most stable configuration for Cu is in the second atomic layer of Pd in thermodynamical equilibrium. This is supported by the calculated segregation energy of 6 kJ/mol according to 63 meV per Cu atom [1].

NEPOMUC allows the study of surface segregation with short measurement times

We succeeded in recording PAES spectra of Cu and Pd with the unprecedented short measurement time of only seven minutes. Thus, it was possible to directly observe the segregation of Cu in the second atomic layer of Pd by time-dependent PAES. The theoretically predicted result of the stable final configuration was confirmed experimentally. Moreover, the migration process itself was observed with a characteristic time constant of τ = 1.38(0.21) h. Time-dependent PAES allows the investigation of elemental selective dynamic processes such as heterogeneous catalysis, surface alloying, or corrosion processes of numerous systems with unprecedented measurement times and extremely high surface sensitivity.

[1] O. Lovvik, Surf. Sci., 583 (1), 100 (2005).
[2] J. Mayer, PhD Thesis, Technische Universität München (2010).
[3] J. Mayer et al., Phys. Rev. Lett., 105 (20), 207401 (2010).

Detection of lithium traces in organic samples

J. Lichtinger[1], R. Gernhäuser[1], R. Krücken[1], E. Mützel[2], J. Schöpfer[2] L. Canella[3,4], P. Kudejova[3], K. Zeitelhack[3]

[1]Technische Universität München, Physik Department E12, Garching, Germany
[2]Ludwig-Maximilians-Universität München, Institut für Rechtsmedizin, München, Germany
[3]Technische Universität München, Forschungs-Neutronenquelle Heinz Maier-Leibnitz (FRM II), Garching, Germany
[4]Technische Universität München, ZTWB Radiochemie München RCM, Garching, Germany

Approximately 9.5 % of the U.S. population above the age of 18 suffers from an affective disorder [1]. In particular, depressive disorder is the leading cause of disability in the U.S. for those aged 15-44 [2] and the dominant reason for suicide [3]. However, the biological reasons underlying the disease are not yet fully understood. Lithium is used to treat affective disorder. However, its exact effectiveness, critical concentration and local enrichments in the human brain are still unknown. As medical studies need to analyse many samples and the natural concentration of lithium in the human brain is small, we have developed an easy, precise and position sensitive method to determine low-level lithium concentrations in organic samples.

Experimental method

^{6}Li (7.5 % nat. abundance) has a high thermal neutron capture cross section of σ_{th} = 940 b. In the capture reaction ^{6}Li(n,α)^{3}H an alpha particle and a triton are emitted back to back with a fixed kinetic energy of E_α = 2055 keV and E_t = 2718 keV respectively.

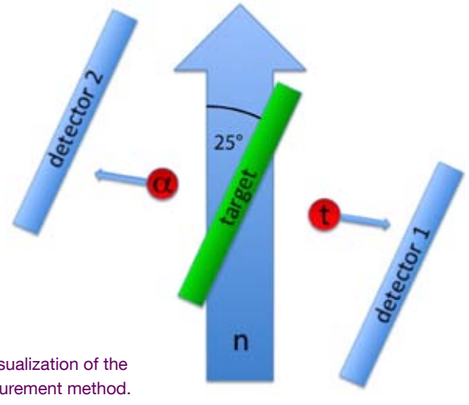

Figure 1: Visualization of the basic measurement method.

The setup shown in figure 1 was mounted at the PGAA facility at the FRM II, which provides a well collimated cold neutron beam (16 x 19 mm^2) with a maximum intensity of Φ_{max} = 1.6·10^{10} n/cm^{2}s. It consists of two position sensitive Si-PSD arranged on both sides of a thin organic sample (thickness d = 10-30 µm), which adhere to a thin substrate foil mounted on an aluminium frame. Irradiated by cold neutrons, the alpha particles and tritons emitted in the lithium capture reactions are detected in coincidence. The particles are identified by the energy deposit in the detectors and their impact position makes it possible to deduce the position of the lithium nucleus in the sample.

Slice of a brain studied at PGAA

In 2010, we performed a first experiment using organic samples to prove the feasibility of the method and to evaluate its limitations in terms of concentration and position sensitivity. A d = 10-30 µm thick slice of the brain of a human treated with lithium before her/his death was irradiated for 24 h with a neutron flux of Φ = 1.5·10^9 n/cm^{2}s. Figure 2 shows the resulting coincidence spectrum of the energy deposit in the two detectors. The two triangles represent the alpha and triton entries, where the alpha particle hits detector 1 and the triton detector 2 and vice versa. Clearly, the measured energy loss limits the useful thickness of the samples.

The large intensity in the lower left corner is due to random coincidences produced by a huge background of betas, gammas and protons from reactions of neutrons with the material of the target setup. In this measurement the single count rate of the detectors was R_s = 14 kHz/cm^2, resulting in a coincident background rate of R_c = 11 Hz, applying a coincidence time window

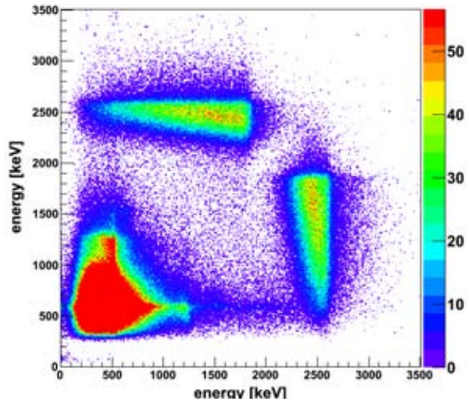

Figure 2: Energy of detector 2 versus the energy of detector 1. The two triangles show the alpha and triton entries.

of Δt = 200 ns. However, alphas and tritons can be clearly separated from this remaining background and figure 3 shows the resulting position distribution of lithium in the sample. Using a reference sample with homogeneous lithium concentration, the influence of solid angle efficiency, beam profile and detector efficiency had been corrected and used for calibration previously. For convenience the spectrum was blurred to compensate for statistical fluctuations. For comparison, figure 3 also shows a photograph of the region of interest measured in the experiment.

The three cracks in the tissue visible in the photograph could be nicely reconstructed. A mean lithium concentration of λ_{Li} = 10.8±1.4 ng/cm^2 was determined for this sample. Using various reference samples, a position resolution of Δx < 2 % of the detector size and a detection limit λ_{min} = 80 pg/cm^2 for the lithium concentration was determined for this test setup.

Using an improved beam collimation and flushing the target chamber with Helium, the single count rate of the detectors due to the background could be drastically reduced to R_s = 1 kHz/cm^2 in further experiments. Together with the usage of larger detectors (A = 20 x 20 mm^2), this allowed a significant reduction of the detection limit. While the analysis of the measured data is still ongoing, a theoretical detection limit of λ_{min} = 80 fg/cm^2 is expected.

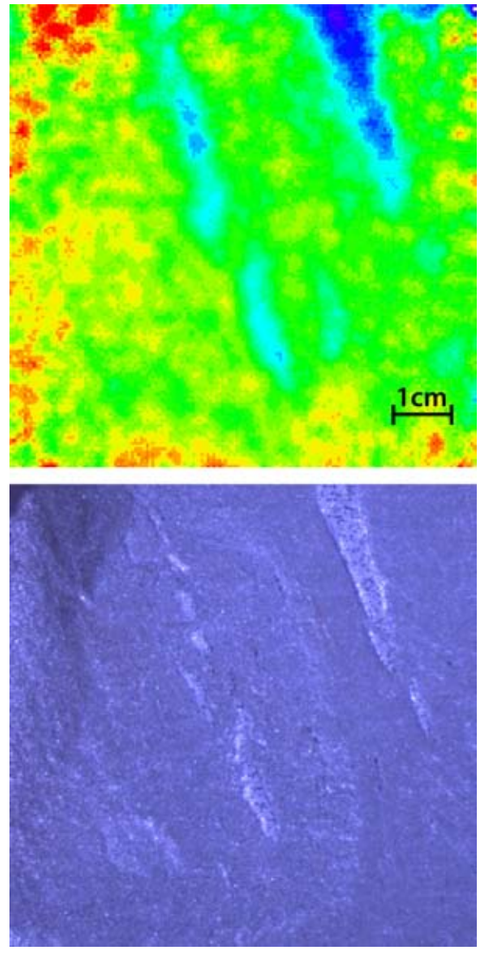

Figure 3: The spectrum (top) shows the lithium distribution of the measured sample. The colours indicate the concentration from 0 (purple) to 15 ng/cm^2 (red). The photo (bottom) shows the measured area.

Position sensitive lithium concentration

In a first series of experiments we were able to demonstrate the feasibility of a method to determine position resolved low-level lithium concentrations in organic tissue using cold neutron capture. With the present setup we achieve a position resolution of Δx ≈ ±37 mm and a theoretical detection limit for lithium in tissue of λ_{min} = 80 fg/cm^2 with a relative precision of 15 %.

[1] R. Kessler et al., Arch. Gen. Psych., 62 (6), 617 (2005).
[2] WHO, The global burden of disease, update (2004).
[3] Centers for Disease Control and Prevention: www.cdc.gov/injury/wisqars/

Improving components and techniques

G. Borchert, J. Peters, K. Zeitelhack, J. Krüger, J. Neuhaus

Technische Universität München, Forschungs-Neutronenquelle Heinz Maier-Leibnitz (FRM II), Garching, Germany

Four central service departments in total, namely, sample environment, detector and electronics, neutron optics and IT infrastructure and software development provide support for the scientific instruments. They develop new components or equipment to improve performance and provide maintenance service to set up the experiments, align neutron optical components or give a hand with trouble-shooting. Major achievements in 2010 comprise the new in-house fabrication of neutron guides, the development of high and low temperature equipment and the completion of the detector bank at the time-of-flight instrument TOFTOF.

Shaping neutron beams

As our main supplier for precision glass cutting and gluing ceased production, we decided to take over the fabrication of neutron guides ourselves. We established a laboratory close to our sputtering facility and equipped it with all necessary tools to machine the glass and glue it together accurately after sputtering, while optically controlling the shape. We constructed and assembled a special glass sawing facility for cutting, grooving and phasing (fig. 1). The first neutron guides were produced successfully, demonstrating a state-of-the-art performance (fig. 2). This enables us to respond quickly to sudden needs and the special requirements of the instruments.

In the neutron guide hall, several neutron guides were equipped with an improved shielding of polyethylene and encased in aluminium housings. For the instrument SANS-1, the adjustment of the neutron guides in the collimation section has been accomplished. After partial removal of the neutron guides at the instrument KWS-2, new supports for a chopper unit had been placed. This was followed by a reconstruction and readjustment of the corresponding neutron guides.

Over the last few years, the feasibility of optimally focusing neutron guides has been demonstrated. An additional challenge arises from the requirement that the focal condition should be kept at the sample position, irrespective of the wavelength used. This was investigated for the time-of-flight spectrometer TOFTOF. Monte Carlo simulations were undertaken for the focussing of the neutron beam and to increase the neutron flux by varying the shape and length of the focusing guide. Since various wavelengths are focused at different positions, we have simulated an adaptive neutron guide to always focus

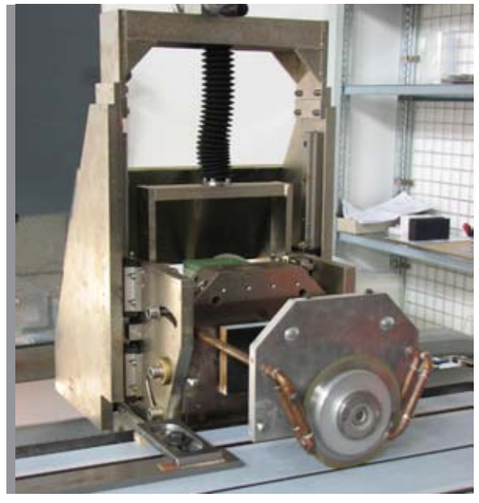

Figure 1: The special glass sawing facility with protection cover removed. The sawing unit can be tilted and is capable of cutting glass plates of length up to 2 m. Along this dimension an accuracy of 10 µm can be achieved.

Figure 2: First demonstration sample of a neutron guide produced by the Neutron Optics group. Only part of the glass has been sputtered to enable a look inside. On the left collimator channels, 1mm wide, have been introduced, on the right, a V-shaped polarization unit is visible.

neutrons to the same point. The gain in flux according to the simulations is 3 for $\lambda = 4$ Å, with no significant increase in the divergence. Since the simulations have shown promising results, we are assembling the mechanical components of a prototype that will be introduced in the time-of-flight instrument TOFTOF.

The optical pumping station HELIOS regularly provides polarized ^{3}He gas for neutron polarization analysis at the FRM II. The polarization analysis of hot neutrons (wavelength 0.087 nm) at the instrument PoliHeidi is based entirely on the use of ^{3}He filter cells. In order to provide an uninterrupted service, four new glass cells have been prepared. To cover the growing demand for the use of polarized ^{3}He gas for neutron polarization analysis, a new additional magnetostatic cavity has been built. This cavity features a very uniform magnetic field and can be used for housing a cell at a neutron instrument for a long time. With the aim of further improving the ^{3}He cells, a new design with glued Si single-crystal windows has been developed. Such cells will provide better neutron transmission with no small-angle scattering from the windows.

Conditioning sample parameters

Within the European NMI3 consortium, the FRM II contributes to the development of dedicated sample environments with the development of an electrostatic levitation furnace. This project is in close collaboration with the Institut für Materialphysik im Weltraum, Deutsches Zentrum für Luft- und Raumfahrt (DLR) in Cologne. The levitation and control technique has been refined at DLR. The design of the recipient and the over all set up, including all peripheral devices, meets the requirements of neutron scattering experiments, especially compact design, easy assembling and installation. Constructional measures to meet safety requirements to avoid laser radiation hazards have been taken. After completion of the CAD work for the Neutron Electrostatic Levitation Furnace (NESL), components of the recipient have been manufactured, assembled and leak tests have been successfully performed. First test runs of the prototype NESL succeeded at DLR using known conductive samples. The remote control software has been tested.

In Mai 2010, the ESL was in operation at the FRM II for a first test run and under real experimental conditions. The experiment was performed at the time-of-flight spectrometer TOFTOF by T. Kordel, D. Holland Moritz and A. Meyer. Samples such as ZrNi with a diameter of

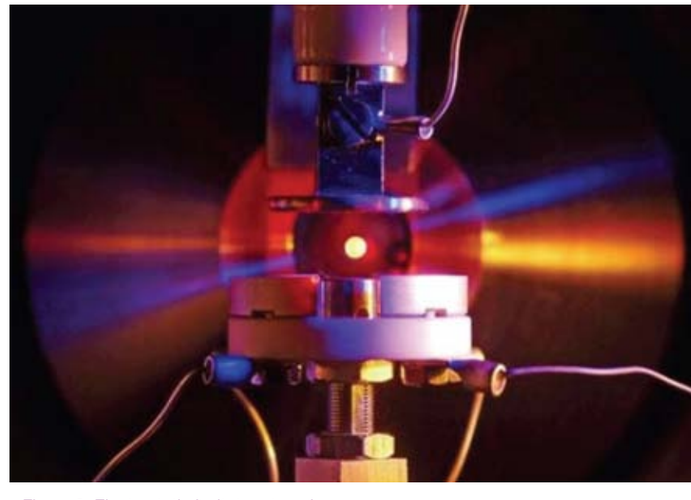

Figure 3: Electrostatic levitator at work.

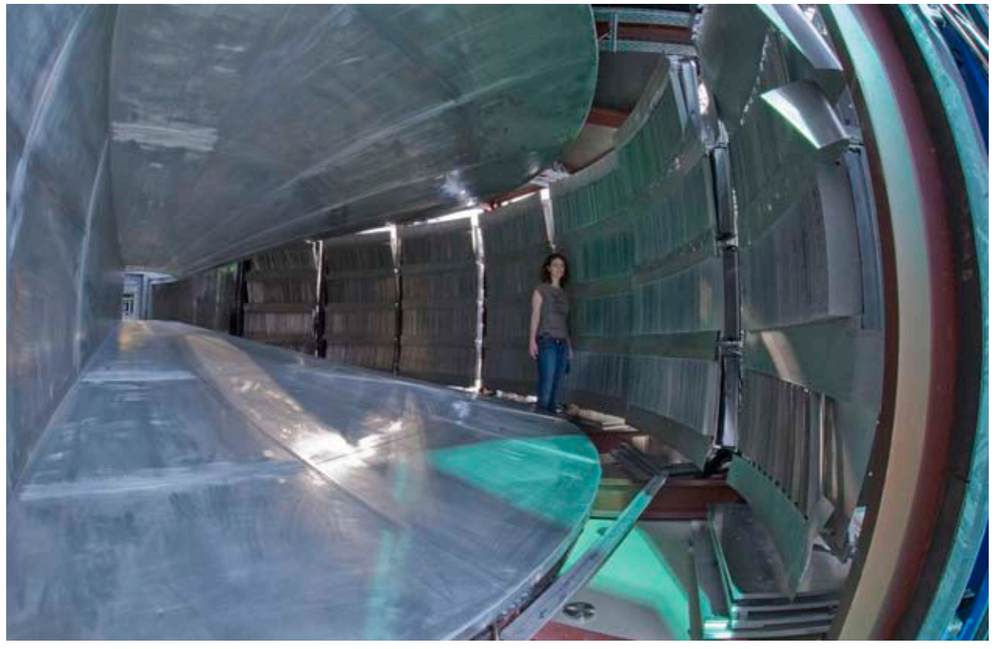

Figure 4: View inside the TOFTOF flight chamber with extended number of detectors.

6 mm were successfully levitated and heated up to 1100 °C. Further software and hardware adjustments and extensive tests have to be carried out in 2011.

Based on our second generation cryogen free top loading refrigerators (CCR), in 2010 we began a collaborative project with the Berlin Neutron Scattering Center (BENSC), a facility of the Helmholtz Zentrum Berlin. Based on the recent upgrade of the CCR developed at FRM II, both facilities use this refrigerator as a basis for further development and adaption. In a first step, two CCRs have been assembled in Garching together with colleagues from Berlin, which will serve as testing machines at the BENSC facility.

The next step in these common developments is the extension of the temperature range of our CCR below the 3 K level given by the cold-head. A newly developed ^{4}He evaporation stage (1 K pot) allows for temperatures down to 1.3 K in a semi-continuous mode by applying gas from a bottle. A continuous operation which involves circulating the helium gas is also possible. Furthermore, a continuous operation using ^{3}He gas via our gas handling system is feasible. Further details have to be investigated in 2011.

Another device brought into operation by the sample environment group is a low temperature system allowing for the conversion of ortho- to para-hydrogen by means of a converter cell mounted at a cold-head and a appropriate gas handling system working under pressure up to 150 bar. The device has been in operation at TOFTOF to load hydrogen adsorbents.

Improving neutron detection

With the commencement of routine operation in 2005, 14 instruments were taken into service. At that time not all options, especially those concerning the detection area, could be realised for technical or budgetary reasons. Since then, continuous improvement of the instruments has taken place. A major upgrade of the time-of-flight instrument TOFTOF has been achieved recently by increasing the number of detector tubes from 600 to 1000. In close collaboration with the manufacturer of the detector tubes, special care was taken to reduce the electronic noise of the tubes themselves. During the extension of the detection area, the electronics was revised in order to improve the background counting rate even further. In addition, the influence of neighbouring electronic devices could be significantly reduced.

^{3}He is still the most efficient neutron absorber used in gaseous detectors. Due to the world wide shortage of ^{3}He, special care has to be taken to recover the precious gas during maintenance on large area two-dimensional detectors. Even for a medium sized, e.g. 30 x 30 cm Multi-Wire Proportional Counter, the filling gas amounts to about 50 barliters of ^{3}He. In order to recover the gas and refill the gas chamber detector after repair, we have constructed a dedicated gas handling station. In addition to the pumping and compression unit, it comprises a purification module where gaseous impurities or the gas mixture can be separated by a cold trap. After the repair, the detector chamber can be refilled with a well defined gas mixture including additions such as CF_4 or CO_2.

To improve the sampling rate of a two-dimensional ^{3}He gas detector, the emitted light of the absorption process can be recorded by means of photo-multipliers. This is the topic of a joint research project involving international collaboration supported by the NMI3 initiative. After building three prototype detectors in 2009, the first data could be recorded as shown in figure 6. A high speed data recording system has provided the necessary data to start the development of the analog and digital circuit. A major challenge will be the position encoding by weighting the integrated signals of the photo-multipliers. Using the entrance window of the used photo-multipliers with a diameter of 38 mm, a full width at half maximum resolution of about 2 mm could already be achieved in the first test runs.

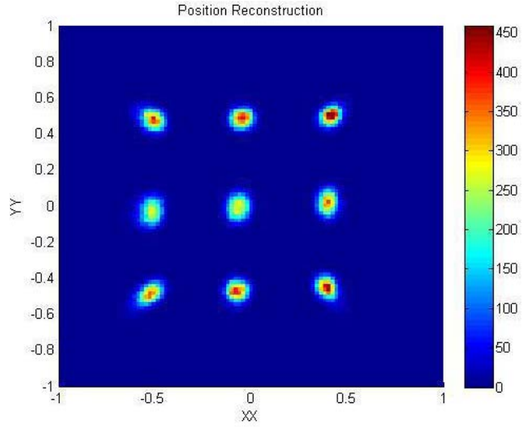

Figure 6: Light read-out of neutrons in a ^{3}He Micro-Strip Gas Chamber.

Instrument control and software development

An ongoing project in 2010 has been the introduction of the new instrument control system TANGO to replace the widely used TACO-system at the FRM II. First installations on running instruments are planned for 2011. Another focus has been the development of new user office software. In a joint collaboration of five research facilities, the new Digital User Office DUO2 will be based on common libraries and tools. Under development is the integrated work flow to make the organisation of the scientific experiments easier and more effective.

Figure 5: Gas handling system for neutron detectors including ^{3}He recovery, purification and refilling.

Levitation at the time-of-flight spectrometer TOFTOF.

3 Scientific Highlights

Asymmetric spin-excitation spectra in Fe-pnictides

J. T. Park[1], D. S. Inosov[1], A. Yaresko[1], S. Graser[2], D. L. Sun[1], P. Bourges[3], Y. Sidis[3], Y. Li[1], J.-H. Kim[1], D. Haug[1], A. Ivanov[4], K. Hradil[5], A. Schneidewind[5,6], P. Link[5], E. Faulhaber[5,6], C. T. Lin[1], B. Keimer[1], V. Hinkov[1]

[1]Max-Planck-Institut für Festkörperforschung, Stuttgart, Germany
[2]Universität Augsburg, Elektronische Korrelationen und Magnetismus, Augsburg, Germany
[3]CEA-Saclay, Laboratoire Léon Brillouin, CEA-CNRS, Gif sur Yvette, France
[4]Institut Laue-Langevin, Grenoble, France
[5]Technische Universität München, Forschungs-Neutronenquelle Heinz Maier-Leibnitz (FRM II), Garching, Germany
[6]Helmholtz-Zentrum Berlin für Materialien und Energie, Gemeinsame Forschergruppe HZB - TU Dresden, Berlin, Germany

It has been shown recently that magnetic excitations in iron-pnictide superconductors behave differently along the directions longitudinal or transverse to their propagation vector, resulting in an elliptical distortion of the observed neutron-scattering pattern. In structurally isotropic compounds, such distortion was previously associated with a spontaneous breaking of the rotational symmetry of the electron subsystem, known as the electron-nematic state. Using inelastic neutron scattering data collected at FRM II, we suggest an alternative explanation for the same effect that does not require a spontaneously broken symmetry, but follows from the peculiar crystal structure of these new compounds.

The ground state of a paramagnetic metal naturally inherits all symmetries of its underlying crystal structure. However, several mechanisms may lead to spontaneous breaking of this crystal symmetry as the system is driven by a change in some control parameter (e.g. temperature, electron doping or pressure) toward an ordered ground state. For such symmetry breaking to occur, both electron and lattice degrees of freedom are often required. Occasionally, though, the electron degrees of freedom alone are sufficient to lead to instability, while the lattice only adjusts itself to the new ground state, offering little contribution to the overall energy gain. In the special case of so-called "electronic nematic" phases, only the rotational symmetry of the electron subsystem is reduced, whereas the translational symmetry and, hence, the size of the **B**rillouin **z**one (BZ) are preserved. Electronic nematicity has been suggested for various iron-arsenide superconductors [1], motivated by the anisotropic in-plane cross-sections of the spin-excitation spectra seen by **i**nelastic **n**eutron **s**cattering (INS) [2].

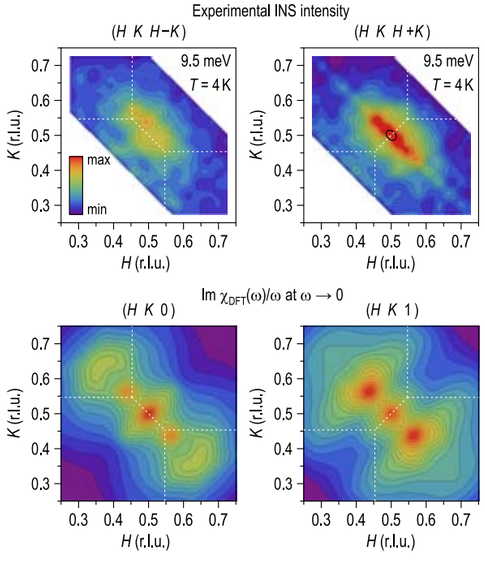

Figure 1: Top: Experimental in-plane intensity distributions for $BaFe_{1.85}Co_{0.15}As_2$ near (1/2 1/2 0) (left) and (1/2 1/2 1) (right), measured at 9.5 meV. Bottom: Results of the density-functional-theory calculations for 7.5 % Co doping (virtual crystal approximation) in the same reciprocal-space regions.

Experiments at PUMA and PANDA

In our recent work stemming from INS experiments performed at the PUMA and PANDA triple-axes spectrometers at FRM II [3], we have mapped out spin excitations in $BaFe_{1.91}Ni_{0.09}As_2$ (T_c = 18 K) and $BaFe_{1.85}Co_{0.15}As_2$ (T_c = 25 K) single crystals, covering energy transfer up to E = 20 meV. In figure 1, we show experimental constant-energy maps, interpolated from a series of Q-scans in the vicinity of the antiferromagnetic wavevector (1/2 1/2 1) and its in-plane projection (–1/2 1/2 0), measured in the (H K [H+K]) scattering plane. The observed anisotropy shows perfect agreement with the calculated dynamic spin susceptibilities of the paramagnetic tetragonal phase, plotted below in equivalent regions of Q-space. As these first-principles calculations do not assume any broken symmetries, we have to conclude that a different mechanism must be responsible for the observed elliptical cross-section of the excitations. It is related to the peculiar crystal structure of these compounds, as we shall illustrate below.

Two Brillouin zone types

In most ferropnictides, it is natural to consider two BZ types: unfolded, i.e. corresponding to the Fe sublattice only, and folded, which takes full account of the remaining nonmagnetic atoms in the unit cell. Because of the higher symmetry of the Fe-sublattice with respect to the crystal itself, the unfolded zones have twice larger volume than their folded counterparts. Figure 2 schematically illustrates the spin-excitation patterns in both notations. In the folded (conventional) notation, the INS signal is observed at the corner of the BZ, which has a four-fold symmetry. Therefore, axial anisotropy has to be introduced to explain its elliptical shape. The four-fold symmetry of the pattern is restored only as a result of electronic twinning (top panel). On the other hand, we argue that the same pattern could result from a change in the translational symmetry, from folded to the unfolded BZ (bottom panel), without invoking any nematic state. Here the higher symmetry of the Fe-sublattice leads to a larger BZ, so that the INS signal is now located at the zone boundary, rather than at its corner. It therefore naturally acquires a two-fold symmetry that is indistinguishable at the first glance from the one that would result from a twinned electron-nematic state. Nevertheless, the temperature independence of the ellipse's aspect ratio and its increase with the decreasing magnetic strength in chemically doped samples [3] corroborates the structural origin of the spectrum's distortion and supports the second alternative, depriving the nematic scenario in tetragonal iron pnictides of its main supporting evidence.

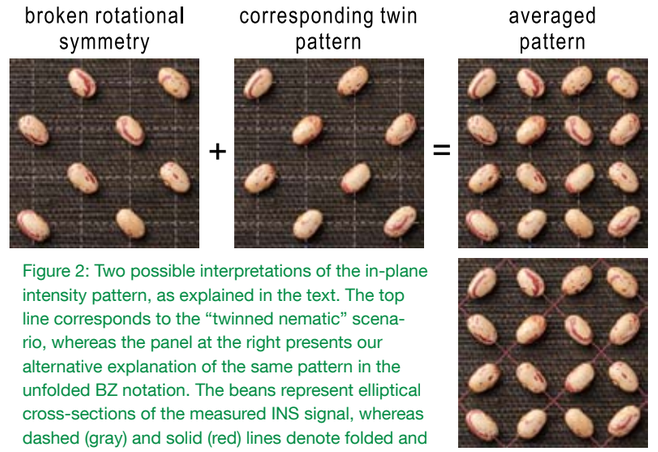

Figure 2: Two possible interpretations of the in-plane intensity pattern, as explained in the text. The top line corresponds to the "twinned nematic" scenario, whereas the panel at the right presents our alternative explanation of the same pattern in the unfolded BZ notation. The beans represent elliptical cross-sections of the measured INS signal, whereas dashed (gray) and solid (red) lines denote folded and unfolded BZ boundaries, respectively. Photos by courtesy of Kawia Scharle.

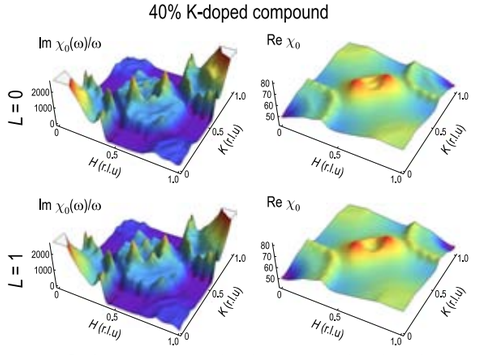

Figure 3: Bare spin susceptibility (Lindhard function) from a density-functional-theory calculation in hole-doped Ba-122. Note the longitudinal elongation of the patterns, as opposed to the transverse anisotropy in fig. 1.

A daring prediction

The agreement between measured data and first-principles calculations led us to a prediction that the anisotropy should vanish and subsequently switch to the longitudinal orientation as the system is doped with more holes [3], as shown in figure 3. This daring prediction sharply opposes the nematic scenario, as any symmetry breaking of magnetic origin would be expected to behave similarly on both sides of the phase diagram in systems with equivalent magnetic structures. As our work [3] went to press, no INS data on single-crystalline hole-doped compounds was yet available to verify this prediction. More recently, however, longitudinal elongation of the anisotropic cross-sections was indeed observed in two independent INS experiments on optimally hole-doped $Ba_{1-x}K_xFe_2As_2$ [4] and fully hole-doped KFe_2As_2 [5], in full agreement with our calculations for the tetragonally symmetric paramagnetic state.

[1] D. Johnston et al., Adv. Phys., 59, 803 (2010).
[2] C. Lester et al., Phys. Rev. B, 81 (6), 064505 (2010).
[3] J.T. Park et al., Phys. Rev. B, 82 (13), 134503 (2010).
[4] C. Zhang et al., arXiv: 1012.4065 (2010).
[5] C.H. Lee et al., Phys. Rev. Lett., 106 (6), 067003 (2011).

Normal-state hourglass dispersion in spin excitations of $FeSe_xTe_{1-x}$

Shiliang Li[1], Chenglin Zhang[2], Meng Wang[1,2], Hui-qian Luo[1], Xingye Lu[1], E. Faulhaber[3,4], A. Schneidewind[3,4], P. Link[4], Pengcheng Dai [1,2,5]

[1]Chinese Academy of Sciences, Institute of Physics, Beijing, China
[2]University of Tennessee, Department of Physics and Astronomy, Knoxville (TN), USA
[3]Helmholtz-Zentrum Berlin für Materialien und Energie, Gemeinsame Forschergruppe HZB - TU Dresden, Berlin, Germany
[4]Technische Universität München, Forschungs-Neutronenquelle Heinz Maier-Leibnitz (FRM II), Garching, Germany
[5]Oak Ridge National Laboratory, Neutron Scattering Science Division, Oak Ridge (TN), USA

The interplay between spin fluctuations and superconductivity has played a key role in many unconventional superconductors. Here, we used the PANDA cold three axes spectrometer to study the low-energy spin excitations of the $FeSe_xTe_{1-x}$ system, one of the newly discovered Fe-based superconductors. In both superconducting and non-superconducting samples, we found the hourglass dispersion which represents the evolution of in-plane incommensurate spin excitations with the change of energy. Our results can be understood within a picture of Fermi surface nesting assuming extremely low Fermi velocities and spin-orbital coupling.

The role of magnetism

The discovery of antiferromagnetism in the Fe-based superconductors has invigorated research into understanding the role of magnetism within superconductivity. Among the different classes of iron pnictides, $FeSe_xTe_{1-x}$ has the simplest crystal structure, being composed of layers of Fe atoms forming a square lattice with Se/Te atoms centered above or below these squares and alternating in a chequerboard fashion (fig. 1a) [1]. To obtain a comprehensive understanding of the role of magnetism in the superconductivity of $FeSe_xTe_{1-x}$, it is important to determine the energy (E) and momentum (Q) dependence of its spin excitations in the normal and the **s**uper**c**onducting (SC) state, and compare these results to those of the other Fe-based [2] and cuprate high-T_c superconductors [3]. A commensurable neutron spin resonance was found in $FeSe_xTe_{1-x}$ with x = 0.4, 0.5 [4]. Further experiments have revealed that the spin excitations at energies near and above the resonance energy are incommensurable (fig. 1b) [5]. Thus we decided to study the spin excitations in this system at very low energies.

The set-up

We carried out our inelastic neutron scattering experiments using the PANDA cold three axes spectrometer at the FRM II. We used pyrolytic graphite PG*(0,0,2)* as monochromator and analyzer without any collimator. The final neutron wave vector was fixed at $\boldsymbol{k}_f$ = 1.55 Å^{-1} with a cooled Be filter in front of the analyzer. We define the momentum transfer Q at (q_x, q_y, q_z) as (H, K, L) = (q_x $a/2\pi$, q_y $b/2\pi$, q_z $c/2\pi$) **r**eciprocal **l**attice **u**nits (rlu), where the lattice parameters of the tetragonal unit cell (*P4/nmm* space group) are a = b = 3.786 Å and c = 6.061 Å. We co-aligned ~15 gr of single crystals of x = 0.4 samples to within 1.5° (prepared using flux method with T_c = 14 K) in the [H,K,0] scattering plane with c-axis vertical. All momentum transfers given as Q = (H,K) are read to be Q = (H,K,0). We also measured a poorly superconducting (NSC) $FeSe_xTe_{1-x}$ (x = 0.45) sample (~23 gr) with a T_c of 10 K and a superconducting volume less than 30 % in the same scattering zone.

Transverse scans

Since the magnetic scattering of the x = 0.4 sample near the resonance energy was highly two-dimensional and showed peaks at (0.5-δ, 0.5+δ) and (0.5+δ, 0.5-δ) positions [2], we focussed our attention on the energy evolution of these two peaks by carrying out transverse scans along the [H,1-H,0] direction.

At 20 K, the scattering at E = 1 meV shows two clear peaks centered at (0.5-δ, 0.5+δ) and (0.5+δ,0.5-δ) positions respectively with δ = 0.132 ± 0.007 (fig. 2a, open circles). Upon cooling to 1.5 K, the incommensurable peaks disappear and the scattering becomes featureless indicating the opening of a spin gap (fig. 2a, filled squares). The scans along the scan-b direction (fig. 2b) also confirmed the incommensurable nature of the excitations.

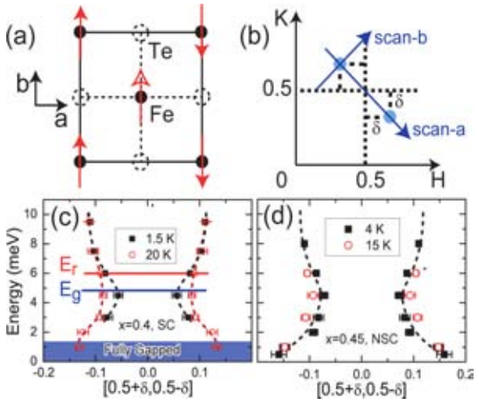

Figure1: (a) Schematic in-plane spin structure of the nonsuperconducting FeTe. (b) The incommensurable scattering in $FeSe_xTe_{1-x}$, which only appear at positions (0.5-δ, 0.5+δ) and (0.5+δ, 0.5-δ). Our transverse scans are along the scan direction a, and the scan along the incommensurate position that is perpendicular to scan-a is marked as scan-b. (c) Experimental determination of the spin excitation dispersions in the normal (open red circles) and SC (black filled squares) states of $FeSe_{0.4}Te_{0.6}$. (d) Hourglass dispersion in the NSC $FeSe_{0.45}Te_{0.55}$ at 4 K and 15 K.

Temperature dependence

The scattering's temperature dependence at E = 1 meV and Q = (0.5-δ, 0.5+δ), where δ = 0.13, (fig. 2c) shows a sudden reduction of intensity near T_c. For comparison, the intensity of the resonance at E = 6 meV and Q = (0.5, 0.5) below T_c (fig. 2c) clearly increases below T_c [4].

We also measured the incommensurable peaks at higher energies and plotted the energy dependence of incommensurability δ (fig. 1c). It is immediately clear that spin excitations of $FeSe_{0.4}Te_{0.6}$ display an hourglass-like dispersion in the normal state. In order to see if the hourglass dispersion in figure 1c is directly connected to superconductivity, we prepared especially a nearly NSC x = 0.45 sample and carried out identical measurements to those for the SC x = 0.4 sample. Although the NSC x = 0.45 exhibits an hourglass dispersion remarkably similar to that in the x = 0.4 SC sample (figs. 1c, 1d), the incommensurable scattering at 1 meV shows no temperature dependence (fig. 2d).

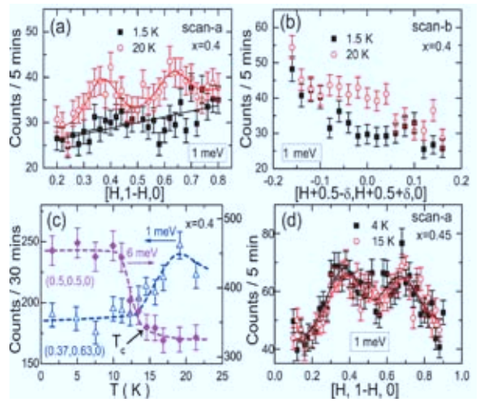

Figure 2: (a) Constant energy scans at E = 1 meV along the scan-a direction below (solid squares) and above T_c (open circles). (b) Constant-energy scans along the scan-b direction below and above T_c. (c) The temperature dependence of the scattering at Q = (0.37, 0.63) and E = 1 meV. (d) Similar scans as (a) in the x = 0.45 NSC sample.

The hourglass dispersion may be understood within a Fermi surface nesting picture similar to the case of pure chromium [6]. In the $FeSe_xTe_{1-x}$ system, we have to consider two nesting wavevectors in a multi-band system, where the two hole pockets (α2 and α3) at Γ point are nested to the electron pockets at the M point. However, an extremely flat band is required to produce the flat dispersion of spin excitations observed at low energies.

In summary, we observe the hourglass dispersion in both SC and NSC $FeSe_xTe_{1-x}$ samples. Further investigations, both experimental ans theoretical, need to be carried out to determine whether the hourglass behaviour of spin excitations is a very common feature in the metallic states of these magnetically-fluctuating systems.

[1] S. Li et al., Phys. Rev. B, 79 (5), 054503 (2009).
[2] M.D. Lumsden et al., Phys. Rev. Lett., 102 (10), 107005 (2009); S. Chi et al., Phys. Rev. Lett., 102 (10), 107006 (2009).
[3] B. Vignolle et al., Nature Phys., 3 (3), 163 (2007); S.M. Hayden et al., Nature (London), 429 (6991), 531 (2004).
[4] Y. Qiu et al., Phys. Rev. Lett., 103 (6), 067008 (2009); H.A. Mook et al., Phys. Rev. Lett., 104 (18), 187002 (2010).
[5] M.D. Lumsden et al., Nature Phys., 6 (3), 182 (2010); D. N. Argyriou et al., Phys. Rev. B, 81 (22), 220503(R) (2010); S.-H. Lee et al., Phys. Rev. B, 81 (22), 220502(R) (2010).
[6] Y. Endoh et al., J. Phy. Soc. Jpn., 63 (10), 3572 (1994); F. S. Fishman et al., Phys. Rev. B, 54 (10), 7252 (1996).

New magnetic excitation elucidates the pseudo-gap mystery in a model high-T_c superconductor

Y. Li[1], V. Balédent[2], G. Yu[3], N. Barišić[4,5], K. Hradil[6], R. Mole[6], Y. Sidis[2], P. Steffens[7], X. Zhao[4,8], P. Bourges[2], M. Greven[3]

[1]Stanford University, Department of Physics, Stanford (CA), USA
[2]CEA-Saclay, Laboratoire Léon Brillouin, CEA-CNRS, Gif sur Yvette, France
[3]University of Minnesota, School of Physics and Astronomy, Minneapolis (MN), USA
[4]Stanford University, T. H. Geballe Laboratory for Advanced Materials, Stanford (CA), USA
[5]Universität Stuttgart, 1. Physikalisches Institut, Stuttgart, Germany
[6]Technische Universität München, Forschungs-Neutronenquelle Heinz Maier-Leibnitz (FRM II), Garching, Germany
[7]Institut Laue Langevin, Grenoble, France
[8]Jilin University, State Key Lab of Inorganic Synthesis and Preparative Chemistry, College of Chemistry, Changchun, China

Almost 25 years after the original discovery of high-temperature superconductivity in the cuprates, a novel magnetic excitation was recently discovered in the model system $HgBa_2CuO_{4+\delta}$ by an international team of scientists in collaboration with the FRM II. The results, reported in the November issue of the journal "Nature", shed new light on the physical origin of the so-called 'pseudo-gap' phase, which precedes the superconducting state upon cooling and which is widely believed to be the key to understanding the entire phase diagram. Measurements performed on the PUMA spectrometer were a key component in the discovery.

Superconductivity and temperature

Superconductivity is a quantum state of matter characterized by the complete absence of electrical resistance and the repulsion of magnetic fields. The phenomenon is potential for a wide range of technical applications, but in most materials it appears only at extremely low temperatures, which in effect restricts the application due to the high cost of cooling. In 1987 and subsequent years, a class of materials based on copper oxide (the 'cuprates') was found to transform into superconductors at relatively high transition temperatures (T_c), well above the boiling point of liquid nitrogen. This has stimulated extensive research, as it is conceivable that an explanation for the cuprates' extraordinary properties could lead to the discovery of materials with even higher T_c and perhaps realize the dream of room-temperature superconductivity. Despite many years of intense research, the mechanism remains a mystery today; it is, however, known that, upon cooling and before becoming superconducting, the cuprates pass through a peculiar state – known as the 'pseudo-gap phase' – in which their many physical properties deviate considerably from those of normal metals. This leads to the widely-accepted empirical expectation that the pseudo-gap phase is the key to understanding the entire phase diagram, including the superconductivity.

Varma's current loop theory

In a distinctive theoretical proposal put forward by C. M. Varma, professor at Riverside (California, USA), the pseudo-gap phase is attributed to a novel electronic state of matter characterized by a spontaneous formation of microscopic current loops flowing on the atomic orbital of adjacent copper and oxygen. These current loops create static as well as fluctuating magnetic moments that should be detectable by magnetic neutron scattering.

A team of scientists from France and the USA has been working for several years on the experimental verification of this theory. The task is extremely difficult, as it requires the polarized neutron scattering technique and the highest performance spectrometers available. In 2006 and 2008, they found the first indication of the predicted static magnetic moments in two prototypical cuprates $YBa_2Cu_3O_{6+\delta}$ and $HgBa_2CuO_{4+\delta}$ [1]. Using the spin-polarized IN20 spectrometer at the ILL in Grenoble, they have now succeeded in observing for the first time an excitation of this ordered state in $HgBa_2CuO_{4+\delta}$ [2]. Based on this result, complementary measurements have been carried out with unpolarized neutrons using the PUMA spectrometer at the FRM II and the IN8 spectrometer at the ILL. These unpolarized measurements benefit from a much higher neutron flux than even the best spin-polarized spectrometer on earth, and have yielded important quantitative information about the excitation.

Theory and reality

According to the theory, the magnetic excitation from the current-loop order should be different from those that arise from an ordered state of electron spins: the former is expected to disperse only weakly due to the discrete symmetry of the underlying order parameter, whereas the latter is generally expected to exhibit substantial dispersion. A mapping of the excitation energy in an underdoped sample of $HgBa_2CuO_{4+\delta}$ along a high-symmetry direction throughout the two-dimensional Brillouin zone, carried out on the PUMA spectrometer (fig. 1), clearly shows that

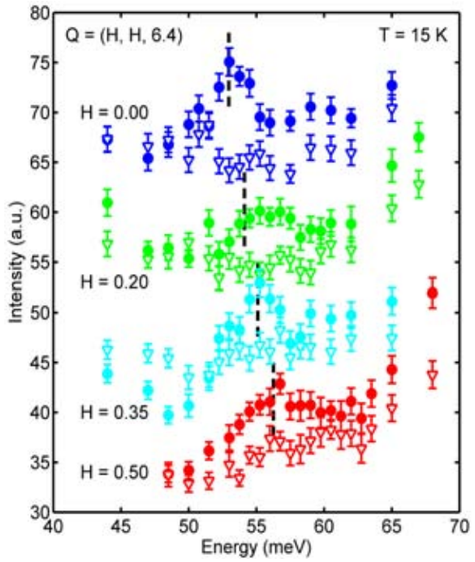

Figure 1: Unpolarized energy scans at T = 15 K for an underdoped sample of $HgBa_2CuO_{4+\delta}$, performed on the PUMA spectrometer at the FRM-II. Filled circles are measurements carried out at momentum positions of (H, H, 6.4) for the given H values, which show a weakly-dispersive excitation indicated by the dashed lines. Empty reversed triangles are an effective measurement of the background intensity at the corresponding momentum positions (after rotating the sample by 90 degrees). The data are offset for clarity.

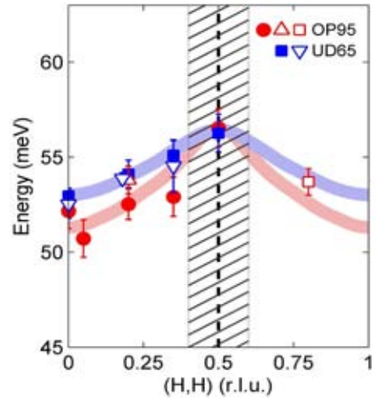

Figure 2: Summary of dispersion along (H, H) of the new magnetic excitation. Data for two doping levels (UD65: underdoped with T_c = 65 K; OP95: optimally-doped with T_c = 95 K) are shown. Conventional antiferromagnetic spin fluctuations are expected in the hatched area only. Square symbols (empty and filled) represent data measured on PUMA.

the dispersion of the excitation is weak, consistent with the prediction of the current-loop theory. The high neutron flux and low background level of PUMA are crucial for observing the relatively weak inelastic signal systematically and directly from the raw data. As summarized in figure 2, the dispersion of the new excitation drastically differs from that of the well-studied antiferromagnetic spin fluctuations, which are only present near (0.5, 0.5) in the same energy range.

Towards better superconductors?

The observation of a weakly-dispersive magnetic excitation in the pseudo-gap phase of the model compound $HgBa_2CuO_{4+\delta}$ helps elucidate the nature of this mysterious state of matter by supporting the validity of the current loop theory. As superconductivity in the cuprates is often thought to have a magnetic origin, the discovery of new magnetic excitations is highly intriguing. If it can be shown that these results are also valid for other cuprate superconductors, they would bring us a huge step toward solving the high-T_c problem, which may ultimately guide researchers to the discovery of better superconductors.

[1] B. Fauqué et al., Phys. Rev. Lett., 96 (19), 197001 (2006); Y. Li et al., Nature, 455 (7211), 372 (2008).
[2] Y. Li et al., Nature, 468 (7321), 283 (2010).

The microscopic spin dynamics in the normal and superconducting state of UBe_{13}

A. Hiess[1], O. Stockert[2], A. Schneidewind[3,4], Z. Fisk[5]

[1]Institut Laue-Langevin, Grenoble, France
[2]Max-Planck-Institut für Chemische Physik fester Stoffe, Dresden, Germany
[3]Helmholtz-Zentrum Berlin für Materialien und Energie, Gemeinsame Forschergruppe HZB - TU Dresden, Berlin, Germany
[4]Technische Universität München, Forschungs-Neutronenquelle Heinz Maier-Leibnitz (FRM II), Garching, Germany
[5]University of California, Department of Physics & Astronomy, Irvine (CA), USA

Neutron spectroscopy has been of particular importance in appreciating the interrelation of magnetism and superconductivity by revealing the microscopic spin dynamics of condensed matter. We present here experimental results on the cubic correlated 5f electron superconductor UBe_{13} obtained on a large single crystal by high-resolution cold neutron **t**hree-**a**xes **s**pectroscopy (TAS). We observed that the spin dynamics develops on cooling for T < 50 K at specific momentum space positions and changes significantly on entering the superconducting state. This divulges not only the magnetic interactions but also unique details on the superconducting properties.

The symmetry of the superconducting order parameter and the mechanism of cooper pair formation not only for cerium- and uranium-based intermetallic but also for copper-oxide- and (more recently) iron-based high-temperature superconductors are still hotly debated. In all these materials, magnetism and superconductivity may not only coexist, but the spin dynamics may actually stabilize an unconventional superconducting state. In many of these compounds, significant changes in the spin dynamics related to the superconducting state have been observed by **i**nelastic **n**eutron **s**cattering (INS). Whereas most of these materials have layered crystal structures, we present here experimental results on the cubic superconductor UBe_{13} (T_c = 0.85 K).

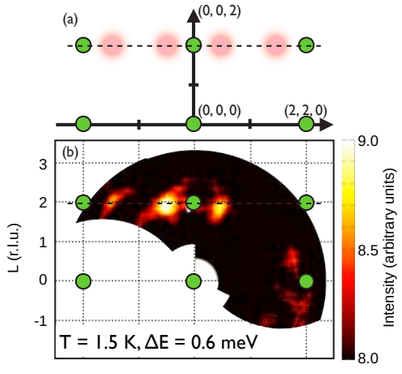

Figure 1: (a) Sketch of the (H H L) plane explored. Green dots indicate nuclear Bragg peak positions. Magenta dots indicate the positions of the broad signal observed. (b) Mapping the normal state dynamic response of UBe_{13} in the (H H L) plane using IN14 FlatCone. The observed neutron scattering intensity is colour-coded varying from black (low intensity) to white (high intensity). Beside the tails from nuclear Bragg peaks (green dots), a broad signal is visible around (±1/2, ±1/2, 2).

Is the spin dynamics longitudinally polarized?

We investigated a large UBe_{13} single crystal of m ~2.5 g on the cold neutron TAS PANDA at the FRM II and IN14 at the ILL. The spin dynamics within the (H, H, L) plane (fig. 1) has been explored at T = 1.5 K with an energy transfer ΔE = 0.6 meV using the multi-analyzer-detector FlatCone set-up [1]. In agreement with previous experiments [2,3], we observed a signal close to Q = (±1/2, ±1/2, 2) only. No such signal is visible at Q = (±3/2, ±3/2, 0). This suggests that the spin dynamics is longitudinally polarized. The dynamic magnetic response builds up on cooling for temperatures below 50 K and changes significantly on entering the superconducting state as shown in figure 2. High-resolution INS measurements were performed to investigate the energy dependence of the spin dynamics (see fig. 3).

Energy scales of the spin dynamics

The data obtained in the normal state can be modeled by superimposing a **q**uasi-**e**lastic (QE) contribution with a Lorentzian line-shape and an inelastic contribution. The QE signal is consistent with fluctuations established in INS experiments on powder samples [4,5] and linked to anomalies in the specific heat, from which a Kondo temperature T_K = 20 K has been deduced [6]. The inelastic contribution shows a maximum at ΔE = 0.55 meV. Its width exceeds the instrumental resolution establishing a finite lifetime, and will result in a Schottky-like anomaly in the specific heat at about 2 K. For this reason, we would argue the inelastic contribution is related to the anomaly observed at the same T in specific heat and thermal expansion of pure UBe_{13} [7]. Any inelastic contribution reduces the weight of low energy (QE) spin dynamics, which in a simplistic BCS-like scenario would be pair-breaking.

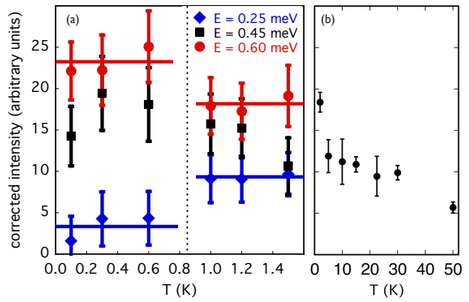

Figure 2: (a) Temperature dependence of the neutron scattering intensity at Q = (½, ½, 2) and at different energy transfers. The magnetic response in the superconducting state is reduced at low energy transfer but augmented at higher energy transfer in respect to the normal state.
(b) Temperature dependence of the neutron scattering intensity at Q = (½, ½, 2) in the energy range 0.15 meV < ΔE < 1.2 meV at higher temperatures.
Data taken on PANDA and corrected for background.

Unconventional superconductivity

Our data taken in the superconducting state shows a shift of spectral weight to higher energies with respect to the normal state, which indicates the opening of a superconducting gap that is reflected in the spin dynamics. The shift observed in UBe_{13} coincides with the inelastic contribution already present in the normal state. This situation resembles the modification observed in underdoped copper-based high-T_c superconductors placing UBe_{13} in the strong coupling regime. Interestingly, in other correlated 4f/5f electron superconductors, such as UPd_2Al_3 [8], $CeCoIn_5$ [9] and $CeCu_2Si_2$ [10], a sharp inelastic excitation (often called 'resonance') has been reported to appear at low T. This is similar to the situation reported in optimum doped copper-oxide-based high-T_c superconductors.

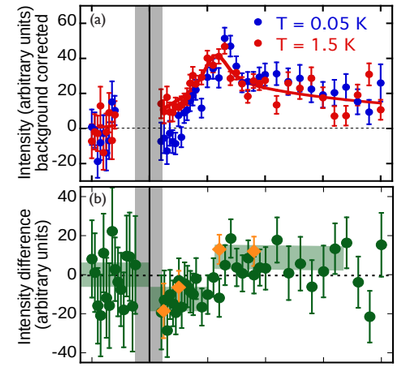

Figure 3: (a) Background corrected neutron scattering intensity at Q = (½, ½, 2) in the normal (red dots) and superconducting (blue dots) state of UBe_{13} as function of energy transfer. Data taken on IN14.
(b) Neutron scattering intensity in the superconducting state subtracted by the neutron scattering intensity in the normal state as a function of energy transfer. Green dots show the temperature difference obtained from panel (a). Orange diamonds are obtained by suppressing superconductivity with magnetic field at low T. Spectral weight is shifted from lower to higher energies in the superconducting state as indicated by the light green bars.

About 25 years after its discovery and by using the most-advanced cold TAS instruments at ILL and FRM II, the observation of longitudinally polarized, short range spin dynamics at commensurate positions in the cubic superconductor UBe_{13} provides new insight into the puzzle of unconventional superconductivity.

[1] M. Kempa et al., Physica B, 385-386 (2), 1080 (2006).
[2] S. Coad et al., Physica B, 276-278, 764 (2000).
[3] A. Hiess et al., Phys. Rev. B, 66 (6), 64531 (2002).
[4] A.I. Goldman et al., Phys. Rev. B, 33 (3), 1626 (1986).
[5] G.H. Lander et al., Phys. Rev. B, 46 (9), 5387 (1992).
[6] R. Felten et al., EPL, 2, 323 (1986).
[7] N. Oeschler et al., Acta Phys. Pol. B, 34 (2), 255 (2003).
[8] A. Hiess et al., J. Phys.: Cond. Matt., 18, R437 and references therein (2006).
[9] C. Stock et al., Phys. Rev. Lett., 100 (8), 087001 (2008).
[10] O. Stockert et al., Nature Phys., 7 (2),119 (2011).

Single magnetic chirality in the magnetoelectric $NdFe_3(^{11}BO_3)_4$

M. Janoschek[1,2], P. Fischer[1], J. Schefer[1], B. Roessli[1], V. Pomjakushin[1], M. Meven[3], V. Petricek[4], G. Petrakovskii[5], L. Bezmaternikh[5]

[1]Paul Scherrer Institut, Villigen, Switzerland
[2]Technische Universität München, Physik Department E21, Garching, Germany
[3]Technische Universität München, Forschungs-Neutronenquelle Heinz Maier-Leibnitz (FRM II), Garching, Germany
[4]Institute of Physics, ASCR, Prague, Czech Republic
[5]Institute of Physics, SB RAS, Krasnoyarsk, Russia

Our detailed single-crystal neutron diffraction measurements show that the magnetoelectric $NdFe_3(^{11}BO_3)_4$ displays the rare property of a monochiral magnetic helix. Below $T_N < 30$ K conventional antiferromagnetic order is observed that transforms continuously into a long-period incommensurate helix below $T_{IC} = 13.5$ K. Additionally, the helix formation is accompanied by the emergence of a magnetic soliton lattice.

Exciting spiral magnetism

Over the past decade, a plethora of interesting effects related to spiral-like forms of magnetic order have been revealed throughout different fields of condensed matter physics. Examples include the **m**agneto**e**lectric (ME) effect in multiferroic compounds such as $TbMnO_3$ [1], complex topological magnetic textures such as the skyrmion lattice [2], the spin-torque effect in helical magnets [3], and the spin chirality of the Fermi surface in topological insulators [4]. These examples demonstrate that spiral magnetism is not only fascinating from a scientific point of view, but also holds the promise of important future applications like novel spintronics or memory/storage devices.

In our study we investigated the compound $NdFe_3(^{11}BO_3)_4$ belonging to the family of ferroborates $RM_3(BO_3)_4$ (R = rare earth) that are intriguing in respect of their magnetic properties. Here, $NdFe_3(BO_3)_4$ is especially exciting as it shows a large ME, i.e. a large coupling between magnetic and electric fields within the sample [5]. The focus of our work was to resolve the magnetic structure of $NdFe_3(^{11}BO_3)_4$, which is essential for an understanding of the ME in a specific material. Interestingly, our results demonstrate that $NdFe_3(^{11}BO_3)_4$ is a new compound exhibiting a rare property of spiral magnetism: monochirality.

Powerful short wavelength neutrons

To determine the magnetic structure of $NdFe_3(^{11}BO_3)_4$ we carried out unpolarized and polarized neutron single crystal diffraction experiments at the Paul Scherrer Institut (PSI) and the FRM II. To resolve a magnetic structure, an exact knowledge of the crystal structure is a necessary prerequisite, since all allowed magnetic structures are constrained by the overall crystal symmetry. For $NdFe_3(^{11}BO_3)_4$ the verification of the crystal structure was particularly important because earlier powder diffraction results indicated that the crystal symmetry of $NdFe_3(^{11}BO_3)_4$ might only be $R3$ at low temperatures, in contrast to the room temperature space group $R32$. The instrument HEiDi at FRM II is optimally suited for this task. The measurements were performed with the neutron wavelength $\lambda = 0.55$ Å available with high intensity at HEiDi. This short wavelength offers two advantages:
(i) more Bragg reflections are accessible, and
(ii) neutron extinction and absorption are significantly less severe compared to longer wavelengths.

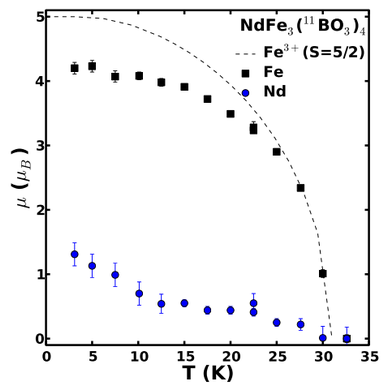

Figure 1: Temperature dependencies of the ordered magnetic Fe and Nd moments in $NdFe_3(^{11}BO_3)_4$. The dashed line represents the moment expected for S = 5/2 of Fe^{3+}.

These advantages are crucial for the accurate measurements of both nuclear and magnetic structure factors. While for the overall determination of the magnetic structure we performed **s**pherical **n**eutron **p**olarimetry (SNP) by means of the device MuPAD at the PSI [6], additional measurements of the magnetic structure were carried out at HEiDi with unpolarized neutrons (fig. 1). Here, SNP provides more detailed information about the directions of the magnetic moments by using the additional degree of freedom provided by the neutron polarization. However, for non-ferromagnetic compounds such as $NdFe_3(^{11}BO_3)_4$ additional unpolarized measurements are required to determine the size of the magnetic moments.

Single magnetic chirality and magnetic soliton lattice

The measurements at HEiDi demonstrate that the chemical structure of $NdFe_3(^{11}BO_3)_4$ is well described with the space group $R32$ down to low temperatures. Further, our results show that the magnetic order of $NdFe_3(^{11}BO_3)_4$ below $T_N = 30$ K consists of antiferromagnetic stacking along the c axis, where the magnetic moments of all Fe^{3+} and Nd^{3+} sublattices are aligned ferromagnetically and parallel to the hexagonal basal plane (fig. 2). Below $T_{IC} = 13.5$ K the magnetic structure turns into an incommensurate helix propagating along the c axis with a period of 1140 Å [7].

Our polarized neutron-diffraction data further suggests that only one of the two possible chiral domains is populated. A single chirality domain is, in principle, not expected, since left- and right-handed spirals are energetically degenerate. However, in the case of $NdFe_3(^{11}BO_3)_4$ this might be related to the noncentrosymmetric chemical structure.

This is similar to MnSi and $Ba_3NbFe_3Si_2O_{14}$ which are both noncentrosymmetric and the only previously reported examples of magnetic monochirality. As indicated by the observation of third-order harmonics of the magnetic Bragg peaks, the phase transition to the helical state in $NdFe_3(^{11}BO_3)_4$ is additionally accompanied by the formation of a magnetic soliton lattice, which is interesting in its own right.

In conclusion, we identified the new monochiral compound $NdFe_3(^{11}BO_3)_4$, which provides us with a new model system for investigating the properties of magnetic chirality.

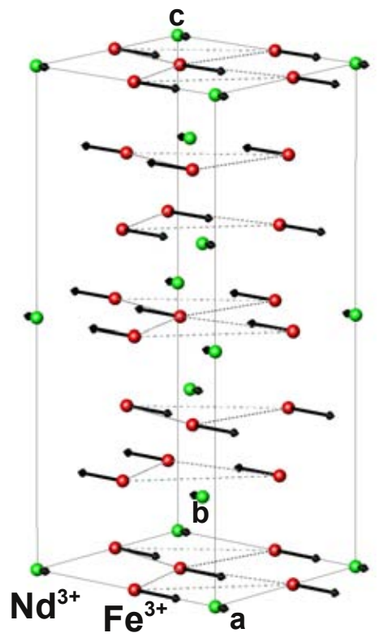

Figure 2: Magnetic structure of $NdFe_3(^{11}BO_3)_4$ in the commensurate state above $T_{IC} = 13.5$ K.

[1] M. Kenzelmann et al., Phys. Rev. Lett., 95 (8), 087206 (2005).
[2] S. Mühlbauer et al., Science, 323 (5916), 915 (2009).
[3] F. Jonietz et al., Science, 330 (6011), 1648 (2010).
[4] D. Hsieh et al., Science, 323 (5916), 919 (2009).
[5] A.K. Zvezdin et al., JETP Lett., 83 (10), 509 (2006).
[6] M. Janoschek et al., Physica B, 397 (1-2), 125 (2007).
[7] M. Janoschek et al., Phys. Rev. B, 81 (9), 094429 (2010).

Spin transfer torques in MnSi at ultra-low current densities

F. Jonietz[1], S. Mühlbauer[1], C. Pfleiderer[1], A. Neubauer[1], W. Münzer[1], A. Bauer[1], T. Adams[1], R. Georgii[1, 2], P. Böni[1], R. A. Duine[3], K. Everschor[4], M. Garst[4], A. Rosch[4]

[1]Technische Universität München, Physik Department E21, Garching, Germany
[2]Technische Universität München, Forschungs-Neutronenquelle Heinz Maier-Leibnitz (FRM II), Garching, Germany
[3]Utrecht University, Institute for Theoretical Physics, Utrecht, The Netherlands
[4]Universität zu Köln, Institut für Theoretische Physik, Köln, Germany

Spin manipulation using electric currents is one of the most promising directions in the field of spintronics. We used neutron scattering to observe the influence of an electric current on the magnetic structure in a bulk material. In the skyrmion lattice of MnSi we observe the rotation of the diffraction pattern in response to currents which are over five orders of magnitude smaller than those typically applied in experimental studies on current-driven magnetization dynamics in nanostructures [1]. We attribute our observations to an extremely efficient coupling of inhomogeneous spin currents to topologically stable knots in spin structures.

The skyrmion lattice in chiral magnets, like MnSi and related B20 compounds, was only recently discovered in neutron scattering studies [2,3] and confirmed to exist in Lorentz force microscopy for $Fe_{1-x}Co_xSi$ (x = 0.5) [4]. It represents a new form of magnetic order that shares remarkable similarities with the mixed state in type II superconductors.

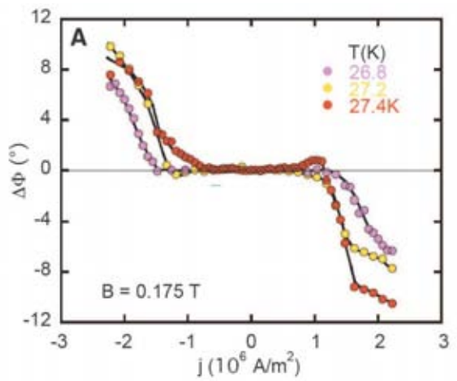

Figure 1: Current dependence of the rotation angle as a function of applied current. Above a clear threshold of 10^6 A/m^2 the rotation appears, which is antisymmetric under field reversal.

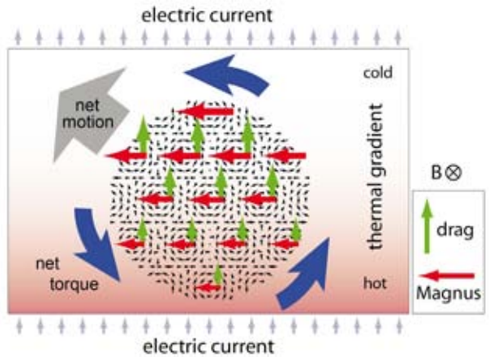

Figure 2: Schematic view of the interplay of an electric current flowing transverse to the skyrmion lattice where Magnus and drag forces arise that vary with the size of the spin polarization. This variation across the sample generates the macroscopic rotation of the spin structure observed in neutron scattering.

Generating quantum bananas

To understand the effect of an electric current, the skyrmion lattice may be viewed as an array of circulating dissipationless spin currents since the skyrmions are characterized by gradients in the spin-orientation related to their quantized winding number. This is analogous to superconductors, where dissipationless charge currents flow around quantized vortices due to gradients of the phase. When an extra spin current is induced by driving an electric current through the magnetic metal, the spin currents on one side of the skyrmion are enhanced while they are reduced on the other side. As for a spinning tennis ball, this velocity difference gives rise to a Magnus force acting on the skyrmions.

Note, however, that spin (due to spin-orbit coupling) is, in contrast to charge, not conserved and therefore this intuitive picture is incomplete.

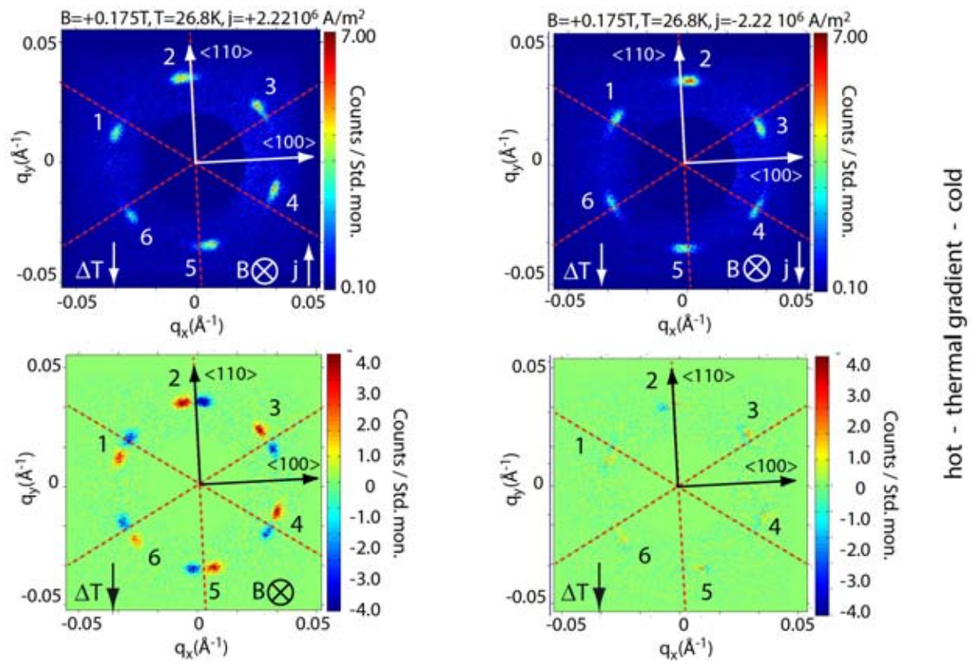

Figure 3: Antisymmetric rotation of the diffraction pattern under current reversal (panels at top). Reversal of the applied magnetic field compensates the change of rotation under current reversal, where the panel at the bottom left shows the difference of the panels shown at the top. The panel at the bottom right shows the difference of intensity under current and field reversal.

Most importantly, further dissipative forces also arise which drag the skyrmions parallel to the current.

Antisymmetric rotations

Above a clear threshold of 10^6 A/m^2 an increasingly strong rotation of the sixfold diffraction pattern of the skyrmion lattice is observed. The rotation is antisymmetric under inversion of the current direction and field direction as shown in figure 1. Moreover, the rotation arises only in the presence of a small temperature gradient along the current direction (the sense of rotation is also antisymmetric under inversion of the temperature gradient). A detailed theoretical account suggests that this rotation is accompanied by a sliding motion of the skyrmion lattice [1].

Perspectives

Our observations identify chiral magnets and systems with nontrivial topological properties as ideal systems to advance the general understanding of the effects of spin transfer torques. For instance, spin transfer torques may even be used to manipulate individual skyrmions, recently observed directly in thin samples [4]. In fact, even complex magnetic structures at surfaces and interfaces may be expected to exhibit the spin torque effects we report here [5].

Acknowledgments

We gratefully acknowledge financial support through SFB608 and TRR80, SFB/TR12 of the German Science Foundation (DFG), the Deutsche Telekom Stiftung (KE), the NSF grant PHY05-51164 (AR) and by FOM, NWO and the ERC (RD).

[1] F. Jonietz et al., Science, 326 (5958), 1348 (2009).
[2] S. Mühlbauer et al., Science, 323 (5916), 915 (2009).
[3] W. Münzer et al., Phys. Rev. B, (R) 81 (4), 041203 (2010).
[4] X.Z. Yu et al., Nature, 465 (7300), 901 (2010).
[5] M. Bode et al., Nature, 447 (7141), 190 (2007).

Critical fluctuations in $Mn_{1-x}Fe_xSi$ studied at RESEDA

A. Tischendorf[1,2] , W. Häussler[1,2], C. Pfleiderer[2], P. Böni[2]

[1]Technische Universität München, Forschungs-Neutronenquelle Heinz Maier-Leibnitz (FRM II), Garching, Germany
[2]Technische Universität München, Physik Department E21, Garching, Germany

One of the major puzzles in the search for novel electronic phases of matter concerns the putative formation of a genuine non-Fermi liquid phase in the B20 transition metal helimagnet MnSi under pressure [1]. The observation of partial magnetic order in MnSi at high pressures indicates that the non-Fermi liquid behaviour is related to the spin dynamics of unusual spin textures [2]. However, since these phenomena occur at high pressures, it has so far not been possible to measure the spin dynamics directly. In a comprehensive study of the magnetization, specific heat, AC susceptibility and electric transport properties we have recently established that the helimagnetic order in MnSi can be suppressed by substitutional Fe- or Co-doping at the Mn-sites [3]. In turn, the resulting quantum phase transitions offer an alternative means of determining the nature of the spin dynamics of itinerant electron systems in the presence of Dzyaloshinsky-Moriya interactions and complex spin textures.

We have performed elastic and quasielastic neutron scattering experiments on $Mn_{1-x}Fe_xSi$, to study the spin dynamics when approaching the quantum phase transition. In our study, we focussed on the lifetime of the paramagnetic fluctuations in pure and doped manganese silicide using the spin echo spectrometer RESEDA at FRM II. With increasing Fe-doping, the transition temperature to the ordered phase is suppressed, leading to a quantum critical transition near x = 0.19. MnSi exhibits a rich magnetic phase diagram: At zero external magnetic field, the spins form a spiral with a pitch of $\Lambda \approx 180$ Å at low temperature. When a moderately small magnetic field is applied, the system transforms into

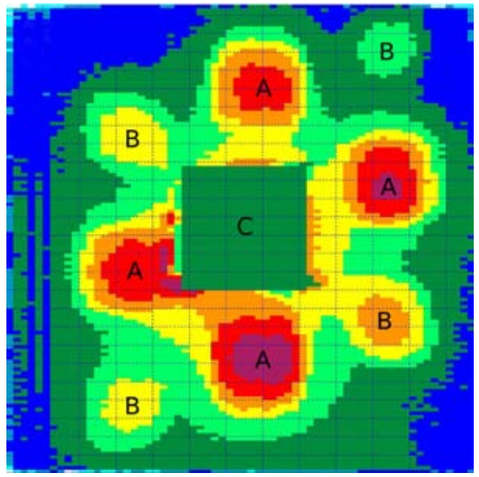

Figure 1: Diffraction pattern in pure MnSi, characterized by four helimagnetic satellite peaks (A) along the <111> directions. The four peaks with reduced intensity arise from double scattering (B), the direct beam was shielded by a boron rubber plate (C).

the A phase, which may be described by a lattice of skyrmions, i.e. particle-like knots in the magnetization [4]. The lattice constant of the skyrmion lattice is close to Λ and therefore much larger than a = 4.558 Å of the underlying crystal lattice. The discovery of the skyrmion lattice establishes the existence of topologically non-trivial spin textures, which may also strongly affect the spin dynamics at the quantum phase transition.

High energy resolution at small scattering angles

The neutron spin echo technique relies on the spin precession of polarized neutrons in two magnetic fields (B_1 and B_2), which are located before (B_1) and after the sample (B_2). B_2 is oriented such that the spin phases φ_1 and φ_2 accumulated in each of the two magnetic fields cancel each other. Ideally, for elastic scattering $\varphi_1 = \varphi_2$ and the polarization at the analyzer-detector is recovered. However, quasielastic or inelastic scattering at the sample leads to a finite precession phase resulting in a decrease of the final polarization P_f. A measurement of $P_f(t)$ yields directly the intermediate scattering function I(Q,t), that is, the time-Fourier transform of the scattering function S(Q,ω), which is essentially proportional to the generalized susceptibility χ(Q,ω).
In order to study the spin dynamics at small scattering angles (NRSE-SANS), we use an appropriate beam collimation to reduce the background scattering of the direct beam and improve the Q-resolution. The incident mean wavelength is λ = 5.5 Å, providing a good trade-off between resolution and highest neutron flux available at RESEDA. This instrument set up is well suited for the investigation of magnetic phase transitions. We used a closed-cycle cryostat to investigate a pure and a Fe-doped crystal near their phase transition temperature. The samples show a high scattering intensity around the magnetic satellite peaks. In our measurements, we varied both the temperature around the phase transition temperature and the momentum transfer around the satellite peak. The typical lifetime of the magnetic fluctuations matches the spin-echo times available at RESEDA well.
We studied two different single crystals, namely x = 0 and x = 0.12. In pure MnSi and Fe-doped MnSi (x = 0.12) the magnetic transition temperatures are T_c = 28.85 K and 6.5 K, and the pitches of the helix are $\Lambda_h \approx 180$ Å and 88 Å, respectively.

Finite line width below T_c

Figure 1 shows a typical diffraction pattern measured in pure MnSi with a CASCADE detector [5]. The direct beam in the middle of the detector was shielded by boron rubber. Between the four magnetic satellite peaks at an ordering vector of Q = k = 0.039 Å^{-1} additional peaks are observed which arise from double scattering.
Figure 2 illustrates the intermediate scattering function of $Mn_{0.88}Fe_{0.12}Si$ measured for Q = k = 0.074 Å^{-1}, corresponding to the helical ordering vector of this composition. The line width Γ of the magnetic fluctuations, which is inversely proportional to the lifetime, is obtained

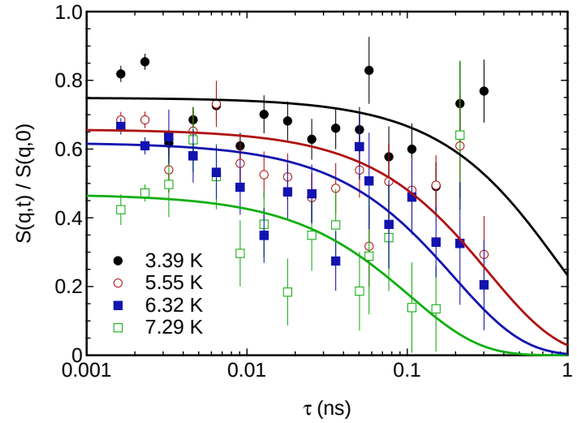

Figure 2: Intermediate scattering function of $Mn_{0.88}Fe_{0.12}Si$ as measured by means of neutron spin echo at Q = 0.074 Å^{-1}. The fluctuations speed up with increasing temperature.

by fitting an exponential decay to the intermediate scattering function. Due to thermal excitations, the line width Γ increases with increasing temperature. In contrast, below T_c, the line width remains finite. This result differs from pure MnSi, where the line width is zero for temperatures well below T_c [6], as expected for an ordered system. Moreover, for both compositions Γ (q = 0) is finite above T_c (here: q = Q - k, where k describes the magnetic ordering vector). This is in contrast to isotropic ferromagnets, where the linewidth is zero at q = Q = 0. The linewidth Γ in pure MnSi is small and increases with temperature, whereas in $Mn_{0.88}Fe_{0.12}Si$ it is larger due to additional damping. Further measurements for different concentrations x are planned for the future to determine the evolution of the linewidth when approaching quantum criticality.

[1] C. Pfleiderer et al., Nature, 414 (6862), 427 (2001).
[2] C. Pfleiderer et al., Nature, 427 (6971), 227 (2004).
[3] A. Bauer et al., Phys. Rev. B, 82 (6), 064404 (2010).
[4] S. Mühlbauer et al., Science, 323 (5916), 915 (2009).
[5] W. Häußler et al., Rev. Sci-. Instrum., 82, 045101 (2011).
[6] A. Tischendorf, Diploma Thesis, Technische Universität München (2010).

Neutron depolarisation imaging of the Kondo system $CePd_{1-x}Rh_x$

P. Schmakat[1], M. Schulz[2], P. Böni[1,2], C. Pfleiderer[1], M. Brando[3], C. Geibel[3], M. Deppe[3], E. Calzada[2], S. Masalovich[2]

[1]Technische Universität München, Physik Department E21, Garching, Germany
[2]Technische Universität München, Forschungs-Neutronenquelle Heinz Maier-Leibnitz (FRM II), Garching, Germany
[3]Max-Planck-Institut für Chemische Physik fester Stoffe, Dresden, Germany

The heavy fermion compound $CePd_{1-x}Rh_x$ undergoes a quantum phase transition as a function of Rh content x, where ferromagnetism is continously suppressed and vanishes at x = 0.87 [1]. In the magnetic phase diagram shown in figure 1 the curvature of the phase boundary at T_C(x) changes sign at x = 0.65. For Rh concentrations x > 0.70 spin-glass behaviour has been reported, which may be the manifestation of a so called Kondo-Cluster-Glass [2]. Metallurgical inhomogeneities causing a random distribution of Kondo temperatures due to the statistical distribution of the Pd and Rh atoms result in cluster formation. For this range of concentrations the low temperature properties are dominated by a freezing transition of these clusters [3]. We have used **n**eutron **d**epolarisation **i**maging (NDI) to explore the nature of the spin freezing in $CePd_{1-x}Rh_x$.

NDI was recently set up at the beam line ANTARES at FRM II [4]. The depolarization of a polarized neutron beam, transmitting the sample, is thereby analyzed. The beam is well collimated, as the instrument is build for radiography. A CCD camera in combination with a LiF/ZnS converter and scintillator film is used as the detector. This allows the polarisation to be resolved spatially across the entire sample. For studies of samples with elevated Rh concentration and thus a transition temperature in the milli-Kelvin range we combined the NDI technique with the standard pulse tube cryostats of the sample environment group at FRM II. This allowed us measurements at temperatures down to 370 mK and 75 mK using a ^{3}He insert and a ^{3}He/^{4}He dilution insert, respectively. A bespoke pair of Helmholtz coils surrounding the cryostat at the sample position allowed us to apply small fields up to 22.5 mT.

Distribution of transition temperatures

Evaluated NDI data of samples with a Rh concentration x = 0.40 and x = 0.60, respectively, are shown in figure 2. The T_C maps were derived from temperature scans in a small magnetic field of B = 7.5 mT. The maps show the distribution of the magnetic ordering temperature over the sample. The colour coding in the histogram below each map represents the corresponding transition temperature. It can be seen from the histograms, that the distribution of transition temperatures of the sample with x = 0.60 is wider than the distribution measured in the sample with x = 0.40.

This may be a signature of the increasing disorder introduced by the chemical substitution. NDI measurements on **z**ero-**f**ield-**c**ooled (zfc) as well as **f**ield-**c**ooled (fc) samples under **f**ield-**h**eating (fh) underscore the role of applied magnetic fields. Figure 3 shows typical depolarisation data from zfc-fh and fc-fh measurements on three $CePd_{1-x}Rh_x$ samples with Rh concentrations

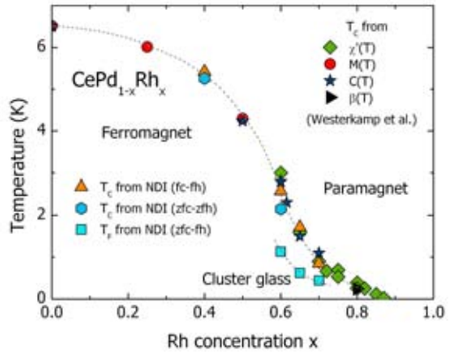

Figure 1: Temperature versus concentration phase diagram of the Kondo lattice system $CePd_{1-x}Rh_x$ as a function of Rh content x. When ferromagnetism is suppressed continuously a Kondo screened state emerges. After Ref. [3].

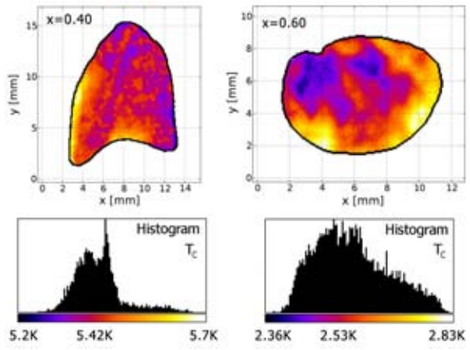

Figure 2: The T_C maps of $CePd_{1-x}Rh_x$ for x = 0.40 and x = 0.60. The colour coding in the corresponding histogram below each map represents the T_C distribution over the sample.

x = 0.40, x = 0.60 and x = 0.65, respectively. The sample with x = 0.40 shows the typical behaviour expected of a ferromagnet. The depolarisation sets in at the transition temperature and remains strong for T → 0. Measurements on samples with x > 0.40 suggest a freezing transition of the magnetic moments under zero-field-cooling. When a small magnetic field of 7.5 mT is applied after zero-field-cooling, the depolarisation remains nearly constant. With increasing temperature the ferromagnetic behaviour is reentrant in a finite temperature interval. At the slightly higher transition temperature the paramagnetic phase is reached.

The competition between the long and short range order can be seen in samples with x > 0.60. The sample with x = 0.65 shows a vanishing depolarisation after zero-field-cooling. A small magnetic field of 7.5 mT enhances the depolarisation remarkably. This means that the long-range order is nearly suppressed, but can be induced by the external magnetic field.

Disorder and cluster formation

For a Rh concentration x = 0.40 we find a clear ferromagnetic transition in the depolarisation curves. Glassy behaviour at intermediate Rh concentrations may be associated with the increase of the splitting of the depolarisation curves which is reminiscent of spin glass behaviour in the magnetisation. Disorder in this concentration range leads to a distribution of Kondo temperatures which results in cluster formation.

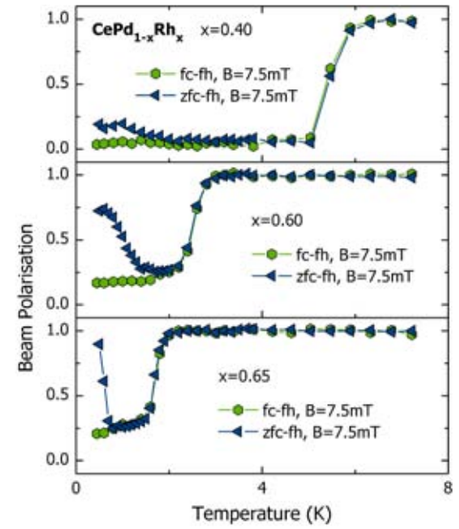

Figure 3: Typical depolarisation curves extracted from both zfc-fh and fc-fh data recorded in $CePd_{1-x}Rh_x$ with Rh concentrations x = 0.40, x = 0.60 and x = 0.65, respectively. The signature of the cluster glass formation is associated with the onset of the splitting of the curves.

These clusters emerge in a surrounding of Kondo screened moments, thereby interacting through RKKY interactions. This results in frustration and random freezing of the clusters at low temperatures. A small external magnetic field seems to enhance the long range magnetic correlations in this concentration regime. For Rh concentrations x > 0.65 short-range order should dominate, since the depolarisation after zero-field-cooling vanishes completely. Further measurements on samples with higher Rh concentrations are required to confirm these considerations.

Acknowledgements

Support from the German Science Foundation under FOR960 (“Quantum Phase Transitions”) and the collaborative research network TRR80 (“From Electronic Correlations to Functionality”) are gratefully acknowledged.

[1] J.G. Sereni et al., Phys. Rev. B, 75 (2), 024432 (2007).
[2] T. Westerkamp et al., Phys. Rev. Lett., 102 (20), 206404 (2009).
[3] T. Westerkamp, PhD Thesis, Technische Universität Dresden (2009).
[4] M. Schulz, PhD Thesis, Technische Universität München (2010); P. Schmakat, Diploma Thesis, Technische Universität München (2011.)

Larmor diffraction in the ferromagnetic superconductor UGe_2

R. Ritz[1], D. Sokolov[2], T. Keller[3,4], A. D. Huxley[2], C. Pfleiderer[1]

[1]Technische Universität München, Physik Department E21, Garching, Germany
[2]The University of Edinburgh, School of Physics and Astronomy, and Centre for Science at Extreme Conditions, Edinburgh UK
[3]Max-Planck-Institut für Festkörperforschung, Stuttgart, Germany
[4]Technische Universität München, Forschungs-Neutronenquelle Heinz Maier-Leibnitz (FRM II), Garching, Germany

UGe_2 is one of only four systems currently known in which superconductivity and ferromagnetism are carried by the same electrons [1]. While most of the scenarios of the coexistence consider ferromagnetic spin fluctuations, it has also been suggested that orbital fluctuations by virtue of the strong spin-orbit-interactions of the uranium 5f electrons are essential for the Cooper pair formation [2]. We report measurements of the thermal expansion under pressure using Larmor diffraction. Our data support the latter scenario and hence may imply that superconductivity in UGe_2 is not purely driven by ferromagnetism.

It was long thought that ferromagnetism and superconductivity could not coexist microscopically. Only in the year 2000 was superconductivity reported to occur in UGe_2 under pressures between 9 kbar and 16 kbar deep inside the ferromagnetic phase, where $T_{sc} << T_C$ (fig. 1) [3]. The superconducting transition temperature T_{sc} has a maximum at a pressure $p_x \approx 12$ kbar, where a transition T_X between two ferromagnetic phases with different magnetic moments, FM1 and FM2, is suppressed [4]. Hence the T_X transition seems to play a vital role for the coexistence of superconductivity and ferromagnetism in UGe_2.
The most prominent scenario proposed to explain the superconductivity in UGe_2 assumes that an abundance of ferromagnetic spin fluctuations near p_X drives the superconductive pairing [5]. This scenario is perfectly compatible with the first order suppression of the FM2 state at p_X inferred from the magnetization. However, more recent propositions recognize that the uranium 5f electrons are subject to strong spin-orbit-coupling. Theoretical calculations thereby

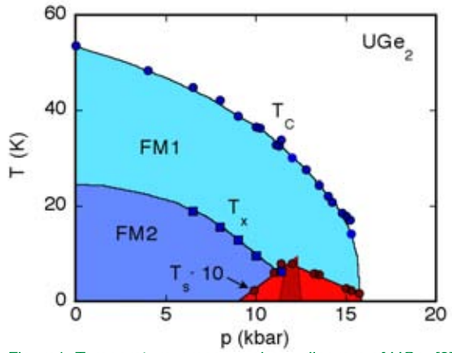

Figure1: Temperature-pressure phase diagram of UGe_2 [3].

suggest the existence of two ground states that differ in the uranium orbital moment, where the T_X transition separates these two orbital states. It has therefore been argued that orbital fluctuations near T_X may act as the pair building mechanism [2].
To resolve this issue, for all three crystallographic axes under pressures up to 12.4 kbar, we have tracked the signatures of the ferromagnetic phase transition as a function of pressure simultaneously in the thermal expansion using Larmor diffraction as well the ferromagnetic moment using normal neutron diffraction.

Strong ferromagnetism does not completely depolarize the neutron beam

All of our measurements were carried out at the spectrometer TRISP at FRM II using Larmor diffraction (LD). LD permits high-intensity measurements of lattice constants with an unprecedented high resolution of $\Delta d/d \approx 10^{-6}$. This is achieved by encoding the lattice spacing in the Larmor phase of a polarized neutron beam rather than in the scattering angle as in conventional scattering experiments. A detailed description of LD is given in ref. [6,7].

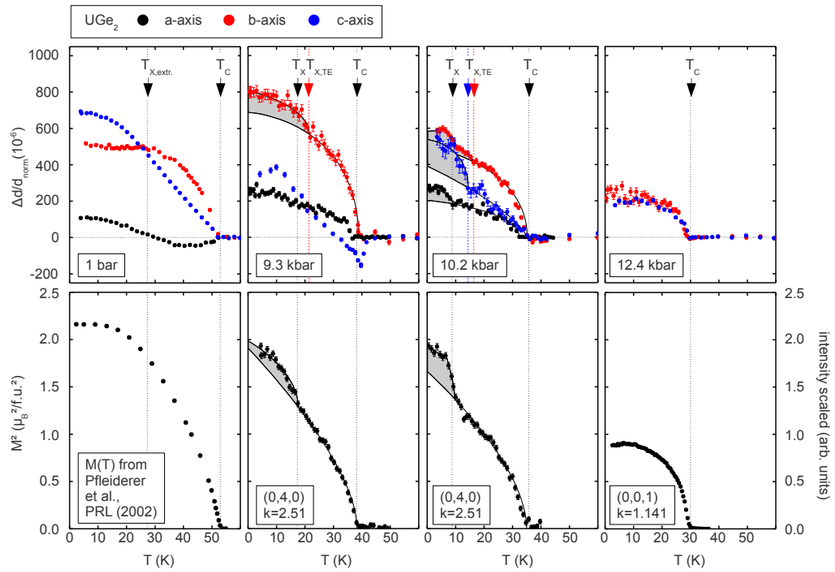

Figure 2: Thermal expansion (TE) of the a,-b- and c-axis normalized to high temperature TE and magnetic peak intensity under pressure measured on TRISP. Black vertical lines indicate T_C and T_X of M(T). Under pressure the TX transitions of the b- and c-axes lie at higher temperatures than T_X of M(T). Note that the data of the c-axis at 9.3 kbar could not be Larmor phase corrected yet.

LD is especially suited to measurements of changes in the lattice constant ($\Delta d/d$) under pressure since no apparatus needs to be installed inside the pressure cell containing the sample. Thus the sample floats completely free in the pressure medium. Also, it is possible to measure $\Delta d/d$ and the intensity of ferromagnetic Bragg peaks - which is proportional to the magnetization M(T) squared - in the same setup. Hence transition temperatures as seen in $\Delta d/d$ and M(T) may be compared directly. This makes LD unique in comparison with other techniques for measuring $\Delta d/d$ such as capacitive dilatometers or strain gauges.
Since LD requires polarized neutrons, it was long believed that samples that depolarize the neutron beam, such as ferromagnets or superconductors, could not be studied. However, after demagnetizing our samples in a small AC-magnetic field while cooling through the Curie temperature T_C, even the strong ferromagnetism in UGe_2 ($\mu_{S,FM1}$=1.2 μ_B/U; $\mu_{S,FM2}$=1.5 μ_B/U [8]) did not completely depolarize the neutron beam and measurements were possible. This behaviour may be attributed to the Ising anisotropy of UGe_2.
For our experiment we used five single crystals of UGe_2 (~0.4 g - 1.3 g) grown in Edinburgh using the Czochralski technique under a purified Ar atmosphere. For measurements under pressure the single crystals were mounted in piston-cylinder pressure cells with a fluorinert mixture as pressure medium. Pressures up to 12.4 kbar were applied.

Existence of an additional energy scale

We found that the transition T_X between the two ferromagnetic phases, which is believed to drive superconductivity (fig. 1) and which can be seen in the magnetization as $T_{X,M}$, can also be clearly observed in the thermal expansion (TE) as $T_{X,TE}$ along the b- and c-axes (fig. 2). However, we also find $T_{X,TE}$ to be systematically a few Kelvin higher than $T_{X,M}$ and $T_{X,TE}$ along the a-axis. In turn this suggests the existence of an additional energy scale. Notably, the suppression of $T_{X,TE}$ may be controlled by orbital fluctuations as proposed in ref. [2].

[1] De Visser, Encyclopedia of Materials: Science and Technology, Eds K.H.J. Buschow et al., Elsevier, Oxford 1-6 (2010).
[2] A.B. Shick et al., Phys. Rev. B, 70 (13), 134506 (2004).
[3] Saxena et al., Nature (London), 406, 587 (2000).
[4] A. Huxley et al., Phys. Rev. B, 63 (14), 144519 (2001).
[5] Sandeman et al., Phys. Rev. Lett., 90 (16), 167005 (2003).
[6] T. Keller et al., Applied Physics A, 74, 127 (2002).
[7] T. Rekveldt et al., Europhys. Lett., 54, 342 (2001).
[8] C. Pfleiderer et al., Phys. Rev. Lett., 89 (14), 147005 (2002).

Microscopic picture of magnetic correlation with swift heavy ion irradiation

A. Paul[1], S. Mattauch[2]

[1]Helmholtz-Zentrum Berlin für Materialien und Energie, Berlin, Germany
[2]Forschungszentrum Jülich GmbH, Institut für Festkörperforschung, Jülich, Germany

Exclusive evidence of magnetic structure modification has been revealed by depth-sensitive polarized neutron scattering measurements in an antiferromagnetically coupled Co/Cu multilayered specimen with swift heavy ion irradiation. The effects are independent of any structural modifications within the system (such as intermixing or roughness) that might normally have also contributed to the changes in magnetic structure. The modifications include (a) the loss of uniaxial anisotropy, (b) changes in the variation of the mean magnetization angle and (c) changes in the variation of the lateral and longitudinal magnetic correlation lengths. We explain the changes within the thermal spike model. From these results, the possibility of controlling local magnetization without damaging the structure is foreseeable. [1].

Ion-irradiation and magnetic correlation

In the low-energy regime, ballistic mixing causes atomic rearrangements, which subsequently modify magnetic properties. Swift heavy ions, on the other hand, are liable to produce amortization in a perturbed cylinder along the (very straight) ion path beyond a threshold of energy transfer. Figure 1 shows the impact on the ion trajectory for (a) 200 MeV ions and (b) 200 keV ions for a Co – Cu layered system. However, the effect on magnetic domains — due to ion irradiation — is heavily shrouded by either strong interfacial structural modification (impact of low-energy ions) or by degradation of the substrate extended to the multilayer (impact of high energy ions). Here we address the effect of swift heavy ions exclusively on magnetic domain correlations in a system that does not show any drastic changes in its structural properties.

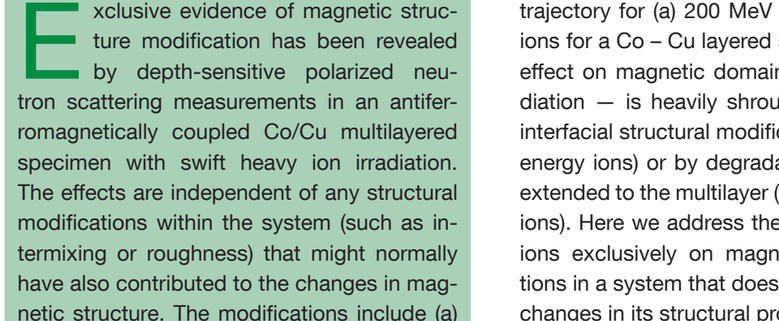

Figure 1: TRIM simulations for 1×105 ions on a Co–Cu layer target for a range of 50.0 nm showing the trajectory in the case of (a) 200MeV and (b) 200 keV energies.

Measurements at FRM II and accelerator

We have investigated multilayers of the composition SiO_2/Co(1.45 nm)/[Cu(1.02 nm)/Co(1.45 nm)] N = 20. The neutron scattering experiments were performed at the polarized neutron reflectometer with polarization analysis TREFF at the FRM II at a wavelength of 4.73 Å. The specimens were kept at room temperature and an external field H_a of up to 1.5 kOe was applied. We used the 15 MV Pelletron accelerator of the Nuclear Science Centre, New Delhi, for the irradiation with 200 MeV Ag^{15+} ions.

Microscopic variation in magnetization

X-ray specular reflectivity as well as off-specular scattering from the samples reveals no significant differences in their respective parameters, such as interface roughness or in-plane or out-of-plane structural roughness correlations with increasing ion fluence. Small differences in the shape of the **m**agneto-**o**ptic **K**err **e**ffect (MOKE) magnetization loops measured parallelly and perpendicularly to the easy axis in the as-deposited case can be seen from the irradiated specimens. These small differences can be seen to be gradually diminishing as we increase the fluence of ion irradiation. Figure 2(a) shows the angular variation in the magnetization of the layer (Φ_B) with applied field as deduced from neutron measurements. At lower fields, the variation is quite different in the case of the ion-beam irradiated specimen as compared to the as-deposited one. The turn angle also refuses to go to 0° before the applied field reaches 1.0 kOe. This obviously indicates a stronger coupling strength. The domain size (ξ) variation, as obtained from the simulation of the diffuse scattering spin-flip spectra, is plotted in Figure 2(b). In the present case, the energy is partially dissipated in the lattice via **e**lectron–**p**honon (E–P) interaction. The deposited energy is shared between the target electrons and the lattice atoms via electron–electron and E–P interactions, respectively. A swift heavy ion interacts mainly with valence and core electrons, producing energetic electrons. The excited electrons lose energy to the lattice through electron–ion interactions, resulting in a cooling of the electrons and an increase in the lattice temperature. The electrons are therefore effectively in equilibrium with the lattice, at least locally. For our system (which can be approximated as $Co_{0.5}Cu_{0.5}$), the electronic energy loss $S_e = dE/dx$ is greater than 35 keV nm^{-1} (TRIM), which can give a latent track radius of about 2–10 nm.

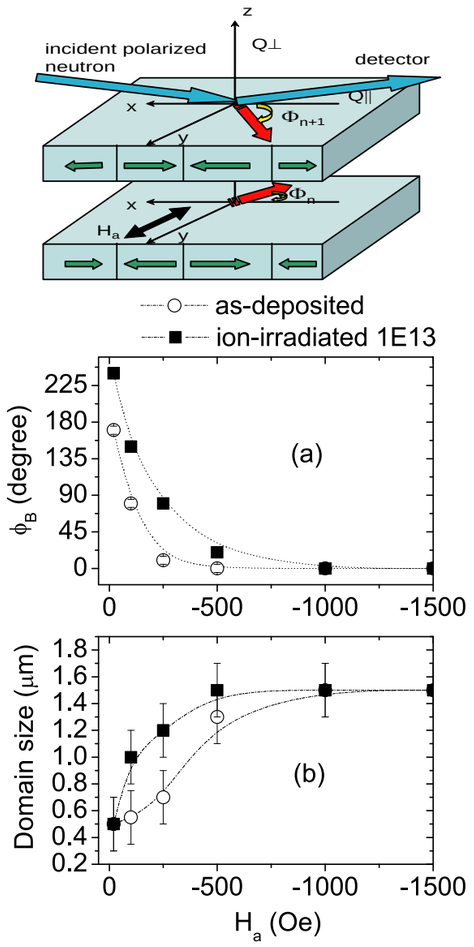

Figure 2: Mean magnetization angle Φ_B between the n^{th} and the $(n + 1)^{th}$ layer for the as-deposited and ion-beam-irradiated specimens as obtained from the fits to the NSF reflectivities. (b) Variation in domain size with field as obtained from the simulation of the SF diffuse spectra along Q_x.

A problem associated with the programming of MRAM (**m**agnetic **r**andom **a**ccess **m**emory) is that the required current is orders of magnitude higher than that needed for many other memory devices (SRAMs or DRAMs). One can tackle this problem by providing local heat sources (which do not affect the structure) in close proximity to the memory elements so that one can lower the threshold of magnetization while programming. Swift heavy ions can cause such local heating (with a radius of a few nanometers) that can be realized through the entire stack of the multilayer. Here we found exclusive evidence of magnetic structure modification that has been revealed by depth sensitive polarized neutron scattering measurements.

[1] A. Paul et al., New. J. Phys. 12 (10), 103003 (2010).

Microscopic origin of training in an exchange bias system

A. Paul[1], S. Mattauch[2]

[1]Helmholtz-Zentrum Berlin für Materialien und Energie, Berlin, Germany
[2]Forschungszentrum Jülich GmbH, Institut für Festkörperforschung, Jülich, Germany

In an exchange coupled antiferromagnet (AF)-ferromagnet (FM) system, we explore the microscopic origin of training [1,2]. As we cooled our system below the blocking temperature in a remanent field, we were able to identify microscopic suppression of training. In a coercive field cooled system, we found coexistent states (single domain and multi-domain). Here, the usual training for the single domain portion and no training for the multi-domain portion were identified [3]. The microscopic origin of training has therefore been identified as the interplay of uniaxial anisotropy and uncompensated spins in the AF grains which are rotatable in polycrystalline AF layer (similar to spin-glass-like behaviour).

Exchange bias and training

An important aspect of exchange bias is the difference in subsequent partial magnetization reversal loops, known as the "training effect."

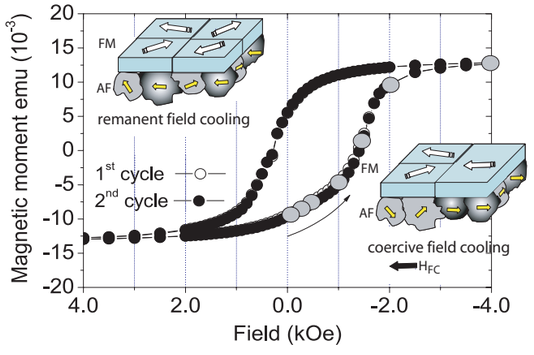

Figure 1: SQUID hysteresis loops of [Co/CoO/Au] multilayer during the 1st and 2nd field cycles for H_{FC}= 0 Oe (remanent field cooling). The gray dots are the points of field along the curve used in neutron measurements. The illustrations show the situation for two field cooled states (no loop is shown for $H_{FC} = H_C$).

Coherent rotation model calculations showed training to originate from symmetries higher than the uniaxial one. Higher anisotropies, such as biaxial anisotropy, can exist even in highly uniaxially anisotropic systems (e.g., CoO). Biaxial anisotropy can be due to an inherent frustration in the system (coupling the two AF sublattices), resulting in perpendicular configuration. Uniaxial anisotropy, on the other hand, can be induced during growth which allows the AF sublattices to be parallel to each other. This scenario of linking biaxial anisotropy with training was contradicted by micromagnetic calculations which predicted training (though much smaller in magnitude and associated with symmetric magnetisation reversal) even for an uniaxially anisotropic system. It should be noted that similar calculations, considering biaxial anisotropy, predicted large training and also asymmetric reversal. The question that remains therefore is: Can uniaxial anisotropy exclusively contribute to training?

Experiments at the TREFF reflectometer

We have investigated multilayers of the composition SiO_2/[$Co_{9.0\ nm}$/$CoO_{7.0\ nm}$/$Au_{25.0nm}$] x 16 with remanent [1] and coercive [3] field cooling. The neutron scattering experiments were performed at the polarized neutron reflectometer with polarization analysis TREFF at the FRM II for a wavelength of 4.73 Å. All measurements were carried out after the sample had been cooled from room temperature to 10 K by a continuous flow cryostat in the presence/ absence of a cooling field provided by an electromagnet.

Multidomain and single-domain ferromagnets

Normal field cooling renders a single domain state (from the saturation state of the FM) and exhibits a clear training response. In figure 1, we show that cooling a system in a remanent state, rendering remanent exchange bias, can lead to macroscopic suppression of the training effect. It should be noted that remanent field cooling is different from demagnetized state cooling, even though a multidomain FM state is realized in both cases.

Polarized neutron scattering measurements are shown in figure 2. This demonstrates microscopic suppression of training which can be attributed

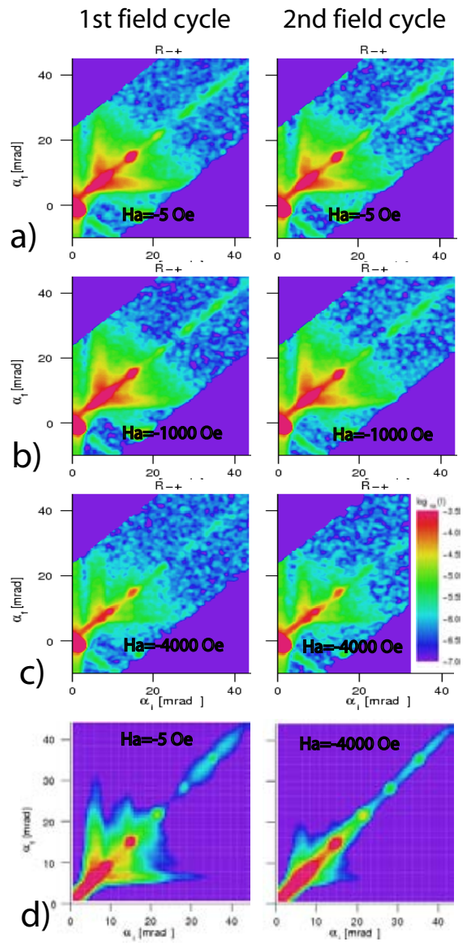

Figure 2: Spin-flip intensity maps from Co/CoO/Au multilayer measured at different applied fields Ha (a-c) after positive saturation and after cooling down the system at H_{FC}=0. The color bar encodes the scattered intensity on a logarithmic scale. The simulated SF intensity maps within DWBA (d) are also shown.

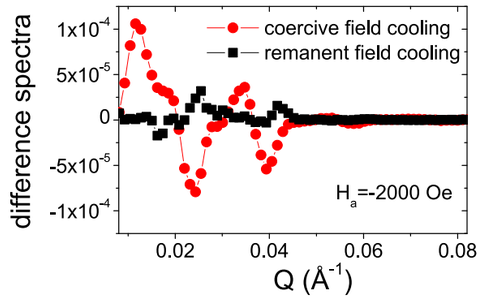

Figure 3: Difference spectra (specular reflectivity) between the 1st and the 2nd field cycles obtained from the spin-flip channels corresponding to the two different field cooled states.

to poorly defined AF uniaxial anisotropy within the AF layer due to remanent field cooling [1]. If we chose to cool the system in a small external field, which would be close to the coercive field of the specimen, coexistence of two different FM micromagnetic configurations could be realized within the same system: multi-domain and single domain. A difference in the spin-flip reflectivity at an applied field, for two consecutive field cycles, can be an indication of training.

In figure 3, the training in the system is convincingly depicted, as compared to the untrained case. In the case of remanent field cooling, the system behaves as a poorly defined uniaxial anisotropic system, or as an isotropic Heisenberg type system (which does not show training). The training can therefore be attributed exclusively to the induced anisotropy in the AF during the process of coercive field cooling.

In summary, Heisenberg type spins can form a local unidirectional anisotropy in a direction which can be away from the FM magnetization direction. Ising type spins, on the other hand, would be restricted along the FM magnetization direction. Upon field cycling, the magnetization for Heisenberg type spins is independent of its history, whereas Ising types are dependent. For a coexisting state of both types of spins, we could convincingly observe the onset of training with induced anisotropy from our polarized neutron scattering measurements.

[1] A. Paul et al., Appl. Phys. Lett., 95 (9), 092502 (2009).
[2] A. Paul, Appl. Phys. Lett., 97 (3), 032505 (2010).
[3] A. Paul et al., Journ. Appl. Phys., 108 (5), 053918 (2010).

Probing ab-/desorption of deuterium in hydrogen storage materials with neutron diffraction in-situ

F. Dolci[1], E. Weidner[1], M. Hoelzel[2,3], P. Moretto[1], W. Lohstroh[4]

[1]European Commission, DG Joint Research Centre, Institute for Energy, Petten, The Netherlands
[2]Technische Universität Darmstadt, FB Material- und Geowissenschaften, Darmstadt, Germany
[3]Technische Universität München, Forschungs-Neutronenquelle Heinz Maier-Leibnitz (FRM II), Garching, Germany
[4]Karlsruher Institut für Technologie (KIT), Institut für Nanotechnologie, Karlsruhe, Germany

Solid state hydrogen storage is an attractive option for a clean energy carrier. Neutron diffraction during deuterium absorption/desorption offers the unique opportunity to probe in real time and under experimental conditions the phase transformation behaviour of the investigated compounds. Deuterium sorption of mixtures of magnesium amide ($MgND_2)_2$ and lithium hydride (LiD) were investigated at 220°C and different deuterium pressures up to 70 bars. An intermediate reaction step was identified and the structures of the corresponding phases were refined. The results are important for optimizing this promising hydrogen storage system.

The increasing worldwide concern for the effects of a growing atmospheric pollution on both climate and human health, calls for a drastic change in energy policies. Renewable energy sources have been proposed as a clean and reliable solution to the problems caused by fossil fuel consumption. Alongside the renewable energy supplies, new methods for safe and efficient energy storage have to be developed, e.g. to buffer fluctuations on the supply side or to replace fossil fuels in automotive applications. One of the most attractive suggestions for an efficient and clean energy carrier is hydrogen. Solid state hydrogen storage materials, in particular, are a possible alternative to gaseous or liquid hydrogen, since they combine high volumetric storage capacity with relative safety.

Metal hydrides as well as light weight complex hydrides have been the focus of much research activity due to either their good cycling stability or a combination of high gravimetric and volumetric capacities [1].

Despite recent progress in the field, many materials require pressure and temperature conditions too high for cycling, which makes them unsuitable for applications. Ultimately, these parameters are determined by the thermodynamic properties of the system. Recently, the idea of mixing different complex hydrides, together or with light metal hydrides, has shown very promising results and opened new possibilities for the design of practical hydrogen storage materials useful for both stationary and automotive applications. To tune the thermodynamics of the system efficiently, a deep understanding of the reaction pathway and structure of the involved phases is mandatory. With mixing, reaction enthalpies can be reduced and more favourable thermodynamic properties achieved. Results obtained by following this approach are, however, different from those expected on the basis of a simple thermodynamic modelling of the system. Research carried on in the last years, in particular, has pointed out as naive the idea of a simple and direct desorption/ absorption reaction between the starting materials, moving to the desorbed products and back [2-6].

Neutron diffraction delivers complete structure

In-situ neutron diffraction seems to be a preferred choice for the study of hydrogen storage materials, since hydrogen (deuterium) is clearly identified and the structural characterization of the compound can be complete and effective. Phase evolution during hydrogen absorption and desorption cycles and detection of new intermediate phases can be successfully performed with a considerable improvement in the basic understanding of the material.

The use of magnesium amide/lithium hydride mixture (Li-Mg-N-H system) illustrates well a typical complex case [7].

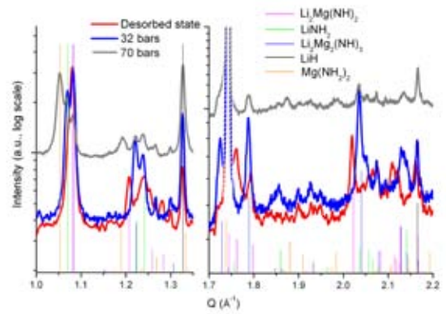

Figure 1: An offset has been applied to the grey diffraction profile to increase clarity. The stick diagrams represent the calculated intensities for each phase. The regions where some of the strongest reflections from steel are present were excluded.

Different mixtures were produced by ball-milling different stoichiometric amounts of magnesium amide/ lithium hydride).

In particular a 3:8 ($3Mg(NH_2)_2$:8LiH) mixture was analyzed at the SPODI instrument, which is suited to carry on structure refinement on complex systems, in particular phase mixtures.

The cell used is a stainless steel 316 L tube, providing the required mechanical properties. The resulting strong reflections of the steel phase of the sample holder can easily be excluded from Rietveld refinement. Deuterium gas is used in preference to hydrogen, owing to its favorable coherent-to-incoherent scattering ratio. For clarity the chemical formulas with hydrogen are given in the following sections.

The results of the in-situ neutron diffraction experiments for the 3:8 sample are shown in fig. 1. There, the relevant sections of three diffraction patterns are presented for a 3:8 sample held at 200°C under different deuterium pressures. Owing to the good angular resolution of the SPODI instrument, a two stage reaction is clearly demonstrated. An equal reaction pathway was also found for other magnesium amide/lithium hydride mixtures.

Tailoring hydrogen storage materials

By probing the PCI (**P**ressure **C**omposition **I**sotherm) of the Li-Mg-N-H system with in-situ neutron diffraction measurements, it is clearly possible to notice an intermediate passage with the formation of new phases [8-9]:

$$2\ Mg(NH_2)_2 + 4\ LiH \rightleftharpoons Li_2Mg_2(NH)_3 + LiNH_2 + LiH + 3\ H_2 \rightleftharpoons 2\ Li_2Mg(NH)_2 + H_2$$

Further experiments in absorption/ desorption mode on the 1:2 and 1:4 systems revealed that this intermediate step is thermodynamically stable and a feature common to all investigated ratios. Hence the reaction (1) has to be extended and in its more general case is: [8-9] (x = 2, 8/3, 4)

$$2\ Mg(NH_2)_2 + 2x\ LiH \rightleftharpoons Li_2Mg_2(NH)_3 + LiNH_2 + (2x\text{-}3)\ LiH + 3\ H_2 \rightleftharpoons 2\ Li_2Mg(NH)_2 + (2x\text{-}4)\ LiH + 4\ H_2$$

From the two step process reported above it becomes obvious that the molar ratio 1:2 set the storage capacity at maximum without compromising the thermodynamic properties. This is an excellent example of how the knowledge of intermediate reaction steps and structural phases helps in tailoring hydrogen storage materials with targeted properties.

The concept of intermediates phases formation during the hydrogen absorption and desorption processes is important for the fundamental understanding of the mechanisms presiding over hydrogen uptake and release. The lack of basic knowledge hampers the development of new strategies for circumventing system limitations and improving performances; furthermore, any theoretical modeling of the system should keep under consideration every possible phase present in the real hydrogen storage system.

[1] S. Orimo et al., Chem. Rev., 107 (10), 4111 (2007).
[2] E. Weidner et al., Chem. Phys. Lett., 444 (1-3), 76 (2007).
[3] J. Rijssenbeek et al., J. Alloys Compd., 454 (1-2), 233 (2008).
[4] H.J. Wu, J. Am. Chem. Soc., 130 (20), 6515 (2008).
[5] S. Garroni et al., Scripta Mat., 61 (12), 1129 (2009).
[6] J. Hu et al., J. Phys. Chem. C, 111 (49), 18439 (2007).
[7] W. Luo, J. Alloys Compd., 381 (1-2), 284 (2004).
[8] E. Weidner et al., J. Phys. Chem. C, 113 (35), 15772 (2009).
[9] F. Dolci et al., Int. J. Hydrogen Energy, 35 (11), 5448 (2010).

Divacancies and the hydrogenation of Mg-Ti films with short range chemical order

S. W. H. Eijt[1], H. Leegwater[1], H. Schut[1], A. Anastasopol[1], W. Egger[2], L. Ravelli[2], C. Hugenschmidt[3], A. Baldi[4], B. Dam[4]

[1]TU Delft, Faculty of Applied Sciences, Department of RRR, Delft, The Netherlands
[2]Universität der Bundeswehr München, Institut für Angewandte Physik und Messtechnik (LRT2), Neubiberg, Germany
[3]Technische Universität München, Forschungs-Neutronenquelle Heinz Maier-Leibnitz (FRM II), Garching, Germany
[4]TU Delft, Faculty of Applied Sciences, Department of Chemical Engineering, Delft, The Netherlands

Mg-Ti thin films are very interesting materials for the development of hydrogen sensors and hydrogen storage media. At Ti-concentrations beyond ~15 at%, a cubic (fluorite) $Mg_{1-y}Ti_yH_x$ metal hydride phase is formed which shows substantially faster hydrogen sorption kinetics than the common tetragonal (rutile) MgH_2 phase. Positron lifetime studies on PLEPS revealed the presence of divacancies in the as-deposited and hydrogenated Mg-Ti metal films. We deduced the presence of relatively large local lattice relaxations around the divacancies in fluorite MgH_2, pointing to a major role played by these divacancies in the mechanism leading to the fast hydrogen sorption kinetics in this cubic MgH_2 phase.

Over the last decade, there has been growing interest in the development of lightweight metal hydrides capable of reversible hydrogen storage at low and medium temperatures for use in zero emission hydrogen cars of the future. Their high volumetric hydrogen capacity can facilitate surpassing the technological limits of high pressure hydrogen storage tanks on the road to economically viable hydrogen storage systems.

Fast hydrogenation kinetics

Mg-Ti alloys are promising materials for applications such as hydrogen storage media and metal hydride rechargeable batteries. Hydrogenation of Mg-Ti films with Ti-concentrations larger than ~15% ($Mg_{0.85}Ti_{0.15}$) leads to the formation of a fluorite $Mg_{1-y}Ti_yH_x$ phase with substantially faster hydrogenation kinetics than the common rutile MgH_2 phase [1]. High hydrogen storage capacity of up to 6.5 wt% capacity can be achieved, close to targets set for application in zero emission hydrogen cars of the future. Further, on hydrogenation, the optical properties of Mg-Ti thin films change markedly from the metallic to the insulating metal hydride state, making these films very attractive for use in fast hydrogen sensors and hydrogen switchable mirrors (fig. 1) [2]. Of central importance is the transport of hydrogen in these materials, as it determines the rate of hydrogen loading and unloading. Metal and hydrogen vacancies can strongly affect the mobility of hydrogen and metal ions in the metal and metal hydrides and, consequently, the hydrogen sorption kinetics. Therefore, we exploited the high sensitivity of **p**ositron **a**nnihilation **l**ifetime **s**pectroscopy (PALS) to determine for the first time the presence and type of vacancies in Mg-Ti and Mg-Ti-H thin films [3,4].

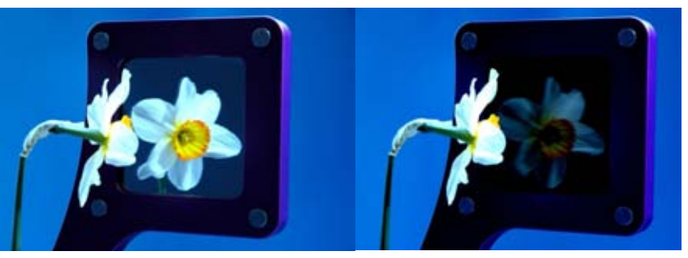

Figure 1: (Left) A mirror consisting of a $Mg_{0.7}Ti_{0.3}$ thin film. (Right) After applying a hydrogen containing gas, the mirror changes into a light absorbing $Mg_{0.7}Ti_{0.3}H_x$ film.

Mg-Ti films were deposited in a UHV system by RF magnetron co-sputtering of Mg and Ti targets in an argon atmosphere, on suprasil glass substrates, and covered with a 1-5 nm Pd capping layer. Four $Mg_{0.90}Ti_{0.10}$, four $Mg_{0.70}Ti_{0.30}$ and two Ti film samples were prepared with layer thicknesses in the range 150-250 nm. Two samples of each type were hydrogenated from the gas phase.

Thin film positron annihilation lifetime spectroscopy was performed using the **p**ulsed **l**ow **e**nergy **p**ositron beam **s**ystem (PLEPS). The positron lifetime is a direct measure of the local electron density at the positron annihilation site, and can therefore be used to extract in a unique manner the size of vacancy-related defects. Positron lifetime spectra were collected at positron implantation energies in the range of 0.5-18 keV. The spectra were fitted using the POSWIN software package using a three lifetime component analysis.

Positron lifetimes

Positron Doppler broadening studies revealed nanoscale chemical segregation of the coherent Mg-Ti films into Mg and Ti domains [3,4]. As a consequence of the large difference in positron affinity for Mg and Ti, positrons have the remarkable capability of monitoring the Mg domains exclusively (fig. 2) [3]. The PALS studies showed that saturation trapping of positrons in vacancy-related defects occurs inside the Mg areas of the Mg-Ti(-H) films, demonstrating that defect concentrations are at least of the order of 10^{-4}, but that higher values are quite likely. Figure 3 presents the extracted positron lifetimes for the Mg layer and for the Mg-Ti layers in the metallic and in the metal hydride states. The measured positron lifetime of 312 ± 4 ps for the Mg film is close to the value of 316 ps for the divacancy in Mg obtained in recent ab-initio calculations. Clearly, the detected positron lifetime in the $Mg_{1-y}Ti_y$ metal phase scales proportional to the volume per metal atom following $\tau = \alpha V_o$, as expected for the divacancy. The Mg-Ti lattice contracts proportionally to the Ti-fraction and reduces the size of the divacancy, leading to a larger electron density at the positron trapping site and correspondingly higher positron annihilation rates.

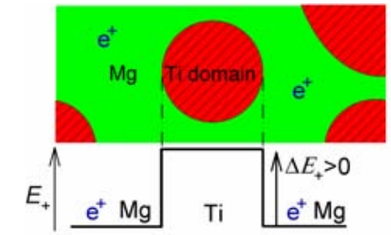

Figure 2: Schematic representation of the nano-scale chemically segregated Mg-Ti domain structure. The schematic drawing for the positron potential energy E+ shows that a Ti domain embedded in Mg acts as a positronic potential barrier with height ΔE+=2.1 eV.

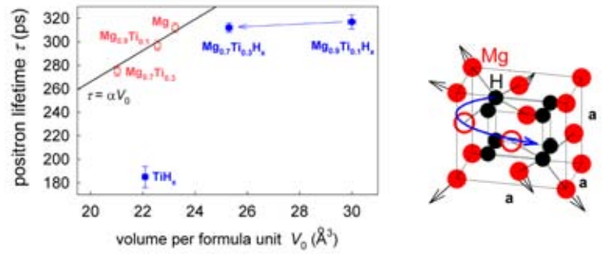

Figure 3: (Left) Positron lifetime of metallic and hydrogenated $Mg_{1-y}Ti_y$ films as a function of volume per formula unit. The fitted solid line indicates the expected effect of increased volume on the experimental positron lifetimes for the divacancies in the metallic films. (Right) Artistic impression of the relaxed geometry of the divacancy and facilitated hydrogen mobility in fluorite phase MgH_2.

Remarkably, the positron lifetime for the fluorite phase $Mg_{0.7}Ti_{0.3}H_x$ is almost equal to the positron lifetime for the rutile phase $Mg_{0.9}Ti_{0.1}H_x$, despite the significantly smaller volume per formula unit, by 16 %, for the fluorite phase. This indicates that the divacancy in the fluorite MgH_2 structure occupies a relatively large open space leading to a low electron density. This requires local lattice relaxations of nearby hydrogen and Mg atoms (fig. 3). The presence of divacancies combined with relatively large local lattice relaxations may effectively lower the migration barriers for hydrogen diffusion in the fluorite MgH_2 phase, leading to fast hydrogen transport.

In summary, experimental evidence is provided for the presence of divacancies in the metal sublattice of both the rutile and fluorite MgH_2 phases exploiting the unique capabilities offered by positron lifetime spectroscopy using PLEPS. The lifetimes of these vacancies are comparable, though their size must differ considerably. Hence, we deduce the existence of local lattice relaxations in the fluorite phase, which may play a crucial role in the enhanced hydrogen transport in fluorite MgH_2.

[1] R.A.H. Niessen and P.H.L. Notten, Electrochem. Solid-State Lett., 8, A534 (2005).
[2] M. Slaman et al., Sens. & Act. B, 123 (1), 538 (2007).
[3] H. Leegwater et al., Appl. Phys. Lett., 96, 121902 (2010).
[4] S.W.H. Eijt et al., J. Alloys Compd. (in press)
doi: 10.1016/j.jallcom.2010.09.157

Free volume and swelling in thin hydrogel films

S. Harms[1], K. Rätzke[1], F. Faupel[1], W. Egger[2], L. Ravelli[2], A. Laschewsky[3], W. Wang[4], P. Müller-Buschbaum[4]

[1]Christian-Albrechts Universität zu Kiel, Institut für Materialwissenschaft/ Materialverbunde, Kiel, Germany
[2]Universität der Bundeswehr München, Institut für Angewandte Physik und Messtechnik (LRT2), Neubiberg, Germany
[3]Universität Potsdam, Institut für Chemie, Potsdam-Golm, Germany
[4]Technische Universität München, Physik Department E13, Garching, Germany

The free volume in thin films of poly(N-isopropylacrylamid) end-capped with n-butyltriocarbonate (nbc-PNIPAM) is probed with **p**ositron **a**nnihilation **l**ifetime **s**pectroscopy (PALS). The PALS measurements are performed as a function of the energy to obtain depth profiles of the free volume of the nbc-PNIPAM thin films. With decreasing film thickness the free volume increases in good agreement with an increase in the maximum swelling capability of the nbc-PNIPAM films. Thus in thin hydrogel films the sorption and swelling behaviour is governed by the free volume.

Hydrogels are three-dimensional networks of polymer chains that swell, but do not dissolve in water. One prominent model for a thermosensitive hydrogel is poly(N-isopropylacrylamide) (PNIPAM). Since PNIPAM expels its liquid contents at a temperature near that of the human body, it is under consideration for applications in controlled drug delivery. As pure PNIPAM homopolymers miss the possibility of internal cross-links to build up a gel, the addition of hydrophobic chain ends is a simple way to overcome this problem.

Recently, swelling of thin films of end-capped PNIPAM with a very short hydrophobic end group, n-butyltrithiocarbonate, at both chain ends (denoted nbc-PNIPAM) was investigated [1,2]. Figure 1 shows this behaviour for films with a swelling factor of 3.2 (40 nm), 1.6 (105 nm) and 1.3 (200 nm) as compared to the dry film. Surprisingly, the thinner the nbc-PNIPAM films are, the stronger the - thickness normalized - response to swelling. This might be caused by a film thickness dependence of the free volume of the films. Therefore, the free volume of dry films of various film thicknesses before swelling should be determined.

Positrons probe the electron density distribution and hence the unoccupied space between the atoms, i.e. the free volume. Once injected, positrons form in most polymers hydrogen-like positronium (Ps) states. The pick-off lifetime of orthopositronium, (το-Ps) i.e. the time between injection and decay, is well correlated to the free-volume hole size in polymers. A simple model assumes the Ps to be confined to spherical holes with infinitely high walls and gives a direct relationship between $\tau_{o\text{-}Ps}$ and the size of the free volume holes [3].

In contrast to analysis of bulk samples with radioisotope based positron sources, for thin film analysis the energy of the positrons has to be reduced and moderated, while the time structure of the positron beam has to be maintained. This and many more requirements are fulfilled for the reactor based **p**ulsed-**l**ow-**e**nergy-**p**ositron-**s**ystem (PLEPS) at the FRM II [4].

Dry hydrogel films prepared by spin-coating

Here, the influence of the free volume on the swelling behaviour of nbc-PNIPAM films of various thicknesses are to be determined by measuring the o-Ps lifetime as a function of the energy. The results should clarify the influence of the free volume.

Dry hydrogel films were prepared by spin-coating as detailed in reference [1]. Positron experiments were performed at PLEPS of the FRM II [4].

In figure 2 the results of PALS in dry PNIPAM films of various thicknesses are summarized. The bottom x-scale is the experimental acceleration voltage E, which has been converted to an average implantation depth z_m (top x-scale) [5]. The left hand scale (for open symbols) is for the

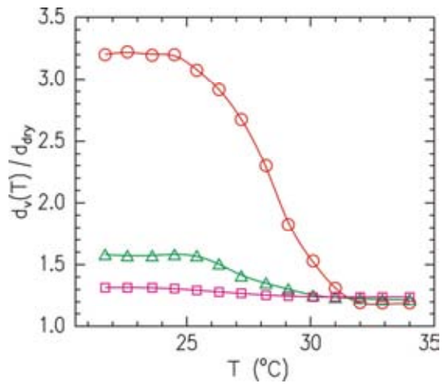

Figure 1: Temperature-dependent changes of the film thickness measured for nbc-PNIPAM films exposed to saturated water vapor normalized by the thickness of the dry films in air dry. Film thickness of 40 (circles), 105 (triangles), and 200 nm (squares).

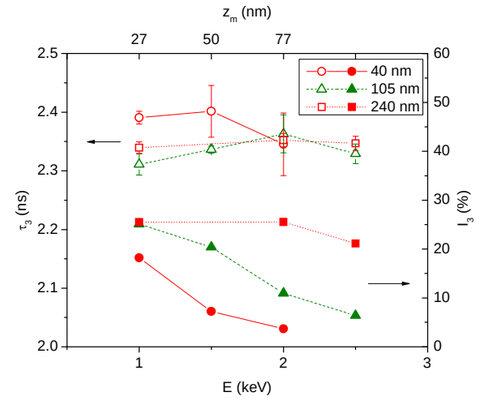

Figure 2: O-Ps lifetime and intensity in three nbc-PNIPAM films as a function of the incident energy. Error bars are statistical errors from the fit of the lifetime spectra. Lines are inserted to guide the eye.

average o-Ps lifetime τ_3, which is a measure for the average free volume (see above). The right hand scale of the o-PS intensity I_3 is related to the o-Ps formation probability.

As we are dealing with thin films, the implantation of positrons into the substrate, which does not allow for the formation o-Ps, has to be taken into account. In figure 2 the o-Ps intensity is nearly equal for all three samples in the range of 1 to 1.5 keV and then decreases, as expected for increasing implantation depth and increasing contributions from the Si-substrate, which does not show Ps-formation, and hence leads to a much lower lifetime.

Swelling is related to free volume

As discussed above, the o-Ps lifetime is a measure for the average free volume in polymers. Application of standard models gives a volume of 0.137 nm^3 for a lifetime of 2.4 ns. As can be seen from figure 2, the o-Ps lifetimes (open symbols) for 1 and 1.5 keV show a clear trend. The lifetime is the larger the thinner the films are. Although the differences in the o-Ps lifetimes are small, they are well above the error bar and hence they are significant. Our results confirm a previous publication [1], which suggests that swelling is related to the availability of free volume. However, one has to consider that the availability of free volume is only a necessary, but not a sufficient condition for swelling. It is necessary for kinetics, but driving forces like solubility and concentration gradient are also required and these are expected to be similar for the samples investigated here. Confinement effects due to the substrate generally give rise to a decrease of the free volume. Hence the observed increase in free volume can be attributed to the additional degrees of freedom near the free surface [6-10] which allow the nbc-PNIPAM chains to adapt a more open chain conformation as compared to the bulk.

[1] W. Wang et al., Macromol., 41 (9), 3209 (2008).
[2] S. Harms et al., Macromol. Rapid Comm., 31 (15), 1364 (2010).
[3] Principles and Applications of Positron and Positronium Chemistry; Eds: Y.C. Jean et al., World Sci. Pub.: Singapore, (2003).
[4] P. Sperr et al., Appl. Surf. Sci., 255 (1), 35 (2008).
[5] J. Algers et al., Phys Rev B, 67 (12), 125404 (2003).
[6] C. Wu and S. Zhou, Macromol., 28 (24), 8381 (1995).
[7] R. Priestley et al., Science, 309 (5733), 456 (2005).
[8] C. Ellison and J. Torkelson, Nature mat., 2 (10), 695 (2003).
[9] J.Erichsen et al., Macromol., 37 (24), 8813 (2004).
[10] J. Erichsen et al., Macromol., 37 (5), 1831 (2004).

Crystal structure and Li motion of Li_8SeN_2 and Li_8TeN_2

D. Bräunling[1], A. Senyshyn[2], R. Niewa[3]

[1]Technische Universität München, Department Chemie, Garching, Germany
[2]Technische Universität Darmstadt, FB Material- und Geowissenschaften, Darmstadt, Germany
[3]Universität Stuttgart, Institut für Anorganische Chemie, Stuttgart, Germany

The orange compounds Li_8EN_2 with E = Se, Te as Li-rich derivatives of Li_3N are potential fast Li-ionic conductors, since prototypic α-Li_3N is regarded as the material with the highest Li-conductivity. However, due to the low scattering power of Li the spacegroup assignment, as well as structure refinements regarding Li positions from X-ray diffraction, were enigmatic. From neutron powder diffraction at SPODI we conducted a full structure refinement and analyzed the thermal behaviour of Li. In accordance with solid state NMR, a Li motional process is active even below room temperature.

The material

α-Li_3N is regarded as the material with the highest Li-conductivity; however it has rarely been applied due to its low decomposition voltage and high moisture sensitivity. One possible way to design new ionic conductors with optimized combinations of material properties is the chemical modification to ternary or higher compounds. Lithium nitride halides have already attracted some attention as fast solid lithium ion conductors [1–3]. Compared to these investigations, data on lithium nitride chalcogenides are extremely rare [4–6].

Experiments at SPODI

The neutron powder diffraction patterns of Li_8SeN_2 and Li_8TeN_2 were collected at 3, 50, 100, 150, 200, 250 and 300 K at the SPODI diffractometer of FRM II. The patterns supported a tetragonal *I*-centered unit cell earlier deduced from X-ray diffraction. However, close inspection of the neutron diffraction patterns revealed the presence of the (310) reflection invisible in X-ray diffraction (b_c(Li) = -1.90 fm; b_c(N) = 9.36 fm; b_c(Se) = 7.97 fm; b_c(Te) = 5.80 fm). This reflection led to the assignment of the non-centrosymmetric spacegroup $I4_1md$ in preference to centrosymmtric $I4_1/amd$. Apparently, the appearance of this reflection is entirely due to the non-centrosymmetric substructure of Li, while the anionic substructure composed of *E* and N species is nearly centrosymmetric.

Crystal structure details

According to joint Rietveld refinements of the RT neutron and X-ray powder diffraction data, Li_8SeN_2 and Li_8TeN_2 are isotypes (fig. 1). The anionic substructure of N and *E* = Se, Te resembles the atomic arrangement in cubic Laves phases, e.g., $MgCu_2$, where N occupies the position of Cu leading to a three-dimensional framework of vertex-sharing (empty) tetrahedra. The chalcogenide atoms are localized in the large voids of this framework within so-called Friauf polyhedra. Li atoms fill the space in the anionic framework

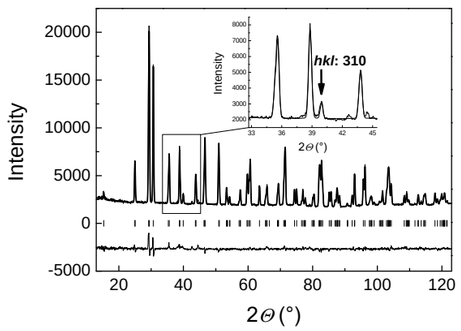

Figure 1: Li_8TeN_2: Rietfeld refinement of the neutron powder diffraction pattern at ambient temperature (λ = 1.5482 Å). The inset enlarges the reflection (310) calling for the spacegroup choice $I4_1md$ rather than $I4_1/amd$.

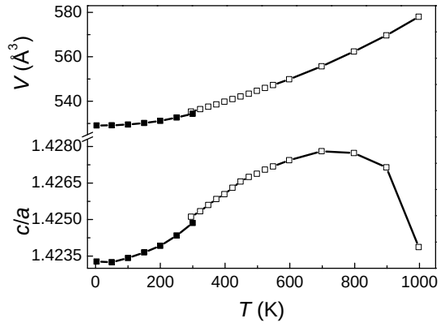

Figure 2: Li_8TeN_2: Temperature dependence of the unit cell volume *V* and the ratio *c*/*a* from neutron powder diffraction (full symbols) and from high resolution X-ray powder diffraction using synchrotron radiation (open symbols).

leading to the quite high coordination number of 9 for nitrogen in a distorted capped quadratic antiprism. *E* is coordinated by 9 Li in a capped tetragonal cuboid.
However, the surroundings of the four crystallographic positions of Li are largely different: Li(1) is tetrahedrally coordinated by 2 N and 2 *E* while Li(2) is in trigonal somewhat non-planar coordination with N (angular sum 341.5°) completed by an *E* at a clearly longer distance. The surroundings of Li(4) are trigonal planar formed by two N and one *E*. Different from these environments is the Li(3) coordination with two N with a bonding angle of 154.13(3)°.
As is also indicated by quantum mechanical calculations and NMR spectroscopic investigations, this arrangement leads to a clearly different bonding situation as compared to the three other Li sites.

Li ion motion

No indication of a structural transition was observed by neutron diffraction at 3–250 K. On cooling, the *c*/*a* ratio monotonically decreases; however, the ideal value of √2 for a cubic metric is not reached even at 3 K (fig. 2). The isotropic displacement parameters of all displacement parameters shrink with decreasing temperature. However, extrapolation of the values for N and *E* to zero K results in small but finite values. The extrapolated displacement parameters for the different sites occupied by Li give quite large values, indicating a significant static contribution additional to the vibration dominating at higher temperatures.
This fact can be related to Li-motional processes also proven in solid state NMR spectroscopy down to temperatures below ambient, which is particularly interesting for applications.

Ionic conductor classification

The title compounds do not suffer any clearly recognizable transition from 3 K to close to 800 K according to diffraction data (high-temperature X-ray diffraction using synchrotron radiation taken at HASYLAB, DESY). The observation of Li motion by NMR spectroscopy without a sharp structural transformation to an ion conducting phase could imply that Li_8TeN_2 and Li_8SeN_2 are comparably rare examples of type II or type III ion conductors according to classification by Keen [7].

[1] P. Hartwig et al., Angew. Chem. Int. Ed. Engl., 19 (1), 74 (1980).
[2] K. Kitahama et al., Solid State Ionics, 3/4, 335 (1981).
[3] Y. Jia and J. Yang, Solid State Ionics, 96, 113 (1997).
[4] R. Marx, Habilitation Thesis, Freie Universität Berlin (2002).
[5] R. Marx et al., Z. Anorg. Allg. Chem., 632, 2151 (2006).
[6] D. Bräunling et al., Z. Anorg. Allg. Chem., 636, 936 (2010).
[7] D.A. Keen, J. Phys.: Condens. Matter, 14, R819 (2002).

Structural changes and refinement of cubic α-Li_2TiO_3 upon heating to high temperatures

A. Laumann[1,2], K. T. Fehr[1], M. Holzapfel[2], M. Hoelzel[3,4], H. Boysen[5]

[1]Ludwig-Maximilians-Universität München, Department für Geo- und Umweltwissenschaften, Sektion für Mineralogie, Petrologie und Geochemie, München, Germany
[2]Süd-Chemie AG, Battery Materials, Moosburg, Germany
[3]Technische Universität München, Forschungs-Neutronenquelle Heinz Maier-Leibnitz (FRM II), Garching, Germany
[4]Technische Universität Darmstadt, FB Material- und Geowissenschaften, Darmstadt, Germany
[5]Ludwig-Maximilians-Universität München, Department für Geo- und Umweltwissenschaften, Sektion Kristallographie, Garching, Germany

A Li_2TiO_3 sample which had been produced by hydrothermal reaction was studied by neutron powder diffraction up to temperatures of 1200°C at the SPODI. The structure of the as-synthesized metastable cubic α-Li_2TiO_3 sample is described in detail for the first time. It is of a disordered NaCl type with a small Li deficit, probably compensated by hydrogen. The sample undergoes two major structural changes upon heating, first to a monoclinic β-phase and then re-enters a cubic γ-phase, isostructural to the α-phase. During the first heating the β-phase is disordered due to stacking faults, but becomes well ordered during cooling. Anomalies around 600°C are related to strains.

The compound Li_2TiO_3

Li-bearing compounds have gained interest due to their use either as active materials in rechargeable Li-ion batteries or, like β-Li_2TiO_3, as solid tritium breeder materials for fusion reactors. The compound Li_2TiO_3 exists in three different modifications. The metastable cubic α-Li_2TiO_3 transforms irreversibly to β-Li_2TiO_3 above 300°C. The β-phase remains stable up to 1155°C, at which temperature it transforms to the cubic γ-Li_2TiO_3. Detailed structural analyses of α-Li_2TiO_3 have not been reported so far.

Experimental and data evaluation

2 g of hydrothermally produced metastable cubic Li_2TiO_3 [1] were studied in a niobium container in a high temperature vacuum furnace. The reflections of niobium were included in all refinements as a second phase. The sample was heated in a stepwise manner from room temperature to 1200°C and then cooled similarly to room temperature. Before each scan (4 h), a holding time of 15 mins was allowed for temperature equilibration. The neutron patterns were recorded from 0° to 160° 2θ with a step width of 0.05° and a wavelength of 1.5483 Å. Data were analysed using the Rietveld program "FullProf"; size and strain parameters were extracted.

Structural phase transitions

At room temperature, α-Li_2TiO_3 exhibits NaCl structure type with randomly disordered Li/Ti and a small Li deficit. The latter is probably compensated by H and disappears with increasing temperature, as also evidenced by the reduction of the incoherent background of hydrogen. At 300°C, broad reflections of the monoclinic modification started to appear. Upon further heating, the ratio of the cubic to the monoclinic phase decreased and the reflections of the monoclinic Li_2TiO_3 sharpened. Between 600°C and 1000°C only the monoclinic phase could be identified. It is a layered derivative of the NaCl structure (space group C2/c) susceptible to stacking disorder. At 1100°C a stoichiometric cubic modification (Fm-3m) reappeared and at 1200°C (inset of fig. 1a) only the cubic γ-Li_2TiO_3 was present. The interlinked data points of the cubic unit cell volume at low temperatures and above 1100°C indicate a constant thermal expansion (fig. 2), confirming the re-entrant behaviour. Upon cooling, the monoclinic Li_2TiO_3 started to form below 1160°C. At 1100°C about 12 % of the cubic phase was left, comparable to the size of the cubic structure at the same temperature upon heating, while below 1100°C, only the monoclinic Li_2TiO_3 modification was found.

During the first heating, the monoclinic structure, which starts to form above 300°C, is disordered due to stacking faults as evidenced by anisotropic line broadening and deviating reflection intensities. Another deviation from the known monoclinic structure is the behaviour of the β angle. It shows lower values below 1000°C than above, and keeps a constant high value upon cooling to room temperature. Anomalies in the thermal expansion behaviour, also noted by other methods such as impedance spectroscopy, are related to strains. Full details can be found in [2].

In this study, the structure of α-Li_2TiO_3 is described for the first time. The (first order) phase transitions of Li_2TiO_3 to the monoclinic β-modification and back to a cubic structure on heating could be proven. Surprisingly, the high temperature modification is isostructural with α-Li_2TiO_3, i.e. Li_2TiO_3 is one of the rare examples of structural phase transitions with re-entrant behaviour. Thus, the hydrothermal technique can be considered as a method to produce cubic Li_2TiO_3 at low temperatures, far below its stability field. On the other hand, fully ordered monoclinic Li_2TiO_3 can only be produced by heating to temperatures > 1000°C, which is important for producing the solid tritium breeder material β-Li_2TiO_3.

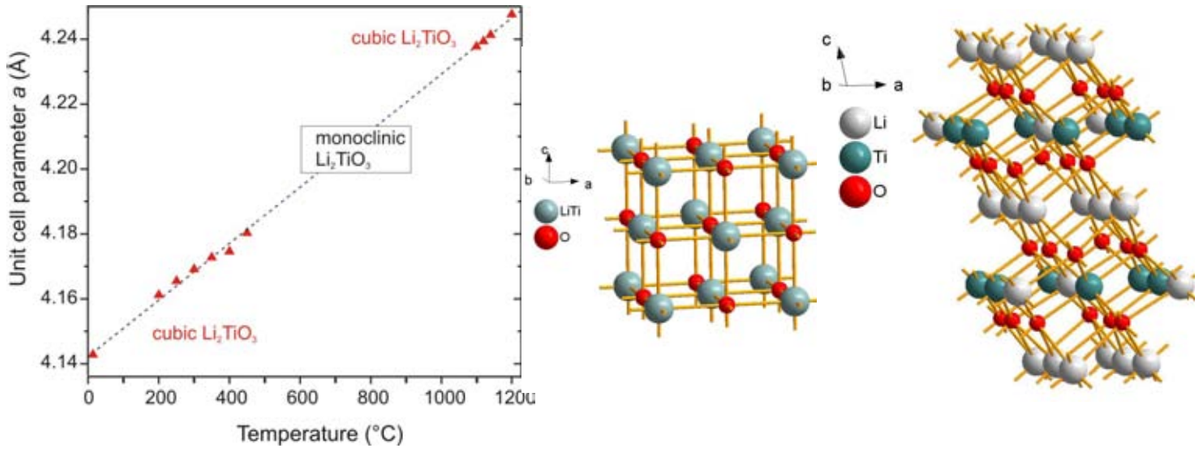

Figure 2: Interlinked data points connecting the cubic α- and γ-Li_2TiO_3. At intermediate temperatures, and upon cooling at low temperatures, the monoclinic modification is stable. On the right: cubic and monoclinic structure.

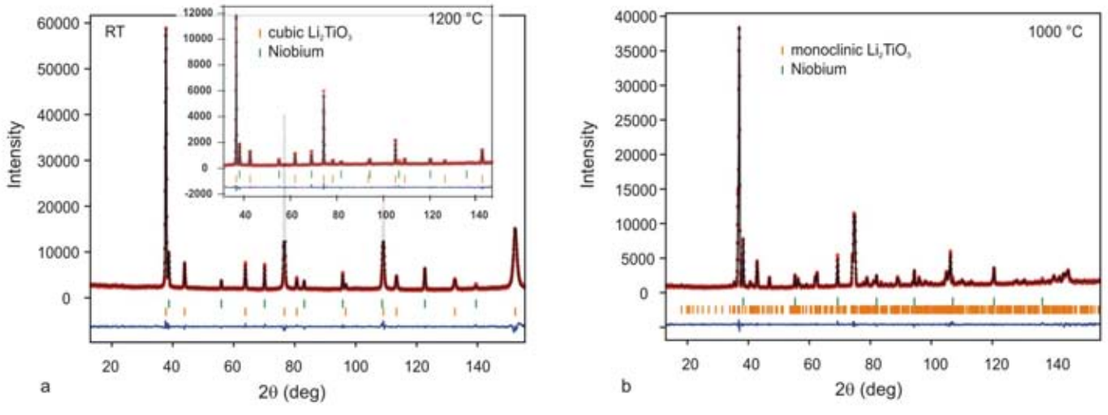

Figure 1: Neutron powder patterns at (a) room temperature (RT) and 1200°C (inset) and (b) 1000°C.

[1] A. Laumann et al., Solid State Ionics, 181 (33-34), 1525 (2010).
[2] A. Laumann et al., Z. Kristallogr., 226 (1), 53 (2011).

Residual stress fields after heat treatment in cladded steel of process vessels

M. J. Marques[1,2], A. Castanhola Batista[1], J. Rebelo Kornmeier[3], M. Hofmann[3], J. P. Nobre[4], A. Loureiro[4]

[1]University of Coimbra, Department of Physics, Coimbra, Portugal
[2]University of Porto, Department of Physics Engineering, Porto, Portugal
[3]Technische Universität München, Forschungs-Neutronenquelle Heinz Maier-Leibnitz (FRM II), Garching, Germany
[4]University of Coimbra, Department of Mechanical Engineering, Coimbra, Portugal

Process vessels are very important in power, petroleum and chemical industries, working in environments requiring specific mechanical and corrosion resistance of the vessel walls. In general, these vessels are made of ferritic base alloys cladded by protective layers of austenitic stainless steels [1,2]. This weld cladding procedure enables productivity savings by using less expensive and more easily workable materials, coated with expensive metals or alloys, selected to achieve the desired properties in specific parts of the equipment. The influence of the heat treatment on the residual stress fields of weld cladded samples is discussed in this paper. The in-depth residual stress profiles were determined by neutron diffraction at the FRM II, on the STRESS-SPEC instrument.

Frequently, process vessels present cracking phenomena in the interface metal/ cladding, compromising their applications [3-5]. Cracking seems to be due to carbon migration to austenitic stainless steel during the welding and post heat treatments, and can be exacerbated, if hydrogen and tensile residual stresses are present in the material. The aim of the present work is to study the effect of the heat treatment parameters on the relaxation of residual stresses of the heat affected zone, where cracking events are common.

Square samples of EN 10028 2 P355 NH carbon steel plate were cladded with stainless steel filler metals by submerged arc welding in one of the faces. The first welding layer was made with an EN 12072 – S 23 12 2 L electrode in order to minimise metallurgical problems. The second and third layers were made with an EN 12072 – S 19 12 3 L electrode. During welding, specimens were constrained in order to prevent coupon plate distortion. This procedure allowed the production of welded specimens with a final thickness equal to 27,5 mm. After the cladding process, some of the samples were submitted to post-welding heat treatments, one at 620°C for a holding time of one hour and the other at 540°C for a period of ten hours.

Heat treatment effects

The residual stress analyses were determined by neutron diffraction at the FRM II, at the Technische Universität München (TUM), on the STRESS-SPEC instrument. The residual strain data were acquired in the three orthogonal directions (longitudinal, transverse and normal to the welding direction), in the central point and in the border of one weld pass (top and bottom) (see fig. 1). This procedure was applied to the three samples: **a**s-**w**elded sample (AW) and **h**eat-**t**reated samples (HT540 and HT620).

The influence of the heat treatment in the in-depth residual stress profile of weld cladded samples was determined. The results for the longitudinal direction can be seen in figure 2. The AW sample showed tensile stresses installed in both regions (top and bottom) of the deposited weld metal, although some discrepancies can be observed in the magnitude of the stresses. The HT540 sample presented some increase in the residual stress level at the top, close to the surface of the layers, as opposed to the weld valley, where a change from tensile to compressive stresses was observed. The HT620 sample showed compressive residual stresses close to the weld surface, both at the top and at the bottom regions; although tensile residual stresses remain in a region beyond 2 mm depth. The corresponding heat treatment of sample HT620 has the industrial benefit of being shorter (only one hour) than the HT540 (10 hours).

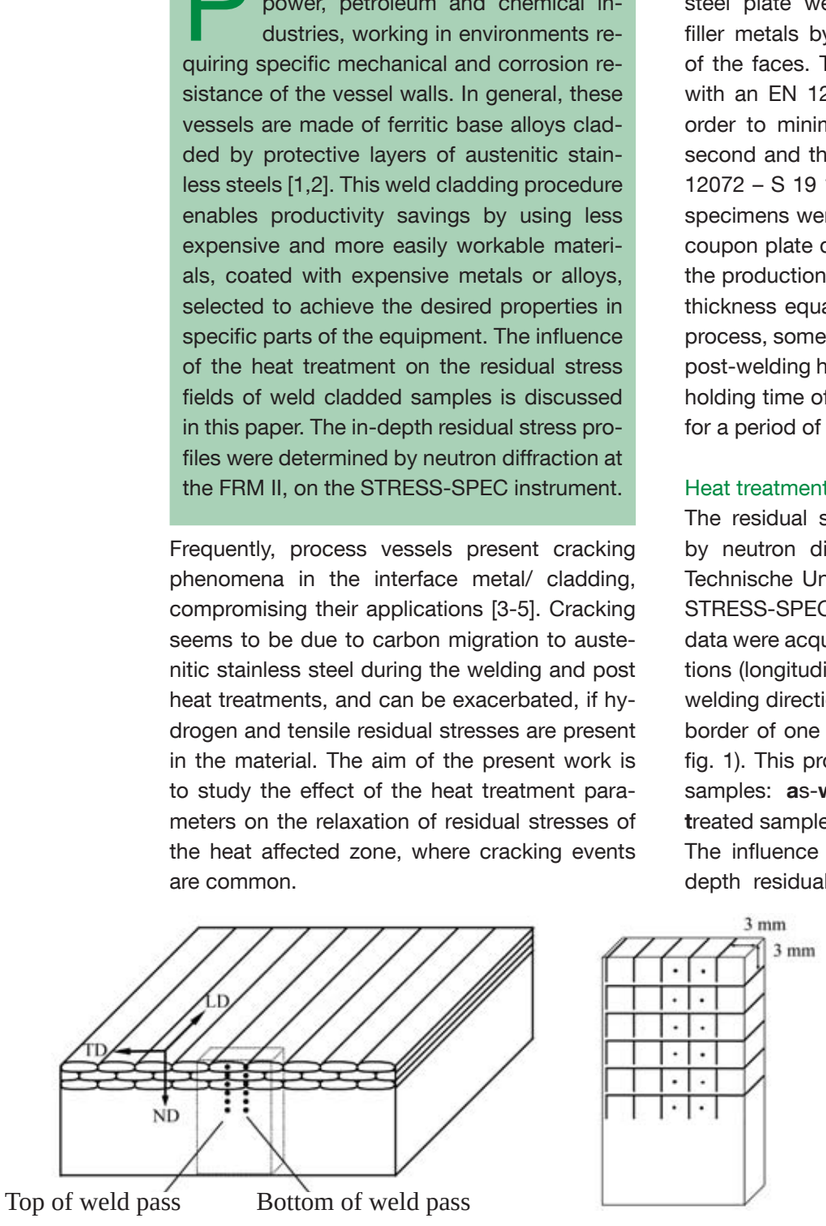

Figure 1: (left) Definitions of the measuring directions: LD, TD and ND, corresponding to **l**ongitudinal, **t**ransverse and **n**ormal **d**irection of welding; (right) Specimen for the determination of the stress free lattice spacing, d_0, of the samples.

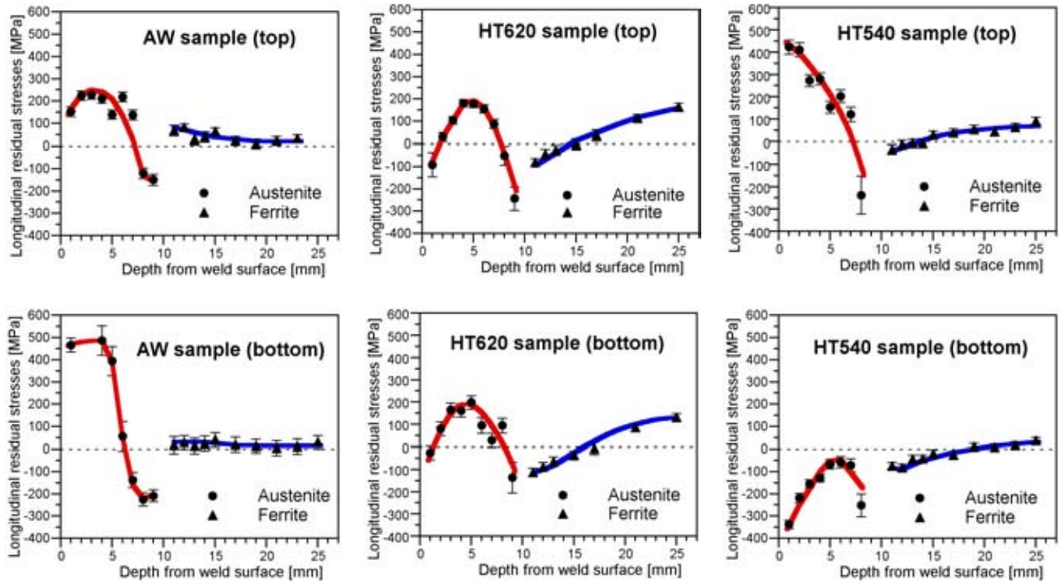

Figure 2: Residual stresses profile in longitudinal direction of the weld in the as-welded sample (AW), the HT540 sample and HT620 sample: in the central region (top) and in the border of one weld pass (bottom).

Improving quality of reactor vessels

The present project is particularly focused on determining to what extent the post heat treatment reduces the residual stress level in order to decrease the cracking phenomena in the interface, without significant degradation of the stainless steel corrosion properties. In the future, the metallurgical and mechanical properties of the welds, as well as their residual stress fields and corrosion behaviour, will be correlated with the welding and heat treatment procedures. It is expected that the results of this research will lead to new post welding heat treatment strategies improving the safety and reliability of reactor pressure vessels currently used in industrial application.

[1] R. Kumar et al., Trans. Ind. Inst. Met., 56 (1), 61 (2003).
[2] N. Muragan and R.S. Parmar, Welding J., 76, 391 (1997).
[3] J. Hohe et al., Proc. of IIW Int. Conf. Safety and Reliability of Welded Components in Energy and Processing Industry, Graz/Austria, 10-11 July, 303 (2008).
[4] P. Dong, J. Press. Vessel Tech. – Transactions of the ASME, 129 (3), 345 (2007).
[5] H. Hoffmeister, Proc. of IIW Int. Conf. Safety and Reliability of Welded Components in Energy and Processing Industry, Graz/Austria, 10-11 July, 491 (2008).

Neutron scattering - a useful tool in development of new CoRe-based alloys for high-T applications

D. Mukherji[1], P. Strunz[2], R. Gilles[3], M. Hofmann[3], M. Hoelzel[3,4], J. Rösler[1]

[1]Technische Universität Braunschweig, Institut für Werkstoffe, Braunschweig, Germany
[2]Nuclear Physics Institute ASCR, Řež near Prague, Czech Republic
[3]Technische Universität München, Forschungs-Neutronenquelle Heinz Maier-Leibnitz (FRM II), Garching, Germany
[4]Technische Universität Darmstadt, FB Material- und Geowissenschaften, Darmstadt, Germany

CoRe-based alloys are being developed at TU Braunschweig to supplement Ni-superalloys at ultra high temperatures for industrial application as turbine blades. The high melting point of CoRe-alloys results from Re addition and distinguishes CoRe-alloys from conventional Co-alloys. The CoRe-system is new for structural applications and available literature is scanty. Basic knowledge building was therefore necessary. Neutron scattering is extensively used in our alloy development to supplement structural investigations. High temperature in-situ neutron diffraction measurements, for example, found for the first time that a hysteresis exists in the hcp ⇆ fcc phase transformation of the Co matrix.

Co alloys are used at high temperatures in gas turbines and at room temperature as surgical implants. In conventional cast Co-based alloys the face centred cubic γ structure (i.e. the high temperature allotrope of Co) is metastable at room temperature and is retained as the matrix phase. In contrast, the CoRe alloys that are being developed at the TU Braunschweig have hexagonal close packed ε Co matrix at room temperature. The high melting point Co-Re-based alloys [1] are developed to supplement Ni-based superalloys at ultra high temperatures: i.e. at temperatures of +100°C beyond the single crystal Ni-superalloys application range. The refractory metal Re is a hcp stabilizer in Co and readily forms an isomorphous solid solution. The hcp matrix structure in CoRe alloys is thermodynamically stable at room temperature. This implies that unlike in conventional Co-systems [where the metastable Co_γ transforms (fcc → hcp) on heating], the reverse transformation (hcp → fcc) at high temperatures is more relevant in CoRe alloys. This phase transformation was observed for the first time at a relatively high temperature by neutron diffraction during in-situ heating experiments at FRM II on two experimental CoRe based alloys.

Diffraction at SPODI and STRESS-SPEC

Phase transformation at high temperatures in two experimental CoRe alloys designated **CoRe-1**: Co-17Re-23Cr-2.6C and **CoRe-2**: Co-17Re-23Cr-1.2Ta-2.6C (in at. %) was investigated by neutron diffraction at the Stress-Spec and SPODI diffractometers at the FRM II. Temperature steps of 5 K were employed at the Stress-Spec and the temperature change during heating and cooling was achieved in 5 seconds. Measurements were done during a 10 minute hold at a given temperature. Diffractograms were collected during this hold time in a limited angular range (2θ between 41° and 55°), where the large peaks from the interesting phases are present. On the other hand, the full angular range (2θ from 39° to 154°) was covered during SPODI measurements to observe with higher resolution, wether other phases were present or peaks covered due to strong overlap. In order to collect diffractograms at SPODI during heating and cooling, the hold time at the chosen measurement temperature was 110 minutes.

One phase transforms into the other

Diffractograms of the in-situ heating and cooling measurements (between 1000° and 1300°C) on CoRe-1 alloy, performed at SPODI, are shown in fig. 1. For clarity, the 3D plot covers only the region of 40°-55° (2θ). An hcp ⇆ fcc transformation of the cobalt matrix on heating and cooling is clearly seen in figure 1. A similar transformation was also observed in CoRe-2 alloy during the measurement at the Stress-Spec [2]. In both alloys the phase transformation: ε (hcp) ⇆ γ (fcc) Co exhibits a large hysteresis (fig. 2), which is about 100 K. The heating and cooling rates in the in-situ experiments at SPODI and Stress-Spec do not play any role, as measurements were done isothermally on holding for at least 10 minutes at different temperatures.

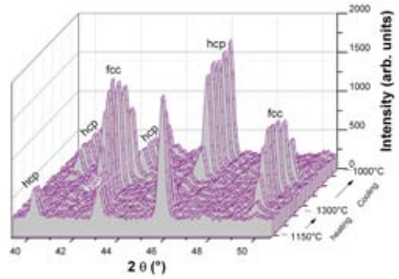

Figure 1: 3D plot of the evolution of the diffractogram with temperature in CoRe-1 alloy showing an extracted region (2θ range 39° to 51°) from the diffractograms measured at SPODI. The hcp ⇆ fcc phase transformation of the Co matrix during heating and cooling (between 1000° and 1300°C) is clearly visible.

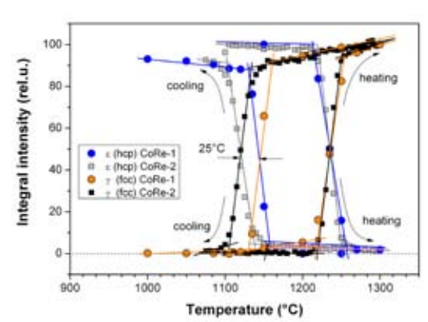

Figure 2: The measured hcp ⇆ fcc hysteresis is visible, where the two hysteresis plots of the ε (hcp) Co phase and the γ (fcc) Co phase are superimposed. It shows that the hcp and the fcc transformations are complementary, indicating one phase transforms into the other. The transformation: hcp → fcc on heating occur at the same temperatures in CoRe-1 and CoRe-2, but on cooling the reverse transformation: fcc → hcp in CoRe-2 lags behind (occurs at lower temperature) by 25°C. CoRe-2 data points were measured at Stress-Spec and CoRe-1 ones at SPODI. The integral intensity values are normalized for a comparison.

In order to compare the measurements done at different instruments, the integral peak intensities are normalized and they then represent the relative phase fractions in the alloy. In figure 2 the hcp ⇆ fcc hysteresis in the CoRe-1 and CoRe-2 alloys are plotted (the Co ε (hcp) and γ (fcc) phases together and overlapped). Straight lines are fitted through the data points, which show that the changes in hcp and fcc phases are complementary to each other – i.e. one phase transforms into the other. A closer scrutiny shows that the hcp → fcc transformation occurs over the same temperature range (γ_{start} = 1210°C and γ_{end} = 1260°C) in both CoRe-1 and CoRe-2 during heating. However, on cooling the reverse transformation fcc → hcp occurs at different temperature ranges in the two alloys. The transformation in CoRe-2 alloy (with Ta addition) lags behind (i.e. transformation occurs at a lower temperature) by 25°C. In CoRe-1 ε_{start} = 1160°C and ε_{end} = 1130°C, while in CoRe-2 the temperatures are ε_{start} = 1135°C and ε_{end} = 1105°C, respectively. In both alloys, the matrix is single phase, hcp at lower temperatures (up to ~ 1100°C at least) and fcc at high temperatures (above 1260°C).

Large hysteresis

In-situ neutron diffraction measurements at high temperature showed, for the first time, the existence of a large hysteresis (~ 100K) in the hcp ⇆ fcc phase transformation in the Co matrix of experimental CoRe alloys CoRe-1 and CoRe-2. The hysteresis observed in CoRe-1 and CoRe-2 alloys is a result of the partitioning of Cr and Re between the matrix and the other minor phases (e.g. $Cr_{23}C_6$ carbides and Cr_3Re_2 type σ phase). Release of Cr due to dissolution of $Cr_{23}C_6$ carbides and its combining with Re from matrix to form σ phase strongly influence the hysteresis [3]. Further neutron experiments are planned to clarify some of the unresolved issues and check the influence of the hcp ⇆ fcc phase transformation on the mechanical properties and the microstructural stability of CoRe alloys.

[1] J. Rösler et al., Adv. Eng. Mater., 9 (10), 876 (2007).
[2] D. Mukherji et al., Mater. Lett., 64 (23), 2608 (2010).
[3] D. Mukherji et al., Mater. Trans. A, submitted (2010).

Phase transition studies of $LaAlO_3$ by high-resolution neutron Larmor diffraction

J. Repper[1], T. Keller[1,2], W. W. Schmahl[3]

[1]Technische Universität München, Forschungs-Neutronenquelle Heinz Maier-Leibnitz (FRM II), Garching, Germany
[2]Max-Planck-Institut für Festkörperforschung, Stuttgart, Germany
[3]Ludwig-Maximilians-Universität München, Department für Geo- und Umweltwissenschaften, München, Germany

$LaAlO_3$ shows a rhombohedral-cubic phase transition at a transition temperature of $T_t \approx 820$ K accompanied by a small lattice strain. Neutron Larmor diffraction (LD) is a high-resolution diffraction technique ($\Delta d/d = 10^{-6}$) based on the Larmor precession of polarized neutrons. Here, we present first results of in-situ studies of the phase transition in $LaAlO_3$ by LD measurements. It turns out that the behaviour of the system is cubic approximately 16 K below the structural phase transition temperature.

$LaAlO_3$ is often used as substrate material for superconducting ($YBa_2Cu_3O_{7-x}$) or ferroelectric ($BaTiO_3$) thin films [1]. In contrast to other rhombohedral perovskites (e.g. $LaGaO_3$, $PrAlO_3$) $LaAlO_3$ possesses a relatively low rhombohedral-cubic phase transition temperature. This phase transition causes twinning in the {100} and the {110} lattice planes of the pseudocubic rhombohedral phase [2]. The mobility of twin walls is responsible for the superelastic behaviour under mechanical load [1]. There is a huge number of publications, which deal with the elastic and plastic properties of $LaAlO_3$ and its symmetry breaking phase transition [1,2,3,4]. This reflects the scientific and technological interest in $LaAlO_3$. Here, we present first results of high-resolution studies of the rhombohedral-cubic phase transition of $LaAlO_3$ by neutron Larmor diffraction.

High-resolution neutron Larmor diffraction

Neutron Larmor diffraction (LD) is a high-resolution diffraction technique based on the Larmor precession of polarized neutrons, first proposed by Rekveldt [5,6]. In this technique the phase and amplitude of the neutron spin polarisation is analysed after passage through two magnetic field regions defined by four radio frequency spin flip coils located before and after the sample region. The basic principle of the LD technique is to mark each single neutron by a Larmor precession phase such that the phase ϕ only depends on the lattice spacing d and is independent of the Bragg angle or the velocity of the single neutron. The phase ϕ of the neutron spin is then:

$$\Phi_{tot} = \frac{2 \cdot m \cdot \omega_L L \cdot d}{\pi \cdot \hbar}$$

where $\omega_L = 2\,\pi\,\gamma\,B$ is the Larmor frequency with $\gamma = 2.916$ kHz/Gauss, m is the neutron mass and L the total length of the magnetic fields. A comprehensive introduction to LD can be found in [5,6].

Peak splitting

A $LaAlO_3$ single crystal was used as sample material. The plate-shaped crystal has dimensions of 10 x 10 x 1 mm^3 and is Czochalsky-grown along the [100] direction. The [110] directions are aligned parallel to the edges of the crystal plate (fig. 1). $LaAlO_3$ shows a cubic-rhombohedral phase transition at $T_T \approx 820$ K [1,2]. In the low-temperature phase some Bragg reflections of the cubic phase split (e.g. (220) in (220)+(208)), others not (e.g. (020)).

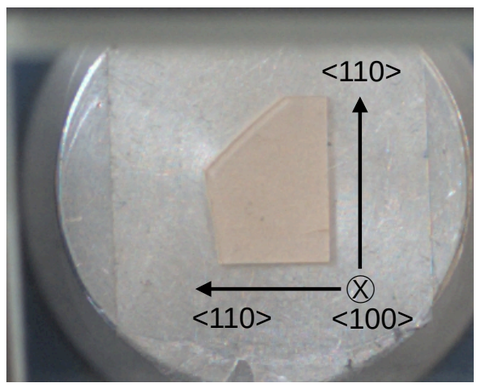

Figure 1: $LaAlO_3$ single crystal in a Laue camera, which was used to align the crystal axes.

The Larmor diffraction experiments were carried out at the neutron resonance spin-echo **tri**ple axis **sp**ectrometer TRISP at the FRM II. A spin echo furnace recently constructed at FRM II makes it possible to study the phase transition by LD under thermal load. We measured the straining of the lattice spacing of the (220) and the (020) lattice planes during the phase transition. The temperature was increased in steps of 20 K from room temperature up to 900 K. Close to T_T the step-width was reduced to 5 K. After each temperature step a data point was collected. We used incident wave vectors of $k_i = 2.85$ Å^{-1} for the measurements at the (220) reflection and of $k_i = 2.03$ Å^{-1} for the measurements at the (020) reflection in order to keep the scattering angle constant at $2\theta \approx 110°$.

Different phase transition temperatures

The strains of the lattice planes determined by LD show errors of around $\Delta d/d = 4 \cdot 10^{-6}$. Figure 2 shows the derivations of the strain curves, which give the thermal expansion coefficients for the measured lattice planes. In addition, the intensity distributions are plotted. The two Bragg reflections contributing to the thermal expansion signal, which are caused by the splitting of the (220) reflection, are responsible for the broad dip of the curve of the (220) plane between 400 K and 640 K. The differences between the d values of the (220) and (208) Bragg reflections decrease with increasing temperature.

The thermal linear expansion coefficient α merges for both lattice planes at $\alpha \approx 9.6 \cdot 10^{-6}$ K^{-1}.

This value is in good agreement with literature ($9.2 \cdot 10^{-6}$ K^{-1} to $10 \cdot 10^{-6}$ K^{-1}). The change in the slopes of both the distribution of α and the intensity distribution at around 800 K indicates the rhombohedral-cubic phase transition. The phase transition temperature analysed on the basis of the thermal expansion coefficients ($T_{Texp} \approx 806$ K) is slightly lower than the temperature analysed on the basis of the measured intensities ($T_{Tint} \approx 822$K). This points to a crystal system,

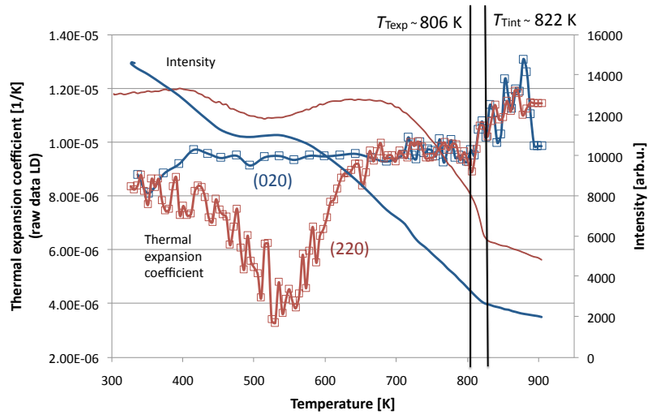

Figure 2: Raw data of the thermal expansion coefficient of the (220) (red line with squares) and the (020) (blue line with squares) lattice planes as measured by LD. In addition, the Bragg peak intensities are given for both reflections (red and blue line).

which shows cubic behaviour approximately 16 K below the structural phase transition temperature of 822 K. This early change of metrics is in agreement with results published by Hayward [3] and Lehnert [4]. The creation of domains which emulate the cubic symmetry by internal strains is probably responsible for this effect. Further analysis will help to clarify the influence of spontaneous strains.

New high-resolution insights in materials

Combining the thermal expansion coefficient measurement and the Fourier transforms of the lattice spacing distributions, which are also accessible by LD, promises new results due to the high-resolution of the Larmor diffraction method. Here, $LaAlO_3$ is a good model for multi-phase materials.

[1] M.A. Carpenter et al., J. Phys.: Condens. Matter, 22 (3) 035403 (2010).
[2] S. Bueble et al., Surf. Sci., 400 (1-3), 345 (1998).
[3] S.A. Hayward et al., Phys. Rev. B, 72 (5), 054110 (2005).
[4] H. Lehnert et al., Z. Kristallogr., 215 (10), 536 (2000).
[5] M.T. Rekveldt, MSF, 321-324, 258 (2000).
[6] M.T. Rekveldt et al., EPL, 54 (3), 342 (2001).

The crystal structure of complex ruthenates: Combining X-ray and neutron diffraction

F. J. Zúñiga[1], F. J. García-García[2], M. Hoelzel[3,4], A. Reller[2]

[1]Universidad del País Vasco, Facultad de Ciencia y Tecnología, Bilbao, Spain
[2]Universität Augsburg, Institut für Physik, Augsburg, Germany
[3]Technische Universität Darmstadt, FB Material- und Geowissenschaften, Darmstadt, Germany
[4]Technische Universität München, Forschungs-Neutronenquelle Heinz Maier-Leibnitz (FRM II), Garching, Germany

The crystal structure of a complex ruthenate has been solved and refined in a two step procedure. By using X-ray diffraction data, the cation sub-structure was solved and refined. In a second step the anion sub-structure was properly determined from neutron powder diffraction data. Furthermore, we have also used electron microscopy to support the refinements. The structure is a rather complicated ABO_3 cubic perovskite related superstructure, where cation vacancies in the A position of the basic cubic perovskite structure are responsible for creating the superstructure.

Superconductivity without copper

Crystal chemistry in ruthenium oxides is quite rich. Ruthenates are known to adopt quite different structure types [1-3]. Their common characteristic is the presence of RuO_6 octahedra that form networks extending in 3, 2 or 1 dimensions by corner, edge or face sharing. Low dimensional structures are also found with isolated units of 1, 2 or 3 [4]. This different dimensionality along with the fact that most of them are metallic conductors, make them a playground of outstanding interest for studying peculiar physical properties. A good example is the compound Sr_2RuO_4 [4], which is the first layered perovskite related compound that shows superconductivity without containing copper. Also, it has been found to belong to the rare group of compounds showing spin-triplet superconductivity [5]. On top of that, it is well known that hybrid rutheno-cuprates materials show coexistence of superconductivity and ferromagnetism [6,7].

The crystal structure reported here is part of a broad project concerning synthesis and characterization of new Ru containing solid state compounds.

Sample mounted in transmission mode

Experiments involve single crystal X-ray diffraction and neutron powder diffraction measurement. Neutron powder diffraction data were collected at the SPODI diffractometer. A vanadium sample container was filled with 4.5 grs of the synthesized material. The sample was mounted in transmission mode. Scan range: 2θmin = 0.95, 2θmax = 151.90, step scan with D(2θ) = 0.05°.

Powder diffraction determined oxygen positions

As a first step, we solved the structure by direct methods using single crystal X-ray diffraction data. Only two space groups, F23 and F43, also confirmed by electron diffraction, gave acceptable results. A rough first approximation to the chemical composition was obtained by energy dispersive X-ray spectroscopy. Refinements of the cation sub-structure with F23 converged and the main features of the structure were then clear. The structure is related with a cubic perovskite ABO_3:

(i) La/Sr and Ba sit in A type positions

(ii) the B type positions are shared by Ru, Al, La/Sr, with two independent crystallographic positions for Ru with one of them shared with Al.

The formula of the compound can be written as $(Ba_8Sr_{32.784}La_{15.216})(Ru_{17.904}Al_{14.096}\ Sr_{20.48}La_{11.52})O_{192-x}$ with x at this step rather ill defined. The composition in terms of the traditional perovskite structure ABO_3 is $A_{56}B_{64}O_{192}$ or $A_{0.875}BO_3$ with A = Ba,La,Sr and B = Ru,Al, La,Sr. The occupancies of oxygen atoms were determined using neutron powder diffraction data in a Rietveld refinement process. The final refinement was performed using only the single crystal X-Ray data, fixing the positional and occupational parameters of O3, O4, O5 and O6 to the values obtained in the Rietveld refinement and restricting occupancies accordingly to a neutral charge condition.

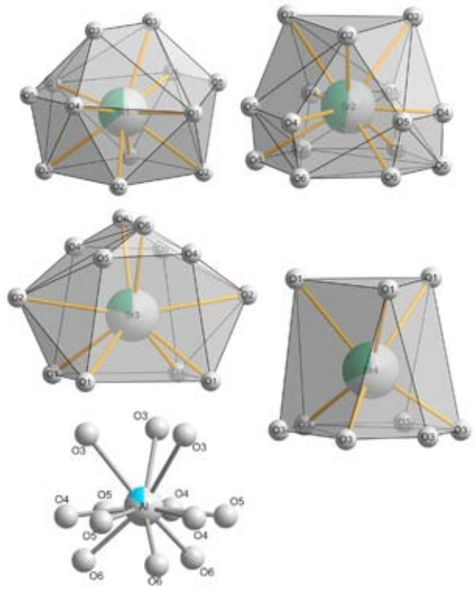

Figure 1: The coordination polyhedra for Sr/La (four independent positions in the unit cell) and for Ru/Al are presented. Note the strong asymmetry in them and the fact that O3, O4, O5 and O6 are all not fully occupied positions, while O1 and O2 are the only ones with occupancies equal to one.

All oxygen atoms in the polyhedra show full occupancy

The combined refinements allowed us to determine the real atomic structure of the compound under study. The final formula for this compound is given above with $x \approx 24.08$. Only Ba and one of the Ru present well defined coordination polyhedra (see fig. 1), the former cuboctahedral and the latter octahedral. Furthermore, all oxygen atoms involved in these polyhedra showed full occupancy. All the rest of the oxygen atoms present in the structure have occupancies below unity. In the same manner all the rest of the cations present disorder as they are all sharing their position with other cations. The polyhedral for all the remaining cations are presented in the figure.

Highly complicated structure

The present investigation is a clear example of a highly complicated structure, which only admits to a proper refinement when X-ray and neutron diffraction data are combined. Taking advantage of the specific benefits of each of these techniques has allowed the structure to be properly described. Note that any investigation to study and analyze the properties of this compound will have to have the structural description reported here as its starting point. The crystal structure of the title compound is a perovskite related structure, where cation vacancies in the A positions are responsible for the superstructure.

Acknowledgments

The Deutsche Forschungsgemeinschaft (DFG) through SFB 484 and the Basque Government (Proj IT-282-07) supported this work. Technical support for single crystal measurements provided by SGIker (UPV/EHU) is gratefully acknowledged.

[1] R.J. Bouchard and J.F. Weiher, J. Solid State Chem., 4 (1), 80 (1972).
[2] Y. Maeno et al., Nature, 372 (6506), 532 (1994).
[3] W.J. Zhu et al., J. Solid State Chem., 129 (2), 308 (1997).
[4] S.G. Ebbinghaus, J. Solid State Chem., 177 (3), 817 (2004).
[5] K. Ishida et al., Nature, 396 (6712), 658 (1998).
[6] L. Bauernfeind et al., Physica C, 254 (1-2), 151 (1995).
[7] L. Bauernfeind et al., J. Low Temp. Phys., 105 (3), 1605 (1996).

Cu-ion active species in ZSM5 zeolites: Heterogeneity and site morphologies

P. A. Georgiev[1], A. Albinati[1], J. Ollivier[2], T. Unruh[3,4]

[1]University of Milan, Department of Structural Chemistry, Milan, Italy
[2]Institut Laue-Langevin, Grenoble, France
[3]Technische Universität München, Forschungs-Neutronenquelle Heinz Maier-Leibnitz (FRM II), Garching, Germany
[4]Friedrich-Alexander-Universität Erlangen-Nürnberg, Lehrstuhl für Kristallographie und Strukturphysik, Erlangen, Germany

By using high resolution **I**nelastic **N**eutron **S**cattering (INS) combined with gas adsorption and hybrid DFT methods we were able to identify and describe the active metal-ion species and their local coordination environments for a series of Cu-exchanged ZSM-5 types of zeolites.

A clean energy medium

Activation of chemical bonds such as H-H, C-H, S-H by metal clusters or ions on the surface of metal oxides or in extra framework positions in zeolites plays an important role in both chemical industries and daily life. Due to their usually low concentration and relatively high level of disorder, the microscopic characterisation of catalytic centres in bulk materials or on surfaces still represents a challenge to current scientific methods. Being regarded as the clean energy medium of the future, dihydrogen stored in various porous materials and dissolved in the lattices of some metals and metal alloys which form hydrides has been intensively studied over the last decades. The aim of these studies was mainly the development of new materials able to absorb and release large amounts of hydrogen, sufficiently quickly, at ambient temperatures and pressures. In more technical language, the aforementioned storage properties of the materials are accordingly labelled as capacity, diffusion coefficient, and heat of adsorption for adsorbed dihydrogen or heat of formation for metal hydrides. More specifically, in practical storage tank applications these main physical parameters must measure at least 4.5 % by weight [1], with diffusion rates of the order of $> 10^{-8}$ cm^2/s, and 25-35 kJ/mol H_2. Recently, a metal-dihydrogen complex in a ZSM-5 zeolite has been shown to form [2,3] and match [4,5] two of the required parameters

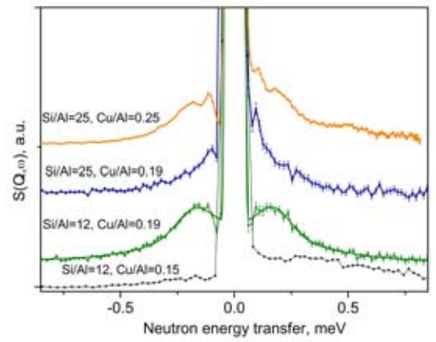

Figure 1: INS spectra measured at 5 K, using neutrons with incident wavelength of 7 Å, of hydrogen adsorbed in different Cu-exchanged zeolite samples as indicated in the figure. The signal from the zeolite substrate has been subtracted. The shown dihydrogen dose corresponds to a complete saturation of all of the available Cu-centres.

while the third, the capacity, is still open to development. Although the chemical nature of the observed species was identified by INS [3], the fine structure of the observed features has remained unaddressed, leaving important questions regarding the exact Cu-ion site position, and corresponding oxidation states, as well as the possibility of polyhydride complex formation. We demonstrate here, how this problem could be solved by measuring the INS rotational spectra of adsorbed dihydrogen, thereby using the H_2 molecule as a fine probe.

Experimental setup

In the present work we have investigated a series of Cu-exchanged ZSM-5 materials with different levels of Cu-exchange and Si/Al ratios, which allows one to differentiate between different possible Cu-sites and their occupancies. The rotational spectrum of free dihydrogen with respect to the ground rotational state J = 0 is given by: EJ = BJ(J+1), with B = 7.35 meV the rotational

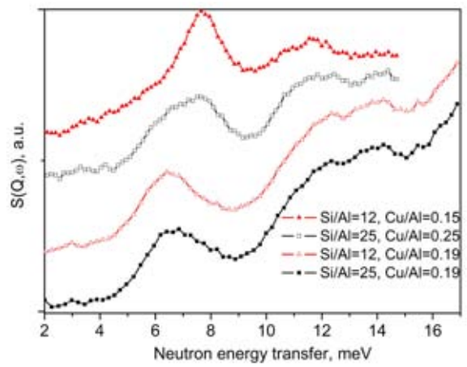

Figure 2: As in fig. 1, but now higher energy, 2 Å, neutrons have been used extending the accessible energy range up to about 18 meV. The signals from the corresponding substrates have been subtracted.

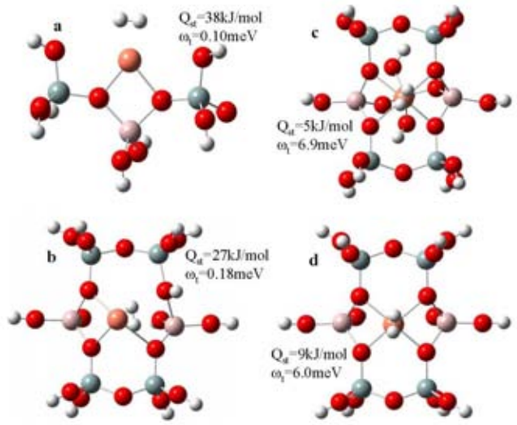

Figure 3: Best match DFT model cluster structures resembling particular ZSM-5 zeolite sites. Monovalent Cu-species are shown in a and b blocks, bivalent Cu-species are shown in c and d.

constant, and J – the rotational quantum number. The first excited state is at 14.7 meV which falls in the range of most of the molecular interactions and can be conveniently measured with INS. In the adsorbed state the molecule experiences certain hindering to rotation by the local adsorption potential and this is reflected in the corresponding rotational spectra. Combining the INS results with sorption thermodynamics measurements and model calculations allows one to precisely reconstruct and distinguish between various adsorption sites and hydrides. We used four samples whose corresponding adsorbed dihydrogen rotational tunnelling spectra are shown in figure 1 for an incident neutron wavelength of 7 Å and figure 2 for 2 Å neutrons. Spectra a and d were measured on the IN5 instrument at the ILL, spectra b and c on TOFTOF at the FRM II. In all cases, the samples with compositions as shown in the legend of figure 1, were evacuated under a dynamic vacuum at temperatures up to 773 K. Their blank (no H_2) spectra were measured at 5 K. These were consequently subtracted from the spectra of the corresponding hydrogen dosed samples. The main dihydrogen related features are to be observed at about 0.1 meV, 0.2 meV in figure 1 and then at about 6, 7, 12 and 14 meV in figure 2. To assign these features, we performed hybrid DFT calculations on 14 different model clusters taken from the ZSM-5 framework. From these calculations we extract dihydrogen tunnelling frequencies and adsorption heats which are compared with the INS and sorption results. The sites that best reproduced the experimental results are shown in figure 3.

Microscopic model of hydrogen adsorption

Our INS studies of adsorbed dihydrogen have served as a most stringent tool for verifying the validity of model calculations from which we were able to derive a microscopic model of the hydrogen adsorption and distribution over the various adsorption sites. These include two monovalent Cu-species, figure 3a and b, which are responsible for the observed strong adsorption at room temperatures and INS features at 0.1 and 0.2 meV as well as bivalent Cu-species, figure 3c and d, whose rotational features are observed at 6-7 meV. Furthermore, at high energies we observed the rotational lines of H_2 adsorbed near acidic protons and the zeolite framework [5].

[1] US Department of Energy, Hydrogen program
[2] X. Solans-Monfort et al., J. Phys. Chem. B., 108 (24), 8278 (2004).
[3] P.A. Georgiev et al., J. Am. Chem. Soc., 129 (26), 8086 (2007).
[4] P.A. Georgiev et al., Chem. Phys. Lett., 449 (1-3), 182 (2007).
[5] P.A. Georgiev et al., in preparation.

In-situ probing of fast defect annealing in Ni with a high-intensity positron beam

B. Oberdorfer[1], E.-M. Steyskal[1], W. Sprengel[1], W. Puff[1], P. Pikart[2], C. Hugenschmidt[2], M. Zehetbauer[3], R. Pippan[4], R. Würschum[1]

[1]Technische Universität Graz, Institut für Materialphysik, Graz, Austria
[2]Technische Universität München, Forschungs-Neutronenquelle Heinz Maier-Leibnitz (FRM II), Garching, Germany
[3]Universität Wien, Fakultät für Physik, Wien, Austria
[4]Austrian Academy of Sciences, Erich Schmid Institute of Materials Science, Leoben, Austria

The high-intensity positron beam of the NEPOMUC positron source was used for specific in-situ monitoring of thermally activated fast defect annealing in Ni on a time scale of minutes. The atomistic technique of positron-electron annihilation was combined with macroscopic, high-precision length-change measurements under the same thermal conditions. The combination of these two methods allows for a detailed analysis of multistage defect annealing in solids distinguishing vacancies, dislocations, and grain growth.

Structural defects such as vacancies, dislocations, and interfaces deliberately introduced into crystalline solids modify their physical properties significantly. Common to these defects is their distinct excess volume as compared to the perfect lattice. Therefore, to study such defect structures, experimental techniques which directly detect changes of the atomic volume are preferable. Furthermore, in complex defect structures that combine different types of these defects as, e.g., after severe plastic deformation [1], the types can be distinguished according to their characteristic annealing kinetics. One experimental technique, dilatometry, is based on macroscopic length-change measurements upon irreversible annealing of defects [2]. Another, of atomistic origin, is based on the positron-electron annihilation in solids. So far, the latter technique for defect characterization has been limited to kinetic processes on time scales of hours due to the limitations in positron intensities achievable on a laboratory scale. This time scale has now been significantly shortened by implementation of the high-intensity positron beam at the positron source NEPOMUC that provides a positron beam with an intensity of at least 2 orders of magnitude higher than at conventional laboratory beam setups. In direct combination with high-precision dilatometry it provides a unique and powerful tool for the analysis of fast defect kinetics.

Deformed disks

Disks of nickel (purity 99.99+) 30 mm in diameter and 10 mm in height were severely deformed by **h**igh-**p**ressure **t**orsion (HPT), resulting in an **u**ltra-**f**ine **g**rained (UFG) structure with a mean grain size, d, of 260 nm as determined by **s**canning **e**lectron **m**icroscopy (SEM). The specimens for the dilatometric and positron annihilation experiments were prepared from equivalent positions where they were subjected to a von Mises equivalent strain of about $\varepsilon \approx 20$ to 30 (see fig. 1). The in-situ positron-electron annihilation experiments were performed at the coincident Doppler-broadening spectrometer at NEPOMUC with 20 keV positrons and a beam diameter of less than 1 mm at the sample position. After temperature calibration, the in-situ annealing experiments were performed up to 473 K. The dilatometric measurements were performed with the same temperature program in a difference-dilatometer with a well annealed Ni specimen as reference.

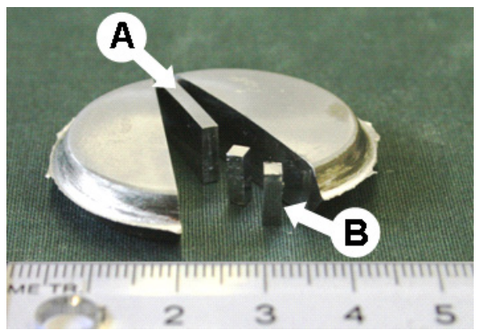

Figure 1: Specimen disk of pure Ni deformed by high-pressure torsion (HPT). Indicated are the different samples prepared for positron annihilation (A) and for dilatometry (B).

Defect analysis

As initial positron saturation trapping is prevalent, the S parameter, i.e., the fraction of the positrons annihilating with valence electrons of the solid, was chosen for monitoring the change in the defect configuration. Figure 2 presents the temperature dependence of the S parameter, normalized to the S parameter in the as-prepared state, superimposed on the dilatometric data $\Delta L/L_0$ as a function of temperature for UFG-Ni. The dilatometric data show a nearly linear, monotonic shrinkage of the specimen in a first stage (A), from 365 to 445 K, followed in a second stage (B) by a sharp decrease of the length between 445 and 483 K.

The sharp decrease of the S parameter at temperatures above 460 K is caused by grain growth from the initial grain size of 260 nm to sizes of several micrometers. As the grain growth is associated with the release of grain boundary volume, this results in an immediate effect on the length-change curve as soon as grain growth sets in. The effect of grain growth resulting in the sharp decrease of the S parameter is noticeable at a temperature about 20 K higher. This is due to the fact that the lowering of the S parameter can only be observed after the grains have grown sufficiently larger than the mean positron diffusion length. It leads to an increased annihilation probability inside the defect-free grains as the positrons are then unable to reach the grain boundaries. Thus, the specimen leaves the state of positron saturation trapping, as calculations of diffusion controlled positron trapping at grain boundaries also show [4]. For grains exceeding a radius of about 200 nm, positron trapping in the defect-free state starts to dominate.

The change of the S parameter in the lower temperature region in the first stage (A) at 425 K, however, is slightly more subtle. The nearly linear shrinkage of the Ni specimen in this stage from

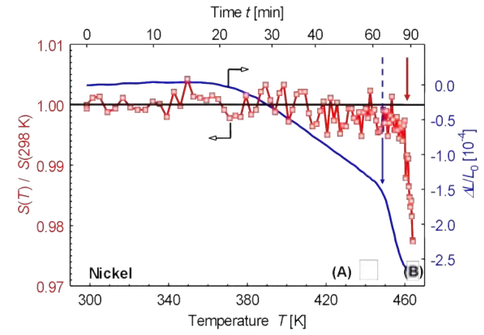

Figure 2: Temperature dependence of the normalized S parameter (red, left ordinate) as determined from positron annihilation; superimposed is the relative length change $\Delta L/L_0$ (blue, right ordinate) as determined by dilatometry of HPT-deformed Ni [3].

365 to 445 K is caused by annealing of vacancies and isolated dislocations and amounts to a total volume change of 4.5×10^{-4} (see fig. 2). Furthermore, from electron irradiation experiments on pure Ni it is well established that Ni vacancies become mobile at temperatures around 360 K. In combination with the dilatometric results, the occurrence of stage (A) is attributed to a change of the dominating positron trapping site. In the case of saturation trapping, the measured S parameter represents an average value of the specific S parameters of the different defect types weighted with the respective trapping rates. The dominant defect type changes from an initial prevalent saturation trapping at vacancies and free dislocations to a state of dominant trapping at grain boundaries. Calculations based on a positron trapping model with respect to the different trapping rates at point defects and at grain boundaries in polycrystalline materials support this conclusion [4].

To summarize, a complex atomic defect structure in solids has been successfully analyzed by a combination of the atomistic technique of fast in-situ temperature dependent positron-electron annihilation and dilatometry [3]. The application of high-intensity mono-energetic positron beams to fast defect kinetics studies opens new experimental fields for the application of positron beams.

[1] R. Valiev, Nature Mater., 3 (8), 511 (2004).
[2] B. Oberdorfer et al., Scripta Mater., 63 (4), 452 (2010).
[3] B. Oberdorfer et al., Phys. Rev. Lett., 105 (14), 146101 (2010).
[4] B. Oberdorfer and R. Würschum, Phys. Rev. B, 79 (18), 184103 (2009).

Porosity and structure of a TiO_2-ceramic composite determined by TOF-GISANS

M. Rawolle[1], K. Sarkar[1], M. A. Niedermeier[1], P. Lellig[2], J. S. Gutmann[2],J.-F. Moulin[3], M. Haese-Seiller[3], P. Müller-Buschbaum[1]

[1]Technische Universität München, Physik Department E13, Garching, Germany
[2]Max-Planck-Institut für Polymerforschung, Mainz, Germany
[3]Helmholtz-Zentrum Geesthacht, Outstation @ FRM II, Garching, Germany

The REFSANS instrument was used in the TOF-GISANS setup to determine the nanoscale pore structure and porosity of titania embedded in a SiOC-type ceramic, a novel material for applications in organic photovoltaics. By utilization of the wavelength spectrum and an asymmetric detector setup, a full morphological characterization was achieved. The scattering length density and thereby the porosity of the titania-ceramic composite was determined precisely. In addition, the pore sizes of the nanostructured hybrid material were probed.

The semiconductor titania, in its anatase polymorph, has contributed considerably to the fast growth in the field of **d**ye-**s**ensitized **s**olar **c**ells (DSSCs) which combine a dye-sensitized titania structure with a hole-conducting electrolyte or, in the case of the **s**olid-**s**tate DSSC (ssDSSC), with a hole-conducting organic solid [1,2].
For solar cell applications the morphology of the titania layer has to be controlled on several length scales. A large surface area is crucial for dye adsorption and therefore for charge generation. In addition, in ssDSSCs the problem of charge recombination at the electrode has to be suppressed with the help of a blocking layer. As a consequence, an approach to combine the structuring with the formation of an integrated blocking layer is of high interest.

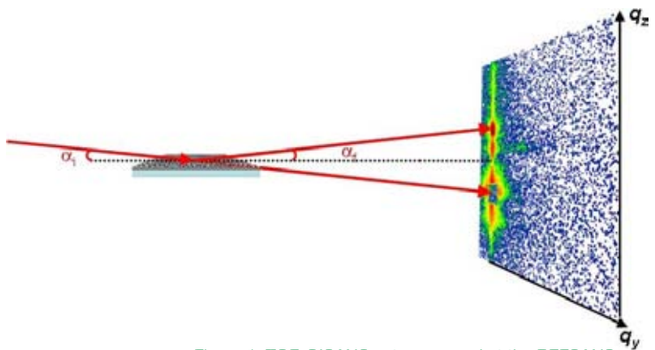

Figure 1: TOF-GISANS setup as used at the REFSANS instrument with an asymmetrically positioned detector. The dashed line indicates the sample horizon, the red arrows the incoming and final neutron beams respectively. The lower final beam points at the beamstop shielding the direct beam. Around the direct beam the transmitted signal is measured. The upper final beam points at the specular peak where incident and exit angle are the same.

Sample preparation

A very promising route to nanostructured titania is the combination of a structure-directing amphiphilic block copolymer template with sol-gel chemistry. Structures are formed in the so-called good-poor solvent pair induced microphase separation in the amphiphilic block copolymer, where the titania precursor is chemically linked to one of the polymer blocks. Recently sol-gel templating of anatase titania films with the amphiphilic diblock copolymer poly(dimethyl siloxane) – *block* – methyl methacrylate poly (ethylene oxide) PDMS-*b*-MA(PEO) was successfully applied to prepare hierarchically structured, thin titania films [3]. Usually the structure directing block copolymer is combusted by calcination in air. When calcining the nanocomposite of the structure directing diblock copolymer and titania in an inert gas, in the special case of a PDMS-containing polymer the polymer can not only be combusted, but the PDMS part is transferred to an SiOC-type ceramic. This type of ceramic has a high dielectric constant and is therefore of high interest as an integrated blocking layer within the titania structure.

Structure investigations

Grazing **i**ncidence **s**mall **a**ngle **n**eutron **s**cattering (GISANS) measurements were performed in the **t**ime-**o**f-**f**light (TOF) mode at the REFSANS instrument [4]. The TOF-GISANS experiment allowed GISANS with a wavelength range of 2.1 up to 18.1 Å. A fixed incident angle of 0.48° was used. Due to gravity effects for very large wavelengths it increased slightly up to 0.50°. With a sample-to-detector distance of 9.475 m the available q-range in the asymmetric setup of the detector is 1.50 x 1.25 nm^{-1} for a wavelength of 18.1 Å and 9.5 x 7.7 nm^{-1} for 2.8 Å. Figure 1 shows a sketch of the asymmetric TOF-GISANS setup used.

Results and Discussion

Real space investigations with SEM, as shown in figure 2, reveal a mesoporous structure of the titania-ceramic network. Quantitative information about the size of this mesoporous structure is probed with GISANS. GISANS gives structural information not only on the surface but for the whole volume of the film. In addition, a large sample area of several square centimeters is probed and thus the determined structures have a very high statistical significance. Figure 3 shows selected two-dimensional GISANS scattering images measured at the titania-ceramic structure. The reflected GISANS signal is seen above the sample horizon. Information on lateral structures can be gained from the structure peak in q_y-direction at the position of the material specific Yoneda peak in q_z-direction. As the examined q-range changes with wavelength, the position of the structure peaks also changes with the wavelength. Due to the applied asymmetric setup of the detector the structure peak can be

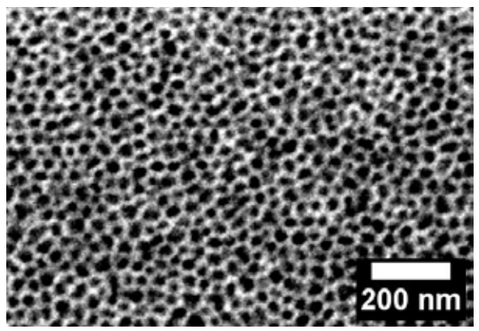

Figure 2: SEM graph of the porous titania-ceramic hybrid network structure with a pore size of about 35 nm.

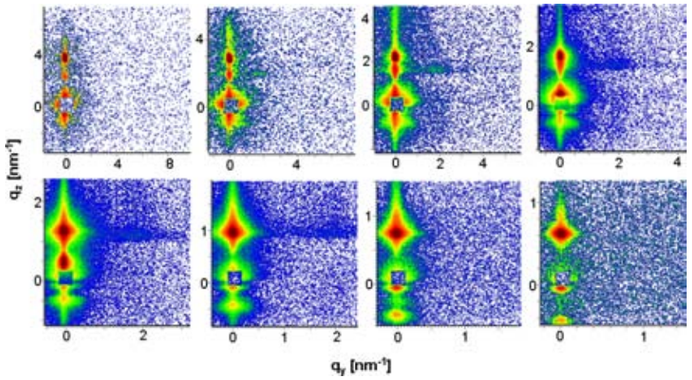

Figure 3: Selected two-dimensional scattering images of the titania-ceramic network structure with the following wavelengths (left to right and top to bottom): 2.8 Å, 3.7 Å, 4.8 Å, 6.4 Å, 8.5 Å, 11.3 Å, 14.9 Å, 18.1 Å. The intensity scale is the same for the eight scattering images.

followed for eleven GISANS data sets, which significantly diminishes the statistical error. From fitting the peak position, the value of the structure sizes inside the volume of the titania-ceramic-film was obtained as 32 nm. Thus the pore structure has a mean size of 32 nm.
In addition, the porosity of the hybrid film is extracted from the TOF-GISANS data. From the wavelength dependent Yoneda peak position (see fig. 3) the **s**cattering **l**ength **d**ensity (SLD) is determined. From the SLD the mass density of the porous hybrid is calculated. From this mass density the porosity is determined to be 0.59 for a 1:1 mixture of titania and SiOC.

GISANS in TOF-mode at REFSANS allowed the determination of the porosity of a titania-ceramic hybrid film, which is not accessible by other means alone. The obtained value of 0.59 is rather high and promises a good applicability of this novel material in ssDSSCs. This high porosity is a result of the mesoporous network structure with pore sizes of 32 nm.

[1] B. O'Regan and M. Grätzel, Nature, 353 (6346), 737 (1991).
[2] M. Wang et al., Small, 6 (2), 319 (2010).
[3] G. Kaune et al., ACS Appl. Mater. Interface, 1 (12), 2862 (2009).
[4] G. Kaune et al., J. Polym. Sci. B: Polym. Phys., 48 (14), 1628 (2010).

Membranes for rapid stem cell adhesion characterized by neutron and X-ray reflectometry

M. Huth[1], S. Hertrich[1], G. Mezo[2], E. Madarasz[3], B. Nickel[1]

[1]Ludwig-Maximilians-Universität München, Fakultät für Physik and CeNS, Munich, Germany
[2]Hungarian Academy of Science, Peptide Chemistry Research Group, Budapest, Hungary
[3]Hungarian Academy of Science, Institute of Experimental Medicine, Budapest, Hungary

We report a biomimetic surface based on the synthetic peptide-conjugate AK-cyclo[RGDfC] which contains multiple copies of the RGD amino acid sequence. The biotinated AK-cyclo[RGDfC] is bound to a supported lipid bilayer via a streptavidin interlayer. Layering, hydration and packing of the coating were quantified by neutron and X-ray reflectometry. We find that AK-cyclo[RGDfC] absorbs to the streptavidin interlayer in a stretched-out on-edge configuration. Neutron contrast variation suggests a highly packed configuration with only 12 % water content. In this configuration, the number of accessible RGD adhesion sites is maximized. On such surfaces, rapid neural cell spreading was observed.

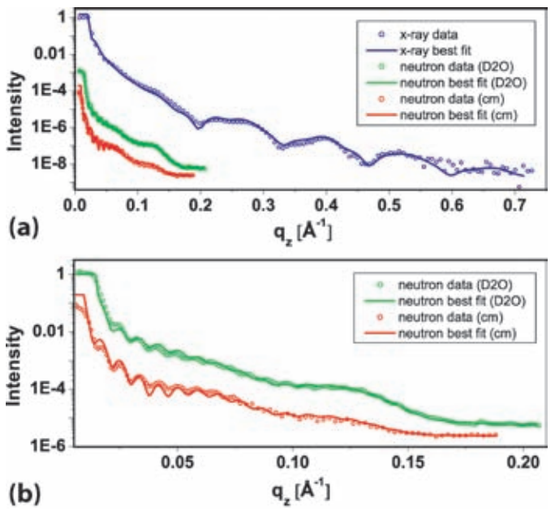

Figure 1: Reflectometry data and best fits. (a) The reflected intensity is plotted against the momentum transfer q_z. The reflectometry data are represented by open symbols, curves represent best fits. The neutron measurements are shown in green [D_2O] and red [cm], the X-ray measurement is shown in blue. (b) Detailed view of the neutron data and best fits. Colour and symbols as in (a).

AK-cyclo[RGDfC]

The control of cell attachment on diverse surfaces is a fundamental requirement in biophysical situations where close contact between cells and a technical surface (metals, oxides, polymers) is required, such as in sensing applications or tissue engineering. Without proper attachment, cells sustain a special apoptotic fate called anoikis. Here, cell attachment is promoted by a synthetic peptide-conjugate AK-cyclo[RGDfC] [1]. AK-cyclo[RGDfC] contains a poly-L-lysine backbone decorated with oligo-D/L alanine side chains. The N-termini of the oligo-alanine side chains carry a RGD sequence (arginyl-glycyl-aspartic acid) in a pentapeptide ring (cyclo[RGDfC]). We use biotinated AK-cyclo[RGDfC] which is bound to a streptavidin template on a biotinilated lipid bilayer [2].

Studies with X-ray and neutron reflectometry

The trilayer structure of adhesion protein, streptavidin interlayer and lipid bilayer is studied by X-ray and neutron reflectometry. We performed the neutron reflectometry measurements at N-REX⁺ for two different contrasts, 100 % D_2O [D_2O], and a mixture which contrast was matched [cm] to the scattering length density (sld) of SiO_2, see figure 1. A single set of structural parameters reproduces the neutron and X-ray reflectometry data. The data (open circles) and final best fits (lines) are shown in figure 1. The results are summarized in figure 2.

The membrane

The head to head distance of the membrane of 36 Å is in agreement with values previously published [3]. A highly hydrated biotin interlayer of 26 Å between the membrane and the streptavidin layer is observed. The thickness of the close packed streptavidin layer (38 Å, no hydration) is in good agreement with the thickness of 40 Å found by Horton et. al [2]. For the AK-cyclo[RGDfC] layer, we obtain a thickness of 30 Å and a water content of 12 %. The width of the AK-cyclo[RGDfC] layer in a stretched out conformation is estimated to be 32 Å by adding the length of two side chains, i.e. the oligo-alanines, the thioether linkage and the diameter of the cyclo[RGDfC] compound. From a comparison of the observed thickness of 30 Å with the estimated width of 32 Å, and the observation that the hydration of the layer is only 12 %, we infer a configuration where the AK-cyclo[RGDfC] molecule is bound in an on edge configuration to the streptavidin surface (fig. 2). Because of its length of 510 Å, the AK-cyclo[RGDfC] molecule in on edge configuration binds to several streptavidin molecules, see figure 2.

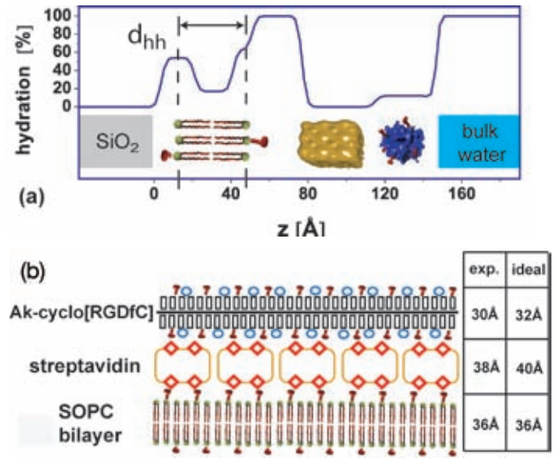

Figure 2: Structure model. (a) Hydration profile of the layers including a schematic of the layer components. dhh indicates the head to head distance of the lipid bilayer. (b) Schematic of the synthetic peptide on top of the streptavidin interlayer. Red hooks depict the biotin residues, blue circles indicate the positions of a cyclo(RGDfC) residue.

A look through the microscope

The rapid adhesion of GFP expressing neural stem cells upon exposure to different surface-coatings was investigated by fluorescence microscopy. For the plain SOPC membrane, a non-spreading, spheroid cell morphology and enhanced formation of cell aggregates indicated poor attachment of the cells to the surface. For the biotinated AK-cyclo[RGDfC] templated by an avidin-SLB support, improved and rapid spreading of the cells was observed [4].

Conclusions

The combination of X-ray and neutron reflectometry experiments allows us to quantify the layered structure of the AK-cyclo[RGDfC]/streptavidin/SLB system in terms of layer thickness, hydration, and packing. AK-cyclo[RGDfC] binds to the streptavidin template in a stretched on edge orientation. A dense layer exposing the RGD adhesion motive was prepared. Neural stem cells readily spread on such surfaces. A large variety of surfaces can be coated by lipid bilayers using physisorption, and various techniques for bilayer patterning are available. Using this approach, the preparation of highly effective coatings for stem cells growth on technical surfaces is possible.

Acknowledgements

This work was supported by the EU-STREP 0032352 BIODOT, BMBF 05KN7WMA and by the National Development Program, Hungary Bio_Surf. The Nanosystems Initiative Munich (NIM) is gratefully acknowledged. Experiments at N-Rex⁺ were performed with help of A. Rühm.

[1] K. Marko et al., Bioconj. Chem., 19 (9), 1757 (2008).
[2] M.R. Horton et al., Langmuir, 23 (11), 6263 (2007).
[3] M.B. Hochrein et al., Langmuir, 22 (2), 538 (2006).
[4] M. Huth et al., Materials, 3 (11), 4994 (2010).

Sticky boundary layer and anisotropic diffusion in nanochannels

A. Kusmin[1], S. Gruener[2], A. Henschel[2], J. Allgaier[1], D. Richter[1], P. Huber[2]

[1]Forschungszentrum Jülich GmbH, Institut für Festkörperforschung, Jülich, Germany
[2]Universität des Saarlandes, Experimentalphysik, Saarbrücken, Germany

Neutron spin echo experiments on the melts of an n-$C_{36}H_{74}$ (C_{36}) and **p**oly(**e**thylene **o**xide) (PEO) confined in nanochannels of porous silicon demonstrate the existence of a wall-adsorbed, immobile boundary layer, as is also inferred from capillary filling experiments. The dynamics of non-adsorbed molecules are bulk-like but, at least in the case of PEO, anisotropic: diffusion along the pore is slower than perpendicular to the pore axis due to a pure geometrical confinement effect.

Liquids for microfluidic devices

The operation of microfluidic devices like chips for DNA and protein separation and determination is based on liquids flowing through nanosized channels [1]. Capillary filling of such nanochannels has been actively studied for more than a decade and in the case of short-length linear hydrocarbons (n-alkanes) the existence of a layer of wall-adsorbed molecules was indirectly inferred from measured flow rates [2,3]. Neutron spin echo (NSE) spectroscopy allows one to follow the motion of liquid molecules on length scales up to 10 nm and timescales of up to 250 ns. Hence, the adsorption of a molecule or any influence of the confinement on the motional properties of non-adsorbed molecules can be detected directly.

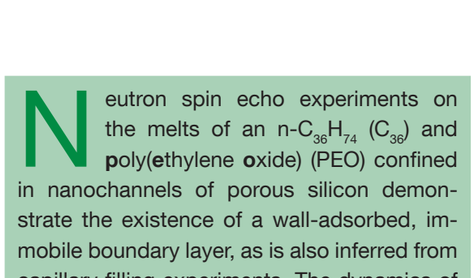

Figure 1: Two orientations of porous silicon wafers (grey bars with pores drawn as a series of white cylinders) employed in the experiment. Q is the neutron wave vector transfer.

Experiments at the J-NSE

Using the J-NSE spectrometer at the FRM II we performed experiments [4,5] on melts of a hydrocarbon, n-$C_{36}H_{74}$ (C_{36}), and a linear poly(ethylene oxide) (PEO), 3 kg/mol, confined in porous silicon wafers [6]. Two sample orientations were employed in order to probe molecular motions along and perpendicular to the pore axis (fig. 1).

Different adsorbtions

C_{36} molecules adsorb on SiO_2-covered inner pore surfaces with their long axis oriented parallel to the surface; a monolayer is approximately 0.5 nm thick. PEO molecules adsorb even more strongly; the thickness of their monolayer is 4.8 nm. As can be seen from figure 2, the fraction of adsorbed molecules is significant, which is why we analyzed the spectra in the framework of a two-state model.

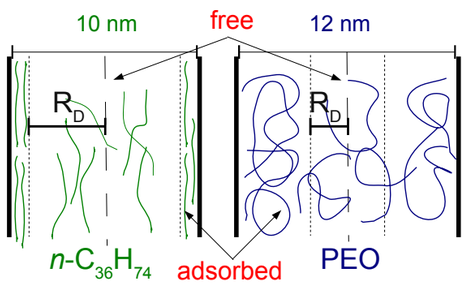

Figure 2: Molecules adsorbed on the surface of the pore are immobile, whereas non-adsorbed molecules diffuse inside a cylinder of radius R_D in the centre of the pore.

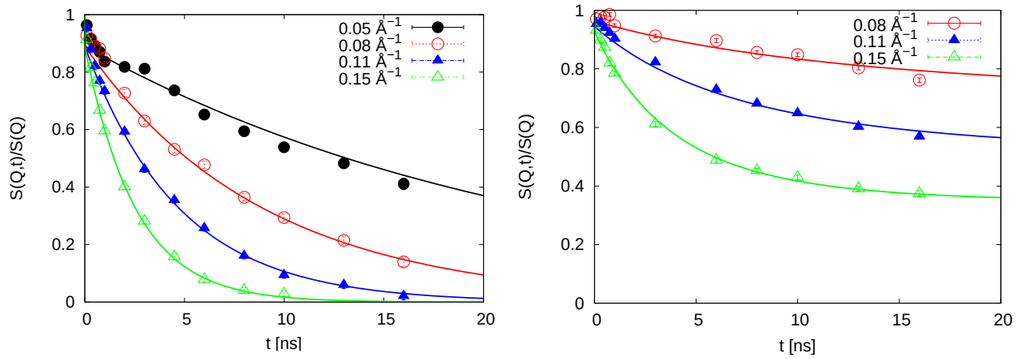

Figure 3: Experimental curves recorded for T = 364 K and several Q values (symbols) and their description by the theoretical model (lines). Left: bulk C_{36}, right: confined C_{36}. Note that for confined C_{36} S(Q,t)/S(Q)-curves decay to a non-zero value from which R_D and, consequently, the thickness of the adsorbed layer can be calculated.

An example of modeling NSE spectra in the case of C_{36} is shown in figure 3. From the comparison of diffusion coefficients for the bulk and confined molecules, the structure of the adsorbed layer was found to change with increasing temperature from a bilayer at 364 K to a monolayer at 435 K, followed by its complete disappearance at 512 K. This is in agreement with the existence of parallel mono- and bilayers of n-alkanes [7]. For PEO, an adsorbed monolayer was found at both 423 K and 453 K.

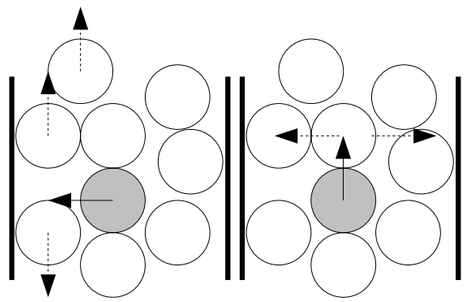

Figure 4: Considering the marked molecule to move perpendicularly to the pore axis neighbouring molecules may easily swerve along the pore. The opposite argumentation applies in the second case. Here, however, the swerving molecules meet more resistance because of the confining walls, which renders this diffusion process less favourable.

Anisotropic diffusion

What is more, we found that, while diffusion of confined C_{36} is isotropic, for PEO diffusion of molecules along the pore is approximately eight times slower than that perpendicular to the pore axis. To our knowledge, this is the first experimental evidence of an effect previously inferred from molecular dynamics simulations [8], as illustrated in figure 4.

In conclusion, our results corroborate the existence of a layer of molecules adsorbed at the pore walls, which has already been indirectly concluded from capillarity driven flow experiments. Moreover our measurements provide the first experimental evidence of anisotropic diffusion in the case where pore diameters are at least twice as large as the dimensions of the molecule.

[1] J.C.T. Eijkel and A. van den Berg, Microfluid. Nanofluid., 1 (3), 249 (2005).
[2] S. Gruener and P. Huber, Phys. Rev. Lett., 103 (17), 174501 (2009).
[3] S. Gruener et al., Phys. Rev. E, 79 (6), 067301 (2009).
[4] A. Kusmin et al., Macromol., 43 (19), 8162 (2010).
[5] A. Kusmin et al., J. Phys. Chem. Lett., 1 (20), 3116 (2010).
[6] P. Kumar et al., J. Appl. Phys., 103 (2), 024303 (2008).
[7] V. del Campo et al., Langmuir, 25 (22), 12962 (2009).
[8] S.T. Cui, J. Chem. Phys., 123 (5), 054706 (2005).

Self-assembling in solution of crystalline-amorphous olefin block-copolymers

A. Radulescu[1], G. Goerigk[1], L. J. Fetters[2], D. Richter[3]

[1]Forschungszentrum Jülich GmbH, Jülich Centre for Neutron Science at FRM II, Garching, Germany
[2]Cornell University, School of Chemical and Biomolecular Engineering, Ithaca (NY), USA
[3]Forschungszentrum Jülich GmbH, Institut für Festkörperforschung, Jülich, Germany

Self-assemblies formed in solution by olefin block-copolymers consisting of alternating crystallizable and amorphous ethylene-octene blocks were investigated within a wide temperature range and over a wide length scale (10 Å ÷ 100 µm) by pinhole- and focusing-SANS (**s**mall-**a**ngle **n**eutron **s**cattering) techniques and optical microscopy with crossed polarizers. The complex morphologies revealing hierarchical structural levels were characterized by interpreting the experimental results in terms of structural models.

The macroscopic behaviour of crystalline-amorphous polymers depends on the constitutive microstructures consisting of molecules arranged in the unit cell (~Å), lamellar crystals (~100 Å), fibrils or boards (~1000 Å) and spherulitic macro-aggregates (~µm). Control and optimization of polymer properties require the knowledge and understanding of these microstructural features in various conditions. Recent developments have led to the synthesis of novel **o**lefinic **b**lock **c**opolymers (OBCs) by using the chain shuttling technology [1]. The ethylene-octene OBCs consist of crystallizable blocks (hard) with very low octene co-monomer content and high melting temperature, alternating with amorphous blocks (soft) with high octene co-monomer content and low glass transition temperature. By varying the hard block content, a broad range of properties can be achieved. Two new INFUSE™ OBCs, 9000 and 9007 (The Dow Chemical Company), in hydrocarbon solutions were studied by wide-Q **s**mall-**a**ngle **n**eutron **s**cattering (SANS) and optical microscopy in order to gain initial insight into their molecular characteristics and self-assembling properties over a broad temperature range. This approach offers a complete characterization of complex block-copolymer structures over a wide length scale, between 10 Å and 100 µm [2,3].

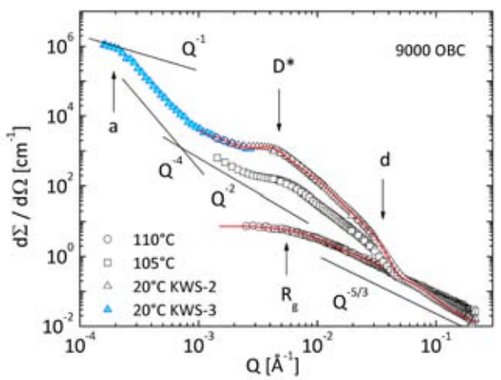

Figure 1: Small angle scattering cross sections from 1 % solutions of the 9000 OBC in dodecane. The power law behaviour ($d\Sigma/d\Omega \approx Q^{-p}$) in different Q ranges (straight solid lines) and the model curves are displayed and the main structural features are indicated.

The SANS measurements were performed over a wave-vector transfer Q range between 2×10^{-4} Å^{-1} and 0.2 Å^{-1} at the KWS-2 pinhole- and KWS-3 focusing-SANS diffractometers of JCNS at the FRM II [4]. The optical microscopy observations were done with a Leica DM6000M light microscope with polarization options. Since the melting temperature of OBCs is around 120°C, the pinhole SANS investigations of dodecane solutions with different polymer volume fractions (0.1 % ÷ 1 %) were performed within the temperature range from 130°C to 0°C.

Typical scattering patterns from an OBC solution at different temperatures are shown in figure 1. At 110°C all polymers are dissolved as single chains as shown by the form factor features identified in the scattering profiles (the low-Q plateau, the Guinier regime and the $Q^{-5/3}$ power law indicative of excluded volume interactions between the chain segments). A complete characterization of the single-chain properties (radius of gyration R_g and molecular weight M_w) following the Zimm approximation [2] indicated that the 9000 OBC chains are stiffer than the 9007 OBC ones. Accordingly, the latter have a higher co-monomer content and thus, lower crystallinity. An overall fit of the scattering pattern with the Beaucage form factor [5] was successful (model curve at 110°C, fig. 1).

A decrease in the temperature results in the formation and evolution of polymer assemblies as a consequence of crystallization of the hard blocks. The 9000 and 9007 OBCs show similar self-assembling behaviour although the former exhibits smaller and more compact structures (the scattering features appear at larger Q compared to the 9007 OBC case), agreeing on the findings about the single chain properties. The scattering profiles display the same peculiarities: a Q^{-2} power-law behaviour of the scattered intensity that spans over a wide Q range and a peak-like feature at intermediate Q. These indicate formation of lamellar aggregates that are correlated over the distance $D^* = 2\pi/Q^*$, where Q^* represents the peak position. The scattering pattern measured at KWS-3 from the 9000 OBC follows a steep power law ($p = 4$) and terminates in a Guinier-like regime where the commencing of a Q^{-1} power law, and thus the presence of micrometer-size one-dimensional structures, may be presumed. On the other hand, the Q^{-2} scattering profile from the 9007 OBC lamellar structures that extends over the entire Q-range explored is an indication that the lateral extension of the lamellae exceeds 1 µm.

Taking into account the observed scattering features and the crystalline-amorphous polymer configuration, the model analysis of the lamellar structures was done in terms of the core-brush two-dimensional form factor combined with the paracrystalline structure factor [2]. The fits yielded for 9000 and 9007 OBCs the average thickness of the lamellar crystals d (around 120 Å for both materials), the average distance between the crystals D* (900 Å and 1500 Å, respectively) and the average polymer density in the amorphous brush region (0.15 and 0.33). An average thickness a = 0.8µm of the lamellar stack in the case of the 9000 OBC was obtained from the one-dimensional Guinier analysis [3] of the focusing-SANS data. The optical micrographs revealed the details of the polymer morphologies at micrometer scale. Figure 2 shows that the OBCs form macro-aggregates about 10-15 µm in size resembling semi-crystalline spherulites. The typical features of fibrillar spherulite (the "Maltese-cross" [6]) are clearly visible in the inset of figure 2.

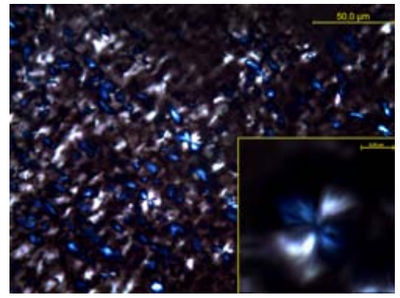

Figure 2: Optical micrographs of aggregates formed in dodecane solution of 9000 OBC (crossed polarizers microscopy); the inset presents a polymer spherulite (scale bar 5 µm).

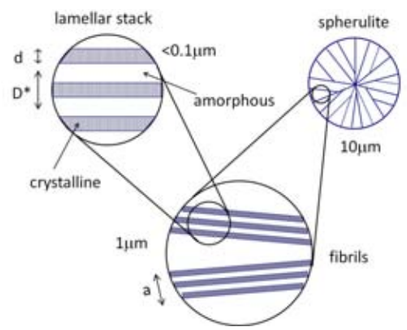

Figure 3: Schematic representation of the OBCs morphology in solution and characteristic structural parameters.

Following the interpretation of scattering features explored over a wide Q-range by different SANS techniques and microscopy observations the hierarchical morphology (fig. 3) of the new crystalline-amorphous olefin block-copolymers in solution could be fully understood: the crystallization of the hard blocks yields stacks of alternating crystalline lamellae and amorphous regions; these structures evolve at micrometer scale in long fibrils which grow up and give further rise to large-scale spherulites.

[1] D.J. Arriola et al., Science, 312 (5774), 714 (2006).
[2] A. Radulescu et al., Adv. Polym. Sci., 210, 1 (2008).
[3] A. Radulescu et al., J. Pol. Sci. B: Pol. Phys., 49 (2), 144 (2011).
[4] A. Radulescu and A. Ioffe, Nucl. Instrum. Meth. A, 586 (1), 55 (2008).
[5] G. Beaucage, J. Appl. Crystallogr., 29 (2), 134 (1996).
[6] J.H. Magil, J. Mater. Sci., 36 (13), 3143 (2001).

Confined polymer dynamics on clay platelets

X. Frielinghaus[1], M. Brodeck[1], O. Holderer[2], H. Frielinghaus[2]

[1]Forschungszentrum Jülich GmbH, Institut für Festkörperforschung, Jülich, Germany
[2]Forschungszentrum Jülich GmbH, Jülich Centre for Neutron Science at FRM II, Garching, Germany

The structure and dynamics of poly (ethylene oxide) adsorbed on dispersed clay platelets are investigated by **s**mall **a**ngle **n**eutron **s**cattering (SANS) and **n**eutron **s**pin **e**cho spectroscopy (NSE). The intermediate scattering function has a mobile contribution described by the Zimm theory, and an immobile contribution which is constant within the time window. The immobile fraction as a function of the scattering vector Q is described by a Lorentz function, from which a localization length is determined.

Nanocomposites consisting of clay and polymer are produced by different methods, depending on the desired raw materials. Different degrees of dispersions are known, ranging from stack dispersion over intercalation to full exfoliation. Usually, the most homogenous state is preferred for the application. One very successful path for natural clays and poly (ethylene oxide) is the intercalation from solution. Here, the two components are dissolved in water independently, and then the solutions are mixed, and finally dried at low pressure and/or elevated temperature. Thus, the states after mixing during the concentration are of principal interest. Another aspect of polymers in the presence of solid clay particles is the confinement which leads to different structural and dynamic behaviour of the polymer. In particular, the neutron spin echo measurements are the first of their kind for non-chemically bonded polymers at hard surfaces. This technique is highly favourable because it aims at the right length scale of polymers.

Experiments at KWS-2 and J-NSE

SANS experiments have been performed at the KWS-2 instrument at the FRM II neutron source. Three different dispersions with 6 % pure clay, and polymer additions of 4 and 8 % have been investigated (fig. 1). Summarizing ref. 1, we found: The 6 % clay dispersion is saturated, and so about 5 % of the clay is found in stacks while only 0.85 % are free clay platelets (in agreement with the gelation point). The free clay particles attract 0.50 and 0.58 % of the original 4 and 8 % polymer, which results in a diffuse clay surface (with power laws $Q^{-2.24}$ and $Q^{-2.46}$ at $Q > 0.06$ Å^{-1}). NSE experiments have been carried out at the J-NSE spectrometer at the FRM II research reactor. The intermediate scattering function S(Q,t)/S(Q,0) of the 4 % sample is depicted in figure 2. At high $Q > 0.05$ Å^{-1} the fractal nature of the clay platelets appears ($Q^{-2.24}$), and so dynamics of the polymer decoration are observed. The scattering function is not fully relaxed at Fourier times of 30 to 40 ns (even at $Q = 0.15$ Å^{-1}). This leads us to the model with two modes, one of which

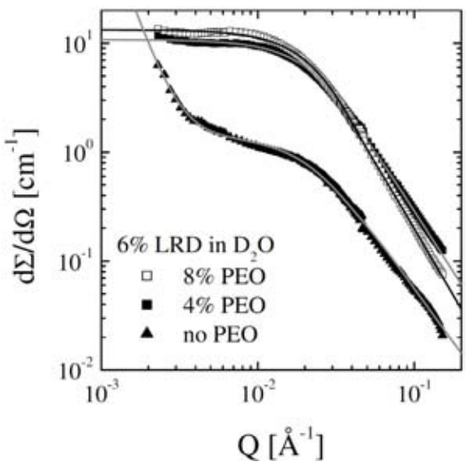

Figure 1: Static macroscopic cross section of 6% LRD in aqueous solution with 0, 4, and 8 % PEO. The solid lines describe model fits with the Beaucage function and describe isolated clay particles with polymer decoration.

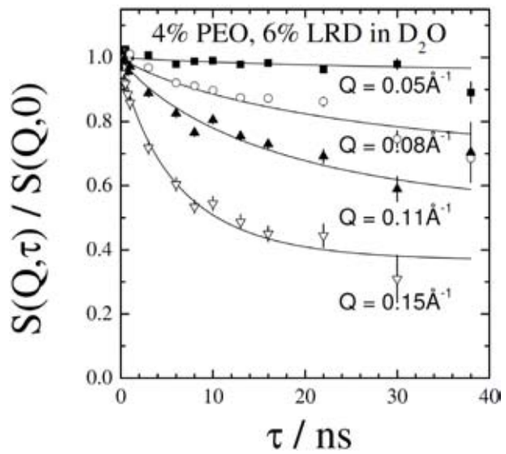

Figure 2: Intermediate scattering function of a clay dispersion with 4 % polymer. The relaxation curves show plateau values dependent on the scattering vector Q. Solid lines are described by eq 1.

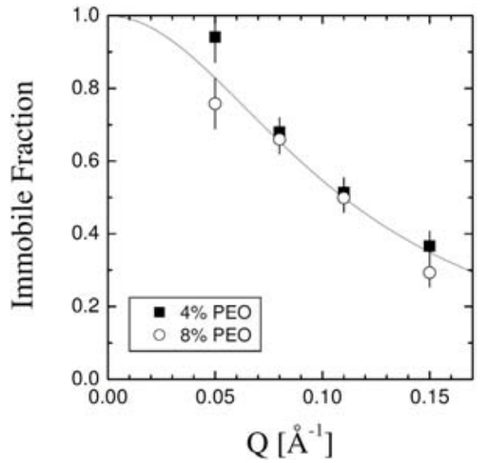

Figure 3: Immobile fraction as a function of the reciprocal scattering vector Q.

describes a free chain in solution (Zimm modes) and the other tightly bound chains, according to:

$$\frac{S(Q,t)}{S(Q,0)} = (1 - f_{(Q)}) \cdot \exp(-(\Gamma_{(Q)} \cdot t)^{\beta}) + f_{(Q)} \quad (1)$$

The Zimm modes are simply described by a stretched exponential function with a fixed exponent $\beta = 0.85$. The relaxation rate Γ and the immobile fraction f(Q) are assumed to be Q dependent, and therefore fitted independently.

Length scale dependent movements

The immobile fraction f(Q) of the polymer is plotted vs. Q in figure 3. Depending on the considered length scale, a certain amount of polymer appears to be attached to the clay particles. At large length scales the whole polymer does not move with respect to the clay, while at smaller length scales movements of the polymer loops become visible. Such length scale dependent movements are often described by a Lorentz curve $f(Q) = (1+\Xi^2Q^2)^{-1}$ [2]. For both polymer concentrations, we obtain the same localization length of $\Xi = 9$ Å. For the static SANS measurements, the polymer decoration appears as a diffuse surface. Only tedious contrast variation SANS measurements might unravel the static structure independently.

In this article we discussed the dynamics of surface bound polymers. The polymer could be described by two fractions: one immobile fraction bound to the clay, and one mobile fraction with rather ideal dynamics of a chain in solution. The immobile fraction f is dependent on the scattering vector Q according to the highlighted spatial region which results in a localization length of 9 Å.

Figure 4: The small angle scattering facilities KWS-1 and KWS-2.

[1] X. Frielinghaus et al., Langmuir, 26 (23), 17444 (2010).
[2] E. Philippidi et al., Langmuir, 23 (9), 5139 (2007).

Near-surface structure of a microemulsion

M. Kerscher[1], P. Busch[2], S. Mattauch[2], H. Frielinghaus[2], D. Richter[1,2], M. Belushkin[1,3], G. Gompper[1]

[1]Forschungszentrum Jülich GmbH, Institut für Festkörperforschung, Jülich, Germany
[2]Forschungszentrum Jülich GmbH, Jülich Centre for Neutron Science at FRM II, Garching, Germany
[3]École Polytechnique Fédérale de Lausanne, School of Basic Sciences, Lausanne, Switzerland

A planar hydrophilic wall induces a lamellar order adjacent to the wall, while the bulk structure is disordered, bicontinuous. This structure is characterized and compared on the basis of computer simulations, neutron reflectivity, and grazing incidence small angle neutron scattering experiments. Characteristic lengths are obtained for the lamellar decay and for the beginning of the bicontinuous structure. From the computer simulations an intermediate structure formed by perforated lamellae is found, while experimentally these are hardly distinguishable from the bicontinuous structure.

For the enhanced oil recovery, aqueous surfactant systems are often applied as fluids for various reasons. The cracking fluid must be highly viscous to deposit the pressure energy in the sand stone. In contact with oil, the fluid forms low viscosity microemulsions, which facilitates the oil production after the application. From this example it becomes clear that surfactant systems adjacent to walls and in porous media are highly interesting for the application. The influence of the wall on the microscopic structure of a microemulsion will help to understand the flow properties of the fluid in a porous medium. Lamellar structures parallel to the walls may lead to finite slip lengths and finally to a facilitated flow.

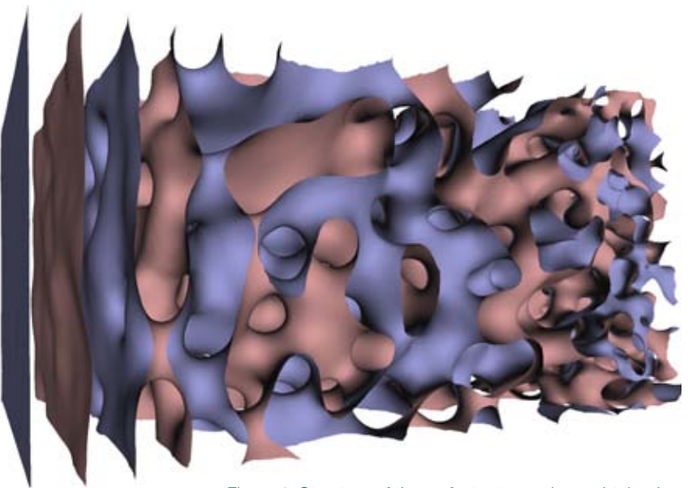

Figure 1: Structure of the surfactant monolayer obtained in a computer simulation. Lamellar order is induced by the hydrophilic surface on the left (surface not shown). The order decays into the volume until the bicontinuous bulk structure is reached. A lamellar structure perforated by passages appears in the intermediate region.

Computer simulations

The computer simulations are based on a Ginzburg-Landau theory with extended terms for the selective hydrophilic surface. A real space example structure is given in figyure 1, while for the simulation details the reader is directed to [1]. The induced lamellar structure can clearly be distinguished from the bulk structure. The perforated lamellar structure is found in between, and can be proven by cuts in parallel to the surface.

Reflectivity curves are obtained from the reflectometer TREFF/NOSPEC at the neutron source FRM II. This method probes the scattering-length density profile along the film normal. Example curves are shown in figure 2. One observes the lamellar order indicated by the correlation peak at $Q_z \approx 0.03$ Å^{-1}. A scattering length density profile is obtained in parallel which compares well with the simulated lamellar structure near the surface. The decay length is 300 Å. At this stage the understanding is based on laterally averaged structure. The realization of the lamellar decay is not resolved by reflectivity experiments, and the bicontinuous structure appears homogeneously.

Varied scattering depth

Grazing **i**ncidence **s**mall **a**ngle **n**eutron **s**cattering experiments (GISANS) were obtained from

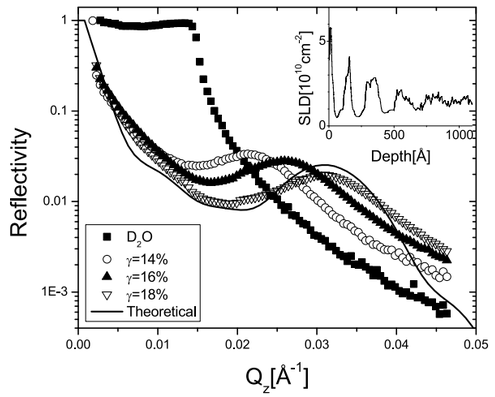

Figure 2: Reflectivity curves of D_2O and samples with different surfactant concentrations γ. The continuous line bases on the Parratt algorithm for the simulated structure. The inset shows the real-space scattering length density profile for the γ = 0.18 sample based on the Parratt algorithm.

KWS-2 at the research reactor FRM II. Example scattering patterns are shown in figure 3. This example is the first of its kind where the scattering depth was varied over a wide range for neutrons. It was achieved by not only varying the incident angle, but also by varying the scattering length density of the overall microemulsion. To a first approximation the scattering depth arises from an exponentially decaying evanescent wave which illuminates the sample with different intensities, while the outgoing, scattered wave is at such high exit angles that refractive processes are negligible. For small scattering depths the lamellar structure dominates the scattering, while at high scattering depths the bicontinuous microemulsion dominates the scattering pattern. From the intensities of the two contributions one obtains a depth of ca. 400 Å from which the isotropic structure could be found. The scattering experiments cannot distinguish between the perforated lamellae which scatter rather isotropically and the bicontinuous structure because the domain spacing is rather similar. At this point the simulation gives clearer hints for the perforated lamellae.

Experiment and simulation

In summary we found good agreement between experiments and simulation. The laterally averaged structures agree very well with reflectivity experiments and a decay length of 300 Å (i.e. 1.5 double layers) is found. The perforated lamellar structure is an intermediate structure between the perfect lamellae and the bicontinuous structure, and is only clearly indicated by the simulations. The GISANS experiments find the beginning of the more isotropic structure (i.e. the perforated lamellae) at a depth of ca. 400 Å. The identified induced lamellar order might facilitate the flow along the surface, which is about to be proved in flow experiments.

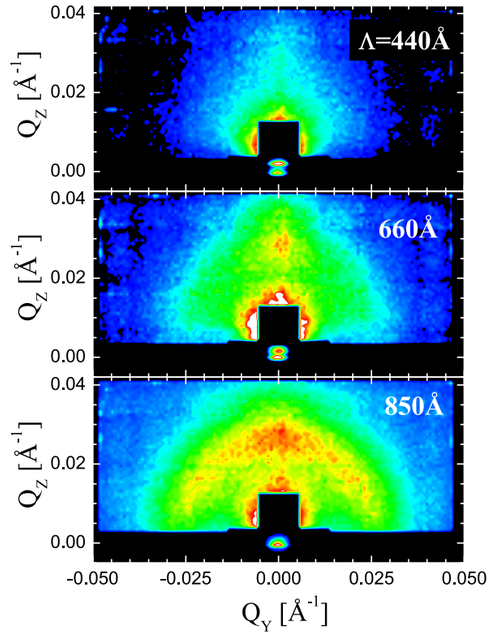

Figure 3: Typical GISANS patterns at different scattering depths Λ. At 440 Å the lamellar Bragg peak is weakly indicated, and a strong surface scattering around the origin superimposes. At 660 Å the Bragg peak is clearly visible, and an isotropic ring is indicated. The isotropic correlation peak dominates at 850 Å.

[1] M. Kerscher et al., Phys. Rev. E, (R), 83 (3), 030401 (2011).

Solvent distribution in block copolymer thin films

A. Sepe[1], E. T. Hoppe[1], D. Posselt[2], J.-F. Moulin[3], D.-M. Smilgies[4], C. M. Papadakis[1]

[1]Technische Universität München, Physik Department E13, Garching, Germany
[2]Roskilde University, Department of Science, Systems and Models, Roskilde, Denmark
[3]Helmholtz-Zentrum Geesthacht, Outstation @ FRM II, Garching, Germany
[4]Cornell University, Cornell High-Energy Synchrotron Source (CHESS), Ithaca (NY), USA

Diblock copolymer thin films form nanostructures by self-assembly. However, the usual preparation methods often result in defects which hamper the application. Solvent vapour treatment is frequently used to anneal such defects. The aim of the project is to determine the distribution of solvents in lamellar poly(styrene-*b*-butadiene) (P(S-*b*-B)) thin films in dependency on the selectivity of the solvent towards PS and PB. **T**ime-**o**f-**f**light **n**eutron **r**eflectometry (TOF-NR) at the instrument REFSANS (fig. 3) together with the use of deuterated solvents enables us to determine the asymmetry of the lamellae upon swelling and thus the distribution of the solvent.

Block copolymer thin films

Nanostructured block copolymer thin films find a number of applications, especially as templates for structuring inorganic materials, which may be used as optical elements or data storage devices [1]. For this reason, it is necessary to promote defect-free structures. However, the self-assembly process during film preparation introduces defects and multi-domain structures, especially during the fast spin-coating process. Solvent vapour treatment is a commonly used technique to anneal defects present in block copolymer thin films after spin-coating [2]. The solvent enters the polymer film, where it has two effects: It screens the repulsive interaction between the two blocks, and increases the mobility of the two blocks, which is of particular importance in the case of glassy blocks [3]. The selectivity of the solvent with respect to the two blocks is essential for the final morphology and orientation [4]. Regarding the lamellar morphology, both parts of the lamellae will swell equally in the case, where the solvent is non-selective. As a function of the selectivity, the degrees of swelling of the two domains will differ, which affects e.g. the mobility of the two blocks in different ways.

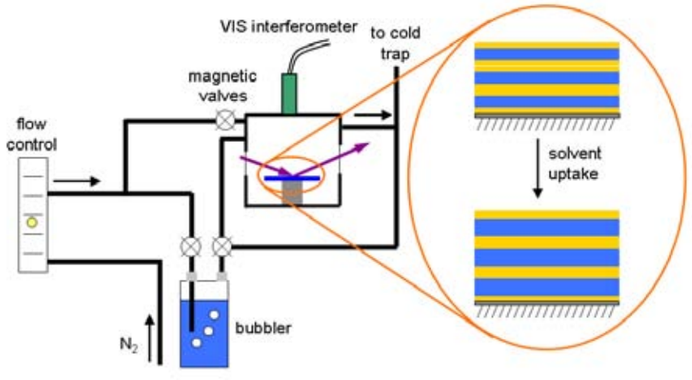

Figure 1: Schematic of the solvent vapour set-up employed for in-situ measurements at the REFSANS instrument together with the thin film morphology in the as-prepared and the asymmetrical swollen state.

Solvent distribution

We aim at determining the solvent distribution in the lamellar structure using fully protonated, lamellar poly(styrene-*b*-butadiene) P(S-*b*-B) diblock copolymer and fully deuterated cyclohexane (CHX-d_{12}) as a solvent slightly selective to the PB block. In equilibrium, the lamellar interfaces of the P(S-*b*-B) film are parallel to the film surface. **T**ime-**o**f-**f**light **n**eutron **r**eflectometry (TOF-NR) allowed us to characterize the lamellar structure of the as-prepared thin film as well as of the solvent-swollen film without moving the sample. Knowledge of the degree of swelling of the PS and the PB parts of the lamellae will enable us to determine the partitioning of CHX-d_{12} among PS and PB and thus give a key to understanding the complex pathway of reorganization of the lamellar stack encountered during solvent vapour treatment [3,5].

We investigated a thin lamellar film from P(S-*b*-B) (28 kg/mol, film thickness D_{film} = 5000 Å) using TOF-NR at REFSANS. NR curves in a q_z-range of 0-0.12 Å^{-1} were measured at four incident angles between 0.22° and 1.14°. The chopper settings provided a primary wavelength band ranging from 2 to 6 Å with a q-resolution of 6 %. The full reflectivity curves were reconstructed from the overlap of the four curves. A custom-made vapour cell based on an aluminium cylinder connected to a solvent bubbler was used to swell the film with CHX-d_{12} vapour (fig. 1). The film thickness and the overall degree of swelling were determined in-situ using a VIS interferometer. The film was measured in the dry state and in the swollen state. Measuring times were 33 h and 48 h for the curves of the as-prepared and the swollen film, respectively.

In-situ neutron reflectometry

The TOF-NR curve of the as-prepared film (fig. 2, lower curve) shows a first-order Bragg reflection at q_z = 0.035 Å^{-1}, evidence of parallel lamellar structures. From the fit of a Lorentzian to this peak, a layer spacing of 180 Å is deduced. No second-order Bragg reflection is observed, in accordance with the system having symmetric lamellae where the PS and the PB parts have the same thickness.

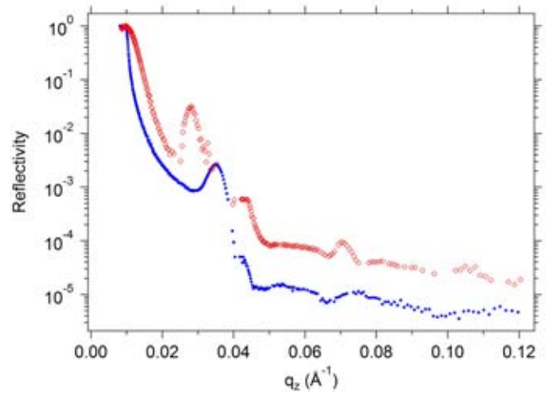

Figure 2: TOF-NR curves of the as-prepared (lower curve, blue) and the swollen P(S-*b*-B) thin film (upper curve, red).

The TOF-NR curve of the film swollen by CHX-d_{12} (upper curve in fig. 2) shows a very pronounced Bragg reflection at 0.028 Å^{-1}, thus at a lower q_z position than in the as-prepared state. This shift reflects the lamellar swelling which amounts to 24 %. Higher-order Bragg reflections are observed. A detailed analysis of their positions and intensities is in progress and will allow us to determine the degree of asymmetric swelling.

We conclude that in-situ TOF-NR experiments, together with the use of deuterated solvents, give detailed insight into the structural changes of the block copolymer thin film during swelling, which are not accessible with other methods. To our knowledge, the partitioning of solvent in the block copolymer mesophase has previously been addressed only theoretically [6]. In-situ TOF-NR experiments are a very promising technique for elucidating the mechanism of gas sensors based on polymer thin films.

Figure 3: The REFSANS reflectometer and its chopper disks.

[1] I.W. Hamley, Progr. Polym. Sci., 34 (11), 1161 (2009).
[2] S.H. Kim et al., Adv. Mater., 16 (3), 226 (2004).
[3] Z. Di et al., Macromol., 43 (1), 418 (2010).
[4] P. Černoch et al., Eur. Polym. J., 43 (4), 1144 (2007).
[5] C.M. Papadakis et al., Langmuir, 24 (24), 13815 (2008).
[6] T.P. Lodge et al., Macromol., 30 (20), 6139 (1997).

The fuel element is changed. The white lid on the left side is the future molybdenum-99 position at the FRM II.

Reactor & Industry

4

The operation of the neutron source in 2010

A. Kastenmüller

Technische Universität München, Forschungs-Neutronenquelle Heinz Maier-Leibnitz (FRM II), Garching, Germany

In 2010 the FRM II was safely operated in four cycles, no. 22b, 23, 24 and 25 for a total of 204 days. All fuel elements were used up to the maximally allowed burnup of 1200 MWd. Cycle no. 24 was stopped due to the sudden malfunction of the motor of the cold neutron source's helium compressor. After the successful and fast replacement of the motor, the cycle was continued. The 25th cycle was interrupted as the temperature of a bearing mounted to the flywheel of a primary cooling pump exceeded a limiting value. After having replaced the bearing, the cycle was continued.

The FRM II delivered a total of 4075,9 MWd in 2010, corresponding to a relative operational availability of 100 % compared to the planned days of operation. The cycles began and ended according to schedule. Only the cycles 24 and 25 had to be interrupted for technical reasons, and the facility was at the scientists' disposal for the number of days planned.

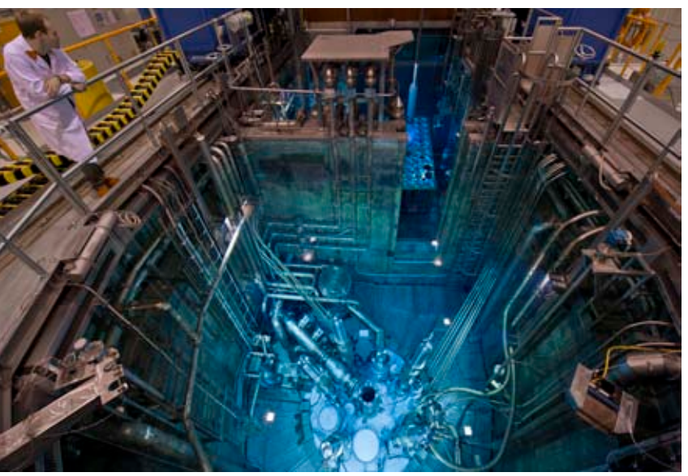

Figure 1: View into the reactor pool. The planned molybdenum-99 facility will be equipped with a thimble, which is one of the key components of the facility and will be inserted into the moderator tank in 2011.

Recurring checkups guarantee safety

A total of 1824 recurring checkups, inspections by independent experts of the regulatory body covering different areas and 91 documented modifications to improve the facility were carried out in 2010. This ensures and improves the high safety standard and availability of the neutron source.

Two reportable incidents occurred in the year 2010. Both were reported in the lowest category N to the authority, the State Ministry for Environment and Health. The incidents were rated in the INES (**I**nternational **N**uclear **E**vent **S**cale) at the level 0, i.e. below-scale events with no safety significance. There was no effect on the safety of the staff or the environment, and no radioactivity was released.

Neutron guide hall east became part of facility

The neutron guide hall east became one of the buildings within the nuclear license of the FRM II in 2010. Work to set up the necessary infrastructure for scientific use was begun when permission had been granted by the authority. Further requirements have to be fulfilled, such as the commissioning of systems in the building and the extension of check lists and recurring checkups.

The licensing process for the ultra cold neutron source has been continued. The FRM II staff presented the status of the design to the authority and its experts. First components have been ordered and the upgrading of the necessary infrastructure confirmed in further detail. For those components of the ultra cold source which are in close vicinity to the reactor core, simulations were made and first tests, such as the conversion of D_2 from a gaseous to a solid state, carried out.

Long maintenance break

In addition to the cold, hot and fission neutron sources, the FRM II also offers another secondary source in the beam tube SR 11. The so-called positron source provides low-energy positrons for material science. The cadmium isotope ^{113}Cd in the beam tube, which generates intense gamma radiation by neutron capture for subsequent conversion to electron-positron pairs, was exhausted after five years of operation and had to be exchanged (see fig. 2). For this, the heavy water moderator tank of the FRM II had to be emptied, dried and filled with light water. This was the main reason for the first long reactor maintenance break since the beginning of the reactor operation in 2004.

As the moderator tank had already been emptied during the maintenance break, there was the possibility of replacing an irradiation thimble in the reactor pool with a longer one for the planned ^{99}Mo-production facility. In future years, the medically important radioisotope molybdenum-99 will be produced at the FRM II. Its decay product, the isotope technetium-99m is used in more than 70 percent of all nuclear medical treatments. The thimble for the ^{99}Mo-production replaces a hitherto unused vertical thimble. Inserting the new, longer irradiation thimble during the maintenance break is a first milestone for the new facility and the planned start of production in 2014 will be realized. In order to design and operate the facility, the licensing process will be started in 2011.

Figure 2: Changing the beam tube of the positron source started in November 2010 and was one of the projects during the long maintenance break.

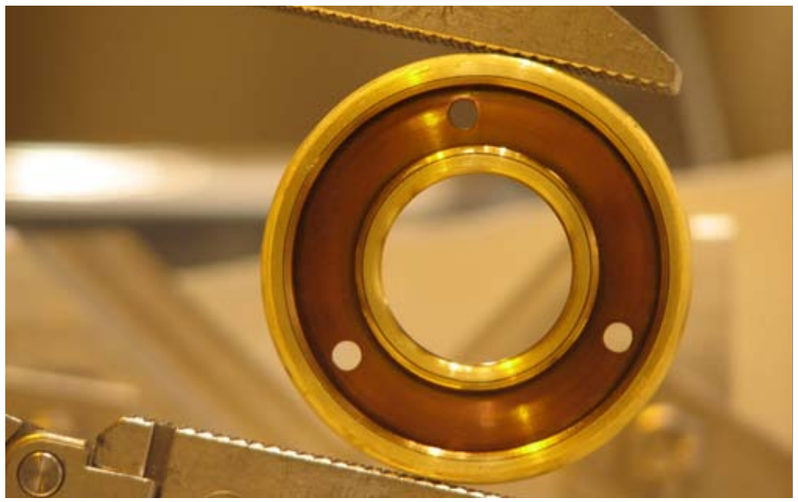

Figure 3: A recurring checkup on a gold plated seal. This sample has been irradiated in high neutron flux to prove its properties. Similar seals are used for beam tubes of the FRM II.

Progress in the development of a 49.9 % enriched UMo dispersion fuel for the FRM II

H. Breitkreutz, J. Sarvas, A. Röhrmoser, W. Petry

Technische Universität München, Forschungs-Neutronenquelle Heinz Maier-Leibnitz (FRM II), Garching, Germany

The coupled calculation scheme X², that has been developed in the past years, has been verified and was successfully used to calculate scenarios for a new fuel element for the FRM II, using medium enriched (MEU) UMo dispersion fuel. First steps in the optimization process already show a significant reduction of the flux loss that is expected when the fuel is changed. The loss is now reduced when compared to the current fuel element from 7.7 % as calculated in first calculations to 5.2 %. This has been achieved by shortening the active fuel zone.

Within the framework of the HEU-MEU conversion process of the FRM II, new fuels are being developed and accordingly new reactorphysical calculations have to be undertaken. Since 2007, a new coupled calculation scheme, X², has been developed in this framework. This program system basically consists of three different codes, MCNPX for the neutronics, MonteBurns / Origen2 for the depletion and CFX for the thermal hydraulics. Using these codes, highly detailed 3D calculations are carried out, using only few approximations [1].

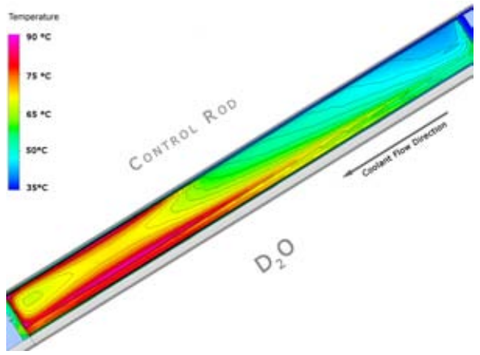

Figure 1: Surface temperatures of the cladding of an UMo dispersion fuel plate. The plate has the same shape as the current fuel plates. In the fuel element, the control rod would be located on the left top side of the plate, the D_2O on the lower right side. Cooling water is entering from top-right. The maximum surface temperature is 90°C at the hotspot in the lower inner corner (very left border of the picture).

The codes

MCNPX is a Monte Carlo neutronic code, "solving" the Boltzmann Transport equation for neutrons and gamma radiation by using random numbers. CFX is a widely used thermal hydraulics code, solving the Navier-Stokes Equation via finite volumes. The codes were coupled using a set of Perl scripts and FORTRAN programs to handle the data transfer between the different applications.

Verification of the program system

The code system was verified by comparing it to the former design calculation system DOT / NBK for the FRM II and also to measured values as far as they were available [1]. The results were generally in good agreement for integral as well as local parameters. Due to the conservative approach that was used in NBK, the traditional calculation scheme yields higher maximum surface heat flux densities and temperatures (fig. 1) at the fuel plate edges.

A rather detailed comparison was performed regarding burn-up and fission products [1,4]. Minor remaining discrepancies with respect to absorber products will be further resolved. The first coupled burn-up calculations which did not use an averaged but a detailed representation of the user installations in the heavy water tank confirmed all relevant former results, especially the slightly asymmetric power distribution. This asymmetry is most pronounced at the beginning of the cycle (5 % in core mid plane). It is reduced to only 2 % at the end of the cycle. Therefore, the slight asymmetry of the burn-up has only negligible influence on the reactivity loss.

A further verification which includes the comparison to a finite elements code, COMSOL, is being performed in cooperation with the Oak Ridge National Laboratory.

MEU: Cycle length of 60 days can be kept

A lower enriched fuel element will in general yield a lower neutron flux due to the increasing parasitic absorption of the higher amount of ^{238}U in the fuel. Parameter studies were performed for the FRM II to minimize the flux loss as far as possible. Unfortunately, the higher absorption in the fuel also leads to less convenient power distribution in the core. In return, the increased precision of the thermal hydraulic calculations and the higher density of the UMo dispersion fuel could allow for a further compaction of the fuel element, which results in an increasing peak neutron flux in the D_2O tank.

In the first calculations for a conversion to UMo dispersion fuel with an enrichment of 49.9 % with same core geometry and same density ratios (see fig. 2), a thermal neutron flux loss of 7.7 % [1] was expected. Preliminary neutronic optimization calculations, which continue the work performed so far [2], showed that the flux loss can be reduced to 5.2 % [3], if the length of the active zone in the fuel element is reduced from 70 cm to 64 cm and the cooling channels are widened from 2.2 mm to 2.4 mm. The current cycle length of 60 days is kept. In this partly optimised case, the ^{235}U inventory is increased from 7.5 kg (current HEU fuel) to 9.7 kg, which is 1 kg less than the amount required in the constant geometry conversion scenario (10.7 kg). The thermal hydraulic investigation of this scenario is still in progress; however, concepts were developed to reduce the heat load in the critical areas, especially in the hot stream filament. An example of these concepts is the usage of a slightly skew density step rather than a strictly vertical step.

The further compaction also poses high qualification burdens for the new fuel, requiring stability up to a maximum fission density of $2.49 \cdot 10^{21}$ cm^{-3}, compared to $2.30 \cdot 10^{21}$ cm^{-3} for the first conversion calculations and $1.98 \cdot 10^{21}$ cm^{-3} for the current fuel element. It as yet unknown if the new fuel will be able to withstand such a high fission density. Burn-up calculations using X² showed that the radioactive waste will increase significantly, including the sevenfold amount of Pu, again confirming earlier results.

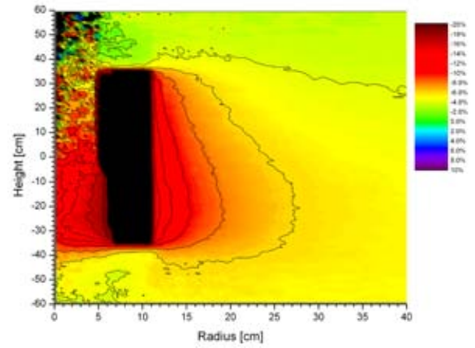

Figure 2: Expected loss of thermal neutron flux for the initial conversion calculations to disperse UMo compared to the current situation.

Other possible scenarios besides the further compaction include an increased reactor power or a longer cycle length [1]. However, the first option in particular imposes very high burdens and is unlikely to be feasible. A longer cycle length will not increase the actual neutron flux but the cycle integrated fluence. This leaves much more room for a thermal hydraulic optimization but increases the demands regarding burn-up even further. In the scenarios calculated so far, a "safety margin" of about 3-5 days of operation is left to allow for further installations in the D_2O tank.

The HEU-MEU group is continuing its efforts to develop a solution for a new, lower enriched core for FRM II, keeping the impact on the users of the reactor as small as possible. Besides the development and qualification of two different fuel candidates, the required calculations and optimisations towards a flux loss as small as possible are performed. The design can benefit especially from the improved thermal hydraulic calculations using up-to-date CFD codes, providing more accurate safety margins.

[1] H. Breitkreutz, PhD Thesis, Technische Universität München (2011).

[2] A. Röhrmoser et al., RERTR (2005).

[3] J. Sarvas, Dipl. Thesis, Technische Universität München (2010).

[4] A. Röhrmoser, RERTR (2010).

Percutaneous medical radiation treatments

B. Loeper-Kabasakal, F. M. Wagner

Technische Universität München, Forschungs-Neutronenquelle Heinz Maier-Leibnitz (FRM II), Garching, Germany

Beam tube SR10 provides unmoderated fission neutrons from a pair of highly enriched uranium plates [1]. Conventional types of radiation generated by clinical linear accelerators are electrons and photons up to 20 MeV. These radiation types have low ionization density, and therefore their biological effectiveness strongly depends on the state of the cells (oxygenation, cell cycle). Fission neutrons display a higher biological effectiveness which is more independent of cell parameters, and allow for a better control of the tumour cell growth. Due to their low mean energy of 2 MeV, the penetration depth is small and therefore, application is restricted to superficial tumours [3].

Between June 2007 and October 2010, 105 treatments were performed, during which 541 fields were irradiated. The majority of patients were looked after at “Klinik für Strahlentherapie des Klinikum rechts der Isar der Technischen Universität München”, to which they were transferred from all regions of Bavaria. The “Universitätsklinik für Strahlentherapie Innsbruck” sends patients who come from Tirol and northern Italy. A close co-operation also exists with “Strahlentherapie, Klinikum Traunstein”. The high ionization density of fission neutrons enhances the clinical effect in a qualitative and quantitative manner. This arises especially after the irradiation of slowly-growing neoplasms like adenoid-cystic tumours of the salivary glands, certain soft tissue sarcoma and malign melanoma of the skin, all of which have a poor response to conventional radiation. The benefit has been demonstrated impressively for the adenoid-cystic tumours in [2]. As the dose rate quickly decreases with depth – at 5 cm depth in tissue, only 50 % of the surface dose can be reached – good results are attainable mainly for tumours situated near to the surface and in the skin.

The enhanced biological effectiveness also appears during neutron therapy of advanced neoplasms which, after multiple cycles of other medical treatments (chemotherapy, conventional irradiations) no longer respond to these methods. This explains the main application of fission neutrons in palliative therapy. In this situation it is also of great advantage that reactions are already visible after 1 or 2 irradiations (fractions), and that generally only 3 to 5 fractions are necessary.

Neutron medical treatment

The beam of the horizontal tube SR10 has a maximum area of 30 x 19 cm (W x H). The therapy fields are mostly smaller and formed by a multi leaf collimator which is adjusted individually to the tumour. The position of the patient on the irradiation couch is adjusted in such a way that the tumour region is sufficiently covered by a light projection which simulates the neutron beam (fig. 1 middle). The duration of the irradiation is determined by the prescribed radiation dose and, to a lesser extent, by the field size; in average it amounts to three minutes per field. The irradiation itself cannot be felt. One treatment usually consists of three to five irradiations (fractions) allocated over on 2 to 3 weeks.

Figure 1: Breast cancer before (left) and after (right) treatment with neutron radiation. The tumour lesions have completely disappeared after the treatment. The light projection and laser markers depict (middle) the radiation field.

In 2010, 117 fields on 25 patients were irradiated on 37 days. The female patients (38 %) mostly suffered from skin and chest wall metastases of mammary carcinoma (fig. 1 left). Another 20 % of the patients had squamous cell carcinoma in lymph nodes, which stem either from metastases of H&N tumours or primarily from the skin. 17 %, 9 % and 8 % of the patients had indications of the above-cited Malign Melanoma, Adenoid-Cystic Carcinoma (ACC), and Soft Tissue Sarcoma, respectively (see fig. 2).

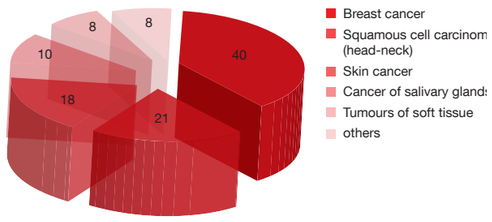

Figure 2: Numbers of different tumours treated at the MEDAPP facility at the FRM II since 2007.

Side effects similar to conventional irradiation

Participating therapists reported that about 70 % of the patients clearly benefited from the neutron medical treatment. This is a good result with respect to the lack of alternative treatment possibilities. Because of the low total case numbers, the effectivity can not be quantified statistically. Since 2007, the results were as follows:

- Four patients from MRI with an adenoid-cystic carcinoma of the salivary glands got a primary therapy consisting of surgery followed by 50 Gy photon and 4,5 to 6 Gy neutron irradiation. Up to now, no recurrence has been observed.
- 77 % of the patients with malign melanoma showed a response to the neutrons with more than 50 % complete remission.
- 50 % of patients with advanced mammary carcinoma displayed a response of which 33 % were in complete remission, see fig. 1 right.

Acute side effects are similar to those following after conventional irradiation and were reversible. In two cases since 2007, serious late effects have been observed: One osteoradionecrosis and a symptomatic pneumonia. In both cases, however, the neutron irradiation is not the only possible cause.

More potential in treating inoperable skin cancer

In 2010 also, the results of the combined photon-neutron medical treatments confirmed the administration for the indications cited previously. Moreover, the participating therapists see a so far unexplored potential of neutron therapy in the treatment of mainly inoperable malign melanoma. To this end, dermatologists from nearby universities and clinics are to be contacted in order to consider how conventional therapy options may be improved for malign melanoma by adjuvant neutron radiation. The aim is to establish a prospective study. In future, appointments for irradiation will be offered twice a week (until now, it was 1-2 times). In this way, the dose per fraction will be lower without a considerable prolongation of the total duration of the course. It is expected that side effects can be minimized without reducing the efficiency of the neutron medical treatment.

[1] F.M. Wagner et al., Strahlenther. Onkol., 184, 643 (2008).
[2] J.G. Douglas James et al., Int. J. Radiat. Oncol. Biol. Phys. 46, 551 (2000).
[3] H. Breitkreutz et al., Proceedings of Third European IRPA Congress June 14-16, Helsinki, Finland (2010).

Automated preparation of a ^{188}Re-compound for skin cancer therapy

J. Moreno[1], P. Juntunen[1], M. Harfensteller[1], R. Henkelmann[1], A. Eursch[2], M. Bichlmaier[2]
B. Stöckert[3], T. Nikula[4], O. Buck[4], A. F. Sedda[5], C. Cipriani[5]

[1]ITG Isotope Technologies Garching GmbH, Garching, Germany
[2]GBN Systems GmbH, Buch am Buchrain, Germany
[3]itm OncoBeta GmbH, Garching, Germany
[4]itm Isotope Technologies Munich AG, Garching, Germany
[5]Physical Technologies and New Materials (FM), ENEA, Rome, Italy

A successful therapeutic treatment of **n**on-**m**elanoma **s**kin **c**ancers (NMSC) such as basal cell and squamous cell carcinomas can be accomplished by using external radioactive sources containing a compound labelled with beta emitting radionuclides. An automated production of a compound which contains Re-sulfide particles labelled with the short-lived beta emitting radionuclide ^{188}Re and homogeneously dispersed in a liquid supporting medium has been developed. The automated system will allow the handling of high radioactivity levels.

Skin cancer is the most prevalent cancer worldwide, the most widespread forms being **b**asal **c**ell **c**arcinoma (BCC) and **s**quamous **c**ell **c**arcinoma (SCC). Different treatments are currently used in the therapy of NMSC. There is a general agreement that surgery is the treatment of choice for BCC and SCC However, the surgical option does not guarantee the complete eradication of the tumour site [1,2].

Epidermal radioisotope therapy

The epidermal radioisotope therapy using a beta emitter is achieved by applying a suspension of ^{188}Re-particles in a water soluble polymeric binding matrix on the affected area (REC). The REC is indirectly deposited (fig. 1) on the lesion utilizing a medical foil as a barrier. The matrix then solidifies as a result of evaporation. Thus an external solid and stable source having a homogenous distribution of radioactive particles is formed on the medical foil which is completely removable without contamination after the patient's individual treatment time which averages 30-60 minutes. The REC source contains the beta-emitting radionuclide ^{188}Re, which releases beta particles with a maximum energy of 2.12 MeV and a mean energy of 0.746 MeV. Consequently > 90 % of the beta particles are absorbed within the first 2 mm of the skin, depositing their energy relevant to the tumour invasion depth, and thus providing the necessary radiation dose. In addition, the small component of high energy particle radiation emitted by ^{188}Re, cannot penetrate further than a depth of 11 mm. Moreover, the short half life of ^{188}Re of only 16.7 hours facilitates the handling of the high activity levels required for this skin cancer therapy (Re-SCT) during both production and treatment.

The concept of the treatment was developed by a pioneering group around Prof Cipriani and Dr. Sedda in Rome, Italy. The treatment has been used in a large variety of BCC and SCC forms, ranging from very large tumours to relapsing or recurrent forms and multifocal lesions. Until the present the treatment has been performed in > 1,500 patients and has shown success rates > 85 % after a single treatment [1,2]. Figure 1 shows an example of the treatment of a SCC patient.

Figure 1: Patient with SCC on face, under treatment and after 181 days

The objective of the ITM Group of Companies (www.itm.ag) is to implement an integrated approach towards radioisotope supply covering the full spectrum from radioisotope production to providing new generation radioisotope therapies and integrated application systems. Within this context, the production of the primary isotope ^{188}W at the neutron reactor, the construction of ^{188}W/^{188}Re generators as well as the production of the REC for Re-SCT is included.

Production of ^{188}W/^{188}Re generators

^{188}Re is obtained from a radionuclide generator containing the mother radionuclide ^{188}W, the latter being produced at a high neutron flux reactor. The ^{188}W/^{188}Re generators are produced at ITG and ^{188}Re is routinely eluted for therapeutic radiopharmaceuticals preparations, including the synthesis of Re-S particles. The aqueous ^{188}Re solutions should not contain activities of the longer-lived parent ^{188}W (breakthrough). This parameter is monitored in all eluates by gamma spectrometry.

Production of particles labelled with ^{188}Re

For the production of ^{188}Re-sulfide particles (Re_2S_7), large activities of up to 100 GBq of ^{188}Re per production batch are required. Hence, it is necessary to carry out relevant processes in a hot cell equipped with Pb shielding for handling high activity levels under automated operations (fig. 2). The chemical technological scheme can be conveniently represented in two steps: synthesis of the Re-S particles and their mixing or dispersion in a polymeric acrylic matrix. For the first step different components are needed: ^{188}Re from the ^{188}W/^{188}Re generator, Re (VII) as perrhenate carrier (stable rhenium) solution, a source of hydrogen sulfide (thioacetamide = TAM) for the precipitation of Rhenium as Re_2S_7, a mineral acid solution to enable the decomposition of TAM, and other ingredients which influence the size of the particles and the chemical yield. The second stage consists of mixing the particles with an acrylic based polymeric matrix in the presence of small quantities of an organic solvent in well defined proportions to get a homogenous dispersion of particles in this medium. The mixture should meet the requirements pre-established for the application: paintability, homogeneity of the radioactive particles in a mass over the surface, thickness of the source, chemical stability, etc.

Figure 2: View of the automated system in the hot cell of the FRM II.

The main chemical operations are carried out in a single reactor. This allows for a compact set up as a reduced number of components are used. In addition, material loss due to surface adsorption of both particles and product is minimized using this type of set-up.

In conclusion, a concept which facilitates automated operations for the production of the ^{188}Re-compound at large activity levels with a high radiochemical yield has been developed. This compact technological process will make the safe production of large quantities of the REC possible, creating a new generation of non-invasive skin cancer therapy (itm Rhenium-SCT™).

[1] A.F. Sedda et al., Clin. Exp. Dermatol., 33 (6), 745 (2008).
[2] M.G. Fabrini et al., Brachytherapy, 7 (3), 270 (2008).

From the bird’s eye view.

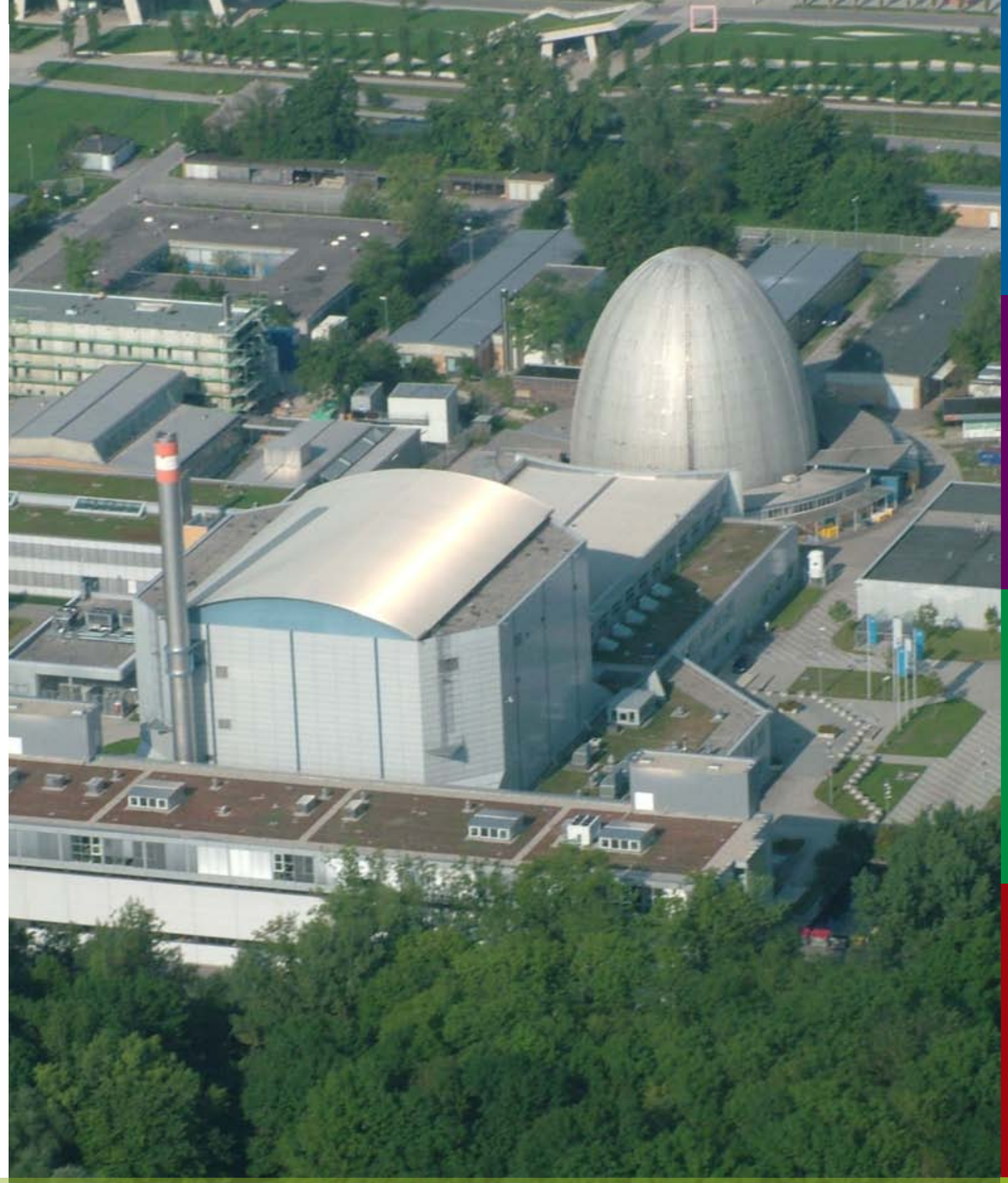

Facts & Figures

5

Events: Schools, workshops, conferences, political visits and industrial expert meeting

A. Voit[1], I. Lommatzsch[1], M. Hofmann[1], J. Peters[1], J. Neuhaus[1], T. Gutberlet[2], R. Georgii[1]

[1]Technische Universität München, Forschungs-Neutronenquelle Heinz Maier-Leibnitz (FRM II), Garching, Germany
[2]Forschungszentrum Jülich GmbH, Jülich Centre for Neutron Science at FRM II, Garching, Germany

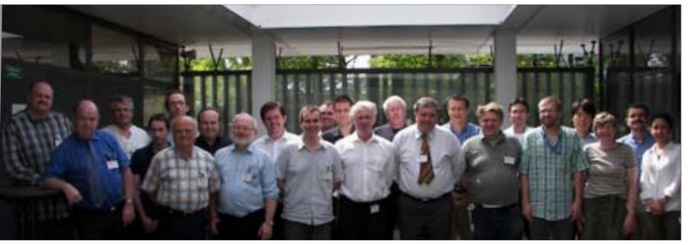

The European NeT-meeting was held at the FRM II, chaired by Michael Hofmann (5th from the right) in June.

Three scientific workshops held at the FRM II in 2010 attracted a considerable number of international researchers to Garching.

NeT-meeting

In June 2010, the FRM II hosted the 17th meeting of the steering committee of the European network on neutron techniques standardization for structural integrity (NeT). The aim of NeT is to develop experimental and numerical techniques and standards for the characterization of residual stresses in structural welds. Dedicated task groups within NeT treat different problems by measuring, modeling and interpreting the results. In June, the 25 scientists from Europe, Japan and Australia reviewed the ongoing round robin exercises and discussed further projects. A tour of the neutron source crowned the meeting.

International workshop on sample environment at neutron scattering facilities

High pressure, magnetic fields and extreme temperatures - these were the topics at the international workshop on sample environment at neutron scattering facilities (SE@NSF), which took place in Garching. During the workshop, the 60 participants from ten different nations also visited the laboratories of the sample environment at the neutron guide hall west of the FRM II.

The workshop was continued at a hotel situated in Herrsching, near lake Ammersee. The experts from 14 different facilities reported on their experiences in more than 20 talks and a poster session. Cryogenic-liquid free refrigerator systems were discussed in a special session.
The SE@NSF meets biannually at different locations. The 2010 meeting in September/ October was organized by Jürgen Peters, head of the FRM II sample environment. For the first time, colleagues from Japan and Korea attended the workshop, which indicates the increasing reputation of the SE@NSF.

Trends and perspectives in neutron scattering in magnetism and correlated electron systems

For the second time, the Jülich Centre for Neutron Science organized the workshop on “Modern Trends and Perspectives in Neutron Scattering” in October 2010. The topic was the investigation of magnetic phenomena and correlated electron systems. Some 80 scientists from Europe, the United States, Japan, China and Australia took part in the meeting in Bernried on lake Starnberg. The emphasis of the invited talks

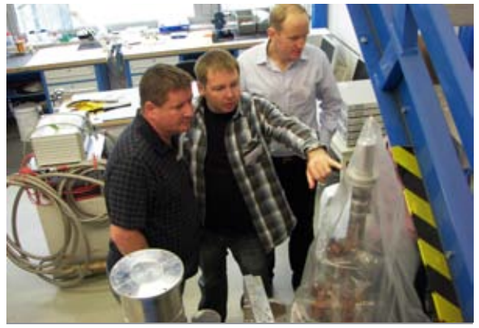

At a tour of the FRM II, the participants of the sample environment workshop explored the laboratories in the neutron guide hall west.

Enthusiastic students with research and large instruments (here: Diffuse scattering neutron time of flight spectrometer DNS) at the JCNS lab course held annually at the FRM II

was on pnictides and multiferroics. Furthermore, new materials, sample preparation and novel instrumentation were discussed. A poster session, a visit to the monastery Benediktbeuern and a tour of the FRM II concluded the meeting.

14th JCNS lab course

60 students had the opportunity to join the JCNS Lab Course in Garching in September. Following the theoretical part of the course had been held in Jülich, the practical sessions, including measurements at five different instruments, were performed at the neutron source FRM II. The hands-on experiments were also ideal for students whose background was in chemistry or biology. Groups of five students discussed the measured data with the instrument scientists and a tutor. Foreign students were supported via travel grants, and half-board accommodation was free for non-locals.

The JCNS workshop on magnetism and correlated electron systems took place at Bernried, south of Munich.

“Fortgeschrittenenpraktikum”

Practical training for undergraduate students of the Technische Universität München was continued in the summer of 2010. Some 30 participants joined the practical of the “Fortgeschrittenenpraktikum” at the FRM II. Each student had the opportunity to perform two different experiments at two instruments out of ten (STRESS-SPEC, PUMA, SPODI, RESI, HEIDI, J-NSE, TOFTOF, SPHERES, RESEDA and KWS-2). At the end of the course, the students were required to write a report on their results and give a presentation in a colloquium.

JCNS school on data analysis

In April, the first school on data analysis was offered to users and instrument scientists who wish to use, or use the program FRIDA. 20 scientists from various universities and research centres in Europe took up the invitation of Joachim Wuttke, instrument scientist at the backscattering spectrometer SPHERES. After a basic introduction to neutron scattering, the participants reduced and analysed data using the programs SLAW and FRIDA.

Colloquium in honour of Dr. Tasso Springer

The JCNS and the FRM II arranged a celebration on the occasion of Tasso Springer's 80th birthday in October 2010. As one of the forefathers of the neutron source in Garching, Tasso Springer is still well known and very popular. Due to ill health, the celebratee was not able to attend the colloquium held in his honour, which attracted around 90 guests. The invited speakers, Thomas Thurn-Albrecht from the university of Halle-Wittenberg and Gero Vogl from Vienna, reviewed Tasso Springer's research with their presentations on "Do we need polymer physics in order to develop better solar cells?" and "Neutrons, men and ideas following the tracks of change". The colloquium ended with a Bavarian dinner in the foyer of the Physics Department.

VDI expert forum

The pros and cons of different methods for nondestructive investigations were discussed at the 3rd expert forum of the FRM II and the advisory board for "Application Oriented Nondestructive Materials and Component Testing" of the German Engineers Association (VDI) in April. 60 representatives from both business and academia joined the meeting in the faculty of mechanical engineering at the Technische Universität München in Garching. The one-day meeting, chaired by Ralph Gilles, offered eight lectures and a variety of posters comparing laboratory methods with neutron scattering. The presentations can be found at www.frm2.tum.de/aktuelles/veranstaltungen/archive/vdi-expertenforum-080/index.html.

The auto manufacturer Ford examined a car door using different imaging methods such as ultra sound, thermography, x-ray and neutron radiography. The aim of the study was to detect intentionally introduced defects as inhomogenous distribution of glue in the car door, which can cause corrosion. Radiography using neutrons at the instrument ANTARES helped develop a detailed analysis of the door, as the hydrogen containing glue caused a higher contrast than other methods.

In further talks, overviews of ultrasonic and thermographic methods were given. Another presentation referred to the moisture measurements in aircraft, which were also undertaken with the help of ANTARES. Furthermore, using the FRM II instrument STRESS-SPEC, the inner stresses of a welded steel tube were investigated. In addition, the question of how to validate and interpret the results of nondestructive materials testing was discussed in a talk. The last session presented the testing of radiation damage on electronics induced by fast neutrons at NECTAR and thermal neutrons at ANTARES. In a final panel discussion, chaired by Heinz Voggenreiter, the different aspects of nondestructive testing were summarized and reviewed.

Many scientists used the poster session of the VDI expert forum to present their industrial applications to the business partners.

At a tour of the FRM II, the participants of the VDI expert forum got an impression of the instruments in the experimental hall.

IAEO Director General, Yukiya Amano (r.), and the Bavarian Minister for Science, Wolfgang Heubisch, visited the FRM II in October. Mr. Amano referred to the neutron source as „one of the most modern nuclear facilites in Europe with robust safety and security features".

IAEA Director General visits FRM II

In October 2010, Yukiya Amano, the Director General of the International Atomic Energy Agency (IAEA), paid his first visit to Germany, the neutron source FRM II being his initial destination. He referred to the FRM II as "one of the most modern nuclear facilities in Europe with robust safety and security features ". Mr. Amano was accompanied by the Bavarian State Minister for Science, Wolfgang Heubisch, the president of the TUM, Wolfgang Herrmann, and the directors of the neutron source. Minister Heubisch welcomed the important visitor "at the neutron source with the broadest spectrum of applications in the world".

Signing the contracts. Front row from left: Thomas Frederking (HZB), Ulrich Krafft (FZJ), Wolfgang A. Herrmann (TUM), Anke Kaysser-Pyzalla (HZB), Wolfgang Kaysser (HZG), Andreas Schreyer (HZG) ; back row from left: Dieter Richter (FZJ), Karl Eugen Huthmacher (BMBF), Wilhelm Friedrich Rothenpieler (StMWFK), Winfried Petry (TUM), Albert Berger (TUM).

Cooperation agreement

The German Federal Ministry of Education and Research (BMBF) will fund the scientific use of the neutron source Heinz Maier-Leibnitz (FRM II) by German and international researchers to the tune of 198 Mio€ over the next ten years. The Helmholtz Centres Jülich, Berlin and Geesthacht are contributing a further 105.2 Mio€ from their budgets. The agreement was signed in December 2010 by Dr. Friedrich Wilhelm Rothenpieler on behalf of the Bavarian State Ministry of Science and the head of the Department for Basic Research at the BMBF, Dr. Karl Eugen Huthmacher. The cooperation contract itself was also signed by TUM President Wolfgang A. Herrmann, Member of the Board of the Research Centre FZ Jülich, Ulrich Krafft, Scientific Director of the Helmholtz Centre Geesthacht, Wolfgang Kaysser, and Scientific Director of the Helmholtz Centre Berlin Anke Kaysser-Pyzalla.

The contract stipulates that the German Federal Government will finance the scientific use of the FRM II via the Helmholtz Centres with 19.8 Mio€ per year. In addition, the three Helmholtz Centres under the auspices of the Centre in Jülich will invest 10.52 Mio€ annually for neutron research. The contract will run over a period of ten years.

Always by the users' side!

T. Gutberlet[1], I. Lommatzsch[2], U. Kurz[2], B. Tonin-Schebesta[2]

[1]Forschungszentrum Jülich GmbH, Jülich Centre for Neutron Science at FRM II, Garching, Germany
[2]Technische Universität München, Forschungs-Neutronenquelle Heinz Maier-Leibnitz (FRM II), Garching, Germany

For the most part unheralded, the FRM II entered the 6th year of its user operation in 2010. Those first users of the facility in 2005 would probably have difficulty visualizing the two present-day guide halls crammed with some two dozen fully operational world class instruments. The FRM II and JCNS User Office is responsible for granting access to all these instruments to scientists who wish to perform experiments at the FRM II. This behind-the-scenes work is carried out as smoothly and effectively as possible. A new peak was reached when more than 1000 visiting scientists performing experiments at FRM II in 2010. Both institutions, the FRM II and JCNS, make every effort to maintain and improve the possibilities for the current as well as future users.

3rd User Meeting

The User Office invites all users of the FRM II to a User Meeting every 18 months. On October 15th, a few days before the maintenance break, this event took place for the third time. It was a special occasion since it celebrated five years of operation of the FRM II. This was reflected by the scientific director of the FRM II, Winfried Petry, when he extended a warm welcome to the participants. More than 160 registrations, 15 talks and 95 posters proved the facility's successful and growing user operation. The poster session in the afternoon displayed many very detailed and exciting examples of research using neutrons, and, accompanied by Bavarian beer and finger food, led to long and intense discussions among the participating users and scientists of the FRM II into the evening. Everybody is looking forward to the fourth User Meeting in 2012!

The official 3rd FRM II User Meeting photo.

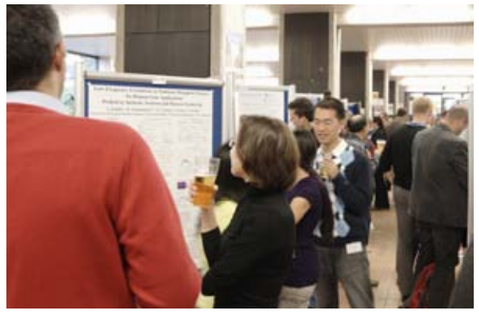

The postersession of the 3rd FRM II User Meeting.

The Blue Book

On the occasion of the 3rd User Meeting, a brand new brochure was presented: With the intention of informing users and those who want to become users, the FRM II published its new booklet dealing with the on-site experimental facilites. The reader finds detailed information, not only on the neutron source in general, but also on the individual instruments arranged by measurement methods. Each instrument is described, examples of possible applications are given and the available sample environment as well as the technical data, is listed. Furthermore, a plan provides the reader with a detailed insight into the structure and dimensions of the instrument.

User Survey

The first half decade was also used as an opportunity to ask users for their opinions, experiences and suggestions regarding their work at the FRM II. This first survey attracted a great response from the users and we would like to thank all of them for their help, answers, and fair comments.

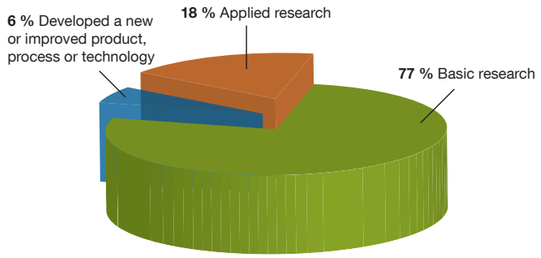

Most of the scientists use their stay at the FRM II for basic research, but nearly 20 % work in the field of applied science, which is probably the highest number in this field at a neutron facility.

The good news was the majority of very positive reactions, which was a great compliment in particular to the scientific staff of the FRM II and the participating institutions. This can possibly be explained by the fact that nearly 75% of the users appreciated the option of access to unique scientific capabilities at FRM II and every second derived benefit from the facilitated collaborative interactions.
On the question, what could be improved to make the stay even more comfortable, the most frequent answer was "establishing a guest house on-site". This task the User Office takes serious and its fulfillment will be one of our future goals.

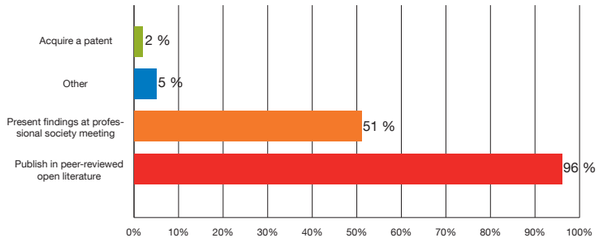

Nearly everyone got great results and planned to publish them in peer reviewed journals. Every second in addition wanted to present the work at conferences and workshops. 2 % of users planned to acquire a patent from the work done.

Statistics

A total of 908 experiments were scheduled at the 26 instruments whereof 7 are operated by the JCNS.

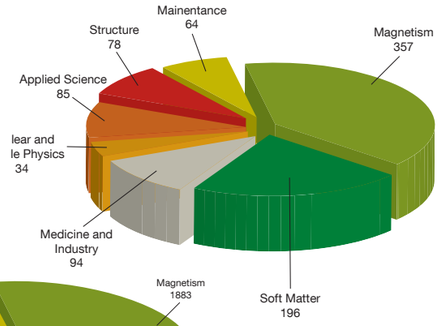

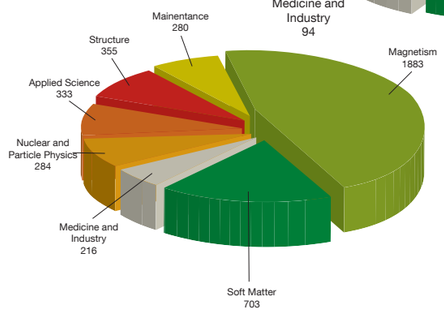

Altogether 4054 days of beam time could be delivered in 2010.

Due to the refurbishment of the positron source and the preparation of the inset for the neutron guides to the instruments in the new guide hall east, the reactor operation was limited in 2010. The reactor was shut down on October 22nd, 2010, having delivered 3.5 cycles with 204 days of beam time for scientific and industrial applications.

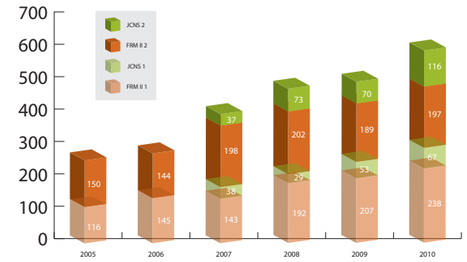

Proposals submitted to the FRM II and JCNS.

A total of 618 proposals were submitted for the proposal rounds of JCNS and FRM II in 2010. The prevailing international scientific reviewing committees picked out the best of these, basing their decisions only on the scientific merit of a proposal. This year, the deadlines for the proposal rounds of FRM II and JCNS were brought into line for the first time. This was the result of the increasing recognition of the scientific options at the FRM II and JCNS.

Attracting pupils and journalists: Public relations and visitors' service

A. Voit[1], U. Kurz[1], B. Tonin-Schebesta[1]

[1]Technische Unviersität München, Forschungs-Neutronenquelle Heinz Maier-Leibnitz (FRM II), Garching, Germany

The FRM II continues to attract visitors. Almost 3000 visited the facility in the course of the year reported on here, including the guests at the long night of science in May. Access to a younger audience was provided via two live video conferences when the instrument MIRA in the neutron guide hall west was presented to grade nine pupils. Another project involving pupils has started: In order to improve the guided tours, the teenagers will develop questionnaires for visitors at the neutron source. In 2010, a number of political visits and scientific highlights, such as the lead coffin from ancient Rome, attracted a number of journalists and led to a number of press clippings.

Long night of science

Another long night of science was held at the Technische Universität München in 2010 after the great success of 2007. This time, May 15th was chosen in order to attract participants at a parallel event: the ecumenical church congress in Munich. The FRM II tours between 16 and 23 h were fully booked within 1.5 hours. At peak times, people queued at the entrance to the physics department. 428 visitors had the good luck to see the neutron source. While waiting, the visitors had the opportunity to watch a film by the company itg, which produces radioisotopes at the FRM II. At the radiation protection booth, Franz Michael Wagner explained the safety features and the natural sources of radiation. Four lectures in the physics department were given by the FRM II: Birgit Loeper-Kabasakal, Winfried Petry, Christoph Hugenschmidt and Ralph Gilles presented the FRM II research in medicine, industry and with positrons to an interested audience.

In total, the number of visitors throughout the year decreased slightly due to the long maintenance break which began in October and blocked the access to the experimental hall for visitors (see fig. 2). 2951 people visited the FRM II in 2010.

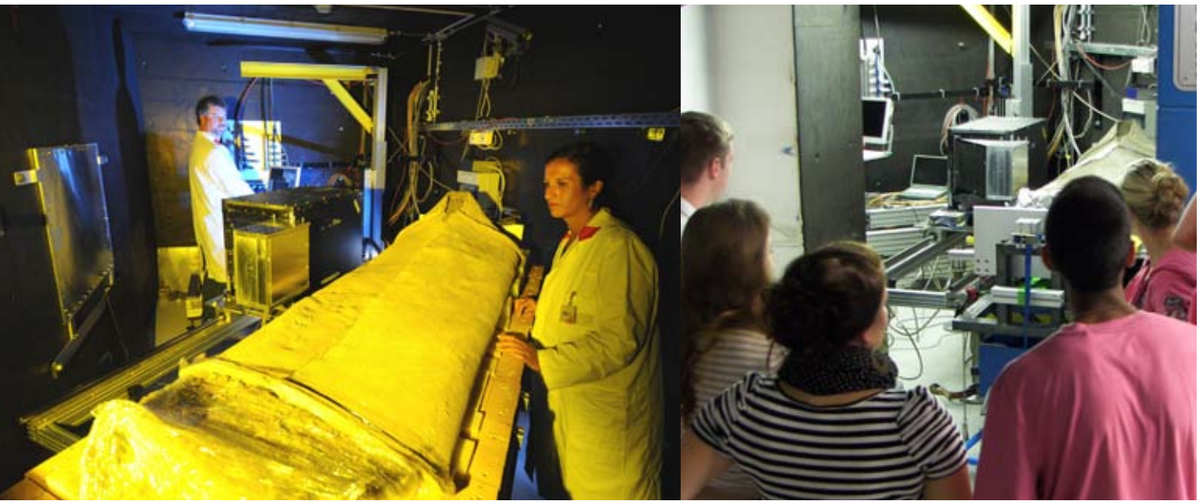

Figure 1: Very attractive to visitors (right image), journalists and scientists (left image): A lead coffin from ancient Rome, which was examined by Anna Gallone (r.) and colleagues at the radiography station ANTARES with Burkhard Schillinger (l.). Unfortunately, the soil within the coffin made it impossible to see any details of bones or other potential contents of the coffin.

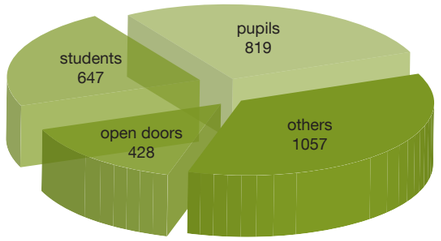

Figure 2: The number of visitors in 2010 amounted to 2951 in total. Due to the maintenance break starting in October, the experimental hall was closed for visitors, reducing the usual number.

Evaluation of visitor tours

Grade ten students from the high school in Garching "Werner von Heisenberg Gymnasium" will evaluate the FRM II guided tours starting in 2011. The project was launched at the end of 2010. The aim is to improve the tours and to develop standards using questionnaires.

Garchinger Reaktor läuft bis 2018 mit atomwaffentauglichem Uran

Unser Brennstoff ist nicht kernwaffenfähig

Ein Gespräch mit Winfried Petry über künftige Pläne beim Forschungsreaktor FRM II

Millionenschwerer Kooperationsvertrag für Forschungsreaktor Garching

Strom schaltet Wirbel

Große Maschinen für kleine Objekte

Verbundforschung in Garching wird mit 10,2 Millionen gefördert

PASSIONE **fisica**

Forscher nutzen Neutronen für die Akku-Optimierung

Gemeinsam Fließen statt einsam Hüpfen - Neutronen untermauern neue Theorie über Bewegung in der Zellmembran

Bayern rüstet gegen medizinischen Notstand auf

Figure 4: Headlines of print and online media in 2010 concerning the FRM II.

Figure 3: Presenting their scientific work to children under the age of 16 via a live video conference (from left to right): Peter Böni, Florian Jonietz, Georg Brandl, Reinhard Schwikowski.

HEU-MEU and lead coffin

The Bavarian prime minister, Horst Seehofer, surprised the media representatives present when he visited Garching in July by announcing that the FRM II will run on highly enriched uranium until 2018. The discussion that followed in the media about the fuel of the FRM II was less prominent than in 2009. Instead, positive topics such as the planned production of radioisotopes and scientific highlights such as the moving magnetic vortices discovered by Florian Jonietz [1] dominated the news coverage in 2010 (fig. 4). The most promising topic for high media interest was the examination of an ancient Roman lead coffin via neutron radiography (fig. 1). Although the results were hard to interpret, a report on the TV show *3sat Nano* and the radio station *Deutschlandfunk* paid homage to the scientists' efforts.

Access for pupils under the age of 16

Due to radiation protection issues, students under the age of 16 do not have access to the neutron source. Using a live video conference (see fig. 3), Peter Böni and his team at MIRA interacted twice with a school class in the "Deutsches Museum" in Munich. The TUM live video conference, organized via the TUMlab, is to be continued in 2011.

[1] F. Jonietz et al., Science, 326 (5958), 1348 (2010).

Publications 2009 and 2010

2009

1. M. A. Abul Kashem, J. Perlich, A. Diethert, W. Wang, M. Memesa, J. Gutmann, E. Majkowa, I. Capek, S. V. Roth, W. Petry and P. Müller-Buschbaum
Array of magnetic nanoparticles via particle co-operated self-assembly in block copolymer thin films
Macromolecules, 42, 6202 (2009).

2. T. Adams, S. Mühlbauer, A. Neubauer, W. Münzer, F. Jonietz, R. Georgii, B. Pedersen, P. Böni, A. Rosch and C. Pfleiderer
Skyrmion lattice domains in Fe_{1-x} Co_xSi
J. Phys.: Conf. Ser., submitted (2009).

3. M. Appavou, G. Gibrat and M. Bellissent-Funel
Temperature dependence on structure and dynamics of Bovine Pancreatic Trypsin Inhibitor (BPTI). - A neutron scattering study
Biochim. Biophys. Acta, 1794, 1398 (2009).

4. J. Arndt, O. Stockert, R. Borth, E. Faulhaber, K. Schmalzl, A. Schneidewind, H. Jeevan, C. Geibel, M. Loewenhaupt and F. Steglich
Do antiferromagnetism and superconductivity coexist in 2 and 10 Ge doped $CeCu_2Si_2$?
J. Phys.: Conf. Ser., 150, 042008 (2009).

5. L. Balsanova, D. Mikhailova, A. Senyshyn, D. Trots, H. Ehrenberg and W. Lottermoser
Structure and properties of α-$AgFe_2(MoO_4)_3$
Solid State Sci., 11, 1137 (2009)

6. B. Bauer, B. Pedersen and P. Gille
Al_4(Cr, Fe): single crystal growth by the Czochralski method and structural investigation with neutrons at FRM II
Z. Kristallogr., 224, 109 (2009).

7. P. Böni, W. Münzer and A. Ostermann
Instrumentation with polarized neutrons
Physica B, 404, 2620 (2009).

8. P. Böni and K. Lefmann
Neutron Optics and Monte Carlo Simulations in NMI3
Neutron News, 20, 26-29 (2009).

9. K. Böning and W. Petry
Test irradiations of full sized U_3Si_2-Al fuel plates up to very high fission densities,
J. Nucl. Mater., 383, 254 (2009).

10. H. N. Bordallo, L. P. Aldridge, P. Fouquet, L. C. Pardo, T. Unruh, J. Wuttke and F. Yokaichiya
Hindered water motions in hardened cement pastes investigated over broad time and length scales
ACS Appl. Mater. Interfaces, 1, 2154 (2009).

11. H. Boysen, I. Kaiser-Bischoff, M. Lerch, S. Berendts, A. Börger, D. Trots, M. Hoelzel and A. Senyshyn
Structures and properties of variously doped Mayenite investigated by neutron and synchrotron powder diffraction
Z. Kristallogr. Suppl., 30, 323 (2009).

12. M. Braden, O. Schuhmann, M. Cwik, M. Kosmala, M. Fernandez-Diaz, M. Meven and A. Cousson
Charge and orbital ordering in layered perovskites.
Acta Crystallogr. A, A65, Abstracts of the 25th European Crystallography Meeting, s 50 (2009).

13. M. Brodeck, F. Alvarez, A. Arbe, F. Juranyi, T. Unruh, O. Holderer, J. Col-menero and D. Richter
Study of the dynamics of poly(ethylene oxide) by combining molecular dynamic simulations and neutron scattering experiments
J. Chem. Phys., 130, 094908 (2009).

14. T. Bücherl, F. M. Wagner and C. Lierse von Gostomski
First steps towards real-time radiography at the NECTAR facility
Nucl. Instrum. Methods Phys. Res., Sect. A, 605, 47 (2009).

15. E. Calzada, F. Grünauer, M. Mühlbauer, B. Schillinger and M. Schulz
New design for the ANTARES-II facility for neutron imaging at FRM II
Nucl. Instrum. Meth., 605, 50 (2009).

16. L. Canella, P. Kudejova, R. Schulze, A. Tuerler and J. Jolie
PGAA, PGAI and NT with cold neutrons: Test measurement on a meteorite sample
Appl. Radiat. Isot., 67, 2070 (2009).

17. H. Chang, M. Zheng, W. Gan, K. Wu, E. Maawad and H.-G. Brokmeier
Texture evolution of the Mg/Al laminated composite fabricated by the accumulative roll bonding
Scripta Mater., 61, 717 (2009).

18. J. Chang, N. Christensen, C. Niedermayer, K. Lefmann, H. Ronnow, D. McMorrow, A. Schneidewind, P. Link, A. Hiess, M. Boehm, R. Mottl, S. Pailhès, N. Momono, M. Oda, M. Ido and J. Mesot
Inelastic neutron-scattering measurement of a magnetic excitation gap in the high-temperature $La_{1.855}$ $Sr_{0.145}$ CuO_4 superconductor: evidence for a field-induced quantum phase transition
Phys. Rev. Lett., 102, 177006 (2009).

19. L. Chang, Y. Su, W. Schweika, T. Brückel, Y. Chen, D. Jang and R. Liu
Neutron polarization analysis on the multiferroic $TbMn_2O_5$
Physica B, 404, 2517 (2009).

20. T. Chatterji, P. Freeman, M. Jiménez-Ruiz, R. Mittal and S. Chaplot
Pressure- and temperature-induced M-3 phonon softening in ReO_3
Phys. Rev. B, 79, 184302 (2009).

21. T. Chatterji, G. J. Schneider, L. van Eijck, B. Frick and D. Bhattacharya
Direct evidence for the Nd magnetic ordering in $NdMnO_3$ from the hyperfine field splitting of Nd nuclear levels
J. Phys.: Condens. Matter, 21, 126003 (2009).

22. T. Chatterji and G. J. Schneider
Low-energy nuclear spin excitations in CoO
Phys. Rev. B, 79, 212409 (2009).

23. T. Chatterji and G. J. Schneider
Anomalous hyperfine interaction in CoF_2 investigated by high resolution neutron spectroscopy
J. Phys.: Condens. Matter, 21, 436008 (2009).

24. T. Chatterji, G. J. Schneider and J. Persson
Low-energy nuclear spin excitations in $NdAl_2$
Phys. Rev. B, 79, 132408 (2009).

25. S. Chi, A. Schneidewind, J. Zhao, L. W. Harriger, L. Li, Y. Luo, G. Cao, Z. Xu, M. Loewenhaupt and P. Dai
Inelastic neutron scattering measure-

ments of a three-dimensional spin resonance in the FeAs-based $BaFe_{1.9}Ni_{0.1}As_2$ superconductor
Phys. Rev. Lett., 102, 107006 (2009).

26. J. Cizek, I. Prochazka, O. Melikhova, M. Vlach, N. Zaludova, G. Brauer, W. Anwand, W. Egger, P. Sperr, C. Hugenschmidt, R. Gemma, A. Pundt and R. Kirchheim
Hydrogen-induced defects in Pd films
Phys. Status Solidi, (c). 6, 2364 (2009)
27. M. Deveaux, S. Amar-Youcef, A. Büdenbender, D. Doering, I. Fröhlich, C. Müntz, J. Stroth and F. Wagner
Random telegraph signal in monolithic active pixel sensors
IEEE (2009).

28. H. Ehrenberg, N. N. Bramnik, A. Senyshyn and H. Fuess
Crystal and magnetic structures of electrochemically delithiated $Li_{1-x}CoPO_4$ phases
Solid State Sci., 11, 18 (2009).

29. G. Festa, C. Andreani, M. P. De Pascale, R. Senesi, G. Vitali, S. Porcinai, A. M. Giusti, R. Schulze, L. Canella, P. Kudejova, M. Muehlbauer, B. Schillinger and A. C. Collaboration
A non destructive stratigraphic and radiographic neutron study of Lorenzo Ghiberti's reliefs from Paradise and North doors of Florence Baptistery
J. Appl. Phys., 106, 074909 (2009).

30. R. Frahm, D. Lützenkirchen-Hecht, M. Jentschel, W. Urban, J. Krempel and K. Schreckenbach
The Miracle of the Electron-Positron Pair Production Threshold
Synch. Rad. News, 22, 28 (2009).

31. R. Frahm, D. Lützenkirchen-Hecht, M. Jentschel, W. Urban, J. Krempel and K. Schreckenbach
Positron-Electron Pair Creation Near Threshold
AIP Conf. Proc., 1090, 554 (2009).

32. J. Francis, M. Turski and P. Withers
Measured residual stress distributions for low and high heat input single weld beads deposited on to SA508 steel
Mater. Sci. Technol., 25, 325 (2009).

33. A. Frei, E. Gutsmiedl, C. Morkel, A. Müller, S. Paul, M. Urban, H. Schober, S. Rols, T. Unruh and M. Hölzel
Density of states in solid deuterium: Inelastic neutron scattering study
Phys. Rev. B, 80, 64301 (2009).

34. H. Frielinghaus, V. Pipich, A. Radulescu, M. Heiderich, R. Hanslik, K. Dahlhoff, H. Iwase, S. Koizumi and D. Schwahn
Aspherical refractive lenses for small-angle neutron scattering
J. Appl. Crystallogr., 42, 681 (2009).

35. M. Frontzek, F. Tang, P. Link, A. Schneidewind, J. Mignot, J. Hoffmann and M. Loewenhaupt
A Generic Phase Diagram for R_2PdSI_3 (R= Heavy Rare Earth)?
J**. Phys.: Conf. Ser.** (2009).

36. R. Garg, A. Senyshyn, H. Boysen and R. Ranjan
Structure of the noncubic phase in the ferroelectric state of Pr-substituted $SrTiO_3$
Phys. Rev. B, 79, 144122 (2009).

37. S. Garny, V. Mares, H. Roos, F. M. Wagner and W. Rühm
Measurement of neutron spectra and neutron doses at the Munich therapy beam with Bonner spheres
Radiat. Meas., accepted (2009).

38. S. Garny, W. Rühm, F. M. Wagner and H. Paretzke
Neutron therapy at the FRM II - calculation of dose inside a Voxel phantom
Transactions: Medical Physics and Biomedical Engineering, World Congress 2009, Sept. 7-12, Munich, Germany (2009)

39. G. Gatta, M. Meven and G. Bromiley
Effects of temperature on the crystal structure of epidote: a neutron single crystal diffraction study at 293 and 1070 K
Phys. Chem. Miner., 37, 475 (2009).

40. J. Gibmeier, J. Kornmeier and M. Hofmann
Neutron diffraction stress analysis of near surface stress gradients of surface treated steel samples
Adv. X-Ray Anal., 52, 279 (2009).

41. R. Gilles, M. Hofmann, Y. Gao, F. Johnson, L. Iorio, M. Larsen, F. Liang, M. Hoelzel and B. Barbier
Probing the relationship of ordering in Nanodomain FeCo alloys with ternary additions using neutron diffraction
Metall. Mater. Trans. A, accepted (2009).

42. J. Guo, T. Bücherl, Y. Zuo, Z. Guo and G. Tang
Comparison of the performance of different converters for neutron radiography and tomography using fission neutrons
Nucl. Instrum. Methods Phys. Res., Sect. A, 605, 69 (2009).

43. F. Hameed, B. Schillinger, A. Rohatsch, M. Zawishky and H. Rauch
Investigations of stone consolidants by neutron imaging
Nucl. Instrum. Meth. Phys. A, 605, 150 (2009).

44. L. W. Harriger, A. Schneidewind, S. Li, J. Zhao, Z. Li, W. Lu, X. Dong, F. Zhou, Z. Zhao, J. Hu and P. Dai
Transition from Three-Dimensional Anisotropic Spin Excitations to Two-Dimensional Spin Excitations by Electron Doping the FeAs-Based $BaFe_{1.96}Ni_{0.04}As_2$ Superconductor
Phys. Rev. Lett., 103, 087005 (2009).

45. W. Häußler and B. Gohla-Neudecker
Diffusive Dynamics in Protein solutions studied by Neutron Spin Echo
C. Chmelik, N. Kanellopoulos, eds., *Diffusion Fundamentals III*, Leipziger Universitätsverlag, Leipzig (2009).

46. J. R. Hervias, M. Hofmann, J. Rebelo-Kornmeier, V. Luzin and M. Elices
Residual Stresses in cold-drawn rods: effect of an alternative treatment
Adv. X-Ray Anal., 52, 747 (2009).

47. K. U. Hess, A. Flaws, B. Schillinger, M. Mühlbauer, M. Schulz, E. Calzada and D. B. Dingwell
Applications of a high to ultra-high resolution neutron computed tomography system for the geosciences
Geosphere, (2009).

48. K.-U. Hess, A. Flaws, A. Gerik, R. Khemaka, M. Mühlbauer, R. Marschallinger, J. H. Kruhl, B. Schillinger and D. B. Dingwell
Analyzing 3D-Structures of Syntectonic Magmatic Rocks: A new Approach Based on High Resolution Neutron Computed Tomography.
EGU General Assembly 2009, held 19-24 April, 2009 in Vienna, Austria, http://meetings.copernicus.org/egu2009, 8562 (2009).

49. K.-U. Hess, A. Flaws, B. Schillinger, B. Cordonnier, M. Mühlbauer, M. Schulz, J. Marti and D. B. Dingwell
Tube pumice kinematics using non-destructive neutron tomography
American Geophysical Union, Fall Meeting 2009, abstract #V13B-2013 (2009).

50. M. Hofmann and R. Wimpory
NET TG1: Residual stress analysis on a single bead weld on a steel plate using neutron diffraction at the new engineering instrument STRESS-SPEC
International Journal of Pressure Vessels and Piping, 86, 122 (2009).

51. D. Holland-Moritz, S. Stüber, H. Hartmann, T. Unruh, T. Hansen and A. Meyer
Structure and dynamics of liquid $Ni_{36}Zr_{64}$ studied by neutron scattering
Phys. Rev. B, 79, 064204 (2009).

52. C. Hugenschmidt, P. Pikart and K. Schreckenbach
Coincident Doppler-broadening spectroscopy of Si, amorphous SiO_2,and alpha-quartz using mono-energetic positrons
Phys. Status Solidi C, 6, 2459 (2009).

53. C. Hugenschmidt, N. Qi, M. Stadlbauer and K. Schreckenbach
Correlation of mechanical stress and Doppler broadening of the positron annihilation line in Al and Al alloys
Phys. Rev. B, 80, 224203 (2009).

54. I. Hurtado, U. Garbe, M. Bamberger and G. Arruebarrena
Texture development in magnesium HPDC alloys
Scr. Mater., (2009).

55. V. Hutanu, M. Meven, M. Janoschek, P. Böni and G. Heger
MuPAD: Test at the hot single-crystal diffractometer HEiDi at FRM II
Nucl. Instrum. Methods Phys. Res., Sect. A, 612, 155 (2009).

56. V. Hutanu, M. Meven, E. Lelièvre-Berna and G. Heger
POLI-HEiDi: The new polarised neutron diffractometer at the hot source (SR9) at the FRM II - Project status
Physica B, 404, 2633 (2009).

57. A. Houben, W. Schweika, T. Brückel and R. Dronskowski
Advanced Nitrides and Neutrons: New Nitridic Itinerant Ferromagnets and the High-performance Time-of-flight Neutron Diffractometer POWTEX
ChemInform, 40, 215 (2009).

58. D. S. Inosov, J. T. Park, P. Bourges, D. Sun, Y. Sidis, A. Schneidewind, K. Hradil, D. Haug, C. Lin, B. Keimer and V. Hinkov
Normal-state spin dynamics and temperature-dependent spin resonance energy in an optimally doped iron arsenide superconductor
Nature Physics online (2009): http://www.nature.com/nphys/journal/v6/n3/abs/nphys1483.html

59. S. Ivanova, A. Senyshyn, E. Zhevcheva, K. Tenchev, V. Nikolov, R. Stoyanova and H. Fuess
Effect of the synthesis route on the microstructure and the reducibility of $LaCoO_3$
J. Alloys Compd., 480, 279 (2009).

60. R. Jungwirth, H. Breitkreutz, W. Petry, A. Röhrmoser, W. Schmid, H. Palancher, C. Jarousse
Optimization of the Si content in UMo/AL(Si) fuel plates
Transactions: RERTR-2009, Nov. 1-5, Beijing, China (2009).

61. T. Jun, F. Hofmann, J. Belnoue, M. Hofmann and A. M. Korsunsky
Triaxial residual strains in a railway rail measured by neutron diffraction
J. Strain Analysis, 44, 563 (2009).

62. S. Kamel, R. Wimpory and M. Hofmann
The Effects of Constraint and Compressive or Tensile Residual Stresses on Brittle Fracture
ASME Conf. Proc., Volume 5: High Pressure Technology; Nondestructive Evaluation Division; Student Paper Competition, ASME, 305 (2009).

63. O. Kirstein, M. Prager and G. Schneider
Rotational dynamics and coupling of methyl group rotations in methyl fluoride studied by high resolution inelastic neutron scattering.
J. Chem. Phys., 130, 214508 (2009).

64. W. Kreuzpaintner, J. Moulin, D. Lott, R. Kampmann, M. Haese-Seiller, M. Störmer and A. Schreyer
Time of flight grazing incidence small angle neutron scattering on Gd nanowires
Eur. Phys. J. E ST, 167, 73 (2009).

65. M. Krott, A. Houben, P. Müller, W. Schweika and R. Dronskowski
Determination of the magnetic structure of manganese carbodiimide with diffraction experiments using polarized neutrons
Phys. Rev. B, 80, 024117 (2009).

66. V. Kršjak, V. Slugen, M. Petriska, S. Sojak and W. Egger
Microstructural study of He-implanted Fe-Cr alloys with the use of conventional lifetime technique and pulsed low energy positron beam
Phys. Status Solidi C, 6, 2339 (2009).

67. M. Krutyeva, J. Martin, A. Arbe, J. Colmenoro, C. Mijangos, G. Schneider, T. Unruh, Y. Su and D. Richter
Neutron scattering study of the dynamics of a polymer melt under nanoscopic confinement
J. Chem. Phys., 131, 174901 (2009).

68. A. Leenaers, S. van den Berghe, F. Charollais, P. Lemoine, C. Jarousse, A. Röhrmoser and W. Petry
Microstructural analysis of ground U (Mo) fuel with and without Si in the matrix, irradiated to high burn-up
Transactions: RERTR-2009, Nov. 1-5, Beijing, China (2009).

69. H. Li, Y. Su, Y. Xiao, J. Perßon, P. Meuffels and T. Brückel
Crystal and magnetic structure of single-crystal La_{1-x} Sr_x MnO_3 (x asymp; 1/8).
Eur. Phys. J. B, 67, 149 (2009).

70. X. Li, H. Gerstenberg and I. Neuhaus
Silicon doping system at the research reactor FRM II
Appl. Radiat. Isot., 67,1220 (2009).

71. C. D. Ling, M. Avdeev, R. Kutteh, V. V. Kharton, A. A. Yaremchenko, S. Fialkova, N. Sharma, R. B. Macquart, M. Hoelzel and M. Gutmann
Structure, phase transitions, hydration, and ionic conductivity of Ba_4 Nb_2 O_9
Chem. Mater., 21, 3853 (2009).

72. X. Lin, H. Gerstenberg, C. Lierse von Gostomski, R. Henkelmann, A. Türler and M. Rossbach
Determination of k_0-values for the reactions ^{94}Zr (n,γ) ^{95}Zr and ^{96} Zr (n, γ) ^{97}Zr-^{97m}Nb by irradiation in highly thermalized neutron flux
Appl. Radiat. Isot., 67, 2092 (2009).

73. I. Major, A. Vorobiev, A. Rühm, R. Maier, M. Major, M. Mezger, M. Nülle, H. Dosch, G. P. Felcher, P. Falus, T. Keller and R. Pynn
A spin-echo resolved grazing incidence scattering setup for the neutron interrogation of buried nanostructures
Rev. Sci. Instrum., 80, 123903 (2009).

74. J. Mayer, K. Schreckenbach and C. Hugenschmidt
Recent development of the PAES set up at NEPOMUC
Phys. Status Solidi C, 11, 2470 (2009).

75. P. Mazzoldi, G. Mattei, L. Ravelli, W. Egger, S. Mariazzi and R. S Brusa
Direct evidence by positron annihilation spectroscopy of defect distributions deeper than R_p in Ar^+ implanted silica glass
J. Phys. D, 42, 115418 (2009).

76. G. McGrady, P. Sirsch, N. Chatterton, A. Ostermann, C. Gatti, S. Altmannshofer, V. Herz, G. Eickerling and W. Schere
Nature of the bonding in metal-silane sigma-complexes
Inorg. Chem., 48, 1588 (2009).

77. G. Meierhofer, P. Kudejova, L. Canella, P. Grabmayr, J. Jochum and J. Jolie
Thermal neutron capture cross-section of ^{76}Ge
Eur. Phys. J. A, 40, 61 (2009).

78. K. Mergia, M. Grattarola, S. Messoloras, C. Gualco and M. Hofmann
Residual Stress Measurements In Mo/CuCrZr Tiles Using Neutron Diffraction
Adv. Mater. Res., 59, 299 (2009).

79. A. Meyer, J. Horbach, O. Heinen, D. Holland-Moritz and T. Unruh
Self-diffusion in liquid titanium: quasi-elastic neutron scattering and molecular dynamics simulation.
Defect Diffus. Forum, 289-292, 609 (2009).

80. S. Meyer, E. Schweda, N. J. M. Meta, H. Boysen, M. Hoelzel and T. Bredow
Neutron powder diffraction study and DFT calculations on the structure of $Zr_{10}Sc_4O_{26}$
Z. Kristallogr., 224, 539 (2009).

81. R. Mole, J. A. Stride, T. Unruh and P. Wood
Non-classical behaviour in an S = 5/2 chain with next nearest neighbour interactions observed from the inelastic neutron scattering of $Mn_2(OD)_2(C_4O_4)$
J. Phys.: Condens. Matter, 21, 076003 (2009).

82. O. Moze, W. Kockelmann, M. Hofmann, J. Cadogan, D. Ryan and K. Buschow
Structural transitions in $RNi_{10}Si_2$ intermetallics
J. Phys.: Condens. Matter, 21, 124210 (2009).

83. S. Mühlbauer, B. Binz, F. Jonietz, C. Pfleiderer, A. Rosch, A. Neubauer, R. Georgii and P. Böni
Skyrmion lattice in a chiral magnet
Science, 323 (5916), 915 (2009).

84. S. Mühlbauer, C. Pfleiderer, P. Böni, E. M. Forgan, M. Laver, U. Keiderling, G. Behr and D. Fort
Morphology of the Superconducting Vortex Lattice in Ultrapure Niobium
Phys. Rev. Lett., 102, 136408 (2009).

85. P. Müller-Buschbaum, E. Metwalli, J. Moulin, V. Kudryashov, M. Haese-Seiller and R. Kampmann
Time-of flight grazing incidence small angle neutron scattering - a novel scattering technique for the investigation of nanostructured polymer films
Eur. Phys. J. E ST, 167, 107 (2009).

86. A. Neubauer, C. Pfleiderer, B. Binz, A. Rosch, R. Ritz, P. G. Niklowitz and P. Böni
Topological Hall Effect in the A Phase of MnSi
Phys. Rev. Lett., 102, 186602 (2009).

87. P. Niklowitz, C. Pfleiderer, S. Mühlbauer, P. Böni, T. Keller, P. Link, J. Wilson, M. Vojta and J. Mydosh
New angles on the border of antiferromagnetism in NiS_2 and URu_2Si_2
Physica B, 404, 2955 (2009).

88. C. Ohms, R. Wimpory, D. Katsareas and A. Youtsos
Residual stress assessment by neutron diffraction and finite element modelling on a single bead weld on a steel plate
International Journal of Pressure Vessels and Piping, 86, 63 (2009).

89. L. Orsingher, A. Fontana, J. R. Carini, G. Tripodo, T. Unruh and U. Buchenau
Vibrational dynamics of densified vitreous GeO_2
J. Chem. Phys. accepted (2009).

90. H. Palancher, N. Wieschalla, P. Martin, R. Tucoulou, C. Sabathier, W. Petry, J. Berar, C. Valot and S. Dubois
Uranium-molybden nuclear fuel plates behaviour under heavy ion irradiation: An x-ray diffraction analysis
J. Nucl. Mater., 385, 449 (2009).

91. S. Park, B. Pedersen, M. Meven and H. Krüger
Cation dynamics in six-membered ring and chain lithosilicates
Z. Kristallogr. Suppl., 29, 122 (2009).

92. S. Parnell, E. Babcock, K. Nünighoff, M. Skoda, S. Boag, S. Masalovich, W. C. Chen, R. Georgii, J. Wild and C. Frost
Study of spin-exchange optically pumped ^{3}He cells with high polarisation and long lifetimes
Nucl. Instrum. Methods Phys. Res., Sect. A, 598, 774 (2009).

93. A. Paul and S. Mattauch
Microscopic origin of training in exchange bias system
Appl. Phys. Lett., 95, 092502 (2009).

94. J. I. Pérez-Landazábal, V. Recarte, V. Sánchez-Alarcos, J. A. Rodríguez-Velamazán, M. Jiménez-Ruiz, P. Link, E. Cesari and Y. Chumlyakov
Lattice dynamics and external magnetic field effects in Ni-Fe-Ga alloys
Phys. Rev. B, 80, 4301 (2009).

95. J. Perlich, V. Koertgens, E. Metwalli, L. Schulz, R. Georgii and P. Müller-Buschbaum
Solvent content in thin spin-coated polystrene homopolymer films
Macromolecules, 42, 337 (2009).

96. W. Petry
Nicht zu schaffen - Die für 2010 vereinbarte Umrüstung des Forschungsreaktors FRM II auf Brennelemente mit geringerer Urananreicherung muss bis mindestens 2016 verschoben werden
Physik Journal, 8, 7 (2009).

97. W. Petry
Neutrons made in Garching
Public Service Review Science and Technology, 3, 330 (2009).

98. L. Peyker, C. Gold, E.-W. Scheidt, V. Eyert, W. Scherer, F. May, T. Unruh, P. Link, S. Kehrein, H. Michor and E. Bauer
Evolution of quantum criticality in $CeNi_{9-x}Cu_xGe_4$
J. Phys. Condens. Mat., 21, 235604 (2009).

99. C. Pfleiderer, T. Adams, A. Bauer, W. Biberacher, B. Binz, F. Birkelbach, P. Böni, C. Franz, R. Georgii, M. Janoschek, M. Jonietz, R. Ritz, S. Mühlbauer, W. Münzer, A. Neubauer, B. Pedersen and A. Rosch
Skyrmion lattices in metallic and semiconducting B_20 transition metal compounds
J. Phys.: Conf. Ser. (2009).

100. C. Pfleiderer, A. Neubauer, S. Mühlbauer, F. Jonietz, M. Janoschek, S. Legel, R. Ritz, W. Münzer, C. Franz, P. Niklowitz, T. Keller, R. Georgii, P. Böni, B. Binz and A. Rosch
Quantum order in the chiral magnet MnSi
J. Phys.: Condens. Matter, 21, 164215 (2009).

101. G. Pigozzi, D. Mukherji, R. Gilles, P. Jencus and C. Siemers
The measurement of internal strain in core–shell $Ni_3Si(Al)–SiO_x$ nanoparticles
Nanotechnology, 20, 245704 (2009).

102. P. Pikart, C. Hugenschmidt and K. Schreckenbach
Doppler-broadening (DB). measurement of ionic liquids using a monoenergetic-positron beam
Phys. Status Solidi C, 6, 2487 (2009).

103. R. Ranjan, R. Garg, A. Senyshyn, M. Hedge, H. Ehrenberg and H. Boysen
Magneto-structural study of a Cr-doped $CaRuO_3$
J. Phys.: Condens. Matter, 21, 326001 (2009).

104. R. Ranjan, V. Kothai, R. Garg, A. Senyshyn, A. Agrawal, A. Senyshyn and H. Boysen
Degenerate rhombohedral and orthorhombic states in Ca-substituted $Na_{0.5}Bi_{0.5}TiO_3$
Appl. Phys. Lett., 95, 042904 (2009).

105. J. Rebelo-Kornmeier, M. Hofmann, U. Garbe, C. Randau, J. Repper, A. Ostermann, W. Tekouo, G. Seidl, R. Wimpory, R. Schneider and H. Brokmeier
New developments at materials science diffractometer STRESS-SPEC at FRM II
Adv. X-Ray Anal., 52, 209 (2009).

106. G. Redhammer, G. Roth, W. Treutmann, M. Hoelzel, W. Paulus, G. Andre and C. Pietzonka
The magnetic structure of clinopyroxene-type $LiFeGe_2O_6$ and revised data on multiferroic $LiFeSi_2O_6$
J. Solid State Chem., 182, 2374 (2009).

107. G. J. Redhammer, A. Senyshyn, G. Tippelt, C. Pietzonka, G. Roth and G. Amthauer
Magnetic and nuclear structure and thermal expansion of orthorhombic and monoclinic polymorphs of $CoGeO_3$ pyroxene
Phys. Chem. Miner., 37, 311 (2009).

108. W. van Renterghem, A. Lennaers, S. van den Berghe, M.-C. Anselmet, F. Charollais, P. Lemoine and W. Petry
TEM Investigation of irradiated atomised and ground U(Mo). dispersion fuel, with or without Si added to the matrix
Trans. RERTR 2009, Nov. 1-5, Beijing, China (2009).

109. J. Repper, T. Keller, M. Hofmann, C. Krem-

pasky, W. Petry and E. Werner
Neutron Larmor diffraction for the determination of absolute lattice spacing
Adv. X-Ray Anal., 52, 201 (2009).

110. J. Repper, M. Hofmann, C. Krempaszky, R. Wimpory, E. Werner and W. Petry
Micro stress accumulation in multiphase superalloys
Powder Diffr. J., 24, 65 (2009).

111. M. R. Ripoll and J. Ocenasek
Microstructure and texture evolution during the drawing of tungsten wires
Engineering Fracture Mechanics, 76, 1485 (2009).

112. A. Röhrmoser and W. Petry
Fuel plate temperatures during operation of FRM II
Transactions: RRFM 2009, March, 23-25, Vienna, Austria (2009).

113. O. Russina, M. Beiner, C. Pappas, V. Arrighi, M. Russina, T. Unruh, C. Mullan, C. Hardacre and A. Triolo
Temperature dependence of the primary relaxation in 1-Hexyl-3-methylimidazolium bis{(trifluoromethyl)sulfonyl}imide
J. Phys. Chem. B, 113, 8469 (2009).

114. A. Sarapulova, D. Mikhailova, A. Senyshyn and H. Ehrenberg
Crystal structure and magnetic properties of Li,Cr-containing molybdates $Li_3Cr(MoO_4)_3$, $LiCr(MoO_4)_2$ and $Li_{1.8}Cr_{1.2}(MoO_4)_3$
J. Solid State Chem., 182, 3262 (2009).

115. A. Sazonov, V. Hutanu, M. Meven and G. Heger
Orbital contribution to the magnetic moment in Co_2SiO_4
Acta Crystallogr., Sect. A, 65, 68 (2009).

116. A. Sazonov, M. Meven, V. Hutanu, G. Heger, T. Hansen and A. Gukasov
Magnetic behaviour of synthetic Co_2SiO_4
Acta Crystallogr., Sect. B, 65, 664 (2009).

117. I. Schaaf, S. Cusenza, M. Bamberger, Y. Amran, K. Weiss, L. Meier, U. Wasmuth and M. Hofmann
Phase transition kinetics in austempered ductile iron (ADI)
International Foundry Research, 61, 14 (2009).

118. T. Schaffran, M. Bergmann, I. Grunwald, R. Peschka-Süss, R. Schubert, F. M. Wagner and D. Gabel
Tumoral hemorrhage induced by dodecaborate cluster lipids
Chem. Med. Chem. (2009).

119. B. Schillinger
Various neutron imaging methods at the FRM II reactor source and potential features at a spallation source installation
Nucl. Instrum. Meth. A, 600, 28 (2009).

120. B. Schillinger, P. Böni, C. Breunig, E. Calzada, C. Leroy, M. Mühlbauer and M. Schulz
A neutron optical periscope used for neutron imaging
Nucl. Instrum. Meth. A, 605, 40 (2009).

121. E. Schmid, F. M. Wagner, H. Romm, L. Walsh and H. Roos
Dose-response relationship of dicentric chromosomes in human lymphocytes obtained for the fission neutron therapy facility MEDAPP at the research reactor FRM II
Radiation and Environmental Biophysics 48, 67 (2009).

122. E. Schmid, F. M. Wagner, H. Romm, L. Walsh and H. Roos
RBE of the fission neutron therapy facility MEDAPP at the new research reactor FRM II determined by dicentrics in human lymphocytes
Radiation and Environmental Biophysics (2009).

123. A. Schönleber, J. Angelkort, S. van Smaalen, L. Palatinus, A. Senyshyn and W. Morgenroth
Phase transition, crystal structure, and magnetic order in VOCl
Phys. Rev. B, 80, 064426 (2009).

124. K. Schreckenbach, C. Hugenschmidt, B. Löwe, J. Maier, P. Pikart, C. Piochacz and M. Stadlbauer
Performance of the (n,).-Based Positron Beam Facility NEPOMUC
AIP Conf. Proc., 1090, 549 (2009).

125. M. Schulz, P. Böni, E. Calzada, M. Mühlbauer, A. Neubauer and B. Schillinger
A polarizing neutron periscope for neutron imaging
Nucl. Instrum. Meth. A, 605, 43 (2009).

126. M. Schulz, P. Böni, E. Calzada, M. Mühlbauer and B. Schillinger
Energy-dependent neutron imaging with a double crystal monochromator at the ANTARES facility at FRM II
Nucl. Instrum. Meth. A, 605, 33 (2009).

127. A. Senyshyn, D. Trots, J. Engel, L. Vasylechko, H. Ehrenberg, T. Hansen, M. Berkowski and H. Fuess
Anomalous thermal expansion in rare-earth gallium perovskites: a comprehensive powder diffraction study
J. Phys.: Condens. Matter, 21, 145405 (2009).

128. S. P. Singh, R. Ranjan, A. Senyshyn, D. Trots and H. Boysen
Structural phase transition study of the morphotropic phase boundary compositions of $Na_{0.5}Bi_{0.5}TiO_3$–$PbTiO_3$
J. Phys.: Condens. Matter, 21, 375902 (2009).

129. M. Skidmore, R. Ambrosi, D. Vernon, E. Calzada, G. Benedix, T. Bücherl and B. Schillinger
Prompt gamma-ray activation analysis of Martian analogues at the Forschungs-Neutronenquelle Heinz Maier-Leibnitz neutron reactor and the verification of a Monte Carlo planetary radiation environment model
Nucl. Instrum. Methods Phys. Res., Sect. A, 607, 421 (2009).

130. C. Smuda, S. Busch, R. Schellenberg and T. Unruh
Methyl group dynamics in polycrystalline and liquid ubiquinone Q0 studied by neutron scattering
J. Phys. Chem. B, 113, 916 (2009).

131. L. Sobczyk, M. Prager, W. Sawaka-Dobrowolska, B. G., A. Pawlukojc, E. Grech, L. van Eijck, A. A. Iwanow, S. Rols, J. Wuttke and T. Unruh
The structure and dynamics of methyl groups in diaminodurene (DAD)
J. Chem. Phys., 130, 164519 (2009).

132. A. Stadler, I. Digel, J. Embs, T. Unruh, M. Tehei, G. Zaccai, G. Büldt and G. Artmann
From powder to solution: hydration dependence of human hemoglobin dynamics correlated to body temperature
Biophys. J., 96, 5073 (2009).

133. A. Strzelec, D. Foster, H. Bilheux, C. Daw, C. Rutland, B. Schillinger and M. Schulz
Neutron Imaging of Diesel Particulate Filters
Conf. SAE international, 2009-01-27,35 (2009).

134. I. Strunz, R. Gilles, D. Mukherji, M. Hofmann, D. Genovese, J. Roesler, M. Hoelzel and V. Davydov
SANS contrast dependence on difference in thermal expansions of phases in two-phase alloys
J. Appl. Crystallogr., 42, 981 (2009).

135. Y. Su, P. Link, A. Schneidewind, T. Wolf, P. Adelmann, Y. Xiao, M. Meven, R. Mittal, M. Rotter, D. Johrendt, T. Brueckel and M. Loewenhaupt
Antiferromagnetic ordering and structural phase transition in $Ba_2Fe_2As_2$ with Sn incorporated from the growth flux
Phys. Rev. B, 79, 064504 (2009).

136. F. Tang, P. Link, M. Frontzek, J. Mignot, J. Hoffmann, W. Löser and M. Loewenhaupt
Neutron diffraction study of magnetic structures in single crystal Ho_2PdSi_3 in magnetic fields up to 5T
J. Phys.: Conf. Ser. (2009).

137. D. Trots, A. Senyshyn, L. Vasylechko, R. Niewa, T. Vad, V. Mikhailik and H. Kraus
Crystal structure of $ZnWO_4$ scintillator material in the range of 3-1423 K

J. Phys.: Condens. Matter, 21, 325402 (2009)

138. I. Troyanchuk, D. Karpinsky, A. Sazonov, V. Sikolenko, V. Efimov and A. Senyshyn
Effect of iron doping on magnetic properties of $Sr_{0.78}Y_{0.22}CoO_{2.625+\square}$ -layered perovskite
J. Mater. Sci., 44, 5900 (2009).

139. N. Tsyrulin, T. Pardini, R. Singh, F. Xiao, P. Link, A. Schneidewind, A. Hiess, C. Landee, M. Turnbull and M. Kenzelmann
Quantum effects in a weakly-frustrated S=1/2 two-dimensional Heisenberg antiferromagnet in an applied magnetic feld
Phys. Rev. Lett., 102, 197201 (2009).

140. M. Vaccarro, G. Mangiapia, A. Radulescu, K. Schillén, G. D'Errico, G. Morelli and L. Paduano
Colloidal particles composed of amphiphilic molecules binding gadolinium complexes and peptides as tumor-specific contrast agents in MRI: physicochemical characterization
Soft Matter, 5, 2504 (2009).

141. R. Valicu and P. Böni
Focusing neutron beams to sub-millimeter size
Phys. Proc. (2009).

142. M. Valldor, Y. Sanders and W. Schweika
High spin frustration in Co based Swedenborgites
J. Phys.: Conf. Ser., 145, 012076 (2009).

143. L. Vasylechko, A. Senyshyn and U. Bismayer
Chapter 242 Perovskite-Type Aluminates and Gallates
Handbook on the Physics and Chemistry of Rare Earths, 39, 113 (2009).

144. F. M. Wagner, B. Loeper, T. Bücherl, H. Breitkreutz and W. Petry
Use of fission radiation in life sciences and materials characterization
Transactions: RRFM 2009, March, 23-25, Vienna, Austria (2009).

145. H. Wang, H. Ehrenberg, A. Senyshyn, R. Schierholz, J. Jaud and H. Fuess
Structural investigation on the (1-x) $Pb(Mg_{1/3}Nb_{2/3})O_{3-x}PbTiO_3$ (x=0; 0.21) solid solution using powder diffraction
Z. Kristallogr. Suppl., 30, 407 (2009).

146. E. Welcomme, H. Palancher, C. Sabathier, P. Martin, J. Allenou, C. Valot F. Charollais, M. Anselmet, R. Jungwirth, W. Petry, L. Beck, C. Jarousse, R. Tucoulou and P. Lemoine
Heavy ion irradiation of UMo7/Al fuel: methological approach
Transactions: RRFM 2009, March, 23-25, Vienna, Austria (2009).

147. R. Wimpory, C. Ohms, R. Schneider, A. Youtsos and M. Hofmann
Statistical analysis of residual stress determination using neutron diffraction
International Journal of Pressure Vessels and Piping, 86, 48 (2009).

148. Y. Xiao, Y. Su, M. Meven, R. Mittal, C. Kumar, T. Chatterji, S. Price, J. Persson, N. Kumar, S. Dhar, A. Thamizhavel and T. Brueckel
Magnetic structure of $EuFe_2As_2$ determined by single crystal neutron diffraction
Phys. Rev. B, 80, 174424 (2009).

2010

1. M.O. Acar, P.J. Bouchard, J. Quinta da Fonseca, M.E. Fitzpatrick and S. Gungor
Intergranular Strains in Pre-Strained and Welded Pipes
MSF, 652, 13 (2010).

2. A. Accardo, R. Mansi, A. Morisco, G. Mangiapia, L. Paduano, D. Tesauro, A. Radulescu, M. Aurilio, L. Aloj, C. Arra and G. Morelli
Peptide modified nanocarriers for selective targeting of bombesin receptors
Mol. Biosyst., 6, 878 (2010).

3. T. Adams, S. Mühlbauer, A. Neubauer, W. Münzer, F. Jonietz, R. Georgii, B. Pedersen, P. Böni, A. Rosch and C. Pfleiderer
Skyrmion lattice domains in $Fe_{1-x}Co_xSi$
J. Phys.: Conf. Ser., 200, 032001 (2010).

4. J. Adelsberger, A. Kulkarni, A. Jain, W. Wang, A.M. Bivigou-Koumba, P. Busch, V. Pipich, O. Holderer, T. Hellweg, A. Laschewsky, P. Müller-Buschbaum and C. Papadakis
Thermoresponsive PS-b-PNIPAM-b-PS Micelles: Aggregation behavior, segmental dynamics, and thermal response
Macromolecules, 43, 2490 (2010).

5. V. Alyoshin, I. Romanova, D. Mikhailova, S. Oswald, A. Senyshyn and H. Ehrenberg
Oxygen Nonstoichiometry of Tetragonal $La_{2-x}Sr_xCuO_{4-x}$ (x = 0.15 - 1.2). and in Situ XPS Studies at Elevated Temperatures
J. Phys. Chem. A, 114, 13362 (2010).

6. J. Aufrecht, A. Leineweber, A. Senyshyn and E. Mittemeijer
The absence of a stable hexagonal Laves phase modification ($NbCr_2$) in the Nb \ Cr system
Scripta Mater., 62, 227 (2010).

7. M. Bakr, A. Senyshyn, H. Ehrenberg and H. Fuess
Structural, magnetic, dielectric properties of multiferroic $GaFeO_3$ prepared by solid state reaction and sol-gel methods
J. Alloy. Compd., 492, L20 (2010).

8. A. Bauer, A. Neubauer, C. Franz, W. Münzer, M. Garst and C. Pfleiderer
Quantum Phase Transitions in Single-Crystal $Mn_{1-x}Fe_xSi$ and $Mn_{1-x}Co_xSi$: Crystal Growth, Magnetization, AC Susceptibility and Specific Heat
Phys. Rev. B, 82, 064404 (2010).

9. A. Bhaskar, N. Bramnik, A. Senyshyn, H. Fuess and H. Ehrenberg
Synthesis, characterization and comparison of electrochemical properties of $LiM_{0.5}Mn_{1.5}O_4$ (M=Fe, Co, Ni). at different temperatures
J. Electrochem. Soc., 157, A689 (2010).

10. D. Blanchard, M. Riktor, J. Maronsson, H. Jacobsen, J. Kehres, D. Sveinbjørnsson, E. Bardaji, A. Léon, F. Juranyi, J. Wuttke, B. Hauback, M. Fichtner and T. Vegge
Hydrogen Rotational and Translational Diffusion in Calcium Borohydride from Quasielastic Neutron Scattering and DFT Calculations
J. Phys. Chem. C, 114, 20249 (2010).

11. H. N. Bordallo, L. P. Aldridge, J. Wuttke, K. Fernando, K. W. Bertram and L. C. Pardo
Cracks and Pores - Their Roles in the Transmission of Water Confined in Cementious Materials
Eur. Phys. J. ST, 189, 197 (2010).

12. H. Boysen, I. Kaiser-Bischoff, M. Lerch, S. Berendts, M. Hoelzel and A. Senyshyn
Disorder and Diffusion in Mayenite
Act. Phys. Pol. A, 117, 38 (2010).

13. D. Brauenling, O. Pecher, D. Trots, A. Senyshyn, D. Zherebtsov, F. Haarmann and R. Niewa
Synthesis, Crystal Structure and Lithium Motion of Li_8SeN_2 and Li_8TeN_2
Z. Anorg. Allg. Chem., 636, 936 (2010).

14. H. Breitkreutz, F. M. Wagner and W. Petry
Die Messung schneller Neutronenspektren und darauf aufbauende Entwicklungen in der Neutronentherapie
StrahlenschutzPRAXIS, 2, 48-53 (2010).

15. H. Breitkreutz, F. M. Wagner, R. Schenk, M. Jungwirth and W. Petry
Measurement and Simulation of Fission Neutron Spectra at the MEDAPP Beam at FRM II and subsequent developments
Proceedings of Third European IRPA Congress, 2010, June 14-16, Helsinki, Session 12 (2010).

16. H.-G. Brokmeier
Neutron and Photon Research for Texture and Stress Characterisation of Advanced Materials
Adv. Mater. Res., 146-147, 891 (2010).

17. H.-G. Brokmeier, C. Randau, W. Tekouo, M. Hofmann, W. Gan, M. Mueller, A.

Schreyer and W. Petry
The Robot Concept at STRESS-SPEC for the Characterisation or Semi-Finished Products
MSF, 652, 197 (2010).

18. P. Brown, T. Chatterji, A. Stunault, Y. Su, Y. Xiao, R. Mittal, T. Brueckel, T. Wolf and P. Adelmann
Magnetisation distribution in the tetragonal phase of $BaFe_2As_2$
Phys. Rev. B, 82, 024421 (2010).

19. R. Brusa, S. Mariazzi, L. Ravelli, P. Mazzoldi, G. Mattei, W. Egger, C. Hugenschmidt, B. Löwe, P. Pikart, C. Macchi and A. Somoza
Study of defects in implanted silica glass by depth profiling Positron Annihilation Spectroscopy
Nucl. Instrum. Meth. B, 268, 3186 (2010).

20. J. Burfeindt, H.-G. Berhardt, R. von Heise-Rotenburg, P. Hoffmann, M. Trieloff, W. Schwarz, J. Hopp, E. Jessbeger, H. Hiesinger, X. Li, L. Canella and H. Breitkreutz
^{40}Ar - ^{39}Ar in-situ dating of the lunar surface
Proc. Global Lunar Conference (2010).

21. S. Busch, C. Smuda, L. Pardo and T. Unruh
Molecular Mechanism of Long-Range Diffusion in Phospholipid Membranes Studied by Quasielastic Neutron Scattering
J. Am. Chem. Soc., 132, 3232 (2010).

22. F. Buschenhenke, M. Hofmann, T. Seefeld and F. Vollertsen
Distortion and residual stresses in laser beam weld shaft-hub joints
Physics Procedia, 5, 89 (2010).

23. L. Chang, Y. Su, Y.-J. Kao, Y. Z. Chou, R. Mittal, H. Schneider, T. Brückel, G. Balakrishan and M. R. Lees
Magnetic correlations in the spin ice $Ho_{2-x}Y_xTi_20_7$ as revealed by neutron polarization analysis
Phys. Rev. B, 82, 172403 (2010).

24. L. Chang, Y. Su, H. Schneider, R. Mittal, M. Lees, G. Balakrishan and T. Brückel
Magnetic correlations in pyrochlore spin ice as probed by polarized neutron scattering
J. Phys.: Conf. Ser., 211, 6 (2010).

25. T. Chatterji, Y. Su, G. N. Iles, Y. Lee, A. Khandahar and K. Krishnan
Antiferromagnetic spin correlations in MnO nanoparticles
J. Magn. Magn. Mater., 322, 3333 (2010).

26. T. Chatterji, J. Wuttke and A. Sazonov
Hyperfine interaction in Co_2SiO_4 investigated by high resolution neutron spectroscopy
J. Magn. Magn. Mater., 322, 3148 (2010).

27. G. D'Errico, A. Silipo, G. Mangiapia, G. Vitiello, A. Radulescu, A. Molinaro, R. Lanzetta and L. Paduano
Characterization of liposomes formed by lipopolysaccharides from Burkholderia cenocepacia, Burkholderia multivorans and Agrobacterium tumefaciens: from the molecular structure to the aggregation architecture
Phys. Chem. Chem. Phys., 12, 13574 (2010).

28. I. Dhiman, A. Das, R. Mittal, Y. Su, A. Kumar and A. Radulescu
Diffuse neutron scattering study of magnetic correlations in half-doped $La_{0.5}Ca_{0.5-x}Sr_xMnO_3$ manganites (x=0.1, 0.3, and 0.4)
Phys. Rev. B, 81, 8 (2010).

29. P. Dietzel, P. Georgiev, J. Eckert, R. Blom, T. Strässle and T. Unruh
Interaction of hydrogen with accessible metal sites in the metal-organic frameworks M_2(dhtp) (CPO-27-M; M = Ni, Co, Mg)
Chem. Commun. 46, 4962 (2010).

30. S. Dirndorfer, W. Schmid, H. Breitkreutz, R. Jungwirth, H. Juranowitsch, W. Petry and C. Jarousse
Characterization of bond strength of monolithic two metal layer systems
*Transactions RRFM (*2010).

31. F. Dolci, E. Weidner, M. Hoelzel, T. Hansen, P. Moretto, C. Pistidda, M. Brunelli, M. Fichtner and W. Lohstroh
In-situ neutron diffraction study of magnesium amide/lithium hydride stoichiometric mixtures with lithium hydride excess
Int. J. Hydrogen Energ., 35, 5448 (2010).

32. W. Doster, S. Busch, A. Gaspar, M. Appavou, J. Wuttke and H. Scheer
Dynamical Transition of Protein-Hydration Water
Phys. Rev. Lett., 104, 098101 (2010).

33. S. Eijt, H. Leegwater, H. Schut, A. Anastasopol, W. Egger, L. Ravelli, C. Hugenschmidt and B. Dam
Layer-resolved study of the Mg to MgH_2 transformation in Mg-Ti films with short-range chemical order
J. Alloys Compd., online October 2 (2010).

34. E. Faulhaber, A. Schneidewind, F. Tang, P. Link, D. Etzdorf and M. Loewenhaupt
Polarized neutron scattering on the triple-axis spectrometer PANDA: first results
J. Phys.: Conf. Series, 211, 012031 (2010).

35. C. Franz, C. Pfleiderer, A. Neubauer, M. Schulz, B. Pedersen and P. Böni
Magnetisation of PdNi near Quantum Criticality
J. Phys.: Conf. Series, 200, 012036 (2010).

36. A. Frei, K. Schreckenbach, B. Franke, F. Hartmann, T. Huber, R. Picker, S. Paul and P. Geltenbort
Transmission measurements of guides for ultra-cold neutrons using UCN capture activation analysis of vanadium
Nucl. Instrum. Meth. A, 612, 349 (2010).

37. F. Frey, E. Weidner, B. Pedersen, H. Boysen, M. Burghammer and M. Hoelzel
Pyroxene from martian meteorite NWA856: Structural investigations by X-ray and neutron diffraction
Z. Kristallogr., 255, 287 (2010).

38. X. Frielinghaus, M. Brodeck, O. Holderer and H. Frielinghaus
Confined polymer dynamics on clay platelets
Langmuir, 26, 17444 (2010).

39. M. Frontzek, F. Tang, P. Link, A. Schneidewind, J. U. Hoffmann, J.-M. Mignot and M. Loewenhaupt
Correlation between crystallographic superstructure and magnetic structures in finite magnetic fields: A neutron study on a single crystal of Ho_2PdSi_3
Phys. Rev. B, 82, 174401 (2010).

40. M. Frontzek, F. Tang, P. Link, A. Schneidewind, J.-M. Mignot, J.-U. Hoffmann and M. Loewenhaupt
A Generic Phase Diagram for R_2PdSi_3 (R= Heavy Rare Earth)?
J. Phys.: Conf. Series, 251, 012126 (2010).

41. M. Frotscher, M. Hoelzel and B. Albert
Crystal structures of the metal diborides ReB_2, RuB_2 and OsB_2 from neutron powder diffraction
Z. Anorg. Allg. Chem., 636, 1783 (2010).

42. F. Gaebler, D. Brauenling, A. Senyshyn, W. Schnelle and R. Niewa
Nitrides with Inverse $K_2[NiF_4]$ Structure: $(R_{1-x}Ca_{3+x}N_{1-x/3})$ Bi_2 with R = Rare-Earth Metal
Z. Anorg. Allg. Chem, 636, 1222 (2010).

43. W. Gan, H.-G. Brokmeier, M. Zheng and K. Wu
Textures in multi-directional forged Mg by neutron diffraction
Adv. Mater. Res., 146-147, 879 (2010).

44. A. M. Gaspar, S. Busch, M.-S. Appavou, W. Haeussler, R. Georgii, Y. Su and W. Doster
Using polarization analysis to separate the coherent and incoherent scattering from protein samples
BBA - Proteins and Proteomics, 1804, 76 (2010).

45. H. Gerstenberg, R. Gilles, M. Hofmann, B.

Schillinger and A. Voit
Industrial applications at the FRM II
Neutron News, 21, 13 (2010).

46. H. Gerstenberg, C. Müller, I. Neuhaus and A. Röhrmoser
U-target irradiation at FRM II aiming the production of Mo-99 - A feasibility study
*Transactions RRFM (*2010).

47. S. Ghedia, T. Locherer, R. Dinnebier, D. L. V. K. Prasad, U. Wedig, M. Jansen and A. Senyshyn
High-pressure and high-temperature multianvil synthesis of metastable polymorphs of Bi_2O_3 : Crystal structure and electronic properties
Phys. Rev. B, 82, 024106 (2010).

48. S. V. Ghugare, E. Chiessi, M. T. F. Telling, A. Deriu, Y. Gerelli, J. Wuttke and G. Paradossi
Structure and Dynamics of a Thermoresponsive Microgel around Its Volume Phase Transition Temperature
J. Phys. Chem. B, 114, 10285 (2010).

49. H. Gibhardt, J. Sidoruk, J. Leist, K. Hradil, M. Meven and G. Eckold
Domain redistribution in $SrTiO_3$
Poster at ECM26 (2010).

50. R. Gilles, M. Hofmann, Y. Gao, F. Johnson, L. Iorio, M. Larson, F. Liang, M. Hoelzel and B. Barbier
Probing the Relationship of Long-Range Order in Nanodomain FeCo Alloys with Ternary Additions Using Neutron Diffraction
Metall. Mater. Trans. A, 41, 1144 (2010).

51. M. Grosse, M. van den Berg, C. Goulet, E. Lehmann and B. Schillinger
In-situ neutron radiography investigations of hydrogen diffusion and absorption in zirconium alloys
Nucl. Instrum. Meth. A, online 21 December (2010).

52. M. Grosse, M. van den Berg, E. Lehmann and B. Schillinger
"**Ex-situ and in-situ neutron radiography investigations of the hydrogen uptake of nuclear fuel cladding materials during steam oxidation at 1000°C and above"**
Mater. Res. Soc. Symp. Proc., 1262 (2010).

53. K. Habicht, M. Enderle, B. Fåk, K. Hradil and P. Böni
Neutron Resonance Spin Echo Spectroscopy on Split Modes
J.Phys.: Conf. Ser., 211, 012028 (2010).

54. D. Habs, M. Gross, P. Thirolf and P. Böni
Neutron halo isomers in stable nuclei and their possible application for the production of low energy, pulsed, polarized neutrons beams of high intensity and high brilliance
Appl. Phys. B, online http://dx.doi.org/10.1007/s00340-010-4276-3 (2010).

55. W. Häussler and J. Kindervater
Using polarized Neutrons for elastic and dynamic studies on protein systems
Proceedings AIP CONFERENCE, Melville, New York, L. G. A. D'Amore, eds., Vth International Conference on times of polymers and composites (2010)

56. K. Hain, C. Hugenschmidt, P. Pikart and P. Böni
Spatially resolved positron annihilation spectroscopy on frictionstir weld induced defects
Sci. Technol. Adv. Mater., 11, 025001 (2010).

57. S. Harms, K. Rätzke, F. Faupel, W. Egger, L. Ravelli, A. Laschewsky, W. Wang and P. Müller-Buschbaum
Free Volume and swelling in thin films of poly(N-isopropylacrylamide). end-capped with n-butyltrithiocarbonate
Macromol. Rapid Comm., 31, 1364 (2010).

58. R. Hengstler, L. Beck, H. Breitkreutz, C. Jarousse, R. Jungwirth, W. Petry, W. Schmid, J. Schneider and N. Wieschalla
Physical properties of monolithic U8 wt. %-Mo
J. Nucl. Mater., 402, 74 (2010).

59. M. Hinterstein, M. Hoelzel, H. Kungl, M. Hoffmann, H. Ehrenberg and H. Fuess
In situ neutron diffraction study of electric field induced phase transitions in lanthanum doped lead zirconate titanate
Z. Kristallogr., 226, 155 (2010).

60. M. Hinterstein, M. Knapp, M. Hoelzel, W. Jo, A. Cervellino, H. Ehrenberg and H. Fuess
Field-induced phase transition in $Bi_{1/2}Na_{1/2}TiO_3$-based lead-free piezoelectric ceramics
J. Appl. Crystallogr., 43, 1314 (2010).

61. M. Hinterstein, K. Schoenau, J. Kling, H. Fuess, M. Knapp, H. Kungl and M. Hoffmann
Influence of lanthanum doping on the morphotropic phase boundary of lead zirconate titanate
J. Appl. Phys., 108, 024110 (2010).

62. P. Hoffmann, J. Burfeindt, H.-G. Bernhardt, M. Trieloff, W. Schwarz, J. Hopp, E. Jessberger, H. Hiesinger, X. Li, L. Canella and H. Breitkreutz.
In-situ age determination of planetary surfaces using the ^{40}Ar - ^{39}Ar method
Proceedings: 61th International Astronautical Congress 2010.

63. O. Holderer, H. Frielinghaus, D. Byelov, M. Monkenbusch, J. Allgaier and D. Richter
Dynamical Properties of Decorated Lamellar Microemulsions in the Brush Regime
Z. Phys. Chem., 224, 243 (2010).

64. F. Hosseinzadeh, P. J. Bouchard and J. A. James
Measurements of Residual Stress in a Welded Compact Tension Specimen Using the Neutron Diffraction and Slitting Techniques
Mater. Sci. Forum, 652, 210 (2010).

65. J. Hu, E. Weidner, M. Hoelzel and M. Fichtner
Functions of the $LiBH_4$ in the hydrogen sorption reactions of the 2LiH - $Mg(NH_2)_2$ system
Dalton Trans., 39, 9100 (2010).

66. C. Hugenschmidt
Physics with many positrons
Proceedings of the International School of Physics Enrico Fermi, Course CLXXIV: . A. Dupasquier, A. Mills and R. Brusa, eds (2010).

67. C. Hugenschmidt, J. Mayer and K. Schreckenbach
High-resolution Auger-electron spectroscopy induced by positron annihilation on Fe, Ni, Cu, Zn, Pd, and Au
J. Phys.: Conf. Ser., 225, 012015 (2010).

68. S. Humphrey, R. Mole, R. Thomson and P. Wood
Mixed Alkali Metal/Transition Metal Coordination Polymers with the Mellitic Acid Hexaanion: 2-Dimensional Hexagonal Magnetic Nets
Inorg. Chem., 49, 3441 (2010)..

69. D. S. Inosov, J. T. Park, P. Bourges, D. Sun, Y. Sidis, A. Schneidewind, K. Hradil, D. Haug, C. Lin, B. Keimer and V. Hinkov
Normal-state spin dynamics and temperature-dependent spin-resonance energy in optimally doped $BaFe_{1.85}Co_{0.15}As_2$
Nature Phys., 6, 178 (2010).

70. R. Inoue, R. Biehl, T. Rosenkranz, J. Fitter, M. Monkenbusch, A. Radulescu, B. Farago and D. Richter
Large Domain fluctuations on 50ns timescale enable catalytic activity in phosphoglycerate kinase
Biophys. J., 99, 2309 (2010).

71. S. Ivanova, A. Senyshyn, E. Zhevcheva, K. Tenchev, R. Stoyanova and H. Fuess
Crystal structure, microstructure and reducibility of $LaNi_xCo_{1-x}O_3$ and $LaFe_xCo_{1-x}O_3$ Perovskites ($0 < x \leq 0.5$)
J. Solid State Chem., 183, 940 (2010).

72. A. Jain, A. Kulkarni, A. Bivigou Koumba, W. Wang, P. Busch, A. Laschewsky, P. Müller-Buschbaum and C. Papadakis
Micellar solutions from symmetrical amphiphilic triblock copolymers having a temperature-responsive shell

Macromol. Symp., 291-292, 221 (2010).

73. M. Janoschek, F. Bernlochner, S. Dunsiger, C. Pfleiderer, P. Böni, B. Roessli, P. Link and A. Rosch
Helimagnon bands as universal excitations of chiral magnets
Phys. Rev. B, 81, 214436 (2010).

74. M. Janoschek, P. Fischer, J. Schefer, B. Roessli, V. Pomjakushin, M. Meven, V. Petricek, G. Petrakovskii and L. Besmaternikh
Single magnetic chirality in the magneto-electric $NdFe_3(^{11}BO_3)_4$
Phys. Rev. B, 81, 094429 (2010).

75. M. Janoschek, F. Jonietz, P. Link, C. Pfleiderer and P. Böni
Helimagnons in the Skyrmion Lattice of MnSi
J. Phys.: Conf. Ser., 200, 032026 (2010).

76. F. Jonietz, S. Mühlbauer, C. Pfleiderer, A. Neubauer, W. Münzer, A. Bauer, T. Adams, R. Georgii, P. Böni, R. Duine, K. Everschor, M. Garst and A. Rosch
Spin Transfer Torques at Ultralow Current Densities
Science, 330, 1648 (2010).

77. E. Josten, U. Rücker, S. Mattauch, D. Korolkov, A. Glavic and T. Brückel
Magnetization flop in Fe/Cr GMR multilayers
J. Phys.: Conf. Ser., 211, 8 (2010).

78. T. Jun, F. Rotundo, X. Song, L. Ceschini and A. Korsunsky
Residual strains in AA2024/AlSiCp composite linear friction welds
Mater. & Design, 31, 117 (2010).

79. R. Jungwirth, W. Petry, H. Breitkreutz, W. Schmid, H. Palancher and C. Sabathier
Study of heavy ion irradiated UMo/Al miniplates: Si and Bi addition to Al and UMo ground powders
RRFM 2010 Conference *Proceedings*, RRFM 2010 Transactions (2010).

80. R. Jungwirth, W. Petry, A. Röhrmoser, J. Allenou and X. Iltis
Microstructure of the unirradiated plates
Proceedings of 32nd RERTR 2010 International Meeting on Reduced Enrichment for Research and Test Reactors (2010).

81. W. Kaltner, K. Lorenz, B. Schillinger, A. Jentys and J. Lercher
Using Tomography for Exploring Complex Structured Emission Control Catalysts
Catal. Lett., 134, 24 (2010).

82. S. Kamel, R. Wimpory, M. Hofmann, K. Nikbin and N. O'Dowd
Predicting the effect of compressive and tensile residual stresses in fracture mechanics specimens
Adv. Mater. Res., 89-91, 275 (2010).

83. G. Kaune, M. Haese-Seiller, R. Kampmann, J.-F. Moulin, O. Zhong and P. Müller-Buschbaum
TOF-GISANS investigation of polymer infiltration in mesoporous TiO_2 films for photovoltaic applications
J. Polym. Sci. Pol. Phys., 48, 1628 (2010).

84. D. J. Keeble, R. A. Mackie, W. Egger, B. Löwe, P. Pikart, C. Hugenschmidt and T. J. Jackson
Identification of vacancy defects in a thin film perovskite oxide
Phys. Rev. B, 81, 064102 (2010).

85. L. Keppas, R. Wimpory, D. Katsareas, N. Anifantis and A. Youtsos
Evaluation of residual stress assessment methods using a repair weld benchmark
J. Strain Anal. Eng., 45, 197 (2010).

86. P. Kudejova, L. Canella, R. Schulze, S. Söllradl, J. Jolie and A. Türler
PGAA: The cold neutron prompt gamma-ray activation analysis instrument at FRM II
Neutron News, 21, 9 (2010).

87. A. Kusmin, S. Gruener, A. Henschel, N. De Souza, J. Allgaier, D. Richter and P. Huber
Polymer dynamics in nanochannels of porous silicon: A neutron spin echo study
Macromolecules, 43, 8162 (2010).

88. A. Kusmin, S. Gruener, A. Henschel, O. Holderer, J. Allgaier, D. Richter and P. Huber
Evidence of a sticky boundary layer in nanochannels: A neutron spin echo study of n-hexatriacontane and poly(ethylene oxide) confined in porous silicon
J. Phys. Chem. Lett., 1, 3116 (2010).

89. H. Leegwater, H. Schut, W. Egger, A. Baldi, B. Dam and S. W. Eijt
Divacancies and the hydrogenation of Mg-Ti films with short range chemical order
Appl. Phys. Lett., 96, 121902 (2010).

90. A. Leenaers, S. van den Berghe, F. Charollais, P. Lemoine, C. Jarousse, A. Röhrmoser and W. Petry
EPMA of ground UMo fuel with and without Si added to the matrix, irradiated to high burn up
Transactions of RRFM 2010, Marakech, (2010).

91. J. Leist, J. Sidoruk, H. Gibhardt, K. Hradil, M. Meven and G. Eckold
Domain redistribution and ferroelectric phase transition in SrTiO3 under the influence of an electric field and mechanical stress
Diffusion Fundamentals, 12, 69 (2010).

92. H. Li, Y. Su, T. Chatterji, A. Nefedov, J. Persson, P. Meuffels, Y. Xiao and T. Brueckel
Soft X-ray resonant scattering study of single-crystal $LaSr_2Mn_2O_7$
Eur. Phys. J. B, 74, 457 (2010).

93. S. Li, C. Zhang, M. Wang, H.-q. Luo, X. Lu, E. Faulhaber, A. Schneidewind, P. Link, J. Hu, T. Xiang and P. Dai
Normal-State Hourglass Dispersion of the Spin Excitations in $FeSe_xTe_{1-x}$
Phys. Rev. Lett., 105, 157002 (2010).

94. Y. Li, V. Balédent, G. Yu, N. Barisic, K. Hradil, R. Mole, Y. Sidis, P. Steffens, X. Zhao, P. Bourges and M. Greven
Hidden magnetic excitation in the pseudogap phase of a model cuprate superconductor
Nature, 468, 283 (2010).

95. B. Loeper-Kabasakal, A. Posch, T. Auberger, F. Wagner, S. Kampfer, P. Kneschaurek, W. Petry, P. Lukas and M. Molls
Fission neutron therapy at frmii: Indications and first results
Radiat. Meas., 45, 1436 (2010).

96. B. Loeper-Kabasakal, F. M. Wagner, S. Büdel, M. Harfensteller, A. Voit and R. Henkelmann
Neutrons for Medicine
Neutron News, 21, 16 (2010).

97. B. Löwe, K. Schreckenbach and C. Hugenschmidt
Positron remoderation by gas cooling within an electric drift field
Nucl. Instrum. Meth. B, 268, 529 (2010).

98. E. Maawad, H.-G. Brokmeier, M. Hofmann, C. Genzel and L. Wagner
Stress distribution in mechanically surface treated $Ti_{2.5}Cu$ determined by combining energy-dispersive synchrotron and neutron diffraction
Mat. Sci. Eng. A-Struct., 527, 5745 (2010).

99. S. Mariazzi, P. Bettotti, S. Larcheri, L. Toniutti and R. S. Brusa
High positronium yield and emission into the vacuum from oxidizedtunable nanochannels in silico"
Phys. Rev. B, 81, 235418 (2010).

100. J. Martin, M. Krutyeva, M. Monkenbusch, A. Arbe, J. Allgaier, A. Radulescu, P. Falus, J. Maiz, C. Mijangos, J. Colmenero and D. Richter
Direct Observation of Confined Single Chain Dynamics by Neutron Scattering
Phys. Rev. Lett., 104, 197801 (2010).

101. J. Mayer, C. Hugenschmidt and K. Schreckenbach

High resolution positron annihilation induced Auger electron spectroscopyof the Cu M_2,3VV-transition and of Cu sub-monolayers on Pd and Fe
Surf. Sci., 604, 1772 (2010).

102. J. Mayer, C. Hugenschmidt and K. Schreckenbach
Direct Observation of the Surface Segregation of Cu in Pd by Time-Resolved-Positron-Annihilation-Induced Auger Electron Spectroscopy
Phys. Rev. Lett., 105, 207401 (2010).

103. L. Meier, P. Schaaf, S. Cusenza, D. Höche, M. Bamberger, Y. Amran, K. Weiss, M. Hofmann and H. Hoffmann
Monitoring Phase Transition Kinetics in Austempered Ductile Iron (ADI).
Mater. Sci. Forum, 638-642, 3394 (2010).

104. G. Meierhofer, P. Grabmayr, J. Jochum, P. Kudejova, L. Canella and J. Jolie
Thermal neutron capture cross section of ^{74}Ge
Phys. Rev. C, 81, (2010).

105. M. Meven, Y. Su and Y. Xiao (2010).
Temperature dependent neutron diffraction studies on iron pnictide single crystals
Contribution at ECM26 (2010).

106. D. Mikhailova, N. Narayanan, W. Gruner, A. Voss, A. Senyshyn, D. Trots, H. Fuess and H. Ehrenberg
The Role of Oxygen Stoichiometry on Phase Stability, Structure, and Magnetic Properties of Sr_2CoIrO_6
Inorg. Chem., 49, 10348 (2010).

107. R. Mittal, R. Heid, A. Bosak, T. Forrest, S. Chaplot, D. Lamago, D. Reznik, K. Bohnen, Y. Su, N. Kumar, S. Dhar, A. Thamizhavel, C. Rueegg, M. Krisch, D. McMorrow, T. Brueckel and L. Pintschovius
Pressure dependence of phonon modes across the tetragonal to collapsed tetragonal phase transition in $CaFe_2As_2$
Phys. Rev. B, 81, 144502 (2010).

108. W. Münzer, A. Neubauer, S. Mühlbauer, F. Franz, T. Adams, F. Jonietz, R. Georgii, P. Böni, B. Pedersen, K. Schmid, A. Rosch and C. Pfleiderer
Skyrmion lattice in the doped semiconductor $Fe_{1-x}Co_xSi$
Phys. Rev. B, 81, 041203(R) (2010).

109. D. Mukherji, P. Strunz, R. Gilles, M. Hofmann, F. Schmitz and J. Rösler
Investigation of phase transformations by in-situ neutron diffraction in a Co-Re-based high temperature alloy
Mater. Lett., 64, 2608-2611 (2010).

110. N. Narayanan, D. Mikhailova, A. Senyshyn, D. M. Trots, R. Laskowski, P. Blaha, K. Schwarz, H. Fuess and H. Ehrenberg
Temperature and composition dependence of crystal structures and magnetic and electronic properties of the double perovskites $La_{2-x}Sr_xCoIrO_6$ (0 > x > 2).
Phys. Rev. B, 82, 024403 (2010).

111. R. Niewa, A. Czulucki, M. Schmidt, G. Auffermann, T. Cichorek, M. Meven, B. Pedersen, F. Steglich and R. Kniep
Crystal structure investigations of $ZrAs_xSe_y$ (x > y, x + y ≤ 2). by single crystal neutron diffraction at 300 K, 25 K and 2.3 K
J. Solid State Chem., 183, 1309 (2010).

112. P. Niklowitz, C. Pfleiderer, T. Keller, M. Vojta, Y. Huang and J. Mydosh
Parasitic small-moment antiferromagnetism and nonlinear coupling of hidden order and antiferromagnetism in URu_2Si_2 observed by Larmor diffraction
Phys. Rev. Lett., 104, 106406 (2010).

113. K. Nusser, S. Neueder, G. Schneider, M. Meyer, W. Pyckhout-Hintzen, L. Willner, A. Radulescu and D. Richter
Conformations of silica-poly(ethylene-propylene) nanocomposites
Macromolecules, 43, 9837 (2010).

114. B. Oberdorfer, E.-M. Steyskal, W. Sprengel, W. Puff, P. Pikart, C. Hugenschmidt, M. Zehetbauer, R. Pippan and R. Würschum
In Situ Probing of Fast Defect Annealing in Cu and Ni with a High-IntensityPositron Beam
Phys. Rev. Lett., 105, 146101 (2010).

115. I. H. Oh, K. S. Lee, M. Meven, G. Heger and C. E. Lee
Crystal Structure of LiH_2PO_4 Studied by Single-Crystal Neutron Diffraction
J. Phys. Soc. Jpn., 79, 074606 (2010).

116. L. Orsingher, A. Fontana, E. Gilioli, J. Carini, G. Tripodo, T. Unruh and U. Buchenau
Vibrational dynamics of permanently densified GeO_2 glasses: Densification-induced changes in the boson peak
J. Chem. Phys., 132, 124508 (2010).

117. A. Papagiannopoulos, M. Karayianni, G. Mountrichas, S. Pispas and A. Radulescu
Self-assembled nanoparticles from a block polyelectrolyte in aqueous media: structural characterization by SANS
J. Phys. Chem. B, 114, 7482 (2010).

118. J. Park, D. Inosov, A. Yaresko, S. Graser, D. Sun, P. Bourges, Y. Sidis, Y. Li, J.-H. Kim, D. Haug, A. Inosov, K. Hradil, A. Schneidewind, P. Link, E. Faulhaber, I. Glavatskyy, C. Lin, B. Keimer and V. Hinkov
Symmetry of spin excitation spectra in the tetragonal paramagnetic and superconducting phases of 122- ferropnictides
Phys. Rev. B, 82, 134503 (2010).

119. L. Peyker, C. Gold, E.-W. Scheidt, H. Michor, T. Unruh, A. Senyshyn, O. Stockert and W. Scherer
Crystal field studies on the heavy fermion compound $CeNi_8CuGe_4$
J. Phys.: Conf. Ser., 200, 012160 (2010).

120. C. Pfleiderer
Magnetismus mit Drehsinn
Physik Journal, 9, 25 (2010).

121. C. Pfleiderer, T. Adams, A. Bauer, W. Biberacher, B. Binz, F. Birkelbach, P. Böni, C. Franz, R. Georgii, M. Janoschek, M. Jonietz, T. Keller, R. Ritz, S. Mühlbauer, W. Münzer, A. Neubauer, B. Pedersen and A. Rosch,
Skyrmion lattices in metallic and semiconducting B20 transition metal compounds
J. Phys Condens. Mat., 22, 164207 (2010).

122. C. Pfleiderer, P. Böni, C. Franz, T. Keller, A. Neubauer, P. Niklowitz, P. Schmakat, M. Schulz, Y.-K. Huang, J. Mydosh, M. Vojta, W. Duncan, F. Grosche, M. Brando, M. Deppe, C. Geibel, F. Steglich, A. Krimmel and A. Loidl
Search for Electronic Phase Separation at Quantum Phase Transitions
J. Low Temp. Phys., 161, 167 (2010).

123. E. Pfuhl, J. Voigt, S. Mattauch, D. Korolkov and T. Brückel
Interlayer exchange coupling in Er/Tb superlattices mediated by short range incommensurate Er order
J. Phys.: Conf. Ser., 211 (2010).

124. A. Pichlmaier, V. Varlamov, K. Schreckenbach and P. Geltenbort
Neutron lifetime measurement with the UCN trap-in-trap MAMBO II
Phys. Lett. B, 693, 221 (2010).

125. K. Rätzke, M. Wiegemann, M. Q. Shaikh, S. Harms, R. Adelung, W. Egger and P. Sperr
Open volume in bioadhesive detected by positron annihilation lifetime spectroscopy
Acta Biomater., 6, 2690 (2010).

126. R. Ranjan, R. Garg, V. Kothai, A. Agrawal, A. Senyshyn and H. Boysen
Phases in the (1 - x) $Na_{0.5}Bi_{0.5}TiO_3$-(x) $CaTiO_3$ system
J. Phys - Condens. Mat., 22, 075901 (2010).

127. G. Redhammer, A. Senyshyn, M. Meven, G. Roth, S. Prinz, A. Pachler, G. Tippelt, C. Pietzonka, W. Treutmann, M. Hoelzel, B. Pedersen and G. Amthauer
Nuclear and incommensurate magnetic structure of $NaFeGe_2O_6$ between 5K and 298K and new data on multiferroic $NaFeSi_2O_6$
Phys. Chem. Miner., 38, 139 (2010).

128. J. Repper, T. Keller, M. Hofmann, C. Krempaszky, W. Petry and E. Werner
Neutron Larmor diffraction measurements for materials science
Acta mater., 58, 3459 (2010).

129. J. Repper, P. Link, M. Hofmann, C. Krempaszky, E. Werner and W. Petry
Interphase microstress measurements in IN718 by cold neutron diffraction
Appl. Phys. A-Mater., 99, 565 (2010).

130. Z. Révay, L. Szentmiklósi and Z. Kis
Determination of new k_0 values for prompt gamma activation analysis at Budapest
Nucl. Instrum. Meth. A, 622, 464 (2010).

131. M. Rheinstadter, R. Sattler, W. Haussler and C. Wagner
Dynamics of polymers in elongational flow studied by the neutron spin-echo technique
Physica B, 405, 3690-3693 (2010).

132. J. S. Robinson, D. A. Tanner, C. E. Trueman and R. C. Wimpory
Measurement and Prediction of Machining Induced Redistribution of Residual Stress in the Aluminium Alloy
Exp. Mech., 7449 (2010).

133. M. Rovira-Esteva, A. Murugan, L. C. Pardo, S. Busch, M. D. Ruiz-Martin, M. S. Appavou, J. L. Tamarit, C. Smuda, T. Unruh, F. J. Bermejo, G. J. Cuello and S. J. Rzoska
Microscopic structures and dynamics of high- and low-density liquid trans-1,2-dichloroethylene
Phys. Rev. B, 81, 092202 (2010).

134. W. Sawka-Dobrowolska, G. Bator, L. Sobczyk, E. Grech, J. Nowicka-Scheibe, A. PawlukojÄ‡ and J. Wuttke
"The (2:1). complex of picric acid with tetramethylpyrazine. The structure, IR spectra and tunnel splitting of methyl groups"
J. Mol. Struct., 975, 298 (2010).

135. A. Sazonov, V. Hutanu, M. Meven, G. Heger, A. Gukasov and A. Rogalev
Neutron diffraction and X-ray magnetic circular dichroism studies of the Co_2SiO_4 magnetic properties
J. Phys.: Conf. Ser., 211, 012011 (2010).

136. A. Sazonov, V. Hutanu, M. Meven, G. Heger, T. Hansen and A. Senyshyn
Anomalous thermal expansion of cobalt olivine, Co_2SiO_4, at low temperatures
J. Appl. Crystallogr., 720 (2010).

137. G. Schierning, R. Theissmann, M. Acet, M. Hoelzel, J. Gruendmayer and J. Zweck
Low-temperature transmission electron microscopy study of superconducting Nb_3Sn
Phys. Status Solidi A, 207, 1918 (2010).

138. W. Schmid, S. Dirndorfer, R. Grossmann, H. Juranowitsch and C. Jarousse
Sputtering as a Coating Technique for Monolithic U-Mo Fuel Foils
Transactions RERTR 2010

139. C. Schmidt, F. Groitl, M. Klein, U. Schmidt and W. Häussler
CASCADE with NRSE: Fast Intensity Modulation Techniques used in Quasielastic Neutron Scattering
J. Phys.: Conf. Ser., 251, 012067 (2010).

140. M. Schöbel, H. P. Degischer, S. Vaucher, M. Hofmann and P. Cloetens
Reinforcement architectures and thermal fatigue in diamond particle-reinforced aluminum
Acta Mater., 58, 6421 (2010).

141. M. Schöbel, S. Vaucher, M. Hofmann, P. Cloetens and H. Degischer
Ermüdung von Diamant verstärktem Aluminium untersucht mittels Neutronen und Synchrotron Experimenten
Verbundwerkstoffe, 17. Symposium Verbundwerkstoffe, W. Krenkel, eds., Wiley-VCH Verlag GmbH & Co. KGaA, Weinheim, 93 (2010).

142. A. Schönhals, S. Frunza, T. Frunza, T. Unruh and R. Zorn
Vibrational und molecular dynamics of nanoconfined liquid crystal
Eur. Phys. J. ST, 189, 251 (2010).

143. L. Schulz, W. Schirmacher, A. Omran, V. Shah, P. Böni, W. Petry and P. Müller-Buschbaum
Elastic torsion effects in magnetic nanoparticle diblock-copolymer structures
J. Phys - Condens. Mat., 22, 6 (2010).

144. M. Schulz, P. Böni, C. Franz, A. Neubauer, E. Calzada, M. Mühlbauer, B. Schillinger, C. Pfleiderer, A. Hilger and N. Kardjilov
Comparison of Polarizers for Neutron Radiography
J. Phys.: Conf. Ser., 251, 012068 (2010).

145. M. Schulz, A. Neubauer, S. Masalovich, M. Mühlbauer, E. Calzada, B. Schillinger, C. Pfleiderer and P. Böni
Towards a Tomographic Reconstruction of Neutron Depolarization Data
J. Phys.: Conf. Ser., 211, 012025 (2010).

146. M. Schulz, A. Neubauer, M. Mühlbauer, E. Calzada, B. Schillinger, C. Pfleiderer and P. Böni
Polarized Neutron Radiography with a Periscope
J. Phys.: Conf. Ser., 200, 112009 (2010).

147. M. Schulz, P. Schmakat, C. Franz, A. Neubauer, E. Calzada, B. Schillinger, P. Böni and C. Pfleiderer
Neutron depolarisation imaging: Stress measurements by magnetostriction effects in Ni foils
Physica B, online 5 November (2010).

148. R. Schulze, L. Szentmiklósi, Z. Kis and the Ancient Charm Collaboration
The Ancient Charm Project: New neutron based imaging methods for cultural heritage studies
Archeologia e Calcolatori, 21, (2010).

149. D. Schumacher, S. Mattauch, U. Rücker and T. Brückel
Preparation and analysis of epitaxial Fe monolayers buried in Pe
J. Phys.: Conf. Ser., 211, (2010).

150. A. Senyshyn, G. Redhammer, M. Meven, M. Hoelzel, B. Pedersen, G. Roth, A. Pachler, G. Tippelt, C. Piezonka, W. Treutmann, G. Amthauer and H. Fuess
Nuclear and magnetic structure of $NaFe(GeO_3)_2$ clynopyroxene
XI International conference on crystal chemistry of intermetallic compounds, Collected Abstracts, 33 (2010).

151. A. Senyshyn, B. Schwarz, T. Lorenz, V. Adamiv, Y. Burak, J. Banys, R. Grigalaitis, L. Vasylechko, H. Ehrenberg and H. Fuess
Low-temperature crystal structure, specific heat, and dielectric properties of lithium tetraborate $Li_2B_4O_7$
J. Appl. Phys., 108, 093524 (2010).

152. V. Šepelák, I. Bergmann, A. Feldhoff, F. Litterst, K. Becker, J. Cadogan, M. Hofmann, M. Hoelzel, J. L. Wang, M. Avdeev and S. J. Campbell
Mechanosynthesis of Nanocrystalline $MgFe_2O_4$ - Neutron Diffraction and Mossbauer Spectroscopy
Hyperfine Interact., 198, 67 (2010).

153. J. Sidoruk, J. Leist, H. Gibhardt, M. Meven, K. Hradil and G. Eckold
Quantitative determination of domain distribution in $SrTiO_3$ - competing effects of applied electric field and mechanical stress
J. Phys - Condens. Mat., 22, 235903 (2010).

154. G. Simeoni, T. Bryk, F. Gorelli, M. Krisch, G. Ruocco, M. Santoro and T. Scopigno
The Widom line as the crossover between liquid-like and gas-like behaviour in supercritical fluids
Nature Phys., 5 (2010).

155. S. Stuber, D. Holland-Moritz, T. Unruh and A. Meyer
"Ni self-diffusion in refractory Al-Ni melts"
Phys. Rev. B, 81, 024204 (2010).

156. A. Suchaneck, V. Hinkov, D. Haug, L. Schulz, C. Bernhard, A. Ivanov, K. Hradil, C. Lin, P. Bourges, B. Keimer and Y. Sidis
Incommensurate magnetic order and

dynamics induced by spinless impurities in $YBa_2Cu_3O_{6.6}$
Phys. Rev. Lett., 105, 037207 (2010).

157. F. Tang, P. Link, M. Frontzek, J.-M. Mignot, J.-U. Hoffmann, W. Löser and M. Loewenhaupt
Neutron diffraction study of magnetic structures in single crystal Ho_2PdSi_3 in magnetic fields up to 5T
J. Phys.: Conf. Ser., 251, 012017 (2010).

158. F. Tang, P. Link, M. Frontzek, A. Schneidewind, W. Löser and M. Loewenhaupt
Magnetic excitations of Er_2PdSi_3 studied by inelastic neutron scattering in fields up to 12 T
J. Phys.: Conf. Ser., 251, 012004 (2010).

159. M. Tegel, F. Hummel, Y. Su, T. Chatterji, M. Brunelli and D. Johrendt
Non-stoichiometry and the magnetic structure of Sr_2CrO_3FeAs
Europhys. Lett., 89, 37006 (2010).

160. M. Tegel, T. Schmid, T. Stuerzer, M. Egawa, Y. Su, A. Senyshyn and D. Johrendt
Possible magnetic order and suppression of superconductivity by V doping in Sr_2VO_3FeAs
Phys. Rev. B, 82, 140507 (2010).

161. M. Trapp, T. Gutberlet, F. Juranyi, T. Unruh, B. Deme, M. Tehei and J. Peters
Hydration dependent studies of highly aligned multilamellar lipid membranes by neutron scattering
J. Chem. Phys., 133, 164505 (2010).

162. D. Trots, A. Senyshyn and B. Schwarz
Low temperature structural variations and molar heat capacity of stolzite, $PbWO_4$
J. Solid State Chem., 183, 1245 (2010).

163. N. Tsyrulin, F. Xiao, A. Schneidewind, P. Link, H. Ronnow, J. Gavilano, C. P. Landee, M. Turnbull and M. Kenzelmann
Two-dimensional square-lattice S=1/2 antiferromagnet $Cu(pz)_2(ClO_4)_2$
Phys. Rev. B, 81, 134409 (2010).

164. I. Ulacia, N. Dudamell, F. Galvez, D. Yi, M. Perez-Prado and I. Hurtado
Mechanical behavior and microstructural evolution of a Mg AZ31 sheet at dynamic strain rates
Acta Mater., 58, 2988 (2010).

165. T. Vad, W. Sager, J. Zhang, J. Buitenhuis and A. Radulescu
Experimental determination of resolution function parameters from small-angle neutron scattering data of a colloidal SiO_2 dispersion
J. Appl. Crystallogr., 43, 686 (2010).

166. G. Vajenine, C. Hoch, R. Dinnebier, A. Senyshyn and R. Niewa
A Temperature-dependent Structural Study of anti-ReO_3-type Na_3N: to Distort or not to Distort?
Z. Anorg. Allg. Chem., 636, 94 (2010).

167. J. Voigt, E. Babcock and T. Brückel
Beam transport and polarization at TOPAS, the thermal time-of-flight spectrometer with polarization analysis
J. Phys.: Conf. Ser., 211, 012032 (2010).

168. F. M. Wagner, B. Loeper-Kabasakal and W. Petry
Radiation therapy by use of fast reactor neutrons
M. A. und V. A. Simonenko, eds., Xth Zababakhin Scientific Talks, RFNC - VNIITF, RFNC - VNIITF, Snezhinsk, 245 (2010).

169. L. Wang, C. Davies, R. Wimpory, L. Xie and K. Nikbin
Measurement and simulation of temperature and residual stress distributions from friction stir welding AA2024 Al alloy
Mater. High. Temp., 27, 167 (2010).

170. M. Y. Wang, H. Q. Luo, J. Zhao, C. L. Zhang, M. Wang, K. Marty, S. X. Shi, J. W. Lynn, A. Schneidewind, S. L. Li and P. C. Dai
Electron-doping evolution of the low-energy spin excitations in the iron arsenide superconductor $BaFe_{2-x}Ni_xAs_2$
Phys. Rev. B, 81, 174524 (2010).

171. L. Willner, R. Lund, M. Monkenbusch, O. Holderer, J. Colmenero and D. Richter
Polymer dynamics under soft confinement in a self-assembled system
Soft Mat. 6, 1559 (2010).

172. R. C. Wimpory, U. Wasmuth, J. Rebelo-Kornmeier and M. Hofmann
The Effect of Grain Size on Strain Determination Using a Neutron Diffractometer
Mater. Sci. Forum, 638-642, 2405 (2010).

173. Y. Xiao, Y. Su, H.-F. Li, C. M. N. Kumar, R. Mittal, J. Persson, A. Senyshyn, K. Gross and T. Brueckel
Neutron diffraction investigation of the crystal and magnetic structures in $KCrF_3$ perovskite
Phys. Rev. B, 82, 094437 (2010).

174. Y. Xiao, Y. Su, R. Mittal, T. Chatterji, T. Hansen, S. Price, C. Kumar, J. Persson, S. Matsuishi, Y. Inoue, H. Hosono and T. Brueckel
Neutron diffraction study on phase transition and thermal expansion of SrFeAsF
Phys. Rev. B, 81, 094523 (2010).

175. Y. Xiao, Y. Su, W. Schmidt, K. Schmalzl, C. Kumar, S. Price, T. Chatterji, R. Mittal, L. Chang, S. Nandi, N. Kumar, S. Dhar, A. Thamizhavel and T. Brueckel
Field induced spin reorientation and giant spin-lattice coupling in $EuFe_2As_2$"
Phys. Rev. B, 81, 220406 (R) (2010).

176. G. Yu, Y. Ki, E. M. Motoyama, X. Zhao, N. Barisic, Y. Cho, P. Bourges, K. Hradil, R. A. Mole and M. Greven
Magnetic resonance in the model high-temperature superconductor $HgBa_2CuO_{4+\delta}$
Phys. Rev. B, 81, 064518 (2010).

177. M. F. Zaeh and G. Branner
Investigations on residual stresses and deformations in selective laser melting
Prod. Engineer., 4, 35 (2010).

178. J. Zaikina, T. Mori, K. Kovnir, D. Teschner, A. Senyshyn, U. Schwarz, Y. Grin and A. Shevelkov
Bulk and Surface Structure and High-Temperature Thermoelectric Properties of Inverse Clathrate-III in the Si-P-Te System
Chem.-Eur. J., 16, 12582 (2010).

179. M. Zbiri, R. Mittal, S. Rols, Y. Su, Y. Xiao, H. Schober, S. Chaplot, M. Johnson, T. Chatterji, Y. Inoue, S. Matsuishi, H. Hosono and T. Brueckel
Magnetic lattice dynamics of the oxygen-free FeAs pnictides: how sensitive are phonons to magnetic ordering?
J. Phys - Condens. Mat., 22, 315701 (2010).

180. O. Zimmer, P. Schmidt-Wellenburg, M. Fertl, H.-F. Wirth, M. Assmann, J. Klenke and B. van den Brandt
Ultracold neutrons extracted from a superfluid-helium converter coated with fluorinated grease
Eur. Phys. J. C, 67, 589 (2010).

181. F. Zuniga, F. Garcia-Garcia, M. Hoelzel and A. Reller
$Al_{14}Ba_8La_{26.3}Ru_{0.18}Sr_{53.7}O_{167}$: a variant from the cubic perovskite with isolated RuO_6 units
Acta Crystallogr. C, 66, I50 (2010).

Theses

Habilitation

T. Unruh,
Structure and dynamics of colloidal dispersions on molecular scale
Technische Universität München (2010).

Doctoral theses

B. Bauer
Einkristallzüchtung und Characterisierung Al-reicher komplexer metallischer Phasen in Al-Cr-Fe und benachbarter Phasen
Ludwig-Maximilians-Universität München (2010).

M. Brodeck
A study of polymer melts combining MD simulations and neutron scattering experiments
Forschungszentrum Jülich GmbH (2009)

S. Disch
The spin structure of magnetic nanoparticles and in magnetic nanostructures
Forschungszentrum Jülich GmbH (2010).

S. Garny
Development of a Biophysical Treatment Planning System for the FRM II Neutron Therapy Beamline
Technische Universität München (2009).

A. Hamann
Neutron scattering on strongly correlated electron systems: MnSi, $CeCu_{5.5}$ $Au_{0.5}$, $La_{2-x}Sr_xCuO_4$ and $HgBa_2CuO_{4+d}$
Karlsruher Institut für Technologie (2010).

E. Josten
Magnetische Korrelationen in lateral strukturierten Fe/Cr Schichtsystemen.
Forschungszentrum Jülich GmbH (2009).

J. Mayer
High energy resolution and first time-dependent positron annihilation induced Auger electron spectroscopy
Technische Universität München (2010).

M. Nülle
Spin-echo resolved neutron scattering from self-organized polymer interfaces
Universität Stuttgart (2010)

J. Repper
Einfluss mikroskopischer Eigenspannungen auf die makroskopische Eigenspannungsanalyse mittels Neutronendiffraktion
Technische Universität München

G.-M. Rotaru
Statics and dynamics of polar nanoregions in Pb based ETH relaxors
ETH Zürich (2010).

M. Schulz
Radiography with polarized neutrons
Technische Universität München (2010).

R. Schulze
Prompt gamma-ray 3D-imaging for cultural heritage purposes
Universität zu Köln (2010).

F. Tang
Neutron scattering study on R_2PdSi_3 (R = Ho, Er, Tm). compounds
Technische Universität Dresden (2010).

N. Tsyrulin
Neutron scattering studies of low-dimensional quantum spin systems
ETH Zürich (2010).

M. Zayed
Novel states in magnetic materials under extreme conditions: A high pressure neutron scattering study of the Shastry-Sutherland compound $SrCu_2(BO_3)_2$
ETH Zürich (2010).

Diploma theses

G. Brandl
First measurements of the linewidth in magnetic phases of MnSi using MIEZE
Technische Universität München (2010).

S. Dirndorfer
Tensile tests on monolithic two metal layer systems for research reactor fuels
Technische Universität München (2010).

M. Jungwirth
Bestimmung des Gammaspektrums in einem intensiven Spaltneutronenstrahl
Technische Universität München (2009)

H. Juranowitsch
Querschnittsuntersuchungen an gesputterten Uran-Molybdän-Kernbrennstoffen
Technische Universität München (2010).

J. Lichtinger
Spurenelementnachweis von Lithium in organischem Gewebe mit Neutronen
Technische Universität München (2010).

F. Lipfert
Wässrige Tensid-Modell-Systeme als Fluide für die verbesserte Ausbeute in der Erdölförderung
Technische Universität München (2010).

M. Meyer
Strukturelle Charakterisierung von Polymer-beschichteten SiO_2-Nanopartikeln in Lösung mittels Kleinwinkelstreuung
Forschungszentrum Jülich GmbH (2009).

R. Schenk
Entwicklung und Konstruktion eines Lamellenkollimators für die Neutronentherapie
Technische Universität München (2009)

A. Tischendorf
Spin echo measurements of magnetic fluctations in helical $Mn_{1x}Fe_xSi$
Technische Universität München (2010).

Master theses

S. Chillal
Lattice dynamics of the ferromagnetic shape memory alloy Ni-Mn-Ga
Technische Universität München (2010).

K. Sarkar
Structural characterization of polymers for application in organic photovoltaics
Ludwig-Maximilians-Universität München (2010).

M. Zani
Impact of phantom depth and FRM II neutron beam composition on the relative biological effectiveness (RBE). in human SCC cells irradiated as single cell suspension or as mega-colonies
University College London (2010).

K. Zechmeister
Evaluierung neuer Detektoren für die kombinierte PET/MR-Bildgebung, basierend auf SiPM und schnellen Szintillationskristallen-
Technische Universität München (2010).

Bachelor theses

A. Chacón Roldán
Design of a uniaxial pressure experiment for neutron scattering
Technische Universität München (2010).

A. Egle
Ein Mikrostreifengasdetektor (MSGC). für einen ^3He-CF_4 gefüllten Gasszintillationszähler zum Nachweis thermischer Neutronen
Hochschule für Angewandte Wissenschaften München (2010).

B. Friedl
Temperature dependent Doppler broadening spectroscopy
Technische Universität München (2010).

S. Obermaier
Entwicklung einer Fernsteuerung zur Bedienung von Maschinenachsen auf Basis eines Atmel AT90USB Mikrocontrollers
Hochschule für Angewandte Wissenschaften München (2010).

D. Rudolph
Development of a three axis option on MIRA
Fachhochschule Enschede (2010).

Miscellaneous

K. Eller
Nutzung von Neutronen in der Wissenschaft
Gymnasium Dachau (Facharbeit) (2010).

L. Sarac
Neutronenstreuung am Beispiel einer Mikroemulsion
Graf-Rasso-Gmnasium Fürstenfeldbruck (Facharbeit) (2010).

S. Schmidtner
Aufbau eines Fortgeschrittenenpraktikum-Versuches zur Prompten Gamma Aktivierungsanalyse am FRM II
Technische Universität München (Zulassungsarbeit für Lehramt) (2010).

T. Stölzl
Aufbau eines Motorteststandes für MIRA“
Hochschule für Angewandte Wissenschaften München (Semestral thesis) (2010).

Committees

Strategierat FRM II

Chairman
Prof. Dr. Gernot Heger
RWTH Aachen
Institut für Kristallographie

Members
MRin Dr. Ulrike Kirste
Bayerisches Staatsministerium für
Wissenschaft, Forschung und Kunst

MinR Stefan Kern
Bundesministerium für Bildung und Forschung

Prof. Dr. Georg Büldt
Forschungszentrum Jülich GmbH
Institut für Biologische Informationsverarbeitung

Prof. Dr. Helmut Dosch
Deutsches Elektronen-Synchrotron DESY
Hamburg

Prof. Dr. Dieter Richter
Forschungszentrum Jülich GmbH
Institut für Festkörperphysik

Prof. Dr. Dirk Schwalm
Max-Planck-Institut für Kernphysik
Heidelberg

Prof. Dr. Helmut Schwarz
Technische Universität Berlin
Institut für Chemie

Prof. Dr. Dr. Michael Wannenmacher
Universität Heidelberg
Radiologische Klinik und Poliklinik
Abteilung Strahlentherapie

Prof. Dr. Ewald Werner
Technische Universität München
Lehrstuhl für Werkstoffkunde und -mechanik

Prof. Dr.-Ing. Heinz Voggenreiter
German Aerospace Center (DLR) Köln
Institute of Structure and Design

Prof. Dr. Markus Braden
Universität zu Köln
II. Physikalisches Institut

Honorary Members
MDgt i.R. Jürgen Großkreutz
Prof. Dr. Tasso Springer

Guests
Prof. Dr. Dr. h.c. mult. Wolfgang A. Herrmann
Präsident
Technische Universität München

Prof. Dr. Winfried Petry
Dr. Anton Kastenmüller
Dr. Klaus Seebach
Technische Universität München
Forschungs-Neutronenquelle
Heinz Maier-Leibnitz (FRM II)

Secretary
Dr. Jürgen Neuhaus
Technische Universität München
Forschungs-Neutronenquelle
Heinz Maier-Leibnitz (FRM II)

Instrumentation advisory board
(Subcommittee of the Strategierat)

Chairman
Prof. Dr. Markus Braden
Universität zu Köln
II. Physikalisches Institut

Members
Prof. Dr. Dirk Dubbers
Universität Heidelberg
Physikalisches Institut

Prof. Dr. Michael Gradzielski
Technische Universität Berlin
Institut für Chemie

Prof. Dr. Rainer Hock
Universität Erlangen-Nürnberg
Lehrstuhl für Kristallographie und Strukturphysik

Prof. Dr. Werner Kuhs
Universität Göttingen
GZG Abteilung Kristallographie

Prof. Dr. Martin Müller
Helmholtz-Zentrum Geesthacht
Institut für Werkstoffforschung

Prof. Dr. Stephan Paul
Technische Universität München
Physik Department E18

Prof. Dr. Wolfgang Scherer
Universität Augsburg
Lehrstuhl für Chemische Physik

Prof. Dr. Wolfgang Schmahl
Deputy of the Chairman
Ludwig-Maximilians-Universität München
Fakultät für Geowissenschaften

Dr. habil. Dieter Schwahn
Forschungszentrum Jülich GmbH
Institut für Festkörperforschung

Prof. Dr. Andreas Türler
Universität Bern
Department für Chemie und Biochemie

Prof. Dr. Albrecht Wiedenmann
Institut Laue-Langevin
Grenoble

Prof. Dr. Regine Willumeit
Helmholtz-Zentrum Geesthacht
Institut für Werkstoffforschung

Guests
Prof. Dr. Olaf Kühnholz
Deutsches Elektronen-Synchrotron DESY
Hamburg

MRin Dr. Ulrike Kirste
Bayerisches Staatsministerium für
Wissenschaft, Forschung und Kunst

Prof. Dr. Gernot Heger
RWTH Aachen
Institut für Kristallographie

Prof. Dr. Winfried Petry
Dr. Anton Kastenmüller
Dr. Jürgen Neuhaus
Dr. Klaus Seebach
Technische Universität München
Forschungs-Neutronenquelle
Heinz Maier-Leibnitz (FRM II)

Secretary
Dr. Peter Link
Technische Universität München
Forschungs-Neutronenquelle
Heinz Maier-Leibnitz (FRM II)

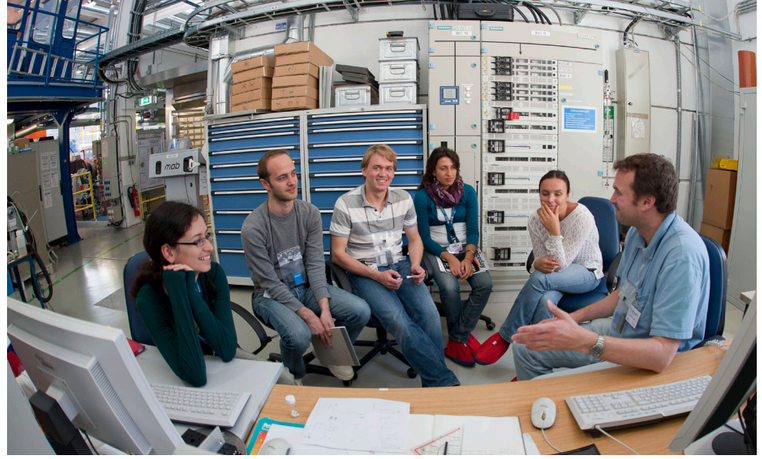

Dr. Olaf Holderer
teaching students at the
JCNS lab course

Committee for industrial and medical use (Subcommittee of the Strategierat)

Chairman
Prof. Dr.-Ing. Heinz Voggenreiter
German Aerospace Center (DLR) Köln
Institute of Structure and Design

Members
Automobile industry
Dr.-Ing. Rainer Simon
BMW AG München

Dr.-Ing. Maik Broda
Ford Forschungszentrum Aachen

Aerospace industry
Dr.-Ing. Rainer Rauh
Airbus Deutschland Bremen

Chemistry and environment
Dr. Jens Rieger
BASF AG Ludwigshafen

Secretary
Dr. Ralph Gilles
Technische Universität München
Forschungs-Neutronenquelle
Heinz Maier-Leibnitz (FRM II)

Scientific committee - Evaluation of beamtime proposals (Subcommittee of the Strategierat)

Members
Dr. Dmitri Argyriou
Helmholtz-Zentrum Berlin
Institut Komplexe Magnetische Materialien

Dr. Françoise Bourrée
CEA Saclay
Laboratoire Léon Brillouin

PD Dr. Reiner Dahint
Universität Heidelberg
Angewandte Physikalische Chemie

Prof. Dr. Antonio Deriu
Università degli Studi di Parma
Dipartimenti di Fisica

Prof. Dr. Helmut Ehrenberg
Leibniz-Institut für Festkörper- und Werkstoffforschung Dresden
Institute for Complex Materials

Dr. Björn Fåk
CEA Grenoble
INAC, SPSMS

Prof. Dr. Rupert Gebhard
Archäologische Staatssammlung München
Abteilung Vorgeschichte

Prof. Dr. Christoph Genzel
Helmholtz-Zentrum Berlin
Institut Angewandte Materialforschung

Dr. Matz Haaks
Universität Bonn
Helmholtz-Institut für Strahlen- und Kernphysik

Dr. Klaus Habicht
Helmholtz-Zentrum Berlin
Institut Methoden und Instrumente der Neutronenstreuung

Dr. Rudi Hackl
Technische Universität München
Walther-Meissner-Institut

Dr. Thomas C. Hansen
Institut Laue-Langevin
Grenoble

Dr. Nikolay Kardjilov
Helmholtz-Zentrum Berlin
Institut Angewandte Materialforschung

Dr. Kim Lefmann
Københavns Universitet
Niels Bohr Institute / Nanofysik

Dr. Eberhard Lehmann
Paul Scherrer Institut
Villigen

Dr. Bernd Leiss
Universität Göttingen
Geowissenschaftliches Zentrum

Dr. Stéphane Longeville
CEA Saclay
Laboratoire Léon Brillouin

Dr. Dieter Lott
Helmholtz-Zentrum Geesthacht
Institut für Werkstofforschung

Dr. Elena Mashkina
Universität Erlangen-Nürnberg
Lehrstuhl für Kristallographie und Strukturphysik

Prof. Dr. Michael Monkenbusch
Forschungszentrum Jülich GmbH
Institut für Festkörperforschung

Prof. Dr. Martin Müller
Helmholtz-Zentrum Geesthacht
Institut für Werkstoffforschung

Dr. Bert Nickel
Ludwig-Maximilians-Universität München
Department für Physik

Prof. Dr. Oskar Paris
Montanuniversität Leoben
Institut für Physik

Prof. Dr. Juan-Manuel Pérez-Mato
Universidad del País Vasco
Departamento de Fisica de la Materia

Dr. Wim Pyckhout-Hintzen
Forschungszentrum Jülich GmbH
Institut für Festkörperforschung

Prof. Dr. Joachim Rädler
Ludwig-Maximilians-Universität München
Department für Physik

Prof. Dr. Klaus Rätzke
Universität zu Kiel
Institut für Materialwissenschaft/ Materialverbunde

Dr. Dmitry Reznik
CEA Saclay
Laboratoire Léon Brillouin

Prof. Dr. Henrik Rønnow
Ecole Polytechnique Fédérale de Lausanne
Laboratory for Quantum Magnetism

Dr. Juerg Schefer
ETH Zürich and Paul Scherrer Institut Villigen
Laboratory for Neutron Scattering

Dr. Henk Schut
TU Delft
Technische Natuurwetenschappen/RRR

Dr. Werner Schweika
Forschungszentrum Jülich GmbH
Institut für Festkörperforschung

Dr. Ivan Sidis
CEA Saclay
Laboratoire Léon Brillouin

Prof. Dr. Jean-Michel Sprauel
Université de la Méditerranée
IUT, Dept. Génie Mécanique et Productique

Members of the scientific committee evaluating beamtime at the proposal round in November.

Dr. Peter Staron
Helmholtz-Zentrum Geesthacht
Institut für Werkstoffforschung

Prof. Dr. Thomas Thurn-Albrecht
Martin-Luther-Universität Halle-Wittenberg
Institut für Physik

Prof. Dr. Helena Van Swgyenhoven
Paul Scherrer Institut
Villigen

Dr. Martin Weik
Institut de Biologie Structurale
Grenoble

Dr. Michael Zawisky
Atominstitut der Österreichischen Universitäten
Wien

Prof. Dr. Oliver Zimmer
Institut Laue-Langevin
Grenoble

Scientific secretaries

Dr. Jürgen Neuhaus
Dr. Ralph Gilles
Dr. Wolfgang Häußler
Dr. Michael Hofmann
Dr. Christoph Hugenschmidt
Dr. Peter Link
Dr. Martin Meven
Dr. Joana Rebelo-Kornmeier
Dr. Tobias Unruh
Technische Universität München
Forschungs-Neutronenquelle
Heinz Maier-Leibnitz (FRM II)

Dr. Astrid Schneidewind
Helmholtz-Zentrum Berlin

TUM Advisory board

Chairman

Prof. Dr. Ewald Werner
Technische Universität München
Lehrstuhl für Werkstoffkunde
und Werkstoffmechanik

Members

Prof. Dr. Peter Böni
Technische Universität München
Physik Department E21

Prof. Dr. Andreas Türler
Universität Bern
Department für Chemie und Biochemie

Prof. Dr. Markus Schwaiger
represented by Prof. Dr. Senekowitsch-Schmidtke
Technische Universität München
Nuklearmedizinische Klinik und Poliklinik
Klinikum Rechts der Isar

Prof. Dr. Bernhard Wolf
Technische Universität München
Heinz Nixdorf-Lehrstuhl für
medizinische Elektronik

Prof. Dr. Arne Skerra
Technische Universität München
Lehrstuhl für Biologische Chemie

Guests

Prof. Dr. Winfried Petry
Dr. Anton Kastenmüller
Dr. Klaus Seebach
Technische Universität München
Forschungs-Neutronenquelle
Heinz Maier-Leibnitz (FRM II)

Scientific steering committee

Chairman

Prof. Dr. Winfried Petry
Technische Universität München
Forschungs-Neutronenquelle
Heinz Maier-Leibnitz (FRM II)

Members

Dr. Hans Boysen
Ludwig-Maximilians-Universität München
Fakultät für Geowissenschaften

Prof. Dr. Bernhard Keimer
Max-Planck-Institut für Festkörperforschung
Stuttgart

Prof. Dr. Dieter Richter
Forschungszentrum Jülich GmbH
Institut für Festkörperforschung

Staff

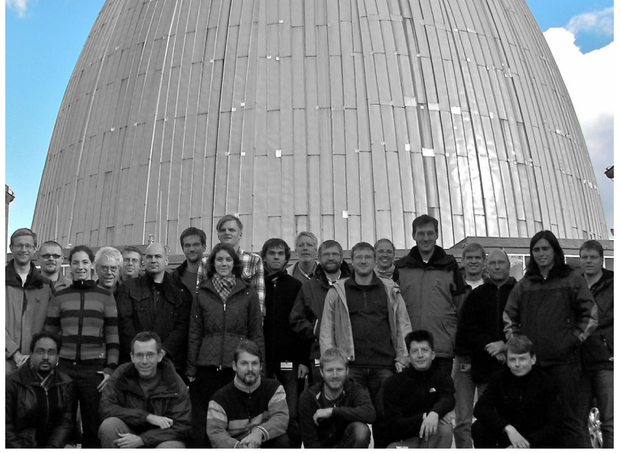

A group photo of scientific staff in front of the Atomic Egg.

[1]Clausthal University of Technology
[2]TUM, Physics Department E21
[3]Max-Planck-Institute for Solid State Research, Stuttgart
[4]TUM, Department for Radiochemistry
[5]Universität der Bundeswehr, München
[6]Helmholtz-Zentrum Berlin
[7]Helmholtz-Zentrum Geesthacht
[8]Technische Universität Darmstadt
[9]Georg-August-Universität Göttingen
[10]RWTH Aachen University
[11]University of Bern
[12]TUM, Physics Department E18

Board of Directors

Scientific director
Prof. Dr. Winfried Petry

Technical director
Dr. Anton Kastenmüller (from 1 April 2010)
Dr. Ingo Neuhaus (until 31 March 2010)

Administrative director
Dr. Klaus Seebach

Experiments

Head
Prof. Dr. Winfried Petry

Deputy
Dr. Jürgen Neuhaus

Executive assistant
Dr. Peter Link

Office
Elisabeth Jörg-Müller
Silvia Valentin-Hantschel

Coordination
Dr. Jürgen Neuhaus
Uwe Reinecke
Harald Türck

Instruments
Alhamdany Nowal[1]
Prof. Dr. Peter Böni[2]
Georg Brandl
Kathrin Buchner[3]
Dr. Thomas Bücherl[4]
Sebastian Busch
Elbio Calzada
Lea Canella[4]
Prof. Dr. Günther Dollinger[5]
Dirk Etzdorf
Dr. Enrico Faulhaber[6]
Jörgen Franke[3]
Florian Gärtner
Dr. Weiman Gan[7]
Dr. Robert Georgii
Dr. Ralph Gilles
Martin Haese-Seiller[7]
Dr. Wolfgang Häußler
Dr. André Heinemann[7]
Tobias Heller
Dr. Michael Hofmann
Dr. Markus Hölzel[8]
Dr. Klaudia Hradil[9]
Dr. Christoph Hugenschmidt
Dr. Vladimir Hutanu[10]
Norbert Jünke[9]
Reinhard Kampmann[7]
Dr. Thomas Keller[3]
Dr. Wilhelm Klein
Dr. Jens Klenke
Dr. Petra Kudejova
Dr. Peter Link
Dr. Birgit Loeper-Kabasakal
Wolfgang Luberstetter
Andreas Mantwill[2]
Dr. Janos Major[3]
Dr. Martin Meven
Dr. Richard Mole
Humphrey Morhenn
Dr. Christoph Morkel
Dr. Jean-François Moulin[7]
Nathalie Munnikes[3]
Dr. Andreas Ostermann
Dr. Bjørn Pedersen
Philip Pikart
Dr. Christian Piochacz
Matthias Pomm[7]
Dr. Joana Rebelo-Kornmeier
Florin Repper
Dr. Julia Repper
Jandal Ringe
Dr. Adrian Rühm[3]
Dr. Burkhard Schillinger
Philipp Schmakat
Martin Schmiele
Dr. Astrid Schneidewind[6]
Prof. Dr. Klaus Schreckenbach[2]
Michael Schulz
Reinhard Schwikowski
Dr. Anatoliy Senyshyn[8]
Günther Seidl
Svatopluk Semecky
Dr. Giovanna Simeoni
Stefan Söllradl[11]
Dr. Oleg Sobolev[9]
Prof. Dr. Torsten Soldner[12]
Martin Stadlbauer
Rainer Stöpler[12]
Dr. Anke Teichert[9]
Alexander Tischendorf
Dr. Tobias Unruh
Martin Völler
Franz-Michael Wagner
Dr. Robert Wimpory[6]
Michael Wipp
Alexander Wolf

Instruments – JCNS
Prof. Dr. Dieter Richter (Director JCNS)
Prof. Dr. Thomas Brückel (Director JCNS)
Dr. Alexander Ioffe (Head of Outstation at FRM II)

Office
Franziska Michel

Dr. Marie-Sousai Appavou
Dr. Earl Babcock
Dr. Wouter Borghols
Dr. Peter Busch
Dr. Zhenyu Di
Andreas Erven
Dr. Henrich Frielinghaus
Christine Gerstl
Thomas Glomann
Marco Gödel
Dr. Günter Goerigk
Dennis Gurzi
Dr. Thomas Gutberlet
Adrian Hamm
Dr. Olaf Holderer
Michael Kerscher
Robert Klopp
Thomas Kohnke
Dr. Denis Korolkov
Harald Kusche
Federik Lipfert
Dr. Stefan Mattauch
Andreas Nebel
Dr. Kirill Nemkovskiy
Klaus Nusser
Vladimir Ossovyi
Dr. Vitaliy Pipich
Dr. Sabine Pütter
Dr. Aurel Radulescu
Alfred Richter
Harald Schneider
Florian Schneider
Dr. Gerald J. Schneider
Dr. Tobias Schrader
Simon Staringer
Dr. Yixi Su

[1]Clausthal University of Technology
[2]TUM, Physics Department E21
[3]Max-Planck-Institute for Solid State Research, Stuttgart
[4]TUM, Department for Radiochemistry
[5]Universität der Bundeswehr, München
[6]Helmholtz-Zentrum Berlin
[7]Helmholtz-Zentrum Geesthacht
[8]Technische Universität Darmstadt
[9]Georg-August-Universität Göttingen
[10]RWTH Aachen University
[11]University of Bern
[12]TUM, Physics Department E18

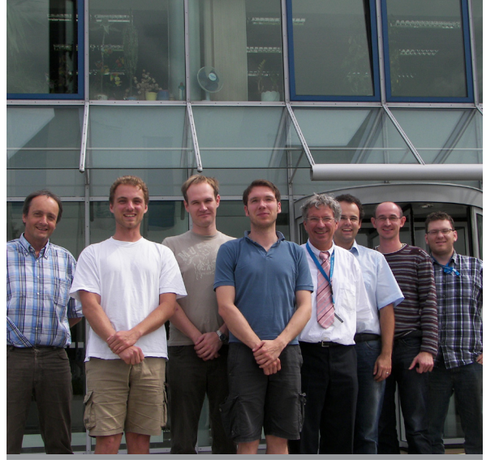

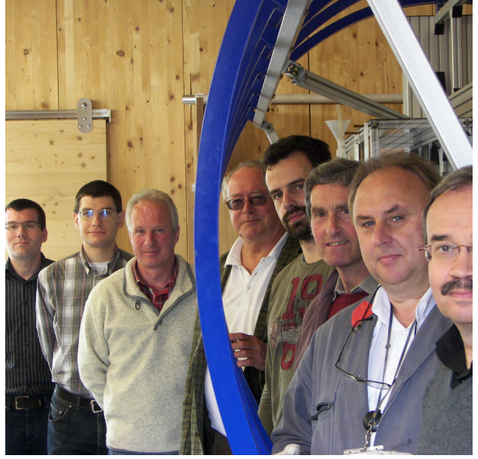

The reactor physics group (left) and the staff of the neutron optics (right).

Dr. Jörg Voigt
Dr. Joachim Wuttke
Dr. Michaela Zamponi

Detectors and electronics
Dr. Karl Zeitelhack
Ilario Defendi
Christian Hesse
Max Panradl
Dr. Markus Petertill
Peter Wind

Sample environment
Dr. Jürgen Peters
Peter Biber
Michael-Marc Fiedler
Markus Göhr
Heinrich Kolb
Alexander Schmidt
Michael Wiesheu
Herbert Weiß
Jank Wenzlaff

Neutron optics
Prof. Dr. Gunther Borchert
Christian Breunig
Robert Iannucci
Eberhard Kahle
Dr. Sergey Masalovich
Andreas Ofner
Tony Reichel
Hermann Schölderle
Roxana Valicu[2]

Reactor physics
Dr. Anton Röhrmoser
Hsin-Yin Chiang
Harald Breitkreutz

Dr. Rainer Großmann
Rainer Jungwirth
Jürgen Sarvas
Robert Schenk
Wolfgang Schmid
Tobias Zweifel

IT Services
Jens Krüger
Jörg Pulz
Harald Wenninger
Josef Ertl
Joao-Paulo Innocente
Nataliya Ivanova
Georg Kaspar
Babette Oberholz
Andreas Steinberger
Jörg Stoll
Manuel Stowasser
Hermann Westermayer

Apprentices at the IT Services
Andreas Erb
Christoph Kick
Alexandra Kornhaas
Alexander Lenz
Alexander Moll
Christian Worf

User office
Dr. Thomas Gutberlet (JCNS)
Dr. Ina Lommatzsch

Public relations
Andrea Voit

Administration

Head
Dr. Klaus Seebach

Deputy
Reinhard Obermeier

Office
Christine Zeller

Staff
Karl-Heinz Drexler
Brigitte Gallenberger
Bernd Heck
Isabella Heinath
Alexandra Ippler
Beate Klein
Karin Lüttig
Sabine Osorio
Günter Wagner
Sabine Wünsch

Visitors' service
Ulrike Kurz
Dott. Bianca Tonin-Schebesta

Reactor Division

Head of reactor division
Ingo Neuhaus (until March 2010)
Anton Kastenmüller (since April 2010)

Sylvia Rubsch
Marita Neuberger
Ludger Stienen
Johann Stephani

Department reactor monitoring and radiation protection
Birgit Wierczinski
Johann Aigner
Christina Auer
Dubravka Bahmet
Rita Bertsch
Wolfgang Dollrieß
Nihad Hodzic
Harry Hottmann
Marcel Kaleve
Vanessa Kindel
Waltraud Kluge
Daniela Lewin
Roland Maier
Petra Müller
Bernhard Neugebauer
Klemens Otto
Susanne Pohle
Thomas Ramel
Adelheid Schindler
Michael Schmidt
Johann Schreiner
David Schrulle
Daniela Strobl
Michaela Uhlmann
Hans-Jürgen Werth
Josef Wetzl

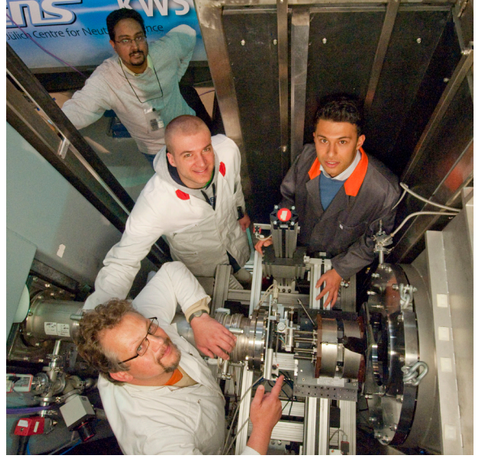

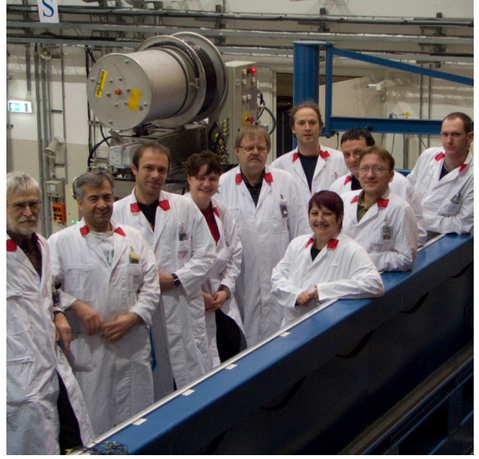

A young student (grey coat) at his internship the instrument KWS-2 with instrument scientists (left to right) Dr. Marie-Sousai Appavou, Frederik Lipfert and Dr. Henrich Frielinghaus (left picture). The Technical Services' Team of the Department Reactor Operation (left page, right picture). The IT-Services group (right page).

Susanne Wolff

Department reactor enhancement

Anton Kastenmüller (until March 2010)
Holger Bamberger
Alen Begic
Christoph Berkel
Wilhelm Bünten
Johann Fink
Thomas Fliegner
Karola Frey
Andreas Galsterer
Christian Herzog
Andreas Huber
Philipp Jüttner
Suzan Kücük
Andreas Kusterer
Manuela Kutschenreuter
Karin Lichtenstein
Ralf Lorenz
Britta Pollom
Andreas Scharl
Robert jun. Schlecht
Michael Schmitt
Uwe Stiegel
Franz-Ludwig Tralmer
Dieter von Plata
Josef Waronitza
Volker Zill

Department reactor operation

Stefan Baldauf
Attila Bancsov
Rainer Becker
Albin Benke
Robert Binsch
Oliver Breu
Andreas Cziasto
Manfred Danner
Christian Feil
Martin Flieher
Stefan Förg
Horst Gampfer
Wolfgang Glashauser
Hubert Groß
Friedrich Gründer
György Guld
Lutz Herdam
Simone Herrmann
Florian Hofstetter
Konrad Höglauer
Thomas Kalk
Georg Kaltenegger
Ulrich Kappenberg
Frank Kewitz
Marc-Guido Krümpelmann
Johann Kund
Adolf Lochinger
Gerd Mauermann
Albert Meilinger
Markus Moser
Klaus Pfaff
Ludwig Rottenkolber
Gerhard Schlittenbauer
Christiane Wickfelder
Michael Wöhner
Christian Ziller
Ismail Zöybek

Department irradiation and sources

Heiko Gerstenberg
Alexander Draack
Jean-Marie Favoli
Wolfgang Fries
Michael Fuß
Wolfgang Lange
Xiaosong Li
Volker Loder
Thomas Metzger
Jens Molch
Christian Müller
Dietmar Päthe
Heike Schulz
Benjamin Schweiger
Katja Singler
Norbert Wiegner
Andreas Wirtz

Department electric and control systems

Roland Schätzlein
Werner Buchner
Andreas Düring
Franz Götz
Robert Krammer
Karl-Heinz Mayr
Üseyin Sarikaya
Johann Wildgruber

FRM (old)

Günter Aigner
Norbert Waasmaier

The FRM II booth at the job fair of the University of Applied Sciences in Munich with Dirk Etzdorf (left) and Herbert Weiß (right) campaign for new students.

Partner institutions

Bayerisches Geoinstitut
Universität Bayreuth
www.bgi.uni-bayreuth.de

Georg-August-Universität Göttingen
Institut für Physikalische Chemie
www.uni-pc.gwdg.de/eckold/

Geowissenschaftliches Zentrum
www.gzg.uni-goettingen.de

Helmholtz-Zentrum Berlin
für Materialien und Energie
www.helmholtz-berlin.de

Helmholtz-Zentrum Geesthacht GmbH
Zentrum für Material- und Küstenforschung
www.hzg.de

Jülich Centre for Neutron Science JCNS
Forschungszentrum Jülich GmbH
www.jcns.info

Ludwig-Maximilians-Universität München
Sektion Kristallographie
www.lmu.de/kristallographie

Sektion Physik
www.softmatter.physik.uni-muenchen.de

Max-Planck-Institut für Festkörperphysik
www.fkf.mpg.de

RWTH Aachen
Institut für Kristallographie
www.xtal.rwth-aachen.de

Institut für Anorganische Chemie
www.ac.rwth-aachen.de

Technische Universität Clausthal
Institut für Werkstoffkunde und Werkstofftechnik
www.iww.tu-clausthal.de

Technische Universität Darmstadt
Fachbereich Material- und Geowissenschaften
www.tu-darmstadt.de/fb/matgeo/

Technische Universität Dresden
Institut für Festkörperphysik
www.physik.tu-dresden.de/ifp

Universität Augsburg
Institut für Physik
www.physik.uni-augsburg.de/cpm/

Universität der Bundeswehr München
Institut für Angewandte Physik und Messtechnik
www.unibw.de/lrt2/

Universität zu Köln
Institut für Kernphysik
www.ikp.uni-koeln.de

II. Physikalisches Institut
www.ph2.uni-koeln.de

Imprint

Publisher:
Technische Universität München
Forschungs-Neutronenquelle
Heinz Maier-Leibnitz (FRM II)
Lichtenbergstr. 1
85747 Garching
Germany

Phone: +49.89.289.14966
Fax: +49.89.289.14995
Internet: www.frm2.tum.de
email: userinfo@frm2.tum.de

Editors:
Dr. Henrich Frielinghaus
Elisabeth Jörg-Müller
Dr. Peter Link
Dr. Ina Lommatzsch
Dr. Jürgen Neuhaus
Dr. Bjørn Pedersen
Andrea Voit

Photographic credits:
Ernst A. Graf, TUM
page 106

Astrid Eckert, Andreas Heddergott, TUM
pages 4, 5 (small), 10 (top left), 96, 97, 110

Thorsten Naeser
page 113

Wenzel Schürmann, TUM
title image, pages 5 (large), 7, 8, 9, 10 (bottom right), 12, 15, 18, 33, 94, 108, 109, 143, 151

Other images: editors, authors, TUM

Design/Graphics:
Ramona Bucher, TUM
Benjamin Sanchez

Typesetting:
Dr. Ina Lommatzsch
Andrea Voit